Transport quantique dans les systèmes complexes

Benoît Grémaud

Université Pierre et Marie Curie - Paris VI
Habiliation à diriger les recherches

Benoît Grémaud
Laboratoire Kastler Brossel

Transport quantique dans les systèmes complexes

Soutenue le 30 juin 2008

devant le jury composé de :
- Oriol Bohigas (examinateur)
- Rémi Carminati (rapporteur)
- Dominique Delande (examinateur)
- Agnès Maître (présidente)
- Sergey Skipetrov (rapporteur)
- Jakub Zakrzewski (rapporteur)

Table des matières

Chapitre 1

Parcours personnel - Introduction

L'essentiel de mon travail de recherche s'est passé au sein du laboratoire Kastler Brossel dans l'équipe *Dynamique des systèmes coulombiens*. Mon arrivée dans cette équipe lors de mon stage de DEA (1992) a été le fruit du hasard : le nombre de propositions de stage étant alors assez limité, nous avions tiré au sort les attributions des stages les plus intéressant ; ayant perdu, j'hésitais entre plusieurs autres stages quand est arrivée (bien après la date requise) la proposition de Dominique Delande, pour laquelle je restait le seul candidat en lice... Ayant extrêmement apprécié le mélange chaos-dynamique quantique, les simulations numériques et l'ambiance de l'équipe, j'ai souhaité y faire mon travail de thèse. Celui-ci a porté sur le problème coulombien à trois corps en mécanique quantique (atome d'hélium...). Après deux années de thèse, je suis parti faire mon service national (94-96) en tant que coopérant scientifique à l'Université Libre de Bruxelles dans l'équipe de Pierre Gaspard, auprès de qui j'ai pu apprendre les subtilités des approches semi-classiques dans le chaos quantique. L'époque (1997) qui a suivi mon travail de thèse a été celle du développement des expériences d'atomes froids dans des potentiels lumineux tels que l'émission stimulée était rendue négligeable. En particulier, il devenait possible de faire des expériences de chaos quantique permettant de mesurer, via les distributions de vitesse, la dynamique du transport chaotique, contrairement aux systèmes coulombiens pour lesquelles les expérimentateurs n'avaient accès qu'à des quantités intégrés et dans l'espace des énergies (section efficace d'ionisation). Ayant eu la chance de rentrer au CNRS (1998) et pour mieux connaître les possibilités des expériences d'atomes froids, j'ai demandé à François Biraben de participer (à mi-temps) à l'élaboration de sa nouvelle expérience de métrologie. Le but était de mesurer très précisément la période des oscillations de Bloch d'atomes froids (masse M) dans un réseau optique, ce qui permettait une détermination très précise du rapport h/M. En parallèle, j'ai commencé à m'intéresser aux phénomènes physiques liés à la propagation d'ondes dans des milieux désordonnés et plus particulièrement à la lumière dans les gaz d'atomes froids. Ce sujet de recherche a de nombreux points communs avec le chaos quantique, puisque l'on s'intéresse à des propriétés de transport mixant les effets d'interférences et une dynamique complexe. Cette thématique avait déjà débuté au sein du groupe, en particulier suite aux expériences menées à l'INLN (Institut Non-Linéaire de Nice) dans l'équipe dirigée par C. Miniatura et R. Kaiser. Dans

ce contexte, les atomes froids se distinguent des diffuseurs classiques par plusieurs aspects : (i) ils sont résonnants, (ii) ils peuvent présenter une structure interne (sous-niveaux Zeeman), (iii) les effets non-linéaires (saturation de la transition atomique) sont facilement observables. Les deux premiers aspects étant bien compris, j'ai donc décidé de m'intéresser aux aspects non-linéaires, sachant que des expériences dans ce domaine étaient envisagés à l'INLN. Ce mélange désordre - non-linéaire, même s'il m'a parfois mené à des difficultés[1] un peu décourageantes[2], m'a conduit à un domaine où la physique est extrêmement riche et intéressante, et qui est devenu d'autant plus d'actualité avec le développement des expériences de transport de condensats de Bose-Einstein dans les potentiels désordonnés.

Au-delà, et anticipant sur les travaux que je présente par la suite, de nombreuses directions restent encore à explorer. En premier lieu, il apparaît clairement que la dynamique (i.e. au-delà des propriétés stationnaires) du transport reste un enjeu important dans la compréhension des phénomènes de localisation dus au désordre. Dans ce contexte, il est très intéressant de remarquer que la dynamique des systèmes désordonnés (instabilités de speckle, de lumière ou d'onde de matière, lasers aléatoires) permet de faire un lien avec le chaos quantique : on peut considérer les systèmes désordonnés comme des systèmes dynamiques chaotiques de haute dimensionnalité (i.e. avec un très grand nombre de degrés de liberté). Dans cette optique, il sera très intéressant de transférer les outils du chaos pour mieux comprendre et analyser la dynamique de ces systèmes instables, par exemple le type de bifurcation, la transition vers le chaos, etc... La moyenne sur le désordre nous amène ensuite à considérer un ensemble de systèmes dynamiques dont on cherche à comprendre non seulement les propriétés moyennes, mais également à caractériser les écarts aux valeurs moyennes. En particulier, dans le régime fortement localisé, on peut s'attendre à ce que la combinaison entre les fluctuations de speckle et les non-linéarités génère des propriétés statistiques particulières, se traduisant probablement dans des comportements singuliers, comme par exemple dans les spectres d'émission des lasers aléatoires. Ensuite, il faut noter que la nature quantique (collective) des objets mis en jeu (onde de matière, champ électromagnétique...) est amenée à jouer un rôle de plus en plus important. Ainsi, dans le cas des lasers aléatoires, l'émission spontanée et plus généralement les corrélations quantiques du champ sont des ingrédients essentiels. De même, dans le cas des ondes de matières, ces aspects quantiques sont cruciaux pour obtenir et expliquer toutes les transitions de phase liées au désordre. Quand on observe l'accroissement du nombre de publications à ce sujet, il est clair que cette direction de recherche est extrêmement riche et prometteuse.

Je tiens à remercier les nombreuses personnes qui m'ont directement ou indirectement permis de mener à bien ce travail de recherche, notamment l'ensemble des membres du laboratoire pour avoir rendu si agréable la vie au jour le jour. Je voudrais également remercier Christian Miniatura et Thomas Wellens dont la collaboration fut à la fois cruciale et enrichissante. Je voudrais remercier particulièrement, Dominique Delande, de m'avoir

[1]Ceci dit, si c'est trop facile, il y a peu de chance que ça soit intéressant...

[2]c'est là qu'on apprend à calibrer ses choix de recherche en fonction de leur intérêt scientifique mais aussi de ses envies personnelles

soutenu toutes ces années, grâce un subtil équilibre entre liberté scientifique (à peine recruté dans son équipe, il m'a laissé aller travailler à mi-temps sur une expérience d'atomes froids), conseils scientifiques et discussions approfondies. Merci à Sandra ! (et Aubin, Adèle et Elvire) ! Tout ce qu'ils m'apportent m'a souvent permis de prendre du recul par rapport à la recherche.

Chapitre 2

Chaos quantique

2.1 Cadre général

La notion de chaos en mécanique classique est apparue, à la fin du XIX^{ème} siècle, avec les travaux de Poincaré sur le problème à trois corps. Plus précisément, il a montré que le nombre de constantes du mouvement était inférieur au nombre de degré de liberté : le système est donc non-intégrable[1]. Peu après, les travaux de Lyapunov ont précisé cette notion en analysant la stabilité des trajectoires classiques : génériquement, i.e. pour un système chaotique, la distance, dans l'espace des phases, entre deux trajectoires, correspondant à des conditions initiales aussi proche que l'on veut, croît exponentiellement avec le temps. Alors que la dynamique est parfaitement déterministe, la moindre incertitude sur les conditions initiales empêche toute prédiction à long terme : c'est le fameux "effet papillon", qui amène parfois un mélange abusif entre chaotique et aléatoire. Au contraire, les travaux des trente dernières années sur le chaos ont montré que l'espace des phases d'un système chaotique est extrêmement bien structuré par une classe particulière de trajectoires : les orbites périodiques. Celles-ci forment en effet un ensemble dense et leur nombre croît exponentiellement avec leur période. De plus, elles jouent un rôle fondamental dans l'analyse des systèmes quantiques.

Du fait du principe d'incertitude de Heisenberg, la notion de chaos n'est pas bien définie pour un système quantique et le terme *chaos quantique* est en fait un raccourci pour désigner l'étude des propriétés quantiques d'un système dont la dynamique classique est chaotique. Essentiellement, on peut distinguer deux approches complémentaires dans le domaine du chaos quantique. D'un coté, les théories semi-classiques ont pour but d'expliquer et de calculer les quantités quantiques (position des niveaux d'énergie, section efficace de photo-ionisation...) à partir des propriétés de la dynamique classique. De l'autre coté, comme la dynamique des systèmes chaotiques présente, aux temps longs, des aspects universels, i.e. indépendants des détails du système considéré, il y a toute une classe d'études basées sur des analyses statistiques des propriétés quantiques, comme par exemple les fluctuations des écarts entre niveaux d'énergie consécutifs.

[1] pour être précis, un système non-intégrable n'est pas nécessairement chaotique, mais cette situation est plutôt pathologique

2.2 Aspects statistiques

2.2.1 Le problème coulombien à trois corps

Ce thème de recherche est la continuation directe de mon travail de thèse, au cours duquel j'ai développé une méthode permettant de calculer numériquement les propriétés des états du problème coulombien à trois corps (atome d'hélium, ion moléculaire H_2^+) : position en énergie, largeur des résonances, fonctions d'onde, forces d'oscillateur... Cette méthode est basée sur l'utilisation de toutes les symétries du système aussi bien géométriques (invariance par rotation, parité, échange des particules) que dynamiques (liées à la forme en $1/r$ des potentiels).

L'allure schématique du spectre de l'hélium est la suivante : le zéro d'énergie est fixé comme étant l'énergie de l'atome doublement ionisé He^{++}. Lorsqu'on lui ajoute un électron, on obtient l'ion He^+ simplement ionisé dont les niveaux forment une série de Rydberg convergeant vers le seuil de double ionisation. A chacun de ces niveaux vient se greffer d'autres séries de Rydberg qui correspondent aux niveaux hydrogénoïdes du deuxième électron. On a donc cette structure d'une infinité de séries de Rydberg, dont les seuils de convergence forment eux-mêmes une série de Rydberg (voir figure 2.1), qui elle converge vers la limite de double ionisation. Au-delà du quatrième seuil de simple ionisation, les premiers niveaux d'une série se mélangent aux séries issues du seuil précédent.

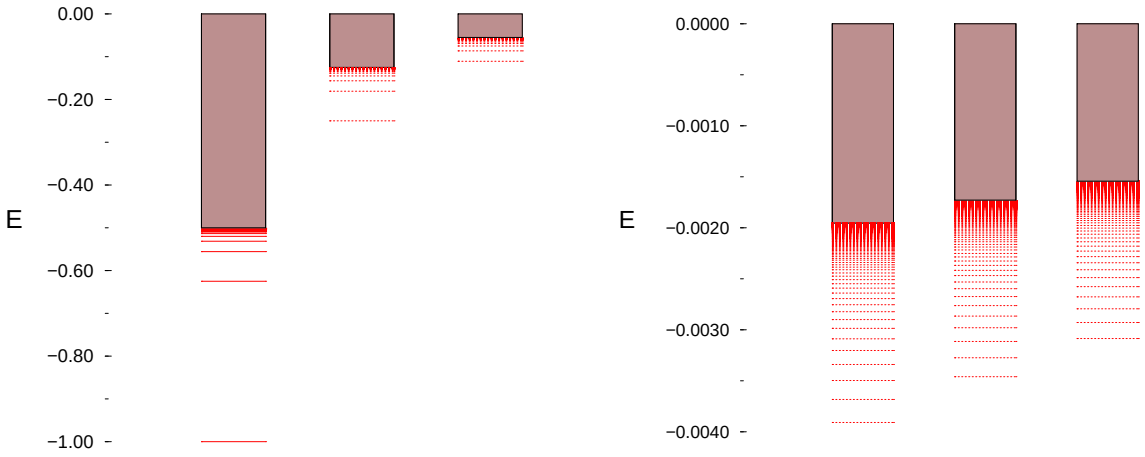

FIG. 2.1 –

Il faut évidemment raffiner cette allure grossière en tenant compte de la répulsion inter-électronique. Un premier effet est de décaler systématiquement les niveaux vers les énergies plus élevées, tout en levant la dégénérescence entre les niveaux de mêmes nombres quantiques principaux n_1 et n_2. Le deuxième effet ne concerne que les séries au-delà du premier seuil, pour lesquelles les deux électrons sont dans des états excités. Tous les états deviennent en fait des résonances. En effet, du fait de l'interaction entre les deux électrons, chaque état est couplé au(x) continuum (continua) issus du ou des seuils plus bas en énergie. Ces résonances correspondent au phénomène physique d'auto-ionisation : un électron en

tombant dans un niveau plus bas, cède suffisamment d'énergie à l'autre électron pour lui permettre de s'ioniser. Ce phénomène est impossible pour les états en dessous du premier seuil d'ionisation et donc ces états restent des états liés, la série est discrète (voir figure 2.1). Ainsi, les niveaux de He^+ donnant les limites d'accumulation des différentes séries de Rydberg deviennent les seuils de simple ionisation.

Dans le cas de l'atome d'hélium, ces méthodes numériques nous avaient permis de reproduire parfaitement les résultats expérimentaux obtenus sur les sections efficaces de photo-ionisation par l'équipe du Prof. G. Kaindl (Institüt für Experimental Physik, Freie Universität, Berlin). Pour ce système, on peut montrer que la dynamique chaotique se manifeste d'autant plus que l'on se rapproche de la limite de double ionisation, c'est-à-dire pour des états pour lesquels les deux électrons sont très excités, ce qui se caractérise, par exemple, par des sections efficaces de photo-ionisation de plus en plus irrégulières.

EUROPHYSICS LETTERS 15 November 1997

Europhys. Lett., **40** (4), pp. 363-368 (1997)

Photo-ionization of the helium atom close to the double-ionization threshold: Towards the Ericson regime

B. Grémaud and D. Delande

Laboratoire Kastler-Brossel, Université Pierre et Marie Curie
4 Place Jussieu, 75005 Paris, France

(received 21 July 1997; accepted in final form 1 October 1997)

PACS. 05.45+b – Theory and models of chaotic systems.
PACS. 31.15Ar – Ab initio calculations.
PACS. 32.80Fb – Photoionization of atoms and ions.

Abstract. – We calculate the photo-ionization cross-section from the ground state of the helium atom, using the complex rotation method and diagonalization of sparse matrices. This produces directly the positions and widths of the doubly excited $^1\mathbf{P}^o$ resonances together with the photo-ionization cross-section. Our calculations up to the $N = 9$ threshold are in perfect agreement with recent experimental data and show the transition from a regular structure at low energy to a chaotic one at high energy, where various resonances strongly overlap.

The helium atom is one of the prototype of atomic systems whose classical dynamics is mainly chaotic and during the past thirty years it has been the matter of numerous studies from both theoretical [1]-[8] and experimental [9]-[11] points of view. But, unlike other atomic systems like, for instance, the hydrogen atom in magnetic field, the effects of chaos are not very well understood and more profound studies are needed. This requires the resolution of the full quantum problem. Especially, one has to take into account all the degrees of freedom and all correlations between the two electrons, as well as the autoionizing character of the doubly excited states.

In this letter, we present numerical calculations of the cross-section of the one-photon photoionization from the ground state of the helium atom and compare them with the recently obtained high-resolution spectra of $^1\mathbf{P}^o$ doubly excited states. The agreement with the most recent experimental data from refs. [10], [11] —up to the $N = 9$ ionization threshold, less than 1 eV from the double-ionization threshold and corresponding to 64 open channels— is excellent for the whole energy range, proving the high efficiency of the method. Predictions for better experimental resolutions are also given. We also show that at low energy the resonances can be classified with respect to Herrick's (N, K, T) approximate quantum numbers [2], ($(N, K)_n$ Lin's simplified notation [3] will be used hereafter). At high energy, this classification progressively breaks down. Eventually, above the $N = 7$ threshold, the various resonances strongly overlap: the mean energy spacing between consecutive resonances becomes smaller than their typical width. Oscillations in the photo-ionization cross-section can then no longer be associated with

individual resonances: random-like fluctuations —known as Ericson fluctuations— should be observed in the cross-section.

The quantum Hamiltonian in atomic units ($\hbar = m_{e^-} = 4\pi\epsilon_0 = e^2 = 1$) is given by

$$H = \frac{\mathbf{P}_1^2 + \mathbf{P}_2^2}{2} - \frac{2}{r_1} - \frac{2}{r_2} + \frac{1}{r_{12}}\,, \tag{1}$$

where $\mathbf{P}_i = -i\hbar\nabla_i$ is the momentum operator of electron i, r_i its distance to the nucleus and r_{12} the inter-electronic distance. All spin-orbits, relativistic and QED effects (at most of the order of a fraction of meV) are neglected, which is consistent with the experimental resolution (of the order of 1 meV). The corrections due the finite mass of the nucleus are taken into account by using the effective values for the double-ionization threshold I_∞ and the Rydberg constant $R_{\rm He}$ given in ref. [10], namely $I_\infty = 79.003$ eV and $R_{\rm He} = 13.6038$ eV.

Using the rotational invariance of the Hamiltonian, the angular dependence of a wave function can be factorized as follows [12]:

$$\Psi_{L\,M} = \sum_{T=-L}^{L} \mathcal{D}^{L\,*}_{MT}(\psi,\theta,\phi)\Phi_T^{(LM)}(x,y,z)\,, \tag{2}$$

where (ψ,θ,ϕ) are Euler angles defining the transformation from the laboratory frame to a molecular-like frame whose z' axis is the inter-electronic axis. $|T|$ is then the Λ (Σ, $\Pi\ldots$) quantum number in a molecule. The $\mathcal{D}^{L\,*}_{MT}$ are the wave functions of the rigid rotor and reduce to the usual spherical harmonics for $T = 0$. Finally (x,y,z) are the perimetric coordinates, symmetric combinations of r_1, r_2 and r_{12}:

$$\begin{cases} x = \quad r_1 + r_2 - r_{12}\,, \\ y = \quad r_1 - r_2 + r_{12}\,, \\ z = -r_1 + r_2 + r_{12}\,. \end{cases} \tag{3}$$

For each pair of good quantum numbers (L,M), we obtain an effective Hamiltonian acting on the different Φ_T's (coupled by Coriolis-like terms). The two remaining discrete symmetries —parity and exchange between the two electrons— are exactly taken into account by adding constraints on the Φ_T's [8].

As stated before, above the first ionization threshold, all states become resonances because of the coupling with the continua (autoionizing states). Using the complex rotation method [5], [13], we obtain these resonances as complex eigenvalues of a complex Hamiltonian $H(\theta)$, which is obtained by the replacements $\mathbf{r}_i \to \mathbf{r}_i e^{\imath\theta}$ and $\mathbf{P}_i \to \mathbf{P}_i e^{-\imath\theta}$, where θ is a real parameter. The fundamental properties of the spectrum of $H(\theta)$ are the following: the continua of H are rotated by an angle 2θ in the lower complex half-plane around their branching point. Each other complex eigenvalue $E_i = \epsilon_i - i\Gamma_i/2$ lies in the lower half-plane and coincides with a resonance of H with energy ϵ_i and width Γ_i. These quantities are independent of θ provided that the complex eigenvalue has been uncovered by the rotated continua. The bound states, which are resonances with zero width, stay on the real axis. This method also allows to compute quantities of physical interest, like photo-ionization cross-section, probability densities or expectation values of operators (*e.g.*, $\cos\theta_{12}$), enlightening the contribution of a given resonance to them. For instance, the cross-section is given by [13]

$$\sigma(\omega) = \frac{4\pi\omega}{c}\mathrm{Im}\sum_i \frac{\langle\overline{E_{i\theta}}|R(\theta)T|g\rangle^2}{E_{i\theta} - E_g - \hbar\omega}\,, \tag{4}$$

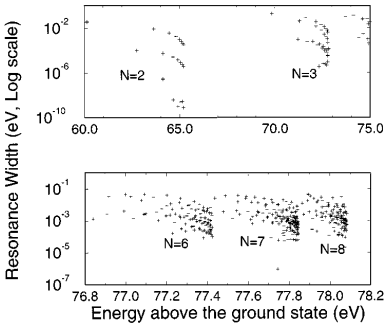

Fig. 1. – Positions (in eV above the ground state) and widths (logarithmic scale) of $^1\mathbf{P}^o$ resonances of the helium atom. The upper plot displays the states below the $N = 2$ and $N = 3$ thresholds, where the various series can be distinguished without ambiguity from their widths, in agreement with Herrick classification of doubly excited states. In the lower plot, displaying the states below the $N = 6, 7, 8$ thresholds, the various series are strongly coupled and overlapping, which is a quantum manifestation of classical chaos in this system.

T is the dipole operator, $\hbar\omega$ is the photon energy, $|g\rangle$ is the ground state (of energy E_g). $\langle\overline{E_{i\theta}}|$ is the transpose of the eigenvector $|E_{i\theta}\rangle$ of $H(\theta)$ for the eigenvalue $E_{i\theta}$ (*i.e.* the complex conjugate of $\langle E_{i\theta}|$). $R(\theta)$ is the rotation operator, essential to obtain the right (complex) oscillator strength.

In the preceding formula, each eigenvalue (resonance or continuum) contributes to the cross-section at energy $\hbar\omega+E_g$, with a Fano profile centered at energy $\mathrm{Re}\, E_i$, of width $-2\mathrm{Im}\, E_i$ whose q parameter is given by [13]

$$q = -\frac{\mathrm{Re}\langle\overline{E_{i\theta}}|R(\theta)T|g\rangle}{\mathrm{Im}\langle\overline{E_{i\theta}}|R(\theta)T|g\rangle}\,. \tag{5}$$

Thus, the Fano q-parameter of one resonance is directly and unambiguously obtained from its associated eigenvector, which is much more efficient than any fitting procedure, especially above the $N = 6$ threshold where the different series strongly overlap (see fig. 1).

For an efficient numerical resolution, the effective Hamiltonian is expanded in the product of three Sturmian-like basis $|n_x\rangle \otimes |n_y\rangle \otimes |n_z\rangle$, one for each perimetric coordinate. The basis states have the following expression:

$$\langle u|n\rangle = \phi_n(u) = \sqrt{\alpha_u} L_n(\alpha_u u) e^{-\alpha_u \frac{u}{2}}\,, \tag{6}$$

where $n_{x,y,z}$ are non-negative integers, $\alpha_{x,y,z}$ are real positive parameters (the scaling parameters) and L_n the n-th Laguerre polynomial. This non-orthogonal basis is associated with a representation of the dynamical group $SO(2,1)$, which gives rise to selection rules. The matrix representation of the effective Hamiltonian in this basis is thus sparse and banded, and the matrix elements are analytically known. Let us emphasize that this approach is "exact" for the non-relativistic He atom and similar to the one used in ref. [8].

For obvious reasons, the basis has to be truncated, the prescription being $n_x + n_y + n_z \leq N_{\max}$ (we used up to $N_{\max} = 58$). The different scaling parameters are related by $\alpha = \alpha_x = 2\alpha_y = 2\alpha_z$, which increases the sparsity of the matrices and gives the correct decrease for r_1 and r_2 going to infinity. The matrices are diagonalized with the Lanczos algorithm, which is

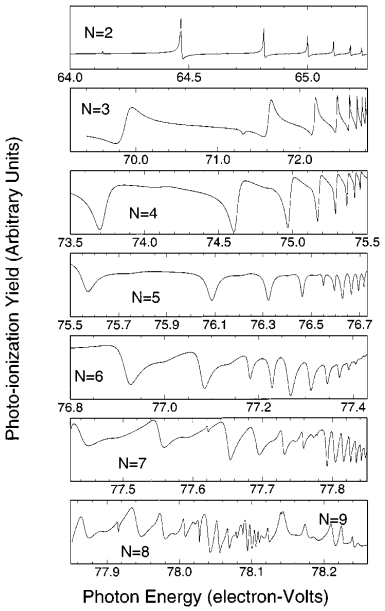

Fig. 2. – Real part of the expectation values of $-N\cos\theta_{12}$ for the various resonances below the $N=2$ and $N=3$ thresholds. As expected from the Herrick classification scheme of doubly excited states, the value is almost constant across a series, although it slightly differs from the predicted value $-(N-1)\leq K\leq(N-1)$. At higher energy, this classification breaks down.

a highly efficient iterative method to obtain few eigenvalues of huge matrices in a short CPU time [14]. Convergence of the results are checked with systematic changes of α and θ. We have thus computed few hundred $^1\mathbf{P}^o$ states, which are the only ones populated in one photon experiment starting from the helium ground state ($^1\mathbf{S}^e$). The resulting cross-section from below the $N=2$ up to above the $N=8$ threshold —the highest energy where experimental spectra are available— is shown in fig. 3, convoluted with a Lorentzian at the experimental resolution (2 meV for $N=2,3$ and 4 meV for $N=4,5,6$) or at a slightly better resolution (1 meV above the $N=6$ threshold). The agreement with the figures from refs. [10], [11] is excellent, emphasizing the efficiency of our calculations. The theoretical positions, linewidths and Fano q-parameters are in good agreement with previous works [8], [10].

Below the $N=2$ (respectively, $N=3$), three (respectively, five) different series are clearly distinguishable, either by their widths (see fig. 1) or by the expectation value of $\cos\theta_{12}$, as shown in fig. 2, where the real part of $-N\cos\theta_{12}$ is plotted (the imaginary part is at least ten times smaller) *vs.* the effective principal quantum number $n_{\rm eff}$ of the outer electron measured from the N-th threshold, proving thus the validity of Herrick's classification in these energy ranges. Still, the chaotic aspect of the helium atom is already observable in the fluctuations of the smallest widths (see fig. 1) (and also in the Fano q-parameters), which will be amplified at higher energies.

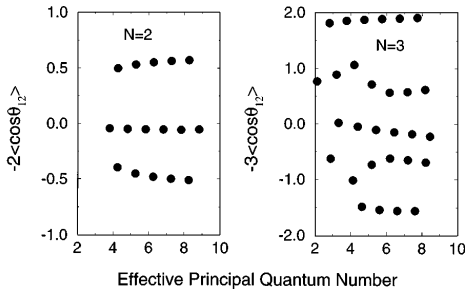

Fig. 3. – Calculated photo-ionization cross-section of the helium atom from the $N = 2$ (upper plot) to the $N = 8$ and 9 (lower plot) series. The raw spectrum has been convoluted by a Lorentzian of width 2 meV for $N = 2, 3$ and 4 meV for $N = 4, 5, 6$ (equal to the experimental resolution) and 1 meV for $N = 7, 8, 9$. The calculated cross-section is in excellent agreement with the experimental results of refs. [10], [11], displaying for $N = 7, 8, 9$ new peaks, not yet experimentally observed. At the highest energies, the various series overlap strongly, leading to irregular fluctuations of the cross-section and breakdown of the classification. Only the fluctuating part of the cross-section is here represented, the smooth background being subtracted.

Below the $N = 5$ and $N = 6$ thresholds, irregularities due to the interaction with the $6, 4_6$ (respectively, $7, 5_7$) state from the upper series are visible, in perfect agreement with the experimental observation. Below the $N = 7$, $N = 8$ and $N = 9$ thresholds, the computed cross-section —represented at a better resolution— reproduces very well the various overlapping series, with an increasing number of perturbers coming from higher series. Furthermore, we show new peaks that are not yet experimentally resolved —such as the members of the $9, 7_n$ series— but whose observation could be possible with a (slight) increase of the experimental resolution and signal-to-noise ratio. In this energy range, the various series are so strongly coupled and overlapping that the approximate Herrick classification breaks

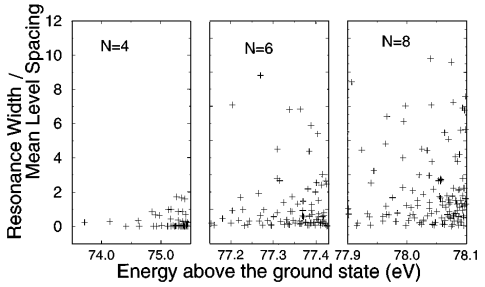

Fig. 4. – Ratio between the widths Γ of the various $^1\mathbf{P}^o$ resonances of the helium atom and the local mean level spacing s, displayed for the $N = 4$, $N = 6$ and $N = 8$ thresholds (from left to right). The transition between the regime of well-separated resonances to the strong overlapping resonances regime is observed. For higher thresholds, the number of resonances lying above the $\Gamma = s$ line will increase, leading to the observation of Ericson fluctuations in the photo-ionization cross-section.

down [15], [16], giving rise to an irregular spectrum, showed by fig. 1 where no general trend can be easily recognized in the widths of the various resonances. This irregularity is the quantum manifestation of the chaotic classical dynamics. In this regime, the photo-ionization cross-section results from the superposition of various overlapping Fano profiles, eventually leading to random-like fluctuations in the cross-section known as Ericson fluctuations [17]. Predicted around the $N = 30$ threshold in the 1-dimensional helium atom [18], this irregular regime takes place at much lower energy in the real helium atom, because of the increased density of states. The ratio between the linewidth Γ and the local mean level spacing s is displayed in fig. 4 for the $N = 4$, $N = 6$ and $N = 8$ thresholds. We clearly see that for $N = 8$, a vast majority of resonances lie above the line $\Gamma/s = 1$, corresponding to the overlapping resonances regime. The published experimental results [11] seem to show irregular fluctuations, the first steps towards the Ericson fluctuations.

In conclusion, our results are, as far as we know, the *ab initio* calculations for the double-excited $^1\mathbf{P}^o$ states of the helium atom at the highest energy ever done. They are in excellent agreement with the presently available experimental data. Importantly, they show that the strongly irregular regime where various resonances overlap leading to Ericson fluctuations in the photo-ionization cross-section is almost reached experimentally, which opens the way to their experimental observation and more generally to a new generation of experiments probing the chaotic aspects of the helium atom.

***

During this research, BG has been financially supported by a fellowship of the European Commission under contract No. ERBCHBICT941418. CPU time on a Cray C98 computer has been provided by IDRIS. Laboratoire Kastler Brossel is laboratoire de l'Université Pierre et Marie Curie et de l'Ecole Normale Supérieure, unité associée 18 du CNRS.

REFERENCES

[1] Cooper J. W., Fano U. and Prats F., *Phys. Rev. Lett.*, **10** (1963) 518.
[2] Herrick D. R. and Sinanoglu O., *Phys. Rev. A*, **11** (1975) 97.
[3] Lin C. D., *Phys. Rev. A*, **29** (1984) 1019.
[4] Feagin J. M. and Briggs J. S., *Phys. Rev. A*, **37** (1988) 4599.
[5] Ho Y. K., *Phys. Rev. A*, **44** (1991) 4154.
[6] Tang J.-Z., Watanabe S. and Matsuzawa M., *Phys. Rev. A*, **48** (1993) 841.
[7] Richter K., Briggs J. S., Wintgen D. and Solov'ev E. A., *J. Phys. B*, **25** (1992) 3929.
[8] Wintgen D. and Delande D., *J. Phys. B*, **26** (1993) L399.
[9] Madden R. P. and Codling K., *Phys. Rev. Lett.*, **10** (1963) 516.
[10] Domke M., Schulz K., Remmers G., Kaindl G. and Wintgen D., *Phys. Rev. A*, **53** (1996) 1424.
[11] Schulz K. *et al.*, *Phys. Rev. Lett.*, **77** (1996) 3086.
[12] Brink D. M. and Satchler G. R., *Angular Momentum* (Academic Press) 1975.
[13] Buchleitner A., Grémaud B. and Delande D., *J. Phys. B*, **27** (1994) 2663.
[14] Ericsson T. and Ruhe A., *Math. Comp.*, **35** (1980) 1251.
[15] Bürgers A., Wintgen D. and Rost J. M., *J. Phys. B*, **28** (1995) 3163.
[16] Grémaud B. and Gaspard P., *Scaled spectroscopy of* $^1\mathbf{S}^e$ *and* $^1\mathbf{P}^o$ *highly excited states of helium*, submitted to *J. Phys. B*.
[17] Ericson T., *Phys. Rev. Lett.*, **5** (1960) 430.
[18] Blümel R., *Phys. Rev. A*, **54** (1996) 5420.

Pour mettre en évidence, le caractère chaotique des spectres, nous avons fait une analyse statistique des propriétés spectrales. En effet, on peut montrer que la distribution des espacements entre les niveaux d'énergie voisins est radicalement différente entre un système chaotique et un système intégrable. Dans le dernier cas, on obtient une loi de poisson, tandis que pour un système chaotique, les distributions statistiques sont bien décrites par la théorie des matrice aléatoires. En particulier, la probabilité de trouver deux états à la même énergie est nulle : c'est la répulsion de niveau, qui traduit le fait qu'un état quantique remplit entièrement l'espace accessible à une énergie donnée.

La difficulté dans le cas de l'hélium est que la dynamique n'est jamais entièrement chaotique. Plus précisément, lorsque l'un des deux électrons est à très grande distance, l'autre électron écrante, en première approximation, l'interaction avec le noyau et on retrouve un atome d'hydrogène. Ceci se traduit par les séries de Rydberg quasi-régulière juste en dessous des seuils de simple ionisation. Pour décrire proprement les propriétés statistiques des spectres, on a donc utilisé un modèle de matrices aléatoires[2] incorporant une partie régulière (non aléatoire) couplée à la partie aléatoire (voir schéma 2.2). Les paramètres

FIG. 2.2 –

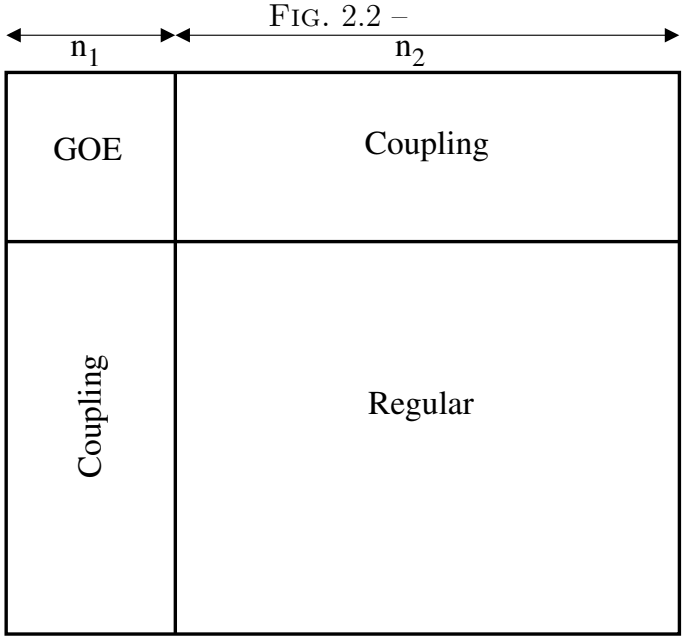

sont d'une part le rapport n_1/n_2 entre la partie chaotique et la partie régulière et d'autre part la force du couplage entre les deux. On a pu alors montrer sur la base des résultats expérimentaux et théorique que plus on s'approchait du seuil de double-ionisation, plus ces deux paramètres augmentaient, démontrant une transition claire vers un régime chaotique, justifiant ainsi que l'aspect aléatoire des signaux expérimentaux observés était bien une manifestation du chaos.

[2] J. Zakrzewski, K. Dupret and D. Delande, Phys. Rev. Lett **74**, 522 (1995)

Statistical Properties of Inter-Series Mixing in Helium: From Integrability to Chaos

R. Püttner,[1] B. Grémaud,[2] D. Delande,[2] M. Domke,[1] M. Martins,[1] A. S. Schlachter,[3] and G. Kaindl[1]

[1]*Institut für Experimentalphysik, Freie Universität Berlin, Arnimallee 14, D-14195 Berlin-Dahlem, Germany*

[2]*Laboratoire Kastler-Brossel T12 E1, Université Pierre et Marie Curie, 4 Place Jussieu, 75005 Paris, France*

[3]*Lawrence Berkeley National Laboratory, 1 Cyclotron Road, Berkeley, California 94720*

(Received 2 June 2000)

The photoionization spectrum of helium shows considerable complexity close to the double-ionization threshold. By analyzing the results from both our recent experiments and *ab initio* three- and one-dimensional calculations, we show that the statistical properties of the spacings between neighboring energy levels clearly display a transition towards quantum chaos.

DOI: 10.1103/PhysRevLett.86.3747 PACS numbers: 32.80.Fb, 05.45.Mt, 31.15.Ar, 31.50.Df

Since the work of Poincaré, it has been known that the general classical three-body problem has only global constants of motion, such as energy and angular momentum. It is thus nonintegrable, since there are not enough nontrivial constants of motion to allow an analytical solution. This typically implies that the phase space is a mixture of regular and chaotic dynamics. Celestial mechanics abounds with examples, e.g., the prototypical earth-moon-sun system [1]. The dynamics of three charged particles is superficially similar since the force law scales also as $1/r^2$, but with two possible signs of the coupling constant. The actual dynamics of the two electrons in helium—the simplest three-body quantum system—is largely chaotic, even for the simplified situation with the nucleus fixed in space. Nonetheless, at low energies the quantum states of helium occur in seemingly regular progressions, labeled by sets of approximately good quantum numbers, and even the doubly excited states have largely been classified [2]. What then are the manifestations of the underlying classical chaos in the quantum spectrum of helium? This is a fundamental question in quantum-classical correspondence, with regard to the nature of semiclassical approximations in the presence of chaos, and in quantum chaos itself. What will be the signatures of the onset of quantum chaos? One expects that the approximate quantum numbers, overviewed, e.g., in Ref. [2], will cease to function, as series of states overlap and mix so strongly that there are essentially no good quantum numbers left, except for the ordering of states by their energies. The doubly excited states of helium are resonances, which will overlap and interact strongly when chaos sets in, giving rise to Ericson fluctuations well known in phenomenological nuclear theory [3]. It is the purpose of this Letter to present new results from experiment and theoretical modeling, which clearly show that the threshold to this new regime has now been passed for the first time in a three-body quantum system with known Hamiltonian.

The $^1P^o$ doubly excited states of helium can be described in Herrick's classification scheme by N, K_n, with N (n) denoting the principal quantum number of the inner (outer) electron, and K the angular-correlation quantum number [4]. For fixed N, the various n, K series converge to the single-ionization threshold $I_N = -4/N^2$ (in Rydberg units). Starting with $N = 5$, the lowest states of the series lie below I_{N-1}. As a consequence, they act as perturbers of the $N - 1$ series, leading to interferences [5], which can be reproduced by numerically complicated *ab initio* calculations [6]. While up to the $N = 8$ threshold, I_8, the effects of the perturbers are quite simple, from I_9 on, the increasing proliferation of perturbers tends to complicate the spectra increasingly, and Herrick's classification starts to break down, at least for a large fraction of states [7].

The most intense series in the spectrum are the principal series with $K = N - 2$. Since $K \cong -N\langle\cos\Theta\rangle$, where Θ is the angle from the nucleus to the two electrons, Θ approaches π for the principal series with large N. Therefore, the experimentally observed series can be related in the semiclassical limit—based on Gutzwiller's trace formula [8]—to periodic orbits of the collinear eZe configuration, with both electrons on opposite sides of the nucleus. It is well known that the classical dynamics of the eZe configuration is strongly chaotic in the radial direction but stable in the angular direction. One can thus expect a mixing of series with different N but constant $N - K$, i.e., a constant number of bending quanta with respect to a collinear eZe configuration [2]. In other words, for highly excited series, $N - K$ is expected to be approximately a good quantum number, while states with the same $N - K$, but different (N, n), strongly interact [6].

There are numerous semiclassical studies of helium based on Gutzwiller's trace formula (see, e.g., Ref. [2]), which aim at understanding the structure of quantum dynamics in terms of its classical counterpart. The present work focuses on the random-matrix approach [9], which deals with universal aspects of quantum chaos, i.e., the general features present in all chaotic quantum systems. We compare the present experimental spectra close to I_9 with the results of our calculations and find excellent agreement. In particular, we show that the statistics of nearest-neighbor level spacings can be well reproduced by a simple random-matrix model adapted to intermittency [10], even though $N - K$ is still a good quantum number. This model mixes regular and chaotic

0031-9007/01/86(17)/3747(4)$15.00

spectra and corresponds to an interaction between regular Rydberg series and chaotic perturbers. Using a simplified one-dimensional (1D) model of helium, we reproduce the transition from the regular to a fully chaotic regime.

The experiments were performed at beam line 9.0.1 of the Advanced Light Source (ALS) in Berkeley, California, using photons with a spectral resolution of $\cong 2$ meV (FWHM) and a setup as described in Ref. [11]. The calculations were performed with the complex-rotation method on a Cray C98, with details given in Ref. [6].

Figure 1(a) shows the spectrum of the $^1P^o$ double excitations in helium in the energy region just below I_9 from 78.1175 to 78.2675 eV, with considerably improved resolution and signal-to-noise ratio as compared to previous results [12]. In Fig. 1(b), we also show the theoretical spectrum, convoluted with a Gaussian of 2-meV width. In the least-squares fit of the measured spectrum, the theoretical values for linewidth and Fano q parameter were used, but the energy positions and intensities of the lines were adjusted to allow for possible deviations between experiment and theory, spectral drifts, and nonlinearities. Details of this analysis have been given elsewhere [11]. As a result, the calculated spectrum matches the experimental data very well. We note that some resonances of the $9, 7_n$ principal and the $9, 5_n$ secondary series reveal Fano parameters $|q| \gg 1$ (up to $|q| \cong 7$, with negative sign, for $9, 7_{14}$), very different from the values found for the principal and secondary series below the I_5 to I_8 thresholds, with $|q| \leq 1$ [12]. However, even these unexpected q values are described well by our calculations. This makes us confident that the energy levels obtained numerically are sufficiently accurate to perform a statistical analysis on the nearest-neighbor spacings (NNS), as discussed in the following.

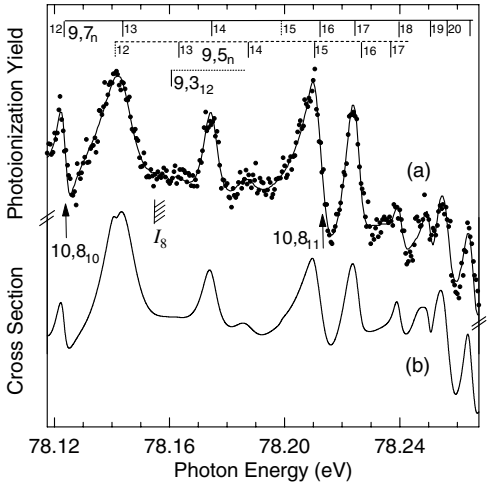

FIG. 1. (a) Double-excitation spectrum of He in the region of the $9, 7_n$ principal Rydberg series, with perturbers $10, 8_{10}$ and $10, 8_{11}$ (vertical arrows). The solid line through the data points represents the best fit. Assignments of the resonances are made by vertical-bar diagrams on top, including resonances of the secondary series $9, 5_n$ and $9, 3_n$. (b) *Ab initio* calculated spectrum in the same region.

The NNS distribution, $P(s)$, measures the distribution of energy spacings between consecutive eigenstates. In order to allow a comparison of large energy spacings far away from threshold with small energy spacings close to threshold, the spectra were unfolded; i.e., the energy spacings were divided by an energy-dependent mean level spacing [13], so that the mean unfolded spacing, s, is unity. For a single unperturbed Rydberg series (or, more generally, for any regularly spaced energy levels), this would lead to a constant unfolded level spacing $s = 1$, i.e., to $P(s) = \delta(s - 1)$, where δ is the delta function. When a good quantum number exists in a system, the spectrum can be divided into various noninteracting but overlapping series. The nearest neighbor of a given state belongs then typically to another series, and the energies of neighboring states are thus completely uncorrelated, giving rise to a Poisson distribution, $P(s) = \exp(-s)$. This happens, e.g., in integrable multidimensional systems, but also if several irregular series overlap without interaction. For a fully chaotic system, the prediction for $P(s)$ can be derived from random-matrix theory. Because of time reversal symmetry of the system, a Gaussian orthogonal ensemble (GOE) of random matrices [13] is used resulting in $P(s)$ to be very close to a Wigner distribution, $P(s) = \frac{\pi}{2} s \exp(-\pi s^2/4)$. Since the number of energy levels for the statistical analysis is rather limited in the present case, one obtains a rather noisy $P(s)$. We therefore use the cumulative NNS distribution, $N(s) = \int_0^s P(x)\, dx$, leading to $N(s) = 1 - \exp(-s)$ and $N(s) = 1 - \exp(-\pi s^2/4)$ for a Poisson and a Wigner distribution, respectively.

The spectra were analyzed by two different procedures: (i) globally by considering all resonances regardless of the series to which they belong; (ii) individually for each series associated with a given value of $N - K$.

We first analyze by the global procedure (i) the calculated levels in the energy region 78.1000–78.2662 eV, where there are 112 resonances, most of them from the $N = 9$ series, with perturbers from higher series. The cumulative NNS distribution is shown in Fig. 2(a) together with a cumulative Poisson distribution. The agreement is very good, showing that an approximately good quantum number exists. This is not surprising, since one can identify experimentally states with different $N - K$ [see Fig. 1(a)]. Occasionally, these states are mixed with other series (in the vicinity of perturbers), but $N - K$ is still approximately a good quantum number. This is also partly true for other series not observed in the experiment [14]: the series with positive K are almost independent, while those with negative K are significantly coupled. In the full spectrum, the various $N - K$ series are superimposed with rather weak mixing, resulting mainly in an uncorrelated

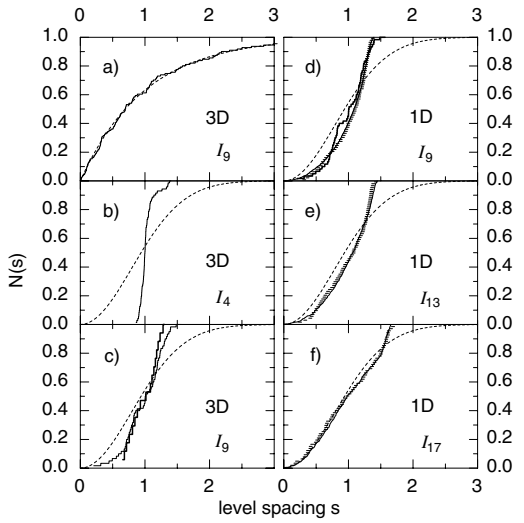

FIG. 2. (a)–(c) Cumulative NNS distributions for the $^1P^o$ states of helium below (b) I_4 and (a),(c) I_9. (a) Global analysis using all levels below I_9. The data (solid line) agree very well with a cumulative Poisson prediction (dashed line). (b),(c) Distributions below I_4 and I_9, respectively, obtained by analyzing separately individual series with different K. For I_9 (c), the bold line is the distribution derived from experiment. (d)–(f) Cumulative NNS distributions for singlet states of 1D helium (horizontal bars) below I_9, I_{13}, and I_{17}, respectively. The solid lines are the fit results (see text). The bold solid line in (d) is the NNS distribution for states of 3D helium below I_9. The dashed lines in (b)–(f) represent the cumulative Wigner distribution.

ensemble of levels, which thus obeys Poisson statistics. This complies with the stability of the eZe collinear configurations with respect to off-collinear perturbations.

Hence, a relevant data analysis must be done individually for each $N - K$ series [procedure (ii)]. The cumulative NNS distributions, $N(s)$, obtained in this way, are shown in Fig. 2(b) for resonances below I_4 and in Fig. 2(c) for those below I_9. The statistical accuracies are limited due to the relatively small number of data points with 71 (60) spacings for I_4 (I_9). Moreover, for I_9, only series with K between 0 and 8 were unfolded because of K mixing for negative K values, while for I_4 all series are used. The I_4 distribution clearly reflects the quasiregularity in this energy region, as it is very close to a step function, which results from integrating over a delta function. This is the statistical analog to the fact that the spectrum below I_4 is composed only of $N = 4$ states and can be described by single-channel quantum defect theory. Below I_9, the situation has slightly changed, although the distribution still does not match a cumulative Wigner distribution. It means that the relative density of chaotic perturbers with $N > 9$ has increased as well as their interaction with the various Rydberg series. The bold line in Fig. 2(c) shows $N(s)$ using only the experimentally observed series $N - K = 2$ and 4. Because of the small number of 17 spacings, the statistics are relatively poor, but it is striking that the bold line closely follows the solid line. As a consequence, *the spectrum in Fig. 1(a) represents the first experimental verification of a transition of the NNS distribution towards quantum chaos in a three-body Coulomb system.*

The complex numerical calculations for 3D helium render it difficult to obtain enough spacings for a quantitative analysis in the case of $N > 9$. However, the fact that $N - K$ remains approximately a good quantum number means that the bending motion can be essentially frozen in the eZe configuration. In other words, the quantum properties are essentially those of 1D helium, a system that has only 2 degrees of freedom. This leads to much simpler numerics allowing higher ionization thresholds to be reached. We have therefore calculated the resonances of 1D helium below I_9, I_{13}, and I_{17} using a new approach (banded sparse matrix representation of the Hamiltonian in a 1D perimetric basis, in the spirit of Ref. [6]) that represents a significant improvement over previous methods [15].

In order to improve statistics, we calculated spacings in a given energy region for slightly different values of the nuclear charge Z, from $1/Z = 0.45$ to $1/Z = 0.55$, in steps of 0.01. These values are statistically uncorrelated and sufficiently close to $Z = 2$ of helium, so that the average density of states and the classical dynamics do not change significantly. Figures 2(d)–2(f) show the cumulative NNS distributions for states below I_9, I_{13}, and I_{17}, respectively, as well as the cumulative Wigner distribution and the 3D result for I_9. The results demonstrate that *the statistical level properties are essentially the same for 1D and 3D helium* and they illustrate the transition from an irregular regime (I_9), with a distribution intermediate between a step function and a cumulative Wigner distribution, to a chaotic regime (I_{17}), with a distribution that is almost Wigner-like. For I_{17}, the lack of large spacings is the only remnant of regularity.

This behavior can be understood in a quantitative way by the model of Zakrzewski *et al.* [10], which was developed to understand the NNS statistics of the hydrogen atom in a magnetic field, whose spectrum is quite similar to that of helium in the sense that "chaotic" perturber states interact with a regular series. In this model, the Hilbert space is composed of two subspaces, a "regular" one and a chaotic one. The model Hamiltonian is diagonal in the regular subspace with equally spaced eigenvalues (representing Rydberg series). In the chaotic subspace (representing the perturbers), the Hamiltonian is modeled by a random matrix, with a coupling v between regular and chaotic states (v in units of the spacing between regular states; for details, see Ref. [10]). For large matrices, this model has only two parameters: the weight ρ of chaotic states ($1 - \rho$ of regular states) and the coupling strength v. Above the first ionization threshold, an imaginary part is

added to the GOE matrix as in [10], with an additional parameter measuring the strength of coupling to the continua; this coupling strength is small playing therefore only a minor role.

The calculated NNS distributions for 1D helium were fitted with this model, which turned out as a good description. The fits reproduce the lack of large spacings and result in $\rho \cong 0.29$, 0.33, and 0.40 for I_9, I_{13}, and I_{17}, respectively. A second estimate for ρ is based on the size of the cutoff value for the level spacings [see Figs. 2(d)–2(f)], which can be related to ρ. In the perturbative regime, when the coupling between chaotic and regular levels is not so strong as to modify their densities, two neighboring states cannot be further apart than two unperturbed regular states. The reason is that a perturber repels neighboring levels and in this way reduces the NNS between them. With $m = \rho/(1 - \rho)$ being the average number of chaotic states per regular state, the largest possible spacing will be $(m + 1) = 1/(1 - \rho)$ times the mean level spacing. This procedure leads to $\rho \cong 0.25$, 0.33, and 0.41 for I_9, I_{13}, and I_{17}, respectively.

A further rough estimate for ρ *not* based on the model, but on the physics of the real system, is possible: the local density of regular states can be estimated assuming that a Rydberg series converging to I_N sees an effective nuclear charge of $Z - 1 = 1$. The density of chaotic states is the sum of densities of states of all series with higher N. As N increases, the upper thresholds lie closer and closer leading to an increase in the fraction of chaotic states. In this way, we obtain $\rho \cong 0.23$, 0.35, and 0.43, respectively, for I_9, I_{13}, and I_{17}. We note that all three approaches provide rather similar results for ρ.

The increase of ρ with N alone, however, is not sufficient to explain the transition to an almost Wigner-like distribution for I_{17}: the coupling strength between chaotic and regular states has to increase, too. This is indeed the case, with the best fits resulting in $\upsilon \cong 0.38$, 0.73, and 1.2 for I_9, I_{13}, and I_{17}, respectively. It clearly shows that the individual influence of each perturber gets more important when one approaches higher thresholds. This leads to a globally chaotic spectrum, where a distinction between regular levels and perturbers loses more and more of its meaning.

In conclusion, we have found—on the basis of statistical analysis—clear evidence of a transition towards quantum chaos in the doubly excited spectrum of helium below I_9, with support from the results of our *ab initio* calculations for 3D and 1D helium. The effects of chaos correspond to a loss of the radial quantum number N, whereas $N - K$ remains approximately a good quantum number, and they are directly related to the instability of the eZe orbits in the radial direction (i.e., preserving collinearity) and their stability with respect to bending. The statistical study of 1D helium provides an estimate for the observation of a fully chaotic regime in 3D helium (for $N \geq 17$). It may happen that this regime appears even at lower N values if $N - K$ breaks down. One can hope that future experiments, as well as numerical calculations for 3D helium in the region above I_9, will provide further insight into the chaotic regime of helium.

The authors appreciate experimental assistance by J. D. Bozek. B. G. and D. D. thank M. Kuś for useful discussions. The work in Berlin was supported by the BMBF, Project No. 05-650-KEA, and by the DFG, Project No. Do-561/1-3, and that at ALS by the DOE, Contract No. DE-AC03-76SF00098. CPU time on a Cray C98 was provided by IDRIS. Laboratoire Kastler Brossel de l'Université Pierre et Marie Curie et de l'Ecole Normale Supérieure is UMR 8552 du CNRS.

[1] M. C. Gutzwiller, Rev. Mod. Phys. **70**, 589 (1998).
[2] G. Tanner, K. Richter, and J.-M. Rost, Rev. Mod. Phys. **72**, 497 (2000).
[3] T. Ericson, Phys. Rev. Lett. **5**, 430 (1960).
[4] D. R. Herrick and O. Sinanoğlu, Phys. Rev. A **11**, 97 (1975); C. D. Lin, Phys. Rev. A **29**, 1019 (1984).
[5] M. Domke *et al.,* Phys. Rev. Lett. **66**, 1306 (1991).
[6] B. Grémaud and D. Delande, Europhys. Lett. **40**, 363 (1997).
[7] A. Bürgers *et al.,* J. Phys. B **28**, 3163 (1995).
[8] M. C. Gutzwiller, *Chaos in Classical and Quantum Mechanics* (Springer, New York, 1990).
[9] O. Bohigas, in *Chaos and Quantum Physics,* Proceedings of the Les Houches Summer School, Session LII, edited by M.-J. Giannoni, A. Voros, and J. Zinn-Justin, (North-Holland, Amsterdam, 1991).
[10] J. Zakrzewski, K. Dupret, and D. Delande, Phys. Rev. Lett. **74**, 522 (1995); K. Dupret, J. Zakrzewski, and D. Delande, Europhys. Lett. **31**, 251 (1995).
[11] R. Püttner *et al.,* J. Electron Spectrosc. Relat. Phenom. **101–103**, 27 (1999).
[12] M. Domke *et al.,* Phys. Rev. A **53**, 1424 (1996).
[13] F. Haake, *Quantum Signatures of Chaos* (Springer, Berlin, 1991).
[14] B. Grémaud and P. Gaspard, J. Phys. B **31**, 1671 (1998).
[15] R. Blümel and W. P. Reinhardt, in *Quantum Nonintegrability,* Directions in Chaos Vol. 4, edited by D. H. Feng and J.-M. Yuan (World Scientific, Singapore, 1992); R. Blümel, Phys. Rev. A **54**, 5420 (1996).

2.2.2 Systèmes quasi-intégrables

Au-delà des systèmes chaotiques ou intégrables, il existe des systèmes dits pseudo-intégrables, c'est-à-dire, tels que la dynamique classique n'est ni régulière, ni chaotique. Par exemple, la dynamique de l'électron externe d'un atome hydrogénoïde (i.e. en présence d'un coeur diffusant) est essentiellement la même que celle d'un atome d'hydrogène sauf pour les trajectoires passant par le coeur. Or, à la limite semi-classique (états très excités) on peut montrer que ces trajectoires forment un ensemble de mesure nulle, on ne s'attendrait pas à une modification des propriétés statistiques des spectres. Pourtant, on peut montrer que ces dernières sont bien décrites par une nouvelle classe d'universalité intermédiaire entre celle des systèmes réguliers (Poisson) et celle des systèmes chaotiques (matrices aléatoires) : elle présente à la fois de la répulsion de niveau comme un système chaotique et une décroissance exponentielle à grand espacement comme un système régulier.

Un autre exemple de ce type de systèmes sont les billards en forme de losange, pour lesquels la non-intégrabilité provient de la diffraction aux angles. En collaboration avec S. Jain, nous avons pu montrer que les propriétés statistiques des niveaux d'énergie sont très bien décrites par cette nouvelle classe d'universalité. En outre, on a pu mettre en évidence que ces propriétés dépendent fortement non seulement du caractère irrationnel de l'angle du losange, mais aussi de la classe de symétrie de la fonction d'onde.

J. Phys. A: Math. Gen. **31** (1998) L637–L643. Printed in the UK PII: S0305-4470(98)93336-4

LETTER TO THE EDITOR

Spacing distributions for rhombus billiards

Benoît Grémaud† and Sudhir R Jain‡

† Laboratoire Kastler Brossel, Université Pierre et Marie Curie, T12 E1, 4 place Jussieu, 75252 Paris Cedex 05, France

‡ Theoretical Physics Division, Bhabha Atomic Research Centre, Central Complex, Trombay, Mumbai 400085, India

Received 15 April 1998, in final form 29 June 1998

Abstract. We show that the spacing distributions of rational rhombus billiards fall in a family of universality classes distinctly different from the Wigner–Dyson family of random matrix theory and the Poisson distribution. Some of the distributions find explanation in a recent work of Bogomolny, Gerland, and Schmit. For the irrational billiards, despite ergodicity, we get the same distribution for the examples considered—once again, distinct from the Wigner–Dyson distributions. All the results are obtained numerically by a method that allows us to reach very high energies.

Statistical analysis of level correlations of a quantum system is one of the many ways to study the effects of chaotic behaviour of its classical counterpart [1]. For such complex systems, the fluctuations are very well described by the random matrix theory, giving rise to three classes of universality corresponding to orthogonal, unitary and symplectic ensembles (OE, UE and SE). On the other hand, for integrable systems, the short-range correlations follow the Poisson distribution. Rhombus billiards [2] are peculiar as they are pseudo-integrable systems and for this reason their statistical properties belong to another class of universality [3]. These non-integrable systems are termed pseudo-integrable as the dynamics occurs on a multiply-connected, compact surface in the phase space. For example, in the case of $\pi/3$-rhombus billiard, the invariant integral surface is a sphere with two handles [2, 4]. It has been shown that the short-range properties (spacing distribution) can be fitted by Brody distributions [5] with parameters depending on the genus [6]. However, a very small number of levels were used to achieve the statistics and, as it was outlined by the authors, the parameters were smoothly changing with the number of levels considered. This last effect is probably a consequence of the pseudo-integrability and thus one has to consider levels lying very high in energy to have converged statistics. Furthermore, Brody distributions are not very convenient for two reasons: (i) they are not on a firm theoretical basis like random matrix theory and so one cannot gain too much knowledge about the system from the Brody parameter; (ii) their behaviour at small spacing is not linear, whereas it is so for rhombus billiards. In contrast, in a recent paper [7], Bogomolny *et al* have proposed a model derived from the Dyson's stochastic Coulomb gas model [8, 9]: eigenvalues are considered as classical particles on a line, with a two-body interaction potential given by $V(x) = -\ln(x)$. In contrast to Dyson's model, where all possible pairs are considered, the same interaction is restricted only to nearest-neighbours. Hereafter, this model will be referred to as the short-ranged Dyson's model (SRDM). The joint probability obtained

0305-4470/98/370637+07$19.50

gives rise to spacing distributions showing linear level repulsion and exponential decrease for large spacing. More precisely, the nearest-neighbour (NN) and next-nearest-neighbour (NNN) distributions are

$$P(s) = 4s\mathrm{e}^{-2s} \qquad \text{and} \qquad P_2(s) = \tfrac{8}{3}s^3\mathrm{e}^{-2s}. \tag{1}$$

It is worth noting that exactly the same functional form was used in the past [10] to explain the intermediate spacing distribution for a rectangle billiard with a flux line—an Aharanov–Bohm billiard. In [7] it is also shown that the level statistics of some rhombus billiards agree very well with these distributions. However, only rhombi with rational angles and with Dirichlet boundary conditions on both the x- and y-axis (i.e. right-angled triangle) were studied. In this letter, we extend the preceding study to rational billiards with Neumann boundary conditions (i.e. 'pure' rhombus) and also to irrational billiards (both classes of boundary conditions). Of course, in a rhombus, making the shorter (longer) diagonal Neumann means that one is considering a larger obtuse (acute) triangle. So, the modifications are expected but here they are non-trivial.

The spectral properties of these systems which are non-integrable and yet non-chaotic is thus an important unsettled problem. The solution of this problem is partly in devising numerical techniques that allow one to go to higher energies, and, partly in developing statistical models like the SRDM [7] mentioned above. In this letter, we first discuss the method and then use levels in the high-energy range to show agreements and disagreements with the results in [7]. To give an idea, the efficiency of the method is such that we were able to compute a very large number of levels (up to 36 000 for a given rhombus and a given symmetry class), so that the statistical properties are fully converged. In the latter part of this letter, we show the effects of both the boundary conditions and the irrationality on the level spacing distributions.

The Schrödinger equation for a particle moving freely in a rhombus billiard (shown by figure 1) is simply

$$-\frac{\hbar^2}{2m}\left(\frac{\partial^2}{\partial x^2} + \frac{\partial^2}{\partial y^2}\right)\psi(x, y) = E\psi(x, y) \tag{2}$$

with the additional condition that $\psi(x, y)$ is vanishing on the boundary (Dirichlet conditions). The geometry of the system leads to a natural change of coordinates: the

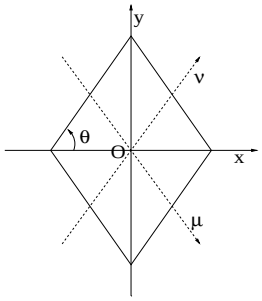

Figure 1. Rhombus-shaped enclosure in which the particle moves freely with elastic bounces on the boundary. The quantum problem corresponds to imposing the Dirichlet conditions for the wavefunctions. The system being symmetric under reflections with respect to the x-axis or the y-axis, Dirichlet or Neumann boundary conditions can be imposed on both the axes, leading to four different classes of symmetry. By considering axes crossing at the centre O of the system and parallel to the edges of the billiard, a non-orthogonal coordinate system (μ, ν) is constructed in which the Dirichlet boundary conditions on the enclosure separate (see text).

two new axes cross at the centre and are parallel to the edges of the billiard (see figure 1):

$$\mu = \frac{1}{2}\left(\frac{x}{\cos\theta} - \frac{y}{\sin\theta}\right)$$
$$\nu = \frac{1}{2}\left(\frac{x}{\cos\theta} + \frac{y}{\sin\theta}\right). \tag{3}$$

In this new coordinate system, the original rhombus is mapped onto a square of length L and thus, in this coordinate system, the boundary conditions separate, of course at the price of a slightly more complicated Schrödinger equation:

$$-\frac{\hbar^2(\partial^2_{\mu\mu} + \partial^2_{\nu\nu} - 2\cos(2\theta)\partial^2_{\mu\nu})}{2m\sin^2(2\theta)}\psi(\mu,\nu) = E\psi(\mu,\nu). \tag{4}$$

The change $\mu \to \frac{2}{L}\mu$, $\nu \to \frac{2}{L}\nu$ and $E \to (\frac{2}{L})^2\frac{m}{\hbar^2}E$ gives rise to the scaled Schrödinger equation (after multiplication by $2\sin^2(2\theta)$):

$$-(\partial^2_{\mu\mu} + \partial^2_{\nu\nu} - 2\cos(2\theta)\partial^2_{\mu\nu})\psi = 2\sin^2(2\theta)E\psi \tag{5}$$

the boundary condition being then at the points $\mu = \pm 1$ and $\nu = \pm 1$.

To solve the eigenvalue problem, a possible idea is to expand any wavefunction in a basis satisfying the boundary conditions

$$\psi(\mu,\nu) = \sum_{n_\mu, n_\nu = 0}^{\infty} a(n_\mu, n_\nu)\phi_{n_\mu}(\mu)\phi_{n_\nu}(\nu). \tag{6}$$

The simplest choice is the Fourier sine and cosine series. Unfortunately, the operator $\partial^2_{\mu\nu}$ has no selection rules in this basis, thus the matrix representation of the left part of the Schrödinger equation (5) is totally filled. Numerically, we will approximate the wavefunction by keeping only a (large) number of terms in the preceding series. For this system and for many other Coulomb-like systems, it has been observed that the rate of convergence of the series is much slower when the matrix is filled than when selection rules occur.

To avoid this difficulty, we introduce the following basis for each coordinate μ and ν:

$$\phi_n(u) = (1-u^2)C_n^{(\frac{3}{2})}(u) \tag{7}$$

where C_n^α are Gegenbauer polynomials [11]. This basis is complete and all operators appearing in equation (5) have selection rules. More precisely, we have

$$|\Delta n_\mu|, |\Delta n_\nu| \leqslant 2 \qquad \Delta n_\mu + \Delta n_\nu = 0, \pm 2, \pm 4. \tag{8}$$

Furthermore, all matrix elements are analytically known and are given by simple polynomial expressions of the two quantum numbers (n_μ, n_ν). The only difficulty is the non-orthogonality of the basis: that is $\langle n'|n\rangle$ does not reduce to $\delta_{nn'}$ but also shows the preceding selection rules.

This basis also allows us to take directly into account the symmetries of the original problem, namely the reflections with respect to the x-axis (S_x) or the y-axis (S_y). In (μ, ν) coordinates, they become

$$S_x \begin{cases} \mu \to \nu \\ \nu \to \mu \end{cases} \qquad S_y \begin{cases} \mu \to -\nu \\ \nu \to -\mu. \end{cases} \tag{9}$$

Using the properties of the Gegenbauer polynomials [11] we are able to construct four different bases in which the two operators S_x and S_y are simultaneously diagonal with eigenvalues, $\epsilon_x = \pm 1$ and $\epsilon_y = \pm 1$. Of course, this transformation preserves the selection

rules and hence the band structure. We shall denote the eigenfunctions vanishing on both the diagonals by $(--)$ and not vanishing on either by $(++)$ parity classes.

The original Schrödinger equation is thus transformed to a generalized eigenvalue problem:

$$A|\psi\rangle = E\,B|\psi\rangle \tag{10}$$

where A and B are real, sparse and banded matrices. This kind of system is easily solved using the Lanczos algorithm [12]. It is an iterative method, highly efficient to obtain few eigenvalues and eigenvectors of very large matrices. We typically obtain 100 eigenvalues of a $10\,000 \times 10\,000$ matrix in a few minutes on a regular workstation. The results presented here have been obtained by diagonalizing matrices of size up to 203 401 for a bandwidth equal to 903. For such matrices, we obtain 200 eigenvalues in 10 min on a Cray C98. The number of levels ($\simeq$36 000) that we are able to compute in this way is slightly larger than with usual boundary matching methods ($\simeq$20 000), which are nevertheless restricted to rational angles. On the other hand, very recent methods developed by Vergini *et al* [13] seems to be more efficient (they were able to reach an energy domain around the 142 000th state for the stadium billiard).

For the present study, various values of angle have been used:

$$\frac{3\pi}{10},\ \frac{(\sqrt{5}-1)\pi}{4},\ \frac{\pi}{\pi},\ \frac{\pi}{3},\ \frac{3\pi}{8} \text{ and } \frac{7\pi}{18} \tag{11}$$

for both $(++)$ and $(--)$ parity†. For all cases, only levels above the 10 000th one have been considered, to avoid peculiar effects in the statistics and at least 5000 levels (up to 24 000) have been used for each case. The convergence of the statistics has been checked by systematically varying the energy around which levels were taken. This is shown in figure 2, where we have plotted the following quantity:

$$\int_0^\infty \mathrm{d}s\ (N_0(s) - N_n(s))^2 \tag{12}$$

with respect to the number n, for $\frac{3\pi}{10}$ (top) and $\frac{\pi}{3}$ (bottom) billiards ($(++)$ parity). $N_0(s)$ is the cumulative NN distribution obtained with the 5000 highest states, whereas $N_n(s)$ is the cumulative NN distribution obtained with levels n to $n + 4999$. One can thus clearly see that the statistics become energy independent (up to fluctuations) only for levels above the 10 000th state, which emphasizes the choice of keeping only those states.

In [7] it was shown that for the $\frac{3\pi}{10}(--)$ billiard, both NN and NNN statistics were following the formula (1). We, of course, reproduce this result, as shown in figure 3(a). However, the same billiard, but with Neumann–Neumann boundary conditions, does not follow the same distribution laws but rather lies in between OE and SRDM distributions, as shown in figure 3(a). The deviations are obviously much larger than statistical fluctuations. The difference is emphasized by looking at the behaviour of the NNN for small spacings (see figure 3(b)). Indeed, whereas for the $(--)$ symmetry, the observed power law is s^4 in the cumulative distribution (i.e. s^3 for $P(1, s)$), it is close to s^5 for the $(++)$ case (i.e. s^4 for $P(1, s)$), which is the OE prediction. This dependency of the statistics with respect to the boundary conditions has already been observed in other systems like the 3D Anderson model [14]. However, the present results are more surprising as there are θ values for which there is practically no difference between the two symmetry classes. Indeed, figure 4 shows the NN (cumulative) distributions for $\frac{3\pi}{8}$ and $\frac{7\pi}{18}$. Besides the statistical fluctuations, one cannot distinguish between the two symmetry classes, whereas the distributions differ: $\frac{3\pi}{8}$ is well described by SRDM, whereas $\frac{7\pi}{18}$ lies between OE and SRDM.

† The $(--)$ parity for the $\frac{\pi}{3}$ rhombus is not shown as it is integrable.

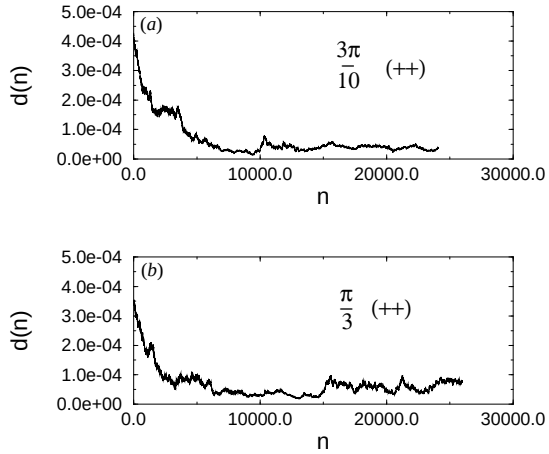

Figure 2. 'Difference' (see equation (12)) between the NN statistics obtained with the 5000 highest states and the NN statistics obtained with levels n to $n + 4999$, as a function of n, for both $\frac{3\pi}{10}$ (top) and $\frac{\pi}{3}$ (bottom) (++ parity). Above the 10 000th level, the distributions become energy independent (apart fluctuations).

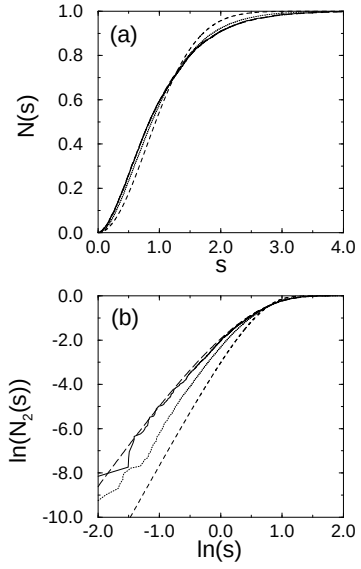

Figure 3. (*a*) The cumulative distribution of NN spacings for the $\frac{3\pi}{10}$ rhombus. The dotted curve corresponds to Neumann–Neumann (++) boundary conditions on both the x- and y-axis; the full curve corresponds to Dirichlet–Dirichlet (−−) boundary conditions. The two distributions are clearly different, the deviation being larger than statistical fluctuations. The (−−) symmetry class is exactly on the top of the distribution introduced by Bogomolny *et al* (SRDM) given by equation (1), corresponding to the long broken curve. The (++) distribution lies in between SRDM and OE prediction (given by the short broken curve). This difference is emphasized in (*b*) depicting the NNN distributions (cumulative) for the same billiards (ln–ln plot). Again, the (−−) (full curve) symmetry class is exactly on the top of SRDM (long broken curve), whereas the (++) symmetry class (dotted curve) lies in between SRDM and OE (short broken curve). In particular the behaviours for small spacing are very different: (−−) shows a s^4 power law, whereas it is s^5 for (++), the OE prediction.

The case of the $\frac{\pi}{3}$ billiard is the most peculiar, since the (−−) parity is integrable whereas the (++) spacing distributions agree with SRDM.

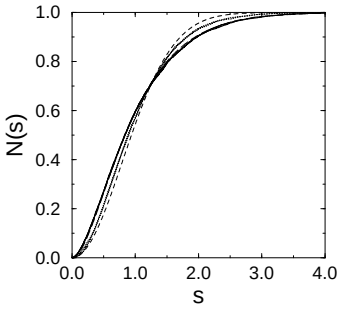

Figure 4. Spacing distributions (cumulative) for two rational billiards: $\frac{3\pi}{8}$ (full curves) and $\frac{7\pi}{18}$ (dotted curves), for both $(++)$ and $(--)$ symmetry classes. In contrast to the $\frac{3\pi}{10}$ billiard (see figure 3), there is no difference between the two symmetry classes: for each billiard the two curves lie on top of each other. Furthermore, these two billiards show distinct spacing distributions, the $\frac{3\pi}{8}$ one corresponds exactly to SRDM (long broken curve) whereas the $\frac{7\pi}{18}$ one is much closer to OE prediction (short broken curve).

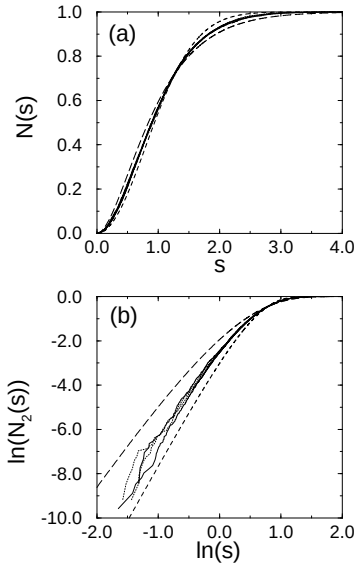

Figure 5. (*a*) NN and (*b*) NNN distributions for two irrational billiards: $\frac{\pi}{\pi}$ (full curves) and $\frac{(\sqrt{5}-1)\pi}{4}$ (dotted curves) for both $(++)$ and $(--)$ symmetry classes. In contrast to the rational billiards, the genus of these billiard is 'infinite' (see text for explanation) and so the classical dynamics is ergodic. The fact that all the four distributions lie on top of each other is quite remarkable and may be related to the fact that these billiards have the 'same' genus. However, from the ergodicity one could expect the distributions to be OE-like, which is not the case. Rather, they lie between SRDM (long broken curve) and OE (short broken curve). Still, the small spacing behaviour of the NNN distributions shows a s^5 power law, i.e. corresponding to OE.

All the rhombi considered are not ergodic, as their genera are finite (e.g. two for the $\pi/3$-rhombus). In contrast, for an irrational angle the genus is 'infinite', and so one could expect a rather different behaviour. Although the concept of genus is applicable only to compact surfaces, we have stated the above phrase in quotes in the following sense: as an irrational rhombus is approximated via continued fraction expansion, the larger and larger denominators will appear, implying larger genus surfaces, until eventually 'infinite'. It is quite possible, and it may, in fact, be true, that this limit is singular. As a result, from the rational convergents, it may not be possible to say anything about the irrational billiard.

Figure 5 displays NN and NNN statistics for $\frac{\pi}{\pi}$ and $\frac{(\sqrt{5}-1)\pi}{4}$ (both symmetry classes) billiards. NN distributions are on top of each other, which is interesting if one believes that the genus is the relevant parameter. On the other hand, from the ergodicity, one could expect the distributions to be OE, which is not the case, even if the small spacing behaviour

of NNN statistics seems to show the same power law s^5 (for cumulative). Thus, if [7] seems to give one class of universality, there must be other classes of universality lying between SRDM and OE, especially for irrational angles. The other possibility is that, although numerically stationary in a wide range of energy, the spacing distributions of the irrational rhombus may evolve exceptionally slowly to OE. If that is the case, one will probably have to find the final answer in a much higher energy range, for which other numerical methods will have to be used [13].

The present study also raises the question of the semiclassical understanding of the boundary dependence of the distributions. Due to a change in the boundary conditions, actions, Maslov indices and also the edge orbits will change resulting in a difference, but the whole explanation of this boundary dependence probably lies beyond these simple considerations. Spectral fluctuations in some of the pseudo-integrable billiards have been studied in detail using the periodic orbit theory. From the detailed information about the periodic orbits [4] it was shown that the spectral rigidity is non-universal [3] with a universal trend. We hope that the method presented here and the ensuing numerical results will help us to model the spectral fluctuations of these apparently simple non-integrable quantum systems.

To summarize: we have cast the problem of a particle in rhombus-shaped enclosure in a way that allows us to go to very high energies. This has led us to confidently obtain statistical results on spacing distributions which are well converged. Subsequently, we have shown that for some rational billiards, the fluctuations agree well with the results recently obtained [7]. However, we have given several examples where the recent model does not explain the obtained distributions. It has been shown that boundary conditions play an important role. Finally, for the irrational rhombus billiards, the distributions seem to be identical for the examples considered. Significantly though, the distribution is still not in the Wigner–Dyson family. We believe that these results point in the direction of having a family of universality classes which, in essence, leads to non-universality with a universal trend for pseudo-integrable billiards.

We acknowledge stimulating discussions with D Delande and E Bogomolny. CPU time on a Cray C98 computer has been provided by IDRIS. Laboratoire Kastler Brossel is the laboratory of the Université Pierre et Marie Curie and of the Ecole Normale Supérieure, unité associée 18 du CNRS.

References

[1] Bohigas O, Giannoni M-J and Schmit C 1984 *Phys. Rev. Lett.* **52** 1
[2] Biswas D and Jain S R 1990 *Phys. Rev.* A **42** 3170
Eckhardt B, Ford J and Vivaldi F 1984 *Physica* **13D** 339
for a review, see Jain S R and Lawande S V 1995 *Proc. Natl Sci. Acad. India* A **61** 275
[3] Parab H D and Jain S R 1996 *J. Phys. A: Math. Gen.* **29** 3903
[4] Jain S R and Parab H D 1992 *J. Phys. A: Math. Gen.* **25** 6669
[5] Brody T A 1973 *Lett. Nuovo Cimento* **7** 482
[6] Shudo A and Shimizu Y 1993 *Phys. Rev.* E **47** 54
[7] Bogomolny E B, Gerland U and Schmit C *Phys. Rev. Lett.* submitted
[8] Mehta M L 1991 *Random Matrices* (London: Academic)
[9] Haake F 1992 *Quantum Signatures of Chaos* (Berlin: Springer)
[10] Date G, Jain S R and Murthy M V N 1995 *Phys. Rev.* E **51** 198
[11] Abramowitz M and Segun A 1968 *Handbook of Mathematical Functions* (New York: Dover)
[12] Ericsson T and Ruhe A 1980 *Math. Comput.* **35** 1251 and references therein
[13] Vergini E and Saraceno M 1995 *Phys. Rev.* E **52** 2204
[14] Braun D, Montambaux G and Pascaud M *Phys. Rev. Lett.* submitted

2.3 Approximation semi-classique

2.3.1 Théorie générale

Le lien entre les propriétés quantiques d'un système chaotique (densité d'état, section efficace de photo-ionisation...) et ses propriétés classiques (trajectoires périodiques et leur stabilité) est fait par les formules de trace, qui sont la généralisation des méthodes du type WKB pour des systèmes à plusieurs degrés de liberté. A la différence d'un système unidimensionnel, il n'y a pas de lien direct entre une énergie propre du système et une trajectoire précise, mais uniquement une relation globale entre toutes les énergies propres (la densité d'état) et toutes les trajectoires périodiques, la contribution des grandeurs classiques se présentant formellement comme un développement asymptotique en puissance de $\hbar$. Si le premier terme du développement est bien compris et a déjà permis la quantification semi-classique de nombreux systèmes chaotiques, la complexité des termes suivants fait qu'ils ne sont jamais pris en compte sauf pour des systèmes comme les billards, pour lesquels les trajectoires classiques sont suffisamment simples (suite de vols libres entrecoupés de rebonds élastiques sur les bords). Or pour des systèmes comme l'atome d'hydrogène en champ magnétique intense, du fait de l'efficacité des méthodes numériques employées (en particulier, l'inversion harmonique[3]), il est maintenant possible d'analyser quantitativement les effets des termes d'ordre supérieur. D'autre part, une des motivations est de pouvoir affiner les calculs semi-classiques, c'est-à-dire, les calculs de propriétés quantiques à partir des grandeurs classiques.

Le point de départ est l'intégrale des chemins de Feynman pour le propagateur quantique d'un point $\mathbf{q}_0$ à un point $\mathbf{q}$ en un temps T :

$$K(\mathbf{q},\mathbf{q}_0,T) = \int d\mathbf{q}_1\, d\mathbf{q}_2 \cdots d\mathbf{q}_{N-1} \prod_{n=0}^{N-1} \langle \mathbf{q}_{n+1}|\hat{K}(\Delta t)|\mathbf{q}_n\rangle \tag{2.1}$$

où $\Delta t = T/N$, $\hat{K}(T) = \exp\left(-i\hat{H}T/\hbar\right)$ et $\mathbf{q}_N = \mathbf{q}$. Pour un hamiltonien indépendant du temps se séparant en une partie cinétique et une partie potentiel,

$$\hat{H} = \frac{\hat{\mathbf{p}}}{2} + V(\hat{\mathbf{q}}) \tag{2.2}$$

l'équation (2.1) devient :

$$\begin{aligned} K(\mathbf{q},\mathbf{q}_0,T) = \int d\mathbf{q}_1\, d\mathbf{q}_2 \cdots d\mathbf{q}_{N-1} (2\pi i\hbar\Delta t)^{-Nf/2} \\ \times \exp\left[\frac{i}{\hbar}\sum_{n=0}^{N-1} L\left(\frac{\mathbf{q}_{n+1}-\mathbf{q}_n}{\Delta t}, \mathbf{q}_n\right)\Delta t + \mathcal{O}(\Delta t)\right] \end{aligned} \tag{2.3}$$

où $L(\dot{\mathbf{q}},\mathbf{q})$ est le lagrangien classique.

[3] B. Grémaud and D. Delande, Phys. Rev. A **61**, 032504 (2000)

Pour des petites valeurs de $\hbar$ (i.e. la limite semi-classique), on peut utiliser la méthode de la phase stationnaire autour des trajectoires classiques $\mathbf{q}_l^{\rm cl}(t)$ allant du point $\mathbf{q}_0$ au point $\mathbf{q}$ en un temps T. Chaque orbite donne une contribution $K_l(\mathbf{q},\mathbf{q}_0,T)$ au propagateur quantique :

$$K_l(\mathbf{q},\mathbf{q}_0,T)=\frac{1}{(2\pi i\hbar)^{f/2}}\left|\det\left(-\frac{\partial^2}{\partial\mathbf{q}\partial\mathbf{q}_0}W_l^{\rm cl}(\mathbf{q},\mathbf{q}_0,T)\right)\right|^{1/2}\exp\left[\frac{i}{\hbar}W_l^{\rm cl}(\mathbf{q},\mathbf{q}_0,T)-i\frac{\pi}{2}\nu_l\right] \tag{2.4}$$

où $W_l^{\rm cl}(\mathbf{q},\mathbf{q}_0,T)$ est l'action classique (i.e. $\int_0^T dt\,L(\dot{\mathbf{q}}_l^{\rm cl}(t),\mathbf{q}_l^{\rm cl}(t))$; le déterminant de la matrice $\frac{\partial^2}{\partial\mathbf{q}\partial\mathbf{q}_0}W_l^{\rm cl}(\mathbf{q},\mathbf{q}_0,T)$ est encore appelé déterminant de Van Vleck ; ν_l est appelé l'indice de Morse de l'orbite et compte le nombre fois où le déterminant s'annule, correspondant à des points conjugués le long de l'orbite.

Comme en général, on s'intéresse plutôt à des quantités liées aux propriétés spectrales du hamiltonien (énergies propres, section efficace de photo-ionisation), on est amené à considérer les expressions semi-classique pour la résolvante $G(z)=1/(z-H)$. Le passage se fait évidemment par transformé de Fourier, laquelle est évaluée par une phase stationnaire supplémentaire. La contribution de chaque orbite à $G(\mathbf{q},\mathbf{q}_0,E)$ est la suivante :

$$G_l(\mathbf{q},\mathbf{q}_0,E)=\frac{2\pi}{(2\pi i\hbar)^{(f+1)/2}}\frac{1}{\left|W_l^{(2)}\det J_1(T_0)\right|^{1/2}}\exp\left[\frac{i}{\hbar}S_l(\mathbf{q},\mathbf{q}_0,E)-i\frac{\pi}{2}\tilde{\nu}_l\right] \tag{2.5}$$

où les trajectoires impliquées sont celles joignant les points $\mathbf{q}_0$ et $\mathbf{q}$, l'énergie de la particule étant E.

Enfin, la densité d'état quantique $n(E)$ étant (la partie imaginaire de) la trace de la résolvante, (i.e. $\int d\mathbf{q}G(\mathbf{q},\mathbf{q},E)$), on en obtient une expression semi-classique faisant intervenir toutes les orbites périodiques du système à cette énergie E :

$$G_l(E)=\frac{1}{i\hbar}\frac{T_0}{\left|\det\left(m(T_0)-\mathbb{1}\right)\right|^{1/2}}\exp\left[\frac{i}{\hbar}S_l(E)-i\frac{\pi}{2}\mu_l\right] \tag{2.6}$$

où $S_l(E)=\oint\mathbf{p}d\mathbf{q}$ est l'action réduite de l'orbite, T_0 sa période ; $m(T_0)$ est la matrice (réduite) décrivant la stabilité de l'orbite et μ_l est l'indice de Maslov.

2.3.2 Au-delà de l'ordre dominant

Les termes correctifs dans les formules précédentes proviennent des différentes approximations de phase stationnaire nécessaires pour obtenir le résultat final. Dans le cas de la densité d'état, il y en a trois : quantique → semi-classique, temps →énergie et enfin la trace de la résolvante. On obtient des expressions relativement compliqués :

$$G_l(E)=\frac{1}{i\hbar}\frac{T_0}{\left|\det\left(m(T_0)-\mathbb{1}\right)\right|^{1/2}}\exp\left[\frac{i}{\hbar}S_l(E)-i\frac{\pi}{2}\mu_l\right]\times\left\{1+i\hbar\left[C_1(T_0)+C_1^{T\to E}(T_0)\right]+\mathcal{O}(\hbar^2)\right\} \tag{2.7}$$

où

$$C_1(T,t_0)=\frac{1}{8}\int_0^T dt\,V^{(4)}_{ijkl}(t)\mathcal{G}_{ij}(t,t)\mathcal{G}_{kl}(t,t)+\frac{1}{2}\frac{V^{(1)}_l(t_0)}{|\dot{\mathbf{q}}^{\rm cl}|^2}\int_0^T dt\,V^{(3)}_{ijk}(t)\mathcal{G}_{lk}(0,t)\mathcal{G}_{ij}(t,t)$$
$$+\frac{1}{24}\int_0^T\int_0^T dtdt'\,V^{(3)}_{ijk}(t)V^{(3)}_{lmn}(t')\big[3\mathcal{G}_{ij}(t,t)\mathcal{G}_{kl}(t,t')\mathcal{G}_{mn}(t',t')+2\mathcal{G}_{il}(t,t')\mathcal{G}_{jm}(t,t')\mathcal{G}_{kn}(t,t')\big] \tag{2.8}$$

et $C_1^{T\to E}(T)$ est donné par :

$$C_1^{T\to E}(T_0)=\frac{1}{2W_l^{(2)}}\left[\left(C_0^{(1)}\right)^2+C_0^{(2)}\right]-\frac{W_l^{(3)}C_0^{(1)}}{2\left(W_l^{(2)}\right)^2}-\frac{W_l^{(4)}}{8\left(W_l^{(2)}\right)^2}+\frac{5}{24}\frac{\left(W_l^{(3)}\right)^2}{\left(W_l^{(2)}\right)^3} \tag{2.9}$$

Dans les expressions précédentes interviennent, d'une part, les fonctions de Green $\mathcal{G}(t,t')$ des orbites périodiques, solutions de :

$$\left(-\frac{\mathrm{d}^2}{\mathrm{d}t^2}\mathbb{1}-\frac{\partial^2 V}{\partial\mathbf{q}\partial\mathbf{q}}\left[\mathbf{q}^{\rm cl}(t)\right]\right)\mathcal{G}(t,t')=\mathbb{1}\,\delta(t-t') \tag{2.10}$$

et d'autre part, les dérivés d'ordres supérieures de l'action classique W_l et de la matrice de stabilité de l'orbite (contenue dans C_0).

Toute la difficulté a été de trouver une façon efficace et précise de calculer toutes ces quantités. Cela a pu être fait en utilisant de manière approfondir les propriétés symplectiques de la dynamique classique dans l'espace des phases. On arrive ainsi à calculer toutes les corrections uniquement en résolvant des systèmes équations différentielles le long des orbites classiques (i.e. du type $\frac{d\mathbf{X}}{dt}=\mathbf{F}(\mathbf{X},t)$) dans lesquels $\mathbf{X}$ et $\mathbf{F}$ sont des quantités parfaitement régulières. Les résultats obtenus montrent un parfait accord entre la théorie développée et les calculs quantiques exacts. En particulier, j'ai pu mettre en évidence une subtilité cachée lors de l'établissement de la formule de trace de Gutzwiller, ce qui engendre un terme supplémentaire dans le calcul des termes d'ordre supérieur, absent des formules habituellement publiées.

PHYSICAL REVIEW E, VOLUME 65, 056207

$\hbar$ corrections in semiclassical formulas for smooth chaotic dynamics

Benoît Grémaud*
Laboratoire Kastler Brossel, Université Pierre et Marie Curie, T12, E1 4, Place Jussieu 75252, Paris cedex 05, France
(Received 13 July 2001; published 30 April 2002)

The validity of semiclassical expansions in the power of $\hbar$ for the quantum Green's function have been extensively tested for billiards systems, but in the case of chaotic dynamics with smooth potential, even if formulas are existing, a quantitative comparison is still missing. In this paper, extending the theory developed by Gaspard *et al.* [Adv. Chem. Phys. **90**, 105 (1995)], based on the classical Green's functions, we present an efficient method allowing the calculation of $\hbar$ corrections for the propagator, the quantum Green's function, and their traces. In particular, we show that the previously published expressions for $\hbar$ corrections to the traces are incomplete.

DOI: 10.1103/PhysRevE.65.056207 PACS number(s): 05.45.Mt, 03.65.Sq

I. INTRODUCTION

Gutzwiller's work has now become a milestone in the understanding of the properties of a quantum system whose classical counterpart depicts chaotic dynamics [1]. Starting from Feynman's path formulation of quantum mechanics, he has been able to complete the early studies of Van Vleck [2], deriving expressions for the semiclassical propagator, and from this, for the quantum level density: the well-known Gutzwiller trace formula. The latter is an asymptotic series in $\hbar$ and can be separated into two parts; the leading order corresponds to the Thomas-Fermi (or extended Thomas-Fermi when including $\hbar$ corrections) average density of states [3]; the other part corresponds to the oscillations around the preceding term and involves contributions from all periodic orbits of the system. This formula has been widely used to obtain approximate values for the quantum energy eigenvalues of classically chaotic systems: the hydrogen atom in magnetic field [4,5], the helium atom [6–8], anisotropic Kepler problem [1], resonant tunnel diode [9], billiards [10–13], etc. Since then, the Gutzwiller trace formula has also been generalized to take into account contributions of other kinds: diffractive effects [14], continuous families of periodic orbits [13,15,16], ghost orbits, etc.

At the same time, because the trace formula as derived by Gutzwiller only contained the leading term of the asymptotic expansion of the quantum level density, the systematic expansion of the semiclassical propagator in powers of $\hbar$ has been the purpose of several studies [12,13,17]. However, these corrections to the trace formula have only been tested for billiards, for which both classical and quantum properties are easier to calculate. In the present paper, we will show how, for quantum systems whose Hamiltonian separates into kinetic and smooth potential energies, $\hbar$ corrections can be computed with great accuracy, extending the method described in Refs. [12,13], based on classical Green's functions. In particular, we will show that the previous derivation [12,13] of the correction to Gutzwiller trace formula is partially wrong.

*Electronic address: Benoit.Gremaud@spectro.jussieu.fr

From a numerical point of view, all quantities involved in the calculation of the $\hbar$ corrections for a given classical path can be obtained as solutions of sets of first order differential equations to be integrated along this path using standard time integrators like the Runge-Kutta method. The number of equations in these sets can be quite large and can be probably reduced with a deeper analysis of their structures, in the same way that the amplitude in the Gutzwiller trace formula for a two-dimensional (2D) system can be obtained by integrating only a (2×2) matrix and not the whole monodromy matrix [18]. However, it would give rise to more complicated expressions and probably to additional difficulties in the numerical implementation, whereas the expressions given in the paper can be put in the computer as they stand. Also, the amount of CPU time and the memory needed by the codes are small enough, so that, on a first stage, the reduction of the number of equations can be skipped.

The paper is divided as follows. In Sec. II, expressions for the classical Green's functions involved in the $\hbar$ correction to the semiclassical propagator $K(\mathbf{q},\mathbf{q}_0,T)$ are derived. Then, we explain how to get a numerical implementation of these formulas allowing an efficient computation of the $\hbar$ correction. In Sec. III, we develop a numerical method to get the additional terms, arising from the time to energy domain transformation, in $\hbar$ correction for the quantum Green's function $G(\mathbf{q},\mathbf{q}_0,T)$. In the case of the trace of the propagator, essential steps for the derivation of the $\hbar$ correction are described in Sec. IV, leading to the proper formulas, along with the way they can be computed. The time to energy transformation is explained in Sec. V, leading to the $\hbar$ correction expression in the case of the quantum Green's function. Finally, Sec. VI shows how to apply theoretical expressions obtained in the four preceding sections in the case of the 2D hydrogen in magnetic field and emphasizes the excellent agreement with numerical coefficients extracted from exact quantum calculation, using harmonic inversion [19–21].

II. THE PROPAGATOR $K(\mathbf{q},\mathbf{q}_0,T)$

A. Feynman path integral

The starting point is the Feynman path integral, whose discrete version, for a time independent Hamiltonian which

separates into kinetic and potential energies, $\hat{H}=\hat{\mathbf{p}}^2/2+V(\hat{\mathbf{q}})$, reads as follows [13]:

$$K(\mathbf{q},\mathbf{q}_0,T)=\int d\mathbf{q}_1 d\mathbf{q}_2,\ldots,d\mathbf{q}_{N-1}(2\pi i\hbar\Delta t)^{-Nf/2}\times\exp\left[\frac{i}{\hbar}\sum_{n=0}^{N-1}L\left(\frac{\mathbf{q}_{n+1}-\mathbf{q}_n}{\Delta t},\mathbf{q}_n\right)\Delta t+O(\Delta t)\right], \tag{1}$$

where $\Delta t=T/N$, $\mathbf{q}_N=\mathbf{q}$, and $L(\dot{\mathbf{q}},\mathbf{q})$ is the classical Lagrangian.

For small values of $\hbar$ (i.e., the semiclassical limit), using the stationary phase approximation, all preceding integrals are expanded around the stationary solutions, that is the classical orbits $\mathbf{q}_l^{\mathrm{cl}}(t)$ going from $\mathbf{q}_0$ to $\mathbf{q}$ during time T, each of them thus giving a contribution $K_l(\mathbf{q},\mathbf{q}_0,T)$ to the propagator, whose final expression reads formally as follows [13]:

$$K_l(\mathbf{q},\mathbf{q}_0,T)=K_l^{(0)}(\mathbf{q},\mathbf{q}_0,T)\{1+i\hbar C_1(\mathbf{q},\mathbf{q}_0,T)+O(\hbar^2)\}, \tag{2}$$

where $K_l^{(0)}(\mathbf{q},\mathbf{q}_0,T)$ is the dominant semiclassical contribution to the propagator $K(\mathbf{q},\mathbf{q}_0,T)$:

$$K_l^{(0)}(\mathbf{q},\mathbf{q}_0,T)=\frac{1}{(2\pi i\hbar)^{f/2}}\left|\det\left(-\frac{\partial^2}{\partial\mathbf{q}\partial\mathbf{q}_0}W_l^{\mathrm{cl}}(\mathbf{q},\mathbf{q}_0,T)\right)\right|^{1/2}\times\exp\left[\frac{i}{\hbar}W_l^{\mathrm{cl}}(\mathbf{q},\mathbf{q}_0,T)-i\frac{\pi}{2}\nu_l\right], \tag{3}$$

where $W_l^{\mathrm{cl}}(\mathbf{q},\mathbf{q}_0,T)$ is the classical action and ν_l is the Morse index of the orbit. The $C_1(\mathbf{q},\mathbf{q}_0,T)$ expression is given by [13]

$$\frac{1}{8}\int_0^T dt\,V_{ijkl}^{(4)}(t)\mathcal{G}_{ij}(t,t)\mathcal{G}_{kl}(t,t)+\frac{1}{24}\int_0^T\int_0^T dt\,dt'\,V_{ijk}^{(3)}(t)V_{lmn}^{(3)}(t')\times[3\mathcal{G}_{ij}(t,t)\mathcal{G}_{kl}(t,t')\mathcal{G}_{mn}(t',t')+2\mathcal{G}_{il}(t,t')\mathcal{G}_{jm}(t,t')\mathcal{G}_{kn}(t,t')], \tag{4}$$

where the $V^{(n)}(t)$ are higher-order derivatives of the potential V, evaluated at $\mathbf{q}_l^{\mathrm{cl}}(t)$.

The classical Green's function $\mathcal{G}(t,t')$, associated with the classical orbit, is an $(f\times f)$ matrix solution of the following equation [13]:

$$\mathcal{D}\cdot\mathcal{G}(t,t')=\mathbb{1}\delta(t-t'), \tag{5}$$

where $\mathcal{D}$ is the Jacobi-Hill operator, controlling the linear stability around the classical orbit in the configuration space [13]

$$\mathcal{D}=-\frac{\mathrm{d}^2}{\mathrm{d}t^2}\mathbb{1}-\frac{\partial^2 V}{\partial\mathbf{q}\partial\mathbf{q}}[\mathbf{q}^{\mathrm{cl}}(t)]. \tag{6}$$

Furthermore, the fact that both initial and final point are fixed in the propagator $K(\mathbf{q},\mathbf{q}_0,T)$ imposes the following boundary conditions on the classical Green's function [13]:

$$\mathcal{G}(0,t')=\mathcal{G}(T,t')=0\quad\forall\,t'\in[0,T]. \tag{7}$$

B. Classical Green's function

If $\mathbf{q}_l(T)$ is a conjugate point of $\mathbf{q}_0$, then the determinant $\det(-\partial^2_{\mathbf{q}\mathbf{q}_0}W_l^{\mathrm{cl}})$ in formula (3) is formally infinite, but this happens only for restricted values of T, so that, in this section, we will focus on the general case, for which $\mathbf{q}_l(T)$ and $\mathbf{q}_0$ are not conjugate points.

Apart from $t=t'$, $\mathcal{G}(t,t')$ obeying the homogeneous Jacobi-Hill equation $\mathcal{D}\cdot\mathcal{G}=0$, so that, introducing the notations

$$\mathcal{G}_-(t,t')=\mathcal{G}(t,t')\quad\text{for}\quad 0\leqslant t\leqslant t',\qquad \mathcal{G}_+(t,t')=\mathcal{G}(t,t')\quad\text{for}\quad t'\leqslant t\leqslant T, \tag{8}$$

one immediately obtains

$$\begin{pmatrix}\mathcal{G}_\pm(t,t')\\ \dot{\mathcal{G}}_\pm(t,t')\end{pmatrix}=M(t)\begin{pmatrix}A_\pm(t')\\ B_\pm(t')\end{pmatrix}, \tag{9}$$

where $M(t)$ is the $(2f\times 2f)$ monodromy matrix, depicting the linear stability around the classical orbit in the phase space. $A_\pm$ and $B_\pm$ are four $(f\times f)$ matrices, whose values are determined from the boundary conditions at time $t=t'$:

$$\mathcal{G}_+(t',t')-\mathcal{G}_-(t',t')=0,\qquad \frac{d\mathcal{G}_-}{dt}(t',t')-\frac{d\mathcal{G}_+}{dt}(t',t')=\mathbb{1} \tag{10}$$

and at times $t=0$ and $t=T$:

$$\mathcal{G}_-(0,t')=0,\qquad \mathcal{G}_+(T,t')=0. \tag{11}$$

For a Hamiltonian which separates between kinetic and potential energy $H=\mathbf{p}^2/2+V(\mathbf{q})$, $M(t)$ has the following simple structure:

$$M(t)=\begin{bmatrix}J_2(t) & J_1(t)\\ \dot{J}_2(t) & \dot{J}_1(t)\end{bmatrix}, \tag{12}$$

which leads us to the following explicit expressions for the four matrices $A_\pm$ and $B_\pm$:

$$
\begin{aligned}
&A_-(t')=0,\\
&B_-(t')=J_2^\top(t')-J_1^{-1}(T)J_2(T)J_1^\top(t'),\\
&A_+(t')=J_1^\top(t'),\\
&B_+(t')=-J_1^{-1}(T)J_2(T)J_1^\top(t'),
\end{aligned}
\tag{13}
$$

provided that $J_1^{-1}(T)$ is invertible. $J_1(T)$ being the upper right $(f\times f)$ submatrix of the matrix M, gives the linear displacement of the final position for a change in the initial momentum (the initial position being fixed to $\mathbf{q}_0$), i.e., $\delta\mathbf{q}(T)=J_1(T)\,\delta\mathbf{p}_0$. Thus, $J_1(T)$ is the inverse matrix of $(-\partial^2_{\mathbf{q}\mathbf{q}_0}W_l^{\mathrm{cl}})$ which has been supposed to be invertible [$\mathbf{q}(T)$ and $\mathbf{q}_0$ are not conjugate points]. Finally, the full expression for the classical Green's function reads

$$
\mathcal{G}(t,t')=\begin{cases} J_1(t) & [J_2^\top(t')-J_1^{-1}(T)J_2(T)J_1^\top(t')] \quad \text{for } 0\leqslant t\leqslant t',\\ & [J_2(t)-J_1(t)J_1^{-1}(T)J_2(T)] \quad J_1^\top(t') \quad \text{for } t'\leqslant t\leqslant T. \end{cases}
\tag{14}
$$

Using the symplectic structure of $M(T)$, one can show that

$$
\mathcal{G}(t',t)=\mathcal{G}^\top(t,t')
\tag{15}
$$

as expected because the operator $\mathcal{D}$ and the boundary conditions are symmetric as it explicitly appears in the discrete version of the problem (see Ref. [13]). This is also emphasized in Fig. 1, where the four matrix elements of a classical Green's function $\mathcal{G}(t,t')$ (for $t'/T=0.6$) are plotted with respect to time t. This example corresponds to a classical orbit of the 2D hydrogen atom in a magnetic field having initial and final points on the nucleus, namely, the closed orbit having code 0—and whose trajectory in (u,v) coordinates is also shown in the figure. (See Sec. VI for all details.) As expected, the Green's function vanishes at initial and final times [i.e., $\mathcal{G}(0,t')=\mathcal{G}(T,t')=0$] and for $t=t'$, the derivatives of each diagonal element $\mathcal{G}_{11}(t',t')$ (continuous line) and $\mathcal{G}_{22}(t',t')$ (long dashed line) are discontinuous whereas, from property (15), the two off-diagonal elements are equal (dotted and dashed lines).

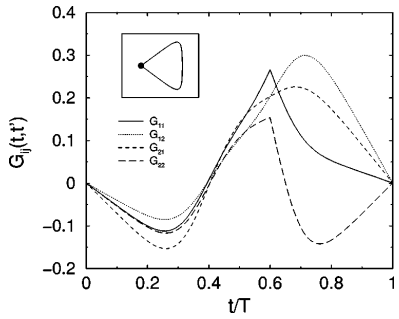

FIG. 1. Example of a classical Green's function $\mathcal{G}(t,t')$ involved in the calculation of the $\hbar$ corrections for the propagator $K(\mathbf{q},\mathbf{q}_0,T)$, for the case $\mathbf{q}=\mathbf{q}_0=\mathbf{0}$. It is associated with the closed orbit $\overline{1243}$ of the 2D hydrogen atom in magnetic field, whose trajectory in (u,v) coordinates is inserted in the plot (see Sec. VI for all details). This trajectory starts and ends at the nucleus, depicted by the black circle. Each curve corresponds to a matrix element $\mathcal{G}_{ij}(t,t')$ plotted with respect to time t, for $t'/T=0.6$. As expected from boundary conditions (7), the Green's function vanishes at initial and final times [i.e., $\mathcal{G}(0,t')=\mathcal{G}(T,t')=0$] and for $t=t'$, the derivatives of diagonal elements, $\mathcal{G}_{11}(t',t')$ (continuous line) and $\mathcal{G}_{22}(t',t')$ (long dashed line), are discontinuous whereas, from symmetry property (15) [i.e., $\mathcal{G}^\top(t,t')=\mathcal{G}(t',t)$], the two off-diagonal elements are equal (dotted and dashed lines).

C. Getting $C_1(\mathbf{q},\mathbf{q}_0,T)$ by integrating a set of first order differential equations

From Eq. (4), there are three contributions to $C_1(\mathbf{q},\mathbf{q}_0,T)$, namely,

$$
\begin{aligned}
I_1(T)&=\int_0^T dt\, V^{(4)}_{ijkl}(t)\mathcal{G}_{ij}(t,t)\mathcal{G}_{kl}(t,t),\\
I_2^+(T)&=\int_0^T\int_0^T dt\,dt'\,V^{(3)}_{ijk}(t)V^{(3)}_{lmn}(t')\\
&\quad\times\mathcal{G}_{ij}(t,t)\mathcal{G}_{kl}(t,t')\mathcal{G}_{mn}(t',t'),\\
I_2^-(T)&=\int_0^T\int_0^T dt\,dt'\,V^{(3)}_{ijk}(t)V^{(3)}_{lmn}(t')\\
&\quad\times\mathcal{G}_{il}(t,t')\mathcal{G}_{jm}(t,t')\mathcal{G}_{kn}(t,t').
\end{aligned}
\tag{16}
$$

Even if, in principle, one can compute $\mathcal{G}(t,t')$ for any (t,t') values using Eq. (14), direct evaluation of the double integrals $I_2^\pm$ would be time consuming and numerically inefficient using standard integration routines, especially because, from its definition, $\mathcal{G}(t,t')$ is not a smooth function around the line $t=t'$. In what follows, we will show that the preceding integrals can be transformed in such a way that their values can be obtained integrating a set of first order differential equations along the classical orbit, in the same way that, for example, the monodromy matrix $M(T)$ can be computed.

Separating $t>t'$ and $t<t'$ contributions in $I_2^{\pm}$, using symmetry property (15) of $\mathcal{G}(t,t')$ and that the matrix $V^{(3)}$ is fully symmetric under index permutations, one gets, after straightforward algebra,

$$I_2^+(T)=2\int_0^T dt\int_0^t dt'\; V^{(3)}_{ijk}(t)V^{(3)}_{lmn}(t')\times\mathcal{G}_{ij}(t,t)\mathcal{G}_{kl}(t,t')\mathcal{G}_{mn}(t',t'),$$

$$I_2^-(T)=2\int_0^T dt\int_0^t dt'\; V^{(3)}_{ijk}(t)V^{(3)}_{lmn}(t')\times\mathcal{G}_{il}(t,t')\mathcal{G}_{jm}(t,t')\mathcal{G}_{kn}(t,t'). \quad (17)$$

In the preceding expressions the Green's function $\mathcal{G}(t,t')$ is used only for (t,t') values in the triangle $0\leqslant t'\leqslant t\leqslant T$ and is formally written $\mathcal{G}(t,t')=B_-^{\top}(t)J_1^{\top}(t')$ [see Eq. (14)], thus separating t and t' contributions:

$$I_2^+(T)=2\int_0^T dt\; V^{(3)}_{ijk}(t)\mathcal{G}_{ij}(t,t)B^-_{pk}(t)\times\int_0^t dt'\; V^{(3)}_{lmn}(t')J_{1lp}(t')\mathcal{G}_{mn}(t',t'),$$

$$I_2^-(T)=2\int_0^T dt\; V^{(3)}_{ijk}(t)B^-_{pi}(t)B^-_{qj}(t)B^-_{rk}(t)\times\int_0^t dt'\; V^{(3)}_{lmn}(t')J_{1lp}(t')J_{1mq}(t')J_{1nr}(t'). \quad (18)$$

This leads us to introduce two intermediate quantities, namely, $P_p(t)$ and $Q_{pqr}(t)$ (for p, q and r running from 1 to f):

$$P_p(t)=\int_0^t dt'\; V^{(3)}_{lmn}(t')J_{1lp}(t')\mathcal{G}_{mn}(t',t'),$$

$$Q_{pqr}(t)=\int_0^t dt'\; V^{(3)}_{lmn}(t')J_{1lp}(t')J_{1mq}(t')J_{1nr}(t') \quad (19)$$

in a way such that $I_2^{\pm}(T)$ [and $I_1(T)$] are solutions of the following set of differential equations [besides equations for $\mathbf{X}(t)$ and $M(t)$]:

$$\begin{aligned}
\dot I_1&=V^{(4)}_{ijkl}(t)\mathcal{G}_{ij}(t,t)\mathcal{G}_{kl}(t,t),\\
\dot P_p&=V^{(3)}_{lmn}(t)J_{1lp}(t)\mathcal{G}_{mn}(t,t),\\
\dot I_2^+&=V^{(3)}_{ijk}(t)\mathcal{G}_{ij}(t,t)B^-_{pk}(t)P_p(t),\\
\dot Q_{pqr}&=V^{(3)}_{lmn}(t)J_{1lp}(t)J_{1mq}(t)J_{1nr}(t),\\
\dot I_2^-&=V^{(3)}_{ijk}(t)B^-_{pi}(t)B^-_{qj}(t)B^-_{rk}(t)Q_{pqr}(t)
\end{aligned} \quad (20)$$

with initial conditions $I_1(0)=I_2^{\pm}(0)=P_p(0)=Q_{pqr}(0)=0$. This set of equations, f^3+4f^2+3f+3 in total (i.e., 33 for a 2D system) is easily integrated using any standard method (fourth order Runge-Kutta in the present case). As mentioned in the Introduction, the size of the preceding differential set is probably not minimal and could be reduced by a deeper analysis of the structure of these equations. However, it allows a fast and easy computation of the correction $C_1(\mathbf{q},\mathbf{q}_0,T)$:

(1) find a trajectory going from $\mathbf{q}_0$ to $\mathbf{q}$ in time T;

(2) integrate the differential set for $\mathbf{X}(t)$ and $M(t)$ along the trajectory to obtain the quantity $J_1^{-1}(T)J_2(T)$;

(3) integrate the set of Eqs. (20) along the trajectory to get the three quantities I_1, $I_2^{\pm}$, entering in the $C_1(\mathbf{q},\mathbf{q}_0,T)$ expression.

III. THE GREEN'S FUNCTION $G(\mathbf{q},\mathbf{q}_0,E)$

A. Going from time to energy domain

Since the quantum Green's function $G(\mathbf{q},\mathbf{q}_0,E)$ is related to the propagator $K(\mathbf{q},\mathbf{q}_0,T)$, through a semisided Fourier transform, this relation also holds between semiclassical contributions arising from each classical orbit, more precisely,

$$G_l(\mathbf{q},\mathbf{q}_0,E)=\frac{1}{i\hbar}\int_0^{+\infty}dT\exp\left(\frac{i}{\hbar}ET\right)K_l(\mathbf{q},\mathbf{q}_0,T). \quad (21)$$

Again, a stationary phase approximation is used to perform the integral, which, for a given trajectory going from $\mathbf{q}_0$ to $\mathbf{q}$, selects its total duration T_0 such that the classical motion is made at energy E. This operation also gives rise to additional terms in $\hbar$ corrections, to be summed with $C_1(\mathbf{q},\mathbf{q}_0,T)$, and whose explicit expressions can be derived starting from Eq. (4) formally written as follows [13]:

$$K_l(\mathbf{q},\mathbf{q}_0,T)=\frac{1}{(2\pi i\hbar)^{f/2}}\exp\left[\frac{i}{\hbar}W_l(\mathbf{q},\mathbf{q}_0,T)-i\frac{\pi}{2}\nu_l+C_0(\mathbf{q},\mathbf{q}_0,T)+i\hbar C_1(\mathbf{q},\mathbf{q}_0,T)\right], \quad (22)$$

$C_0(\mathbf{q},\mathbf{q}_0,T)$ being the (logarithm of) usual semiclassical amplitude. Then $W_l(\mathbf{q},\mathbf{q}_0,T)$ and $C_0(\mathbf{q},\mathbf{q}_0,T)$ are systematically expanded around T_0:

$$\begin{aligned}
W_l(\mathbf{q},\mathbf{q}_0,T)&=W_l^{(0)}+\delta T\,W_l^{(1)}+\frac{\delta T^2}{2}W_l^{(2)}+\frac{\delta T^3}{6}W_l^{(3)}+\frac{\delta T^4}{24}W_l^{(4)},\\
C_0(\mathbf{q},\mathbf{q}_0,T)&=C_0^{(0)}+\delta T\,C_0^{(1)}+\frac{\delta T^2}{2}C_0^{(2)},
\end{aligned} \quad (23)$$

with $\delta T=(T-T_0)$. Terms arising from $C_1(T)$ expansion would contribute only to $\hbar^2$ correction and can be discarded. Performing the imaginary Gaussian integrals leads to the additional $\hbar$ corrections:

$$C_1^{T\to E}(\mathbf{q},\mathbf{q}_0,T_0)=\frac{1}{2W_l^{(2)}}[(C_0^{(1)})^2+C_0^{(2)}] -\frac{W_l^{(3)}C_0^{(1)}}{2(W_l^{(2)})^2}-\frac{W_l^{(4)}}{8(W_l^{(2)})^2}+\frac{5}{24}\frac{(W_l^{(3)})^2}{(W_l^{(2)})^3}. \tag{24}$$

The preceding formula is similar to the one in Ref. [13], where the authors have expressed the coefficient $C_1^{T\to E}(\mathbf{q},\mathbf{q}_0,T_0)$ in terms of derivatives of amplitude and action with respect to energy E. The full expression of $G_l(\mathbf{q},\mathbf{q}_0,E)$ is then given by

$$G_l(\mathbf{q},\mathbf{q}_0,E)=\frac{2\pi}{(2\pi i\hbar)^{(f+1)/2}}\frac{1}{|W_l^{(2)}\det J_1(T_0)|^{1/2}} \times\exp\left[\frac{i}{\hbar}S_l(\mathbf{q},\mathbf{q}_0,E)-i\frac{\pi}{2}\tilde{\nu}_l\right] \times\{1+i\hbar[C_1(\mathbf{q},\mathbf{q}_0,T_0)+C_1^{T\to E}(\mathbf{q},\mathbf{q}_0,T_0)] +O(\hbar^2)\}, \tag{25}$$

where $S_l(\mathbf{q},\mathbf{q}_0,E)$ is the reduced action and

$$\tilde{\nu}_l=\nu_l \quad \text{if } W_l^{(2)}>0, \qquad \tilde{\nu}_l=\nu_l+1 \quad \text{if } W_l^{(2)}<0. \tag{26}$$

B. Getting $C_1^{T\to E}(\mathbf{q},\mathbf{q}_0,T_0)$ by integrating a set of first order differential equations

In Sec. II C, we have shown that $C_1(\mathbf{q},\mathbf{q}_0,T_0)$ can be computed by integrating a set of differential equations along the classical orbit going from $\mathbf{q}_0$ to $\mathbf{q}$ in time T_0. In this section we will show that it is also true for $C_1^{T\to E}(\mathbf{q},\mathbf{q}_0,T_0)$, which involves derivatives of both $W_l(\mathbf{q},\mathbf{q}_0,T)$ and $\det J_1(T)$ with respect to T.

For all T, we have the following functional relation ($\mathbf{q}_0$ and $\mathbf{q}$ being fixed):

$$\frac{\partial W_l(\mathbf{q},\mathbf{q}_0,T)}{\partial T}=-E(\mathbf{q},\mathbf{q}_0,T), \tag{27}$$

where $E(\mathbf{q},\mathbf{q}_0,T)$ is the energy of the classical trajectory, $\mathbf{q}(t,T)$, going from $\mathbf{q}_0$ to $\mathbf{q}$ in time T, that is, the value of the Hamiltonian H taken at any point on the corresponding phase space trajectory $\mathbf{X}(t,T)=[\mathbf{q}(t,T),\mathbf{p}(t,T)]$.

Writing $T=T_0+\delta T$, the Taylor expansion of $H[\mathbf{X}(t,T_0+\delta T)]$ is easily deduced from the Taylor expansion of $\mathbf{X}(t,T_0+\delta T)$ around the reference trajectory $\mathbf{X}(t,T_0)$ [noted hereafter as $\mathbf{X}^{(0)}(t)$]:

$$\mathbf{X}(t,T_0+\delta T)=\mathbf{X}^{(0)}(t)+\delta T\,\mathbf{X}^{(1)}(t)+\frac{\delta T^2}{2}\mathbf{X}^{(2)}(t) +\frac{\delta T^3}{6}\mathbf{X}^{(3)}(t)+\cdots \tag{28}$$

and from which one obtains the higher derivatives of the classical action $W_l^{(n)}$ at $T=T_0$:

$$\begin{aligned} W_l^{(1)}&=-H[\mathbf{X}^{(0)}(t)],\\ W_l^{(2)}&=-X_i^{(1)}H_i^{(1)},\\ W_l^{(3)}&=-(X_i^{(2)}H_i^{(1)}+X_i^{(1)}X_j^{(1)}H_{ij}^{(2)}),\\ W_l^{(4)}&=-(X_i^{(3)}H_i^{(1)}+3X_i^{(1)}X_j^{(2)}H_{ij}^{(2)}+X_i^{(1)}X_j^{(1)}X_k^{(1)}H_{ijk}^{(3)}), \end{aligned} \tag{29}$$

where all derivatives of H are evaluated at $\mathbf{X}^{(0)}(t)$.

Equations for $\mathbf{X}^{(n)}(t)$ are deduced from Hamilton's equations governing $\mathbf{X}(t,T)$ evolution:

$$\begin{aligned} \dot{X}_i^{(1)}&=\Sigma_{ij}H_{jk}^{(2)}X_k^{(1)},\\ \dot{X}_i^{(2)}&=\Sigma_{ij}H_{jk}^{(2)}X_k^{(2)}+\Sigma_{ij}H_{jkl}^{(3)}X_k^{(1)}X_l^{(1)},\\ \dot{X}_i^{(3)}&=\Sigma_{ij}H_{jk}^{(2)}X_k^{(3)}+3\Sigma_{ij}H_{jkl}^{(3)}X_k^{(1)}X_l^{(2)} +\Sigma_{ij}H_{jklm}^{(4)}X_k^{(1)}X_l^{(1)}X_m^{(1)}, \end{aligned} \tag{30}$$

where again all derivatives of H are evaluated at $\mathbf{X}^{(0)}(t)$. Thus, we are facing three differential sets of the form $\dot{\mathbf{X}}^{(i)}=\Sigma H^{(2)}\mathbf{X}^{(i)}+\Sigma\mathbf{Y}^{(i)}$ (i.e., nonhomogeneous linear differential equations), with the important property that the vector $\mathbf{Y}^{(i)}$ only depends on vectors $\mathbf{X}^{(j)}$ with $j<i$, so that they can be solved one after the other. Solutions of these nonhomogeneous linear differential equations are expressed with the monodromy matrix $M^{(0)}$:

$$\begin{aligned} \mathbf{X}^{(1)}(t)&=M^{(0)}(t)\mathbf{X}^{(1)}(0),\\ \mathbf{X}^{(2)}(t)&=M^{(0)}(t)\mathbf{X}^{(2)}(0)+\mathbf{F}^{(2)}(t),\\ \mathbf{X}^{(3)}(t)&=M^{(0)}(t)\mathbf{X}^{(3)}(0)+\mathbf{F}^{(3)}(t). \end{aligned} \tag{31}$$

Among the $3\times(2f)$-dimensional space of solutions given by preceding expressions, the relevant one is selected by transposing on initial values $\mathbf{X}^{(i)}(0)$ (for $i=1,2,3$) the two boundary conditions

$$\mathbf{q}(0,T_0+\delta T)=\mathbf{q}_0 \quad \text{and} \quad \mathbf{q}(T_0+\delta T,T_0+\delta T)=\mathbf{q}. \tag{32}$$

Introducing position $\mathbf{q}^{(i)}$ and momentum $\mathbf{p}^{(i)}$ parts for vectors $\mathbf{X}^{(i)}$, the Taylor expansion of the preceding equations leads to the following boundary conditions:

$$\begin{aligned}
&\mathbf{q}^{(1)}(0)=0 && \mathbf{q}^{(1)}(T_0)=-\dot{\mathbf{q}}^{(0)}(T_0),\\
&\mathbf{q}^{(2)}(0)=0 && \mathbf{q}^{(2)}(T_0)=-\ddot{\mathbf{q}}^{(0)}(T_0)-2\dot{\mathbf{q}}^{(1)}(T_0),\\
&\mathbf{q}^{(3)}(0)=0 \quad \text{and} && \mathbf{q}^{(3)}(T_0)=-\dddot{\mathbf{q}}^{(0)}(T_0)-3\ddot{\mathbf{q}}^{(1)}(T_0)-3\dot{\mathbf{q}}^{(2)}(T_0).
\end{aligned} \tag{33}$$

Thus, the initial values $\mathbf{p}^{(i)}(0)$ are implicitly determined by the final values $\mathbf{q}^{(i)}(T_0)$, through the integral expressions (31), which for $\mathbf{X}^{(1)}$ reads

$$\begin{pmatrix}\mathbf{q}^{(1)}(T_0)\\ \mathbf{p}^{(1)}(T_0)\end{pmatrix}=\begin{bmatrix}J_2(T_0) & J_1(T_0)\\ \dot{J}_2(T_0) & \dot{J}_1(T_0)\end{bmatrix}\begin{pmatrix}\mathbf{0}\\ \mathbf{p}^{(1)}(0)\end{pmatrix}, \tag{34}$$

showing thus that $\mathbf{p}^{(1)}(0)=-J_1^{-1}(T_0)\dot{\mathbf{q}}^{(0)}(T_0)$.

Then $\mathbf{F}^{(2)}(T_0)$ and $\mathbf{F}^{(3)}(T_0)$ are easily computed by integrating sets of differential equations obtained from Eq. (30), allowing us to derive $\mathbf{p}^{(2)}(0)$ and $\mathbf{p}^{(3)}(0)$ values from Eq. (31), solving systems similar to Eq. (34):

$$\begin{aligned}
\mathbf{p}^{(2)}(0)&=-J_1^{-1}(T_0)[\ddot{\mathbf{q}}^{(0)}(T_0)+2\dot{\mathbf{q}}^{(1)}(T_0)+\mathbf{f}^{(2)}(T_0)],\\
\mathbf{p}^{(3)}(0)&=-J_1^{-1}(T_0)[\dddot{\mathbf{q}}^{(0)}(T_0)+3\ddot{\mathbf{q}}^{(1)}(T_0)\\
&\quad+3\dot{\mathbf{q}}^{(2)}(T_0)+\mathbf{f}^{(3)}(T_0)],
\end{aligned} \tag{35}$$

where we have introduced the notation $(\mathbf{f}^{(i)},\mathbf{g}^{(i)})$ for vectors $\mathbf{F}^{(i)}$. Quantities like $\dot{\mathbf{q}}^{(1)}(T_0)$, $\ddot{\mathbf{q}}^{(1)}(T_0)$, and $\dot{\mathbf{q}}^{(2)}(T_0)$ can also be expressed in terms of $\mathbf{X}^{(0)}(T_0)$ and its derivatives.

At this point, from the values of the three vectors $\mathbf{X}^{(i)}(T_0)$ and using Eqs. (29) at time T_0, all derivatives $W^{(n)}$ of the classical action can be computed.

We now explain how to compute derivatives of $\det J_1(T)$. More precisely one has to calculate the two coefficients $C_0^{(1)}$ and $C_0^{(2)}$, which are derivatives of $-\ln\sqrt{|\det J_1(T)|}$, so that, using the well-known formula

$$\frac{d}{dT}(\ln|\det J|)=\mathrm{Tr}\left(J^{-1}\frac{dJ}{dT}\right) \tag{36}$$

[J being any (invertible) matrix], expressions of $C_0^{(1)}$ and $C_0^{(2)}$ become

$$\begin{aligned}
C_0^{(1)}&=-\frac{1}{2}\mathrm{Tr}\left(J_1^{-1}(T_0)\frac{dJ_1(T_0)}{dT}\right),\\
C_0^{(2)}&=-\frac{1}{2}\mathrm{Tr}\left(J_1^{-1}(T_0)\frac{d^2J_1(T_0)}{dT^2}\right.\\
&\quad\left.-J_1^{-1}(T_0)\frac{dJ_1(T_0)}{dT}J_1^{-1}(T_0)\frac{dJ_1(T_0)}{dT}\right),
\end{aligned} \tag{37}$$

where $dJ_1(T_0)/dT$ means derivative of $J_1(T_0)$ when changing total time T (and thus the classical orbit), which must not be confused with $\dot{J}_1$ (time derivative of J_1 along a given classical orbit). $J_1(T)$ being the $(f\times f)$ upper right submatrix of the monodromy matrix $M(T)$, $d^nJ_1(T_0)/dT^n$ is also stored at the same position in matrix $d^nM(T_0)/dT^n$, for which we will derive general expressions. For this purpose, we first introduce the explicit notation $M(t,T)$, representing the value of the monodromy matrix at time t along the orbit going from $\mathbf{q}_0$ to $\mathbf{q}$ in time T. Writing $T=T_0+\delta T$, the Taylor expansion of $M(t,T)$ for a given time t reads

$$M(t,T_0+\delta T)=M^{(0)}(t)+\delta T\,M^{(1)}(t)+\frac{\delta T^2}{2}M^{(2)}(t), \tag{38}$$

where $M^{(0)}(t)$ is the monodromy matrix along the reference orbit (i.e., going from $\mathbf{q}_0$ to $\mathbf{q}$ in time T_0). Then $dM(T_0)/dT$ and $d^2M(T_0)/dT^2$ are the Taylor coefficients of monodromy matrix $M(T_0+\delta T,T_0+\delta T)$ and thus have the following expression:

$$\begin{aligned}
\frac{dM(T_0)}{dT}&=\dot{M}^{(0)}(T_0)+M^{(1)}(T_0),\\
\frac{d^2M(T_0)}{dT^2}&=\ddot{M}^{(0)}(T_0)+2\dot{M}^{(1)}(T_0)+M^{(2)}(T_0).
\end{aligned} \tag{39}$$

Equations governing $M^{(i)}(t)$ evolution are easily deduced from the one for $M(t,T)$:

$$\begin{aligned}
\dot{M}^{(1)}_{ij}&=\Sigma_{ik}[H^{(2)}_{kl}M^{(1)}_{lj}+H^{(3)}_{klm}X^{(1)}_mM^{(0)}_{lj}],\\
\dot{M}^{(2)}_{ij}&=\Sigma_{ik}[H^{(2)}_{kl}M^{(2)}_{lj}+2H^{(3)}_{klm}X^{(1)}_mM^{(1)}_{lj}\\
&\quad+H^{(3)}_{klm}X^{(2)}_mM^{(0)}_{lj}+H^{(4)}_{klmn}X^{(1)}_mX^{(1)}_nM^{(0)}_{lj}],
\end{aligned} \tag{40}$$

with initial conditions $M^{(1)}(0)=M^{(2)}(0)=0$. Obviously these equations are similar to those governing $\mathbf{X}^{(i)}$ evolution, so that $M^{(1)}(T_0)$ and $M^{(2)}(T_0)$ values will be obtained by integrating similar differential sets. Actually, it can be shown that all these sets (for both $\mathbf{X}^{(i)}$ and $M^{(i)}$) can be concatened in only one (larger) set of differential equations, whose integration can be done at once.

Finally, gathering all quantities in Eq. (39), the two matrices $dJ_1(T_0)/dT$ and $d^2J_1(T_0)/dT^2$ are inserted in Eq. (37) thus giving values for $C_0^{(1)}$ and $C_0^{(2)}$, which, along with the values for $W_l^{(n)}$, allow us to compute the numerical value for $C_1^{T\to E}(\mathbf{q},\mathbf{q}_0,T_0)$.

Obviously, the number of equations in the preceding differential sets can be reduced, especially for Hamiltonian separating into kinetic and potential energy, for which $H^{(3)}_{jkl}$ and $H^{(4)}_{jklm}$ coefficients are nonvanishing only when $1\leqslant j,k,l,m\leqslant f$. However, these sets are straightforward to

implement and need only a small amount of CPU time to be solved using any conventional integrator (fourth order Runge-Kutta in the present case).

IV. TRACE OF THE PROPAGATOR $K(T)$

The diagonal elements $K(\mathbf{q}_0,\mathbf{q}_0,T)$ of the propagator are related to classical orbits starting from $\mathbf{q}_0$ and returning to this point after time T, i.e., closed orbits. Summing all these diagonal elements, that is performing the integral $\int d\mathbf{q}_0\, K(\mathbf{q}_0,\mathbf{q}_0,T)$, will select, through another stationary phase approximation, closed orbits for which initial and final momentum are equal: periodic orbits. ħ corrections to leading order of the semiclassical contribution to $K(T)$ from each periodic orbit can be derived following the same scheme previously used for the propagator itself [1,13].

A. Feynman path integral

Adding the integral over the initial and final positions in Eq. (1) yields [13]

$$K(T)=\int d\mathbf{q}_0\, d\mathbf{q}_1\, d\mathbf{q}_2,\ldots,d\mathbf{q}_{N-1}(2\pi i\hbar\Delta t)^{-Nf/2}\times\exp\left[\frac{i}{\hbar}\sum_{n=0}^{N-1}L\left(\frac{\mathbf{q}_{n+1}-\mathbf{q}_n}{\Delta t},\mathbf{q}_n\right)\Delta t+O(\Delta t)\right] \tag{41}$$

with $\mathbf{q}_N=\mathbf{q}_0$.

The stationary phase approximation around a given periodic orbit $\mathbf{q}_l^{\rm cl}(t)$ is made explicit when replacing the preceding Nf integral with [13]

$$\int dq_0^{\parallel}\, d\boldsymbol{\xi}_0^{\perp}\, d\boldsymbol{\xi}_1\, d\boldsymbol{\xi}_2,\ldots,d\boldsymbol{\xi}_{N-1} \tag{42}$$

with $\boldsymbol{\xi}_n=\mathbf{q}_n-\mathbf{q}_l^{\rm cl}(n\Delta t)$. For $n=0$ (i.e., initial position), only deviations perpendicular to the periodic orbit $\boldsymbol{\xi}_0^{\perp}$ have been introduced because the classical action $W_l(\mathbf{q}_0,\mathbf{q}_0,T)$ is constant along the orbit (depicted by $q_0^{\parallel}$). The contribution $K_l(T)$ of this periodic orbit to $K(T)$ then reads [13]

$$K_l(T)=\left(\frac{N}{2\pi i\hbar T}\right)^{Nf/2}\exp\left(\frac{i}{\hbar}W_l\right)\int dq_0^{\parallel}\, d\boldsymbol{\xi}_0^{\perp}\, d\boldsymbol{\xi}_1\times d\boldsymbol{\xi}_2,\ldots,d\boldsymbol{\xi}_{N-1}\exp\left(\frac{i}{2\hbar}W_{,ab}\xi_a\xi_b\right)\times\left[1+\frac{i}{6\hbar}W_{,abc}\xi_a\xi_b\xi_c+\frac{i}{24\hbar}W_{,abcd}\xi_a\xi_b\xi_c\xi_d-\frac{1}{72\hbar^2}W_{,abc}W_{,def}\xi_a\xi_b\xi_c\xi_d\xi_e\xi_f\right], \tag{43}$$

where $\xi_a=\xi_{0i}^{\perp}$ when $a=(0,i)$ and $\xi_a=0$ when $a=(0,0)$. W_l is, in the large N limit, the classical action of the periodic orbit. Full expressions for $W_{,ab}$, $W_{,abc}$, and $W_{,abcd}$ can be found in Ref. [13].

Then, the next step would consist of performing all imaginary Gaussian integrals, leaving out the integral along the orbit. However, in the preceding coordinate transformation (42), there is an hidden subtlety, affecting only ħ corrections, which probably explains why it is not mentioned in usual textbooks [1,3], where authors are only looking at leading semiclassical amplitudes.

Actually, the problem is that the integral over $q_0^{\parallel}$ corresponds to the length of the classical orbit, only when $\boldsymbol{\xi}_0^{\perp}=\mathbf{0}$; for a nonzero value, it will correspond to integration on a closed curve, slightly displaced from the original trajectory, whose length will thus depend on the $\boldsymbol{\xi}_0^{\perp}$ value. To enlighten this, let us suppose that we have a bidimensional system, for which one periodic orbit is a circle of radius R_0, traveled at constant speed $V_0=2\pi R_0/T$. The coordinate transformation is then easily made using polar coordinates (r,θ):

$$r=R_0-\xi_0^{\perp}. \tag{44}$$

The negative sign appears to preserve orientation. The volume element $dx\,dy$ becomes

$$dx\,dy=r\,d\theta\,dr=(R_0-\xi_0^{\perp})\,d\theta\,d\xi_0^{\perp}, \tag{45}$$

which shows that, in this case, $dq_0^{\parallel}$ is not simply $R_0\,d\theta$, the length on the periodic orbit, but is given by

$$dq_0^{\parallel}=(R_0-\xi_0^{\perp})\,d\theta\neq R_0\,d\theta. \tag{46}$$

This simple example shows actually that the variable $q_0^{\parallel}$ is not independent of $\boldsymbol{\xi}_0^{\perp}$, whereas θ is.

For a general system, the variable that can play the θ role is actually the time t, whose variation domain $[0,T]$ is fixed and then obviously independent of $\boldsymbol{\xi}_0^{\perp}$. Thus one has to generalize the relation $dq_0^{\parallel}=|\dot{\mathbf{q}}^{\rm cl}|dt_0$, valid only on the periodic orbit. This is done by writing explicitly the coordinate transformation $\mathbf{q}\rightarrow(t_0,\boldsymbol{\xi}_0^{\perp})$:

$$\mathbf{q}=\mathbf{q}^{\rm cl}(t_0)+\xi_{0i}^{\perp}\mathbf{n}_i(t_0), \tag{47}$$

where $\mathbf{n}_i(t_0)$ are $f-1$ orthogonal unit vectors lying in the plane perpendicular to the periodic orbit at time t_0. The Jacobian of the transformation reads

$$\det\frac{\partial\mathbf{q}}{\partial(t_0,\boldsymbol{\xi}_0^{\perp})}=\det[\dot{\mathbf{q}}^{\rm cl}+\xi_{0i}^{\perp}\dot{\mathbf{n}}_i,\mathbf{n}_1,\cdots,\mathbf{n}_{f-1}]=|\dot{\mathbf{q}}^{\rm cl}|-\frac{1}{|\dot{\mathbf{q}}^{\rm cl}|}\boldsymbol{\xi}_0^{\perp}\cdot\ddot{\mathbf{q}}^{\rm cl}. \tag{48}$$

Inserting the volume element in Eq. (43), the contribution $K_l(T)$ of the periodic orbit now reads, keeping only terms giving rise to ħ corrections,

$$K_l(T)=\left(\frac{N}{2\pi i\hbar T}\right)^{Nf/2}\exp\left(\frac{i}{\hbar}W_l\right)\times\int|\dot{\mathbf{q}}^{\rm cl}|dt_0\,d\boldsymbol{\xi}_0^{\perp}d\boldsymbol{\xi}_1d\boldsymbol{\xi}_2,\ldots,d\boldsymbol{\xi}_{N-1}\times\exp\left(\frac{i}{2\hbar}W_{,ab}\xi_a\xi_b\right)\times\left[1+\frac{\xi_{\tilde{d}}V_{,\tilde{d}}}{|\dot{\mathbf{q}}^{\rm cl}|^2}+\frac{i}{6\hbar}W_{,abc}\xi_a\xi_b\xi_c+\frac{i}{24\hbar}W_{,abcd}\xi_a\xi_b\xi_c\xi_d+\frac{i}{6\hbar}\frac{V_{,\tilde{d}}W_{,abc}\xi_{\tilde{d}}\xi_a\xi_b\xi_c}{|\dot{\mathbf{q}}^{\rm cl}|^2}-\frac{1}{72\hbar^2}W_{,abc}W_{,def}\xi_a\xi_b\xi_c\xi_d\xi_e\xi_f\right],\tag{49}$$

where we have seen that $\ddot{\mathbf{q}}^{\rm cl}=-\partial_{\mathbf{q}}V$ and we have introduced the index $\tilde{d}$ for $(0,j)$.

As explained in Ref. [13], the imaginary Gaussian integrals can be expressed in terms of another classical Green's functions $\mathcal{G}(t,t')$, whose boundary conditions are extracted when comparing the detailed expression of $W_{,ab}$ with the discrete version of the Jacobi-Hill operator $\mathcal{D}$, see Eq. (6). Especially, it can be shown that, in the large N limit, they become

$$\begin{aligned}&\mathcal{G}(0,t')=\mathcal{G}(T,t'),\\&\mathcal{P}_{t_0}\mathcal{G}(0,t')=\mathcal{P}_{t_0}\mathcal{G}(T,t')=0,\ \forall\, t'\in[0,T],\\&\mathcal{Q}_{t_0}\dot{\mathcal{G}}(0,t')=\mathcal{Q}_{t_0}\dot{\mathcal{G}}(T,t'),\end{aligned}\tag{50}$$

where we have introduced $\mathcal{P}_{t_0}$ the projector along the periodic orbit at time t_0 and $\mathcal{Q}_{t_0}=1-\mathcal{P}_{t_0}$. In Ref. [13], only the f^2+f boundary conditions corresponding to the first two lines were given, whereas the f^2-f ones corresponding to the last line were missing.

Performing all imaginary Gaussian integrals and taking the large N limit in Eq. (49), the contribution of the given periodic orbit to the trace of the propagator reads as follows:

$$K_l(T)=K_l^{(0)}(T)\left\{1+i\hbar\,\frac{1}{T}\int_0^T dt_0 C_1(T,t_0)+O(\hbar^2)\right\},\tag{51}$$

$K_l^{(0)}(T)$ being the usual semiclassical leading order [1,13,22]

$$K_l^{(0)}(T)=\frac{1}{\sqrt{2\pi\hbar}}\frac{T}{|\partial_E T\det[m(T)-1]|^{1/2}}\times\exp\left[\frac{i}{\hbar}W_l(T)-i\frac{\pi}{2}\mu_l+i\,\mathrm{sgn}\,\partial_E T\right],\tag{52}$$

where $W_l(T)$ is the classical action of the periodic orbit and μ_l its Maslov index.

The first $\hbar$ correction $C_1(T)$ to $K_l^{(0)}(T)$ is then obtained by averaging over the time t_0 (i.e., over the full periodic orbit) the coefficient $C_1(T,t_0)$, given by

$$\begin{aligned}C_1(T,t_0)=&\frac{1}{8}\int_0^T dt\,V_{ijkl}^{(4)}(t)\mathcal{G}_{ij}(t,t)\mathcal{G}_{kl}(t,t)\\&+\frac{1}{2}\frac{V_l^{(1)}(t_0)}{|\dot{\mathbf{q}}^{\rm cl}|^2}\int_0^T dt\,V_{ijk}^{(3)}(t)\mathcal{G}_{lk}(0,t)\mathcal{G}_{ij}(t,t)\\&+\frac{1}{24}\int_0^T\int_0^T dt\,dt'\,V_{ijk}^{(3)}(t)V_{lmn}^{(3)}(t')[3\mathcal{G}_{ij}(t,t)\\&\times\mathcal{G}_{kl}(t,t')\mathcal{G}_{mn}(t',t')\\&+2\mathcal{G}_{il}(t,t')\mathcal{G}_{jm}(t,t')\mathcal{G}_{kn}(t,t')],\end{aligned}\tag{53}$$

where t_0 represents thus the position $\mathbf{q}_0$ on the periodic orbit at which boundary conditions (50) on the classical Green's function $\mathcal{G}(t,t')$ are applied. $\mathbf{q}_0$ is also the initial (and final) position on the periodic orbit for classical motions corresponding to times t and t' entered in the preceding expression.

B. Classical Green's function

As in Sec. II B, where expressions for classical Green's functions for the propagator $K(\mathbf{q},\mathbf{q}_0,T)$ where derived, we introduce the $\mathcal{G}_{\pm}(t,t')$ notations and $A_{\pm}(t')$, $B_{\pm}(t')$ matrices. Using all boundary conditions (at times $t=t'$, $t=0$ and $t=T$) gives rise to the following equation:

$$\begin{bmatrix}1&0\\0&\mathcal{Q}_{t_0}\end{bmatrix}[M(T)-1_{2f}]\begin{pmatrix}A_-(t')\\B_-(t')\end{pmatrix}=\begin{bmatrix}1&0\\0&\mathcal{Q}_{t_0}\end{bmatrix}M(T)\begin{pmatrix}-J_1^{\top}(t')\\J_2^{\top}(t')\end{pmatrix}.\tag{54}$$

The preceding set of linear equations, formally written $\mathcal{A}\mathcal{X}=\mathcal{B}$, cannot be solved directly because the $(2f\times 2f)$ matrix $\mathcal{A}$ is obviously singular. More precisely, existence and number of solutions for the system $\mathcal{A}\mathbf{x}=\mathbf{b}$ are determined by the two following properties:

(1) Solutions exists if for all vectors $\mathbf{y}$ such that $\mathcal{A}^{\top}\mathbf{y}=\mathbf{0}$, then $\mathbf{y}\cdot\mathbf{b}=0$.

(2) If the preceding condition is fulfilled, and if $\mathbf{x}$ is a solution, then for all vectors $\mathbf{x}_0$ such that $\mathcal{A}\mathbf{x}_0=\mathbf{0}$, $\mathbf{x}+\mathbf{x}_0$ is also a solution, showing that the dimension of the solution space is that of the nullspace of $\mathcal{A}$.

In the present case, equation $\mathbf{A}^{\top}\mathbf{y}=\mathbf{0}$ leads to either

$$\begin{bmatrix}1&0\\0&\mathcal{Q}_{t_0}\end{bmatrix}\mathbf{y}=\mathbf{0}\Rightarrow\mathbf{y}\propto\begin{pmatrix}\mathbf{0}\\\dot{\mathbf{q}}(t_0)\end{pmatrix}\tag{55}$$

or

$$[M(T)-1_{2f}]\tilde{\mathbf{y}}=\mathbf{0}\quad\text{with}\quad\tilde{\mathbf{y}}=\Sigma\begin{bmatrix}1&0\\0&\mathcal{Q}_{t_0}\end{bmatrix}\mathbf{y}\neq\mathbf{0}.\tag{56}$$

For a generic unstable periodic orbit, the eigenspace associated with the eigenvalue 1 of $M(T)$ (T being the period), is of dimension one and is spanned by the vector parallel to the flow (see the Appendix) $\dot{\mathbf{X}}(t_0)=[\dot{\mathbf{q}}(t_0),\dot{\mathbf{p}}(t_0)]$, so that, in the second case, one gets $\tilde{\mathbf{y}}\propto\dot{\mathbf{X}}(t_0)$ and $\mathbf{y}$ is a solution of

$$\begin{bmatrix} 1 & 0 \\ 0 & \mathcal{Q}_{t_0} \end{bmatrix} \mathbf{y} \propto \begin{pmatrix} -\dot{\mathbf{p}}(t_0) \\ \dot{\mathbf{q}}(t_0) \end{pmatrix}, \tag{57}$$

which is impossible unless $\dot{\mathbf{q}}(t_0)=\mathbf{0}$, which, for Hamiltonian separating into kinetic and potential energies, corresponds to a self-retracing periodic orbit, for which a slightly modified approach should be developed [18]. Nevertheless, this case is peculiar, and we will suppose in the rest of the section that $\dot{\mathbf{q}}$ never vanishes along the periodic orbit in consideration.

Thus, the nullspace of $\mathcal{A}^\top$ being one-dimensional and spanned by the vector $[\mathbf{0},\dot{\mathbf{q}}(t_0)]$, Eq. (54) immediately shows that for any column of matrix $\mathcal{B}$, we get $[\mathbf{0},\dot{\mathbf{q}}(t_0)]\cdot\mathcal{B}_i=0$, fulfilling thus the first condition. Denoting $\mathcal{X}_0$ as a solution of Eq. (54), which can be easily obtained using singular value decomposition (SVD) of matrix $\mathcal{A}$, and the nullspace of $M(T)-\mathbb{1}$ being spanned by $\dot{\mathbf{X}}(t_0)$, the general solution of Eq. (54) reads

$$\mathcal{X}=\mathcal{X}_0+[\alpha_1\dot{\mathbf{X}}(t_0),\alpha_2\dot{\mathbf{X}}(t_0),\ldots,\alpha_f\dot{\mathbf{X}}(t_0)], \tag{58}$$

where α_i are unknown real parameters still to be determined. Actually, in Eq. (54) one boundary condition has not been taken into account, namely, that $\mathcal{P}_{t_0}\mathcal{G}_-(0,t')=0$ which, using that the projector $\mathcal{P}_{t_0}$ reads

$$(\mathcal{P}_{t_0})_{ij}=\left(\frac{\dot{\mathbf{q}}(t_0)\dot{\mathbf{q}}^\top(t_0)}{|\dot{\mathbf{q}}(t_0)|^2}\right)_{ij}=\frac{\dot{\mathbf{q}}_i(t_0)\dot{\mathbf{q}}_j(t_0)}{|\dot{\mathbf{q}}(t_0)|^2}, \tag{59}$$

allows us to get α_i values and, from that, the final expression

$$\begin{pmatrix} A_-(t') \\ B_-(t') \end{pmatrix}=\mathcal{X}_0-\frac{1}{|\dot{\mathbf{q}}(t_0)|^2}\begin{bmatrix} \dot{\mathbf{q}}(t_0)\dot{\mathbf{q}}^\top(t_0) & 0 \\ \dot{\mathbf{p}}(t_0)\dot{\mathbf{q}}^\top(t_0) & 0 \end{bmatrix}\mathcal{X}_0, \tag{60}$$

which, of course, is now independent of the particular solution $\mathcal{X}_0$.

Whereas in the case of the propagator $K(\mathbf{q},\mathbf{q}_0,T)$, for which we were able to give an explicit expression (14), the classical Green's function associated with the trace of the propagator $K(T)$ is only defined trough a linear system (54), which nevertheless allows us to obtain its numerical value for any (t,t'). Although it clearly appears that matrix $W_{,ab}$ expression (see Ref. [13]) is symmetric, meaning that the classical Green's function must fulfill the property $\mathcal{G}^\top(t,t')=\mathcal{G}(t',t)$, getting the later directly from Eq. (54) is not obvious. However, in the case of the 2D hydrogen in a magnetic field (see Sec. VI for all details), we have numerically checked that the property holds. For example, in Fig. 2 the four coefficients of classical Green's function $\mathcal{G}(t,t')$ (for $t'/T=0.3$) of the periodic orbit 1234 are plotted with respect to time t. The starting point t_0 on the periodic orbit is depicted by the cross. Actually, we have plotted the coefficient of the rotated matrix $\tilde{\mathcal{G}}(t,t')$, such that its first row corresponds to the direction parallel to the orbit; $\tilde{\mathcal{G}}_{11}(t,t')$ (continuous line) and $\tilde{\mathcal{G}}_{12}(t,t')$ (dotted line) are thus equal to zero for initial $(t=0)$ and final $(t=T)$ points. The other boundary conditions can also be verified in the figure: the dashed line $[\tilde{\mathcal{G}}_{21}(t,t')]$ [respectively, the long dashed line, $\tilde{\mathcal{G}}_{22}(t,t')$] has not only the same value at initial and final time, but also the same slope, which means that $\tilde{\mathcal{G}}_{21}(t,t')$ [respectively, $\tilde{\mathcal{G}}_{22}(t,t')$] and its time derivative fulfill the periodic boundary conditions (50). Finally, for $t=t'$, the off-diagonal coefficients $\tilde{\mathcal{G}}_{12}(t',t')$ (dotted line) and $\tilde{\mathcal{G}}_{21}(t',t')$ (dashed line) are equal, as expected from the symmetry property.

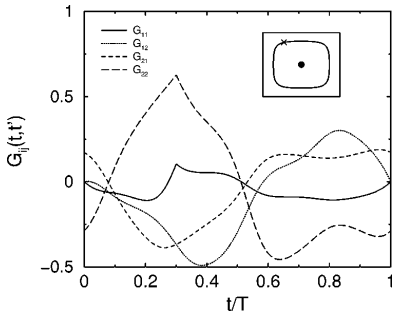

FIG. 2. Example of a classical Green's function $\mathcal{G}(t,t')$ involved in the calculation of the $\hbar$ corrections for the trace of the propagator $K(T)$. It is associated with the periodic orbit $\overline{1234}$ of the 2D hydrogen atom in a magnetic field, whose trajectory in (u,v) coordinates is inserted in the plot (see Sec. VI for all details). The black circle depicts the nucleus, whereas the cross corresponds to the initial and final points on the periodic orbit at which $\mathcal{G}(t,t')$ fulfills the boundary conditions (50). Each curve corresponds to a matrix element $\mathcal{G}_{ij}(t,t')$ plotted with respect to time t, for $t'/T=0.3$. Actually, we have plotted the coefficient of the rotated matrix $\tilde{\mathcal{G}}(t,t')$, such that its first row corresponds to the direction parallel to the orbit; $\tilde{\mathcal{G}}_{11}(t,t')$ (continuous line) and $\tilde{\mathcal{G}}_{12}(t,t')$ (dotted line) are thus equal to zero for initial $(t=0)$ and final $(t=T)$ points. The other boundary conditions can also be verified in the figure; the dashed line $[\tilde{\mathcal{G}}_{21}(t,t')]$ [respectively, the long dashed line, $\tilde{\mathcal{G}}_{22}(t,t')$] has not only the same value at initial and final time, but also the same slope, which means that $\tilde{\mathcal{G}}_{21}(t,t')$ [respectively, $\tilde{\mathcal{G}}_{22}(t,t')$] and its time derivative fulfills the periodic boundary conditions (50). Finally, for $t=t'$, the off-diagonal coefficients $\tilde{\mathcal{G}}_{12}(t',t')$ (dotted line) and $\tilde{\mathcal{G}}_{21}(t',t')$ (dashed line) are equal, as expected from the symmetry property $\mathcal{G}^\top(t,t')=\mathcal{G}(t',t)$.

C. Getting $C_1(T,t_0)$ by integrating a set of first order differential equations

As seen previously (see Sec. II C), we will explain how the numerical value of coefficients $C_1(T,t_0)$ can be obtained

by integrating a set of differential equation, using the standard Runge-Kutta method. There are now four contributions to $C_1(T,t_0)$, namely

$$I_1(T)=\int_0^T dt\, V^{(4)}_{ijkl}(t)\mathcal{G}_{ij}(t,t)\mathcal{G}_{kl}(t,t),$$

$$I_l(T)=\int_0^T dt\, V^{(3)}_{ijk}(t)\mathcal{G}_{lk}(0,t)\mathcal{G}_{ij}(t,t),$$

(61)

$$I_2^+(T)=\int_0^T\int_0^T dt\,dt'\, V^{(3)}_{ijk}(t)V^{(3)}_{lmn}(t') \times\mathcal{G}_{ij}(t,t)\mathcal{G}_{kl}(t,t')\mathcal{G}_{mn}(t',t'),$$

$$I_2^-(T)=\int_0^T\int_0^T dt\,dt'\, V^{(3)}_{ijk}(t)V^{(3)}_{lmn}(t') \times\mathcal{G}_{il}(t,t')\mathcal{G}_{jm}(t,t')\mathcal{G}_{kn}(t,t').$$

The two main difficulties now are that $\mathcal{G}(t,t')$ does not factorize anymore in a product of matrix at time t and a matrix at time t', nor does the symmetric property $\mathcal{G}^\top(t,t')=\mathcal{G}(t',t)$ explicitly appear (even if we have numerically checked that it is fulfilled). Nevertheless, as seen previously, separating $(t>t')$ and $(t<t')$ contributions in $I_2^\pm(T)$ expressions and introducing four quantities $P_p^{(i)}$ for $1\leqslant i\leqslant 4$, allows us to compute I_2^+, by integrating the following set of differential equations from $t=0$ to T [besides equations for $\mathbf{X}(t)$ and $M(t)$]:

$$\dot P_p^{(1)}=A^+_{pl}(t)V^{(3)}_{lmn}(t)\mathcal{G}_{mn}(t,t),\quad \dot P_p^{(3)}=J_{1lp}(t)V^{(3)}_{lmn}(t)\mathcal{G}_{mn}(t,t),$$

$$\dot P_p^{(2)}=B^+_{pl}(t)V^{(3)}_{lmn}(t)\mathcal{G}_{mn}(t,t),\quad \dot P_p^{(4)}=J_{2lp}(t)V^{(3)}_{lmn}(t)\mathcal{G}_{mn}(t,t),$$

$$\begin{aligned}\dot I_2^+ &= V^{(3)}_{ijk}(t)\mathcal{G}_{ij}(t,t)J_{2kp}(t)P_p^{(1)}(t)+V^{(3)}_{ijk}(t)\mathcal{G}_{ij}(t,t)J_{1kp}(t)P_p^{(2)}(t)\\ &\quad+V^{(3)}_{ijk}(t)\mathcal{G}_{ij}(t,t)A^-_{pk}(t)P_p^{(3)}(t)+V^{(3)}_{ijk}(t)\mathcal{G}_{ij}(t,t)B^-_{pk}(t)P_p^{(4)}(t)\end{aligned}\tag{62}$$

with vanishing initial conditions for $P_p^{(i)}$ and I_2^+. For each time step, one must compute matrices A_- and B_- (and from there matrices A_+ and B_+), solving the linear system described in the previous section, using singular value decomposition of matrix $\mathcal{A}$, which, being independent of t, is done before starting the Runge-Kutta integration. Skipping intermediate steps, the differential equations leading to $I_2^-(T)$ computation reads as follow, introducing another eight quantities $Q^{(i)}_{pqr}$:

$$\dot Q^{(1)}_{pqr}=V^{(3)}_{lmn}(t)A^+_{pl}(t)A^+_{qm}(t)A^+_{rn}(t),\quad \dot Q^{(5)}_{pqr}=V^{(3)}_{lmn}(t)J_{2lp}(t)J_{2mq}(t)J_{2nr}(t),$$

$$\dot Q^{(2)}_{pqr}=V^{(3)}_{lmn}(t)A^+_{pl}(t)A^+_{qm}(t)B^+_{rn}(t),\quad \dot Q^{(6)}_{pqr}=V^{(3)}_{lmn}(t)J_{2lp}(t)J_{2mq}(t)J_{1nr}(t),$$

$$\dot Q^{(3)}_{pqr}=V^{(3)}_{lmn}(t)A^+_{pl}(t)B^+_{qm}(t)B^+_{rn}(t),\quad \dot Q^{(7)}_{pqr}=V^{(3)}_{lmn}(t)J_{2lp}(t)J_{1mq}(t)J_{1nr}(t),$$

$$\dot Q^{(4)}_{pqr}=V^{(3)}_{lmn}(t)B^+_{pl}(t)B^+_{qm}(t)B^+_{rn}(t),\quad \dot Q^{(8)}_{pqr}=V^{(3)}_{lmn}(t)J_{1lp}(t)J_{1mq}(t)J_{1nr}(t),$$

$$\begin{aligned}\dot I_2^- &= V^{(3)}_{ijk}(t)J_{2ip}(t)J_{2jq}(t)J_{2kr}(t)Q^{(1)}_{pqr}(t)+3V^{(3)}_{ijk}(t)J_{2ip}(t)J_{2jq}(t)J_{1kr}(t)Q^{(2)}_{pqr}(t)\\ &\quad+3V^{(3)}_{ijk}(t)J_{2ip}(t)J_{1jq}(t)J_{1kr}(t)Q^{(3)}_{pqr}(t)+V^{(3)}_{ijk}(t)J_{1ip}(t)J_{1jq}(t)J_{1kr}(t)Q^{(4)}_{pqr}(t)\\ &\quad+V^{(3)}_{ijk}(t)A^-_{pi}(t)A^-_{qj}(t)A^-_{rk}(t)Q^{(5)}_{pqr}(t)+3V^{(3)}_{ijk}(t)A^-_{pi}(t)A^-_{qj}(t)B^-_{rk}(t)Q^{(6)}_{pqr}(t)\\ &\quad+3V^{(3)}_{ijk}(t)A^-_{pi}(t)B^-_{qj}(t)B^-_{rk}(t)Q^{(7)}_{pqr}(t)+V^{(3)}_{ijk}(t)B^-_{pi}(t)B^-_{qj}(t)B^-_{rk}(t)Q^{(8)}_{pqr}(t)\end{aligned}\tag{63}$$

with vanishing initial conditions for $Q^{(i)}_{pqr}$ and I_2^-. Finally, one must add equations leading to I_l and I_1 computation, namely

$$\dot I_1=V^{(4)}_{ijkl}(t)\mathcal{G}_{ij}(t,t)\mathcal{G}_{kl}(t,t),$$

$$\dot I_l=V^{(3)}_{ijk}(t)A^-_{lk}(t)\mathcal{G}_{ij}(t,t),\tag{64}$$

where we have used $\mathcal{G}_{lk}(0,t)=A^-_{lk}(t)$. Taking into account equations for $\mathbf{X}(t)$ and $M(t)$, this gives rise to a total of $8f^3+4f^2+7f+3$ equations, that is 97 for a 2D system.

In practice, having found a periodic orbit and for a given t_0 along this orbit, the coefficient $C_1(T,t_0)$ is computed in two steps:

(1) achieve the SVD decomposition of the matrix $\mathcal{A}$, appearing on the left-hand side of Eq. (54), and compute the projector matrix appearing on the right-hand side of Eq. (60);

(2) integrate the differential set (63) along the periodic orbit (starting at point depicted by t_0). At any time t, use the preceding SVD decomposition to obtain a solution $\mathcal{X}_0$ and the projector matrix to get the true solution $[A_-(t),B_-(t)]$ and thus $[A_+(t),B_+(t)]$, using Eq. (60).

Finally, the coefficient $C_1(T,t_0)$, being a smooth function of t_0, the average over time t_0, leading to the $\hbar$ correction term $C_1(T)$, can be handled by any conventional integrator.

V. TRACE OF THE GREEN'S FUNCTION $G(E)$

Steps leading to the semiclassical contribution $G_l(E)$ from a given periodic orbit to the trace of the Green's function $G(E)$ are identical to those giving the $G_l(\mathbf{q},\mathbf{q}_0,E)$ expression, so that $G_l(E)$ reads

$$G_l(E)=\frac{1}{i\hbar}\frac{T_0}{|\det[m(T_0)-1]|^{1/2}}\exp\left[\frac{i}{\hbar}S_l(E)-i\frac{\pi}{2}\mu_l\right]\times\{1+i\hbar[C_1(T_0)+C_1^{T\to E}(T_0)]+O(\hbar^2)\},\quad(65)$$

where $C_1^{T\to E}(T)$ is given by

$$C_1^{T\to E}(T_0)=\frac{1}{2W_l^{(2)}}[(C_0^{(1)})^2+C_0^{(2)}]-\frac{W_l^{(3)}C_0^{(1)}}{2(W_l^{(2)})^2}-\frac{W_l^{(4)}}{8(W_l^{(2)})^2}+\frac{5}{24}\frac{(W_l^{(3)})^2}{(W_l^{(2)})^3}.\quad(66)$$

$W_l^{(i)}$ (respectively, $C_0^{(i)}$) are the Taylor coefficients of the $W_l(T)$ [respectively, $C_0(T)$] expansion around T_0.

Computation of $W_l^{(i)}$ is much the same as in the Green's function case, because the functional relation

$$\frac{\partial W_l(T)}{\partial T}=-E(T)\quad(67)$$

still holds for a given periodic orbit, $E(T)$ being its energy as function of its period, which is still given by the value of the Hamiltonian H taken at any point on the corresponding phase space trajectory $\mathbf{X}(t,T)=[\mathbf{q}(t,T),\mathbf{p}(t,T)]$. Thus, the Taylor expansion of $\mathbf{X}(t,T)$ around the periodic orbit $\mathbf{X}(t,T_0)$, will lead to the same expressions for $W_l^{(i)}$ coefficients [Eq. (29)] and for $\mathbf{X}^{(n)}(t)$ equations [Eq. (30)]. The only differences with the preceding section arise from the boundary conditions fulfilled by $\mathbf{X}^{(n)}(t)$, deduced from the equation $\mathbf{X}(0,T)=\mathbf{X}(T,T)$, i.e., $\mathbf{X}(t,T)$ is a periodic orbit of period T. The Taylor expansion of this relation leads to the following conditions:

$$\begin{aligned}\mathbf{X}^{(1)}(0)&=\mathbf{X}^{(1)}(T_0)+\dot{\mathbf{X}}^{(0)}(T_0),\\ \mathbf{X}^{(2)}(0)&=\mathbf{X}^{(2)}(T_0)+\ddot{\mathbf{X}}^{(0)}(T_0)+2\dot{\mathbf{X}}^{(1)}(T_0),\\ \mathbf{X}^{(3)}(0)&=\mathbf{X}^{(3)}(T_0)+\dddot{\mathbf{X}}^{(0)}(T_0)+3\ddot{\mathbf{X}}^{(1)}(T_0)+3\dot{\mathbf{X}}^{(2)}(T_0).\end{aligned}\quad(68)$$

Solutions of the differential set (30) still have the following formal expressions (31), which, inserted in the boundary conditions (68), leads to equations on $\mathbf{X}^{(i)}(0)$ only:

$$\begin{aligned}[1-M(T_0)]\mathbf{X}^{(1)}(0)&=\dot{\mathbf{X}}^{(0)}(T_0),\\ [1-M(T_0)]\mathbf{X}^{(2)}(0)&=\ddot{\mathbf{X}}^{(0)}(T_0)+2\dot{\mathbf{X}}^{(1)}(T_0)+\mathbf{F}^{(2)}(T_0),\\ [1-M(T_0)]\mathbf{X}^{(3)}(0)&=\dddot{\mathbf{X}}^{(0)}(T_0)+3\ddot{\mathbf{X}}^{(1)}(T_0)+3\ddot{\mathbf{X}}^{(2)}(T_0)+\mathbf{F}^{(3)}(T_0).\end{aligned}\quad(69)$$

The matrix $1-M(T_0)$ being singular, solving the preceding linear equations need additional discussion, which, for simplicity, will focus on $\mathbf{X}^{(1)}(0)$ only. First, the nullspace of $1-M(T_0)^\top$ is spanned by $\Sigma\dot{\mathbf{X}}^{(0)}(T_0)$, which is obviously orthogonal to $\dot{\mathbf{X}}^{(0)}(T_0)$, the right-hand side of the equation for $\mathbf{X}^{(1)}(0)$, thus showing that this equation admits solutions. Then, the nullspace of $1-M(T_0)$ being spanned by $\dot{\mathbf{X}}^{(0)}(T_0)$, the whole set of solutions reads

$$\mathbf{X}^{(1)}(0)=\mathbf{X}_0^{(1)}(0)+\alpha\dot{\mathbf{X}}^{(0)}(T_0),\quad(70)$$

where $\mathbf{X}_0^{(1)}(0)$ is a particular solution of the equation. Actually, the term $\alpha\dot{\mathbf{X}}^{(0)}(T_0)$ corresponds to a displacement of the initial conditions along the flow, which, of course, gives back the same periodic orbit (at first order in $T-T_0$). We thus expect that this term has a vanishing contribution to $W_l^{(2)}$, which is easily verified when inserting the general solution in the $W_l^{(2)}$ expression (taken at time $t=T_0$):

$$\begin{aligned}W_l^{(2)}&=-[\mathbf{X}_0^{(1)}(0)-\dot{\mathbf{X}}^{(0)}(T_0)+\alpha\dot{\mathbf{X}}^{(0)}(T_0)]\cdot\boldsymbol{\nabla}H[\mathbf{X}^{(0)}(T_0)]\\ &=-\mathbf{X}_0^{(1)}(0)\cdot\boldsymbol{\nabla}H[\mathbf{X}^{(0)}(T_0)]\end{aligned}\quad(71)$$

because of the Hamilton's equations $\dot{\mathbf{X}}^{(0)}(T_0)=\Sigma\boldsymbol{\nabla}H[\mathbf{X}^{(0)}(T_0)]$.

These two properties also hold in the cases of $\mathbf{X}^{(2)}(0)$ and $\mathbf{X}^{(3)}(0)$, but are slightly more complicated to establish because the right-hand sides of the equations involve $\mathbf{F}^{(i)}(T_0)$ and derivatives of $\mathbf{X}^{(i)}(T_0)$.

Thus, integrating the same differential sets that were used for $G(\mathbf{q},\mathbf{q}_0,E)$, one is able to compute the first four derivatives of the action, $W_l^{(i)}$, with respect to the period.

Starting from the $C_0^{(0)}(T)$ expression

$$C_0^{(0)}(T)=\ln T-\tfrac{1}{2}\ln|\partial_E T|-\tfrac{1}{2}\ln|\det[m(T)-1]|\quad(72)$$

and using the fact that $\partial_E T=1/\partial_T E=-1/\partial_T^2 W_l$, one obtains

$$C_0^{(1)}(T_0)=\frac{1}{T_0}+\frac{1}{2}\frac{W_l^{(3)}}{W_l^{(2)}}-\frac{1}{2}\frac{d}{dT}\ln|\det[m(T)-1]|,$$
$$C_0^{(2)}(T_0)=-\frac{1}{T_0^2}+\frac{1}{2}\frac{W_l^{(4)}}{W_l^{(2)}}-\frac{1}{2}\left(\frac{W_l^{(3)}}{W_l^{(2)}}\right)^2-\frac{1}{2}\frac{d^2}{dT^2}\ln|\det[m(T)-1]|, \tag{73}$$

which means that one is left with the calculation of derivatives of $\ln|\det[m(T)-1]|$ with respect to the period T. As shown in the Appendix, $\det[m(T)-1]$ is given by the determinant of the $2f\times 2f$ matrix $N(T)$ defined as follows:

$$N(T)=M(T)-[1-\mathcal{P}_\parallel(T)-\mathcal{P}_\perp(T)], \tag{74}$$

where we have introduced $\mathcal{P}_\parallel(T)$ [respectively, $\mathcal{P}_\perp(T)$] the projector on the direction parallel to the flow (respectively, perpendicular to the energy shell), more precisely, the $\mathcal{P}_\parallel(T)$ and $\mathcal{P}_\perp(T)$ expressions are

$$\mathcal{P}_\parallel=\mathbf{e}_\parallel\cdot\mathbf{e}_\parallel^\top \quad \text{and} \quad \mathcal{P}_\perp=\mathbf{e}_\perp\cdot\mathbf{e}_\perp^\top=-\Sigma\mathcal{P}_\parallel\Sigma, \tag{75}$$

where $\mathbf{e}_\parallel$ is the unit vector tangent to the flow at initial (and thus final) time and $\mathbf{e}_\perp=\Sigma\mathbf{e}_\parallel$. Now, using again formula (36), derivatives of $\det[m(T)-1]$ with respect to the period read

$$\frac{d}{dT}\{\det[m(T)-1]\}=\mathrm{Tr}\left(N(T_0)^{-1}\frac{dN(T_0)}{dT}\right),$$
$$\frac{d^2}{dT^2}\{\det[m(T)-1]\}=\mathrm{Tr}\left(N^{-1}(T_0)\frac{d^2N(T_0)}{dT^2}-N(T_0)^{-1}\frac{dN(T_0)}{dT}N(T_0)^{-1}\frac{dN(T_0)}{dT}\right) \tag{76}$$

with

$$\frac{dN(T_0)}{dT}=\frac{dM(T_0)}{dT}+\frac{d\mathcal{P}_\parallel(T_0)}{dT}-\Sigma\frac{d\mathcal{P}_\parallel(T_0)}{dT}\Sigma,$$
$$\frac{d^2N(T_0)}{dT^2}=\frac{d^2M(T_0)}{dT^2}+\frac{d^2\mathcal{P}_\parallel(T_0)}{dT^2}-\Sigma\frac{d^2\mathcal{P}_\parallel(T_0)}{dT^2}\Sigma. \tag{77}$$

As seen previously (Sec. III B), $dM(T_0)/dT$ and $d^2M(T_0)/dT^2$ are expressed in terms of the coefficients $M^{(i)}(t)$ of the Taylor expansion of the monodromy matrix $M(t,T)$ [associated with the periodic orbit $\mathbf{X}(t,T)$ of period T] around the periodic orbit $\mathbf{X}^{(0)}(t)$ of period T_0, see Eq. (39).

Inserting the Taylor expansion of $\dot{\mathbf{X}}(T)$ around T_0 in the $\mathcal{P}_\parallel(T)$ expression, namely,

$$\mathcal{P}_\parallel(T)=\frac{1}{\|\dot{\mathbf{X}}(T)\|^2}\dot{\mathbf{X}}(T)\cdot\dot{\mathbf{X}}(T)^\top, \tag{78}$$

one obtains the derivatives of $\mathcal{P}_\parallel(T)$ with respect to T:

$$\frac{d\mathcal{P}_\parallel(T_0)}{dT}=\frac{1}{\|\dot{\mathbf{X}}^{(0)}\|^2}(\dot{\mathbf{X}}^{(1)}\cdot\dot{\mathbf{X}}^{(0)\top}+\dot{\mathbf{X}}^{(0)}\cdot\dot{\mathbf{X}}^{(1)\top})-2\frac{\dot{\mathbf{X}}^{(0)\top}\cdot\dot{\mathbf{X}}^{(1)}}{\|\dot{\mathbf{X}}^{(0)}\|^2}\mathcal{P}_\parallel(T_0),$$
$$\frac{d^2\mathcal{P}_\parallel(T_0)}{dT^2}=\frac{1}{\|\dot{\mathbf{X}}^{(0)}\|^2}(\dot{\mathbf{X}}^{(2)}\cdot\dot{\mathbf{X}}^{(0)\top}+\dot{\mathbf{X}}^{(0)}\cdot\dot{\mathbf{X}}^{(2)\top}+2\dot{\mathbf{X}}^{(1)}\cdot\dot{\mathbf{X}}^{(1)\top})+\left(8\frac{(\dot{\mathbf{X}}^{(0)\top}\cdot\dot{\mathbf{X}}^{(1)})^2}{\|\dot{\mathbf{X}}^{(0)}\|^4}-2\frac{\dot{\mathbf{X}}^{(0)\top}\cdot\dot{\mathbf{X}}^{(2)}}{\|\dot{\mathbf{X}}^{(0)}\|^2}-2\frac{\dot{\mathbf{X}}^{(1)\top}\cdot\dot{\mathbf{X}}^{(1)}}{\|\dot{\mathbf{X}}^{(0)}\|^2}\right)\mathcal{P}_\parallel(T_0)$$
$$-4\frac{\dot{\mathbf{X}}^{(0)\top}\cdot\dot{\mathbf{X}}^{(1)}}{\|\dot{\mathbf{X}}^{(0)}\|^4}(\dot{\mathbf{X}}^{(1)}\cdot\dot{\mathbf{X}}^{(0)\top}+\dot{\mathbf{X}}^{(0)}\cdot\dot{\mathbf{X}}^{(1)\top}), \tag{79}$$

where all $\dot{\mathbf{X}}^{(i)}$ are evaluated at time $t=0$.

Gathering the preceding expressions into Eq. (76) allows us to compute $\ln\det[m(T)-1]$ derivatives, which, inserted together with derivatives of the action, in Eq. (73) gives the numerical values for $C_0^{(1)}(T_0)$ and $C_0^{(2)}(T_0)$, which finally leads to the additional $\hbar$ correction $C_1^{T\to E}(T_0)$.

VI. APPLICATION TO THE 2D HYDROGEN ATOM IN A MAGNETIC FIELD

The hydrogen atom is one example of a quantum system whose classical counterpart depicts a chaotic behavior and has been widely studied (see, e.g., Ref. [4] for a complete review). It has now become a very useful tool for testing new ideas and tools in the quantum chaos area, both on the semiclassical [20,23] or universality [24] points of view, especially because computing very highly excited states has become a standard task on a regular workstation, allowing the semiclassical regime to be reached easily. Even if one would have preferred to work with the real hydrogen atom (i.e., the three-dimensional one), in this paper we will focus on the two dimensional hydrogen atom in a magnetic field, because taking into account invariance by rotation around the magnetic field, gives rise to centrifugal terms in the Hamiltonian (typically $\mathbf{L}^2\hbar^2/2r^2$) which would also contribute to $\hbar$ corrections and would need a study on its own. One must also notice that, even if the classical dynamics are identical for both cases, the fact that the magnetic field axis is no longer a rotation axis in the 2D case gives rise to slight modifications in the Maslov indices [18,23,25].

A. Quantum and Classical Properties

In atomic units the Hamiltonian of the 2D hydrogen in a magnetic field reads

$$H=\frac{1}{2}\mathbf{p}^2-\frac{1}{\sqrt{x^2+y^2}}+\frac{1}{8}\gamma^2y^2, \tag{80}$$

where $\gamma=B/B_0$, with $B_0=2.35\times10^5T$. The classical counterpart of this Hamiltonian has a scaling property, that is, if we define new variables by

$$\begin{aligned}\tilde{\mathbf{r}}&=\gamma^{2/3}\mathbf{r},\\ \tilde{\mathbf{p}}&=\gamma^{-1/3}\mathbf{p},\\ \tilde{t}&=\gamma t,\end{aligned} \tag{81}$$

we obtain a new Hamiltonian $\tilde{H}$ given by

$$\tilde{H}=\gamma^{-2/3}H=\frac{\tilde{\mathbf{p}}^2}{2}-\frac{1}{\sqrt{\tilde{x}^2+\tilde{y}^2}}+\frac{\tilde{y}^2}{8}, \tag{82}$$

which does not depend on γ anymore. The classical dynamics of this Hamiltonian is entirely fixed by the scaled energy ϵ given by

$$\epsilon=\gamma^{-2/3}E. \tag{83}$$

All properties of the classical trajectories of the original Hamiltonian can be deduced from the scaled dynamics using the scaling transformation (81). From the quantum point of view, this scaling introduces an effective $\hbar$ value, which is easily seen on the scaled Schrödinger equation, $\tilde{H}\psi=\epsilon\psi$, for a fixed scaled energy ϵ:

$$\left[-\frac{\gamma^{2/3}}{2}\Delta_{\tilde{\mathbf{r}}}-\frac{1}{\sqrt{\tilde{x}^2+\tilde{y}^2}}+\frac{\tilde{y}^2}{8}\right]\psi=\epsilon\psi. \tag{84}$$

Thus, the effective $\hbar$ is given by $\gamma^{1/3}$ and so at a fixed value of the scaled energy ϵ, the semiclassical limit is obtained when γ tends to 0.

The singularity in the classical equations of motion due to the divergence of the Coulomb potential at $\mathbf{r}=\mathbf{0}$ is regularized using the semiparabolic coordinates ($u=\sqrt{\tilde{r}+\tilde{x}}, v=\sqrt{\tilde{r}-\tilde{x}}$), giving rise to the following effective classical Hamiltonian [4,26]:

$$\mathcal{H}=\tfrac{1}{2}p_u^2+\tfrac{1}{2}p_v^2-\epsilon(u^2+v^2)+\tfrac{1}{8}u^2v^2(u^2+v^2), \tag{85}$$

the trajectories corresponding to the original problem are obtained when fixing total energy $\mathcal{H}=2$. The associated quantum Hamiltonian reads

$$\hat{\mathcal{H}}(\hbar)=-\frac{\hbar^2}{2}\left(\frac{\partial^2}{\partial u^2}+\frac{\partial^2}{\partial v^2}\right)-\epsilon(u^2+v^2)+\frac{1}{8}u^2v^2(u^2+v^2), \tag{86}$$

which separates into kinetic and potential energy, so that the semiclassical formula derived in the preceding sections applied to the associated quantum Green's function $G(z,\hbar)$, the hydrogen in a magnetic field being recovered for $z=2$ (actually $z/2$ corresponds to the nucleus charge)

$$G(z,\hbar)=\frac{1}{z-\hat{\mathcal{H}}(\hbar)}=\sum_\tau\frac{|\tau,\hbar\rangle\langle\tau,\hbar|}{z-\lambda_\tau(\hbar)}, \tag{87}$$

where $|\tau,\hbar\rangle$ is an (normalized) eigenvector of $\hat{\mathcal{H}}(\hbar)$ for the eigenenergy $\lambda_\tau(\hbar)$, τ representing the set of quantum labels, i.e., level number and symmetry properties (see below), describing $|\tau,\hbar\rangle$. The matrix element $\langle\mathbf{q}|G(z,\hbar)|\mathbf{q}_0\rangle$, where $\mathbf{q}=(u,v)$ then reads

$$\langle\mathbf{q}|G(z,\hbar)|\mathbf{q}_0\rangle=\sum_\tau\psi_{\tau,\hbar}(\mathbf{q})\psi_{\tau,\hbar}(\mathbf{q}_0)\frac{1}{z-\lambda_\tau(\hbar)}, \tag{88}$$

where $\psi_{\tau,\hbar}(\mathbf{q})=\langle\mathbf{q}|\tau,\hbar\rangle$ has been supposed to be real, with $\hat{\mathcal{H}}(\hbar)$ being invariant under $\mathbf{p}\to-\mathbf{p}$. Taking $z=\lambda$ on the real axis, the imaginary part of $\langle\mathbf{q}|G(z,\hbar)|\mathbf{q}_0\rangle$, becomes

$$-\frac{1}{\pi}\mathrm{Im}\langle\mathbf{q}|G(\lambda,\hbar)|\mathbf{q}_0\rangle=\sum_\tau\psi_{\tau,\hbar}(\mathbf{q})\psi_{\tau,\hbar}(\mathbf{q}_0)\delta[\lambda-\lambda_\tau(\hbar)] \tag{89}$$

to which any classical path going from $\mathbf{q}$ to $\mathbf{q}_0$ at energy λ, gives the following contribution [see Eq. (25)]:

$$-\frac{1}{\pi}\mathrm{Im}\langle\mathbf{q}|G(\lambda,\hbar)|\mathbf{q}_0\rangle_l=\frac{2}{(2\pi\hbar)^{3/2}}\mathcal{A}_l\left\{\cos\left(\frac{1}{\hbar}S_l+\phi_l\right)-\hbar\mathcal{C}_l\sin\left(\frac{1}{\hbar}S_l+\phi_l\right)\right\} \tag{90}$$

provided it is far enough from any bifurcation and that $\mathbf{q}$ and $\mathbf{q}_0$ are not conjugate points for this trajectory. Amplitudes and phases being defined by

$$\begin{aligned}&\mathcal{A}_l=\frac{1}{|W_l^{(2)}\det J_1(T_0)|^{1/2}},\\&S_l=S(\mathbf{q},\mathbf{q}_0,\lambda),\\&\phi_l=-\frac{\pi}{2}\left(\tilde{\nu}_l+\frac{1}{2}\right),\\&\mathcal{C}_l=C_1(\mathbf{q},\mathbf{q}_0,T_0)+C_1^{T\to E}(\mathbf{q},\mathbf{q}_0,T_0).\end{aligned} \tag{91}$$

Neglecting $\hbar$ corrections in Eq. (90), the Fourier transform with respect to the variable $\zeta=1/\hbar$ of the following function:

$$\begin{aligned}g_0(\zeta)&=\frac{(2\pi)^{3/2}}{2\zeta^{3/2}}\times-\frac{1}{\pi}\mathrm{Im}\langle\mathbf{q}|G(\lambda,\zeta)|\mathbf{q}_0\rangle\\&=\frac{(2\pi)^{3/2}}{2}\sum_\tau\ \psi_{\tau,\zeta}(\mathbf{q})\psi_{\tau,\zeta}(\mathbf{q}_0)\zeta^{-3/2}\delta[\lambda-\lambda_\tau(\zeta)]\end{aligned} \tag{92}$$

will depict peaks at the classical actions $S_l/2\pi$, with complex amplitude $\mathcal{A}_l\exp i\phi_l/2$, which has been extensively used to compare the exact quantum Green's function with its semiclassical estimation at the leading order in $\hbar$. In the same way, the Fourier transform of the following function:

$$g_1(\zeta)=-\frac{(2\pi)^{3/2}}{2}\sum_\tau\ \psi_{\tau,\zeta}(\mathbf{q})\psi_{\tau,\zeta}(\mathbf{q}_0)\zeta^{-1/2}\times\delta[\lambda-\lambda_\tau(\zeta)]-\zeta\sum_l\ \mathcal{A}_l\cos(\zeta S_l+\phi_l) \tag{93}$$

will also depict peaks at the classical actions $S_l/2\pi$, whose complex amplitude, given by

$$\frac{1}{2i}\mathcal{A}_l\mathcal{C}_l\exp i\phi_l \tag{94}$$

allows us to extract the numerical value of the $\hbar$ correction C_l.

The energy λ being fixed, the $\delta[\lambda-\lambda_\tau(\zeta)]$ function selects the values $\zeta_\tau(\lambda)$ of ζ for which λ is an eigenvalue, transforming Eqs. (92) and (93) into

$$\begin{aligned}g_0(\zeta)&=\frac{(2\pi)^{3/2}}{4}\sum_\tau\frac{\psi_{\tau,\zeta}(\mathbf{q})\psi_{\tau,\zeta}(\mathbf{q}_0)}{\langle\tau,\zeta|\mathbf{p}^2/2|\tau,\zeta\rangle}\zeta^{3/2}\delta[\zeta-\zeta_\tau(\lambda)],\\g_1(\zeta)&=-\frac{(2\pi)^{3/2}}{4}\sum_\tau\frac{\psi_{\tau,\zeta}(\mathbf{q})\psi_{\tau,\zeta}(\mathbf{q}_0)}{\langle\tau,\zeta|\mathbf{p}^2/2|\tau,\zeta\rangle}\\&\quad\times\zeta^{5/2}\delta[\zeta-\zeta_\tau(\lambda)]-\zeta\sum_l\ \mathcal{A}_l\cos(\zeta S_l+\phi_l).\end{aligned} \tag{95}$$

Moving to the case of the trace of the Green's function, the preceding relations (89) and (90) become

$$-\frac{1}{\pi}\mathrm{Im\,Tr}\,G(\lambda,\hbar)=\sum_\tau\ \delta[\lambda-\lambda_\tau(\hbar)] \tag{96}$$

and, see Eq. (65):

$$-\frac{1}{\pi}\mathrm{Im\,Tr}\,G(\lambda,\hbar)_l=-\frac{1}{\pi\hbar}\mathcal{A}_l^{\mathrm{tr}}\left\{\cos\left(\frac{1}{\hbar}S_l^{\mathrm{tr}}+\phi_l^{\mathrm{tr}}\right)-\hbar\mathcal{C}_l^{\mathrm{tr}}\sin\left(\frac{1}{\hbar}S_l^{\mathrm{tr}}+\phi_l^{\mathrm{tr}}\right)\right\}, \tag{97}$$

where S_l^{tr} is the action of the periodic orbit and

$$\begin{aligned}&\mathcal{A}_l^{\mathrm{tr}}=\frac{T_0}{|\det[m(T_0)-\mathbb{1}]|^{1/2}},\\&\phi_l^{\mathrm{tr}}=-\frac{\pi}{2}\mu_l,\\&\mathcal{C}_l^{\mathrm{tr}}=C_1(T_0)+C_1^{T\to E}(T_0),\end{aligned} \tag{98}$$

so that the classical quantities S_l^{tr}, $\mathcal{A}_l^{\mathrm{tr}}$, and the $\hbar$ correction $\mathcal{C}_l^{\mathrm{tr}}$ can be obtained by taking the Fourier transform of the following expressions with respect to the variable ζ:

$$\begin{aligned}g_0^{\mathrm{tr}}(\zeta)&=\frac{\pi}{2}\sum_\tau\frac{1}{\langle\tau,\zeta|\mathbf{p}^2/2|\tau,\zeta\rangle}\zeta^2\delta[\zeta-\zeta_\tau(\lambda)],\\g_1^{\mathrm{tr}}(\zeta)&=-\frac{\pi}{2}\sum_\tau\frac{1}{\langle\tau,\zeta|\mathbf{p}^2/2|\tau,\zeta\rangle}\zeta^3\delta[\zeta-\zeta_\tau(\lambda)]\\&\quad-\zeta\sum_l\ \mathcal{A}_l^{\mathrm{tr}}\cos(\zeta S_l^{\mathrm{tr}}+\phi_l^{\mathrm{tr}}).\end{aligned} \tag{99}$$

B. Computing quantum quantities

Focusing on the $\lambda=2$ value, the 2D hydrogen in a magnetic field case, one has to find effective $\hbar$ values for which 2 is an eigenvalue of the Schrödinger equation $\hat{\mathcal{H}}(\hbar)\psi(u,v)=2\psi(u,v)$, which is conveniently written as follows:

$$\left[2+\epsilon(u^2+v^2)-\frac{1}{8}u^2v^2(u^2+v^2)\right]\psi(u,v)$$
$$=\hbar^2\left[-\frac{1}{2}\left(\frac{\partial^2}{\partial u^2}+\frac{\partial^2}{\partial v^2}\right)\right]\psi(u,v) \quad (100)$$

such that $\sigma=\hbar^2$ appears to be a solution of a generalized eigenvalue problem $(A-\sigma B)\psi=0$, with

$$A=2+\epsilon(u^2+v^2)-\frac{1}{8}u^2v^2(u^2+v^2),$$
$$B=-\frac{1}{2}\left(\frac{\partial^2}{\partial u^2}+\frac{\partial^2}{\partial v^2}\right). \quad (101)$$

The preceding operators A, B, and thus $\hat{\mathcal{H}}(\hbar)$ are invariant under all transformations belonging to the symmetry group C_{4v}, leading to four nondegenerate series of energy levels, labeled EEE, EEO, OOE, and OOO according to Ref. [27] and a twofold degenerate series EO and OE, where E means even and O means odd, the first two letters referring to the $u\rightarrow -u$ and $v\rightarrow -v$ symmetries, the third letter to $u\leftrightarrow v$. Actually, because of the definition of the semiparabolic coordinates (u,v), only eigenvectors invariant under the parity symmetry $\psi(-u,-v)=\psi(u,v)$ correspond to eigenvectors of the 2D hydrogen in magnetic field, allowing us, in principle, to drop the OE and EO series [4,26]. However, from the semiclassical point of view, one would have to extend all preceding sections to symmetry-projected propagator and Green's function [28], and thus to take into account symmetry properties of the classical Green's function, which is beyond the scope of this paper. For this reason, we also include the OE and EO series in the remainder of this paper.

Finally, eigenvalues and eigenvectors are obtained by solving the matrix representation of the generalized eigenvalue problem $(A-\sigma B)\psi=0$ in sturmian bases (one for each symmetry class) [4], using the Lanczos algorithm. Typically, we have computed effective $\hbar$ values ranging from 0 to 124, which for scaled energy $\epsilon=-0.1$ corresponds to roughly 61 000 eigenvalues in total. One must notice that the generalized eigenvectors $|\widetilde{\tau,\hbar}\rangle$, for a fixed $\hbar$ value, are actually orthogonal for the scalar product defined by operator $B=\mathbf{p}^2/2$:

$$\langle\widetilde{\tau,\hbar}|\frac{\mathbf{p}^2}{2}|\widetilde{\tau',\hbar}\rangle=\delta_{\tau\tau'} \quad (102)$$

so that the $|\widetilde{\tau,\hbar}\rangle$ and $|\tau,\hbar\rangle$ relations read

$$|\tau,\hbar\rangle=\frac{1}{\sqrt{\langle\widetilde{\tau,\hbar}|\widetilde{\tau,\hbar}\rangle}}|\widetilde{\tau,\hbar}\rangle,$$
$$|\widetilde{\tau,\hbar}\rangle=\frac{1}{\sqrt{\langle\tau,\hbar|B|\tau,\hbar\rangle}}|\tau,\hbar\rangle, \quad (103)$$

giving rise to $g_{0,1}(\zeta)$ (95) and $g^{\mathrm{tr}}_{0,1}(\zeta)$ (99) expressions in terms of the computed eigenvectors:

$$g_0(\zeta)=\frac{(2\pi)^{3/2}}{4}\sum_\tau \tilde{\psi}_{\tau,\zeta}(\mathbf{q})\tilde{\psi}_{\tau,\zeta}(\mathbf{q}_0)\zeta^{3/2}\delta[\zeta-\zeta_\tau(2)],$$
$$g_1(\zeta)=-\frac{(2\pi)^{3/2}}{4}\sum_\tau \tilde{\psi}_{\tau,\zeta}(\mathbf{q})\tilde{\psi}_{\tau,\zeta}(\mathbf{q}_0)\zeta^{5/2}\delta[\zeta-\zeta_\tau(2)]-\zeta\sum_l \mathcal{A}_l\cos(\zeta S_l+\phi_l),$$
$$g^{\mathrm{tr}}_0(\zeta)=\frac{\pi}{2}\sum_\tau \langle\widetilde{\tau,\zeta}|\widetilde{\tau,\zeta}\rangle\,\zeta^2\delta[\zeta-\zeta_\tau(2)],$$
$$g^{\mathrm{tr}}_1(\zeta)=-\frac{\pi}{2}\sum_\tau \langle\widetilde{\tau,\zeta}|\widetilde{\tau,\zeta}\rangle\,\zeta^3\delta[\zeta-\zeta_\tau(2)]-\zeta\sum_l \mathcal{A}^{\mathrm{tr}}_l\cos(\zeta S^{\mathrm{tr}}_l+\phi^{\mathrm{tr}}_l). \quad (104)$$

As explained previously, the Fourier transform of the two functions g_1 and g^{tr}_1 will depict peaks at classical actions and $\hbar$ corrections are obtained from the amplitude of these peaks. However, in the case of signal given by $c(t)=\Sigma a_n\exp(i\omega_n t)$, it is now well known that the harmonic inversion method is very well suited and is much more powerful than the conventional Fourier transform to extract unknown frequencies ω_n and amplitudes a_n [20]. In our case the signals are the two functions $g_1(\zeta)$ and $g^{\mathrm{tr}}_1(\zeta)$, which are of the form $\Sigma_l\mathcal{A}_l\mathcal{C}_l\sin(\zeta S_l+\phi_l)$ besides contributions from all other types of orbits (ghost, continuous family, etc.).

C. $\hbar$ corrections for $G(\mathbf{q},\mathbf{q}_0,2)$

Orbits having initial and final points at the nucleus (i.e., $\mathbf{q}=\mathbf{q}_0=\mathbf{0}$) are of special interest because they are involved in semiclassical estimation of the photoionization cross section [25,29], which can be directly compared to experimental results [30,31]. Even if the full $\hbar$ expansion of the cross section does not reduce to $G(\mathbf{0},\mathbf{0},2)$ contributions, all closed orbits are well known and classified, so that this case remains a nice example of $\hbar$ corrections for $G(\mathbf{q},\mathbf{q}_0,2)$.

The Fourier transforms of both functions $g_0(\zeta)$ (upper plot, solid line) and $g_1(\zeta)$ (lower plot, solid line), for scaled

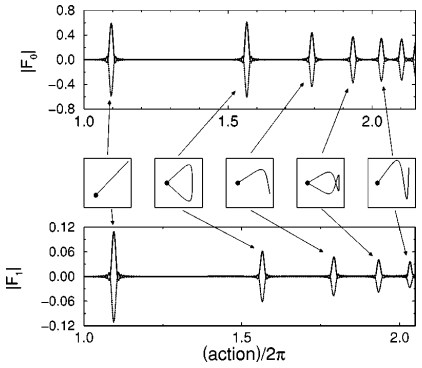

FIG. 3. Modulus of the windowed Fourier transforms F_0 (solid line, upper plot) and F_1 (solid line, lower plot), see Eq. (105), of the quantum functions g_0 (leading order in $\hbar$) and g_1 (first order $\hbar$ correction), see Eq. (104), associated with the quantum Green function $G(\mathbf{q},\mathbf{q}_0,2)$ in the case of the 2D hydrogen atom in a magnetic field and for $\mathbf{q}=\mathbf{q}_0=\mathbf{0}$ (see Sec. VI for all details). As expected from semiclassical formula (25), peaks are appearing at action (i.e., $\int \mathbf{p}\, d\mathbf{q}/2\pi$) corresponding to classical orbits having initial and final positions at the nucleus. For the first five ones, the trajectory in the (u,v) plane are also plotted, the nucleus being depicted by the black circle. The agreement with the semiclassical estimations of these functions (dotted lines) is excellent, even if discrepancies in the amplitude of last two peaks in the lower plot can be observed. These are actually a manifestation of limitation of the Fourier transform and not inaccurate calculations of the $\hbar$ corrections, as it is emphasized by the quantitative comparison (using harmonic inversion) displayed by Table II.

energy $\epsilon=-0.1$, are displayed in Fig. 3. More precisely, $g_0(\zeta)$, and $g_1(\zeta)$ being known only on a finite interval $[0,\zeta_{\max}]$, we have plotted the modulus of their windowed Fourier transforms, defined as follows:

$$F_0(s)=\frac{6}{(\zeta_{\max})^3}\int_0^{\zeta_{\max}} d\zeta\,\zeta(\zeta_{\max}-\zeta)g_0(\zeta)e^{-i2\pi s\zeta},$$

$$F_1(s)=\frac{6}{(\zeta_{\max})^3}\int_0^{\zeta_{\max}} d\zeta\,\zeta(\zeta_{\max}-\zeta)g_1(\zeta)e^{-i2\pi s\zeta}. \tag{105}$$

As expected, they depict peaks at the classical actions of closed orbits, whose trajectories in (u,v) plane have been inserted in the figure, the black circle corresponding to the nucleus position. In the figure, the dotted lines corresponds to the semiclassical estimations of the same functions using the classical properties given by Table I. The closed orbits being either half of a periodic orbit or a periodic orbit, we label a given close orbit with the four-disk code of the corresponding periodic orbit [32,33].

For the leading order in $\hbar$ (upper plot), as expected, the agreement between the quantum results and the semiclassical estimation is excellent. For the first order $\hbar$ correction, the agreement is very good, but one can notice that there is a discrepancy for the amplitude of the last two peaks. This is not due to errors or inaccurate calculations in the semiclassical estimation, but rather a manifestation of the limitations of the Fourier transform. To emphasize this point, we have used the harmonic inversion to extract, for each of these orbits, the $\hbar$ correction coefficients $\mathcal{C}_l^{HI}$, from the quantum function $g_1(\zeta)$. The results are compared to the classical calculation $\mathcal{C}_l$ in Table II. The agreement is excellent, the relative error on the amplitude being lower than 10^{-2}. As usual, the phase extracted using harmonic inversion, being the most sensitive quantity, the agreement on the sign of the $\mathcal{C}_l$, rather nice for the first four orbits, decreases rapidly. Finally, one must mention that this good agreement between quantum and semiclassical calculations has also been found when considering quantum Green's functions $G(\mathbf{q},\mathbf{q}_0,2)$ with other initial or final points.

D. $\hbar$ corrections for Tr $G(\mathbf{q},\mathbf{q},2)$

Still working at scaled energy $\epsilon=-0.1$, Fig. 4 depicts the modulus of the windowed Fourier transforms of $g_0^{\mathrm{tr}}(\zeta)$ and $g_1^{\mathrm{tr}}(\zeta)$, F_0^{tr} (upper plot, solid line), and F_1^{tr} (lower plot, solid line), defined, as previously, as follows:

$$F_0^{\mathrm{tr}}(s)=\frac{6}{(\zeta_{\max})^3}\int_0^{\zeta_{\max}} d\zeta\,\zeta(\zeta_{\max}-\zeta)g_0^{\mathrm{tr}}(\zeta)e^{-i2\pi s\zeta},$$

$$F_1^{\mathrm{tr}}(s)=\frac{6}{(\zeta_{\max})^3}\int_0^{\zeta_{\max}} d\zeta\,\zeta(\zeta_{\max}-\zeta)g_1^{\mathrm{tr}}(\zeta)e^{-i2\pi s\zeta}. \tag{106}$$

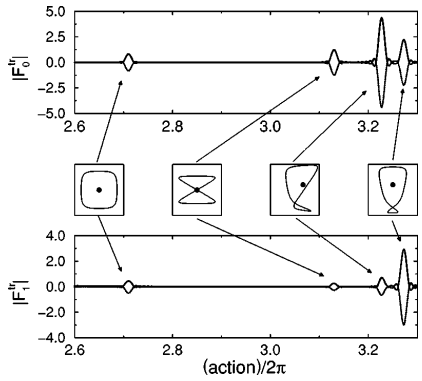

FIG. 4. Modulus of the windowed Fourier transforms F_0^{tr} (solid line, upper plot) and F_1^{tr} (solid line, lower plot), see Eq. (106), of the quantum functions g_0^{tr} (leading order in $\hbar$) and g_1^{tr} (first order $\hbar$ correction), see Eq. (104), associated with the trace of the quantum Green's function Tr $G(\mathbf{q},\mathbf{q},2)$ in the case of the 2D hydrogen atom in a magnetic field (see Sec. VI for all details). As expected from semiclassical formula (65), peaks are appearing at action (i.e., $\oint \mathbf{p}\, d\mathbf{q}/2\pi$) corresponding to classical periodic orbits, whose trajectories in the (u,v) plane are plotted (the nucleus being depicted by the black circle). The agreement with the semiclassical estimation (dotted lines) is excellent, as it is emphasized by the quantitative comparison (using harmonic inversion) displayed by Table IV.

TABLE I. Classical properties of closed orbits involved in the semiclassical expansion of the quantum Green's function $G(\mathbf{q},\mathbf{q}_0,2)$ of the 2D hydrogen atom in a magnetic field, for the case $\mathbf{q}=\mathbf{q}_0=\mathbf{0}$. Because each closed orbit corresponds either to a half-periodic orbit or a periodic orbit, we have labeled them with the four-disk code of the corresponding periodic orbit [32,33]. Their trajectories in the (u,v) plane are shown in Fig. 3. S_l is the reduced action (i.e., $\int \mathbf{p}\, d\mathbf{q}/2\pi$), T_l is the period, $\mathcal{A}_l$ is the leading semiclassical amplitude, $\tilde{\nu}_l$ is the Maslov index, $\mathcal{C}_l$ is the first order $\hbar$ correction, given by the sum $C_1(\mathbf{0},\mathbf{0},T_l)+C_1^{T\to E}(\mathbf{0},\mathbf{0},T_l)$, see Eq. (91).

Code	S_l	T_l	$\mathcal{A}_l$	$\tilde{\nu}_l$
$\overline{13}$	1.094 570 5	2.425 093 3	0.295 342 6	1
$\overline{1243}$	1.564 998 2	3.600 137 4	0.152 365 0	2
$\overline{121343}$	1.791 060 7	4.286 257 7	0.109 503 9	3
$\overline{12124343}$	1.933 522 1	4.796 775 8	0.093 368 7	4
$\overline{1212134343}$	2.031 948 2	5.214 323 3	0.086 142 0	5

Code	$C_1(\mathbf{0},\mathbf{0},T_l)$	$C_1^{T\to E}(\mathbf{0},\mathbf{0},T_l)$	$\mathcal{C}_l$
$\overline{13}$	−0.202 769 9	0.016 539 4	−0.186 230 5
$\overline{1243}$	−0.119 409 3	0.019 741 2	−0.099 668 1
$\overline{121343}$	−0.148 282 2	0.041 175 5	−0.107 106 7
$\overline{12124343}$	−0.172 990 6	0.071 748 0	−0.101 242 7
$\overline{1212134343}$	−0.192 904 3	0.117 464 5	−0.075 439 8

The trajectories in the (u,v) plane associated with the peaks are also plotted in the figure. The classical properties of the corresponding periodic orbits are displayed by Table III. Again the agreement is excellent between the quantum results (solid lines) and the semiclassical estimation (dotted lines). The quantitative comparison between the classical coefficients $\mathcal{C}_l^{\mathrm{tr}}$ and the values $\mathcal{C}_l^{HI}$ extracted from the quantum function $g^{\mathrm{tr}}(\zeta)$ is given in Table IV. The agreement is excellent for the amplitude of the coefficients and is rather good for their phases, which emphasized the validity of the semiclassical formula developed in the preceding sections, especially the additional term arising from the Jacobian describing the change from the Cartesian to local (along the periodic orbit) coordinates [see Eq. (48)] and which contributes to a large part of the $\hbar$ correction for the present orbits.

TABLE II. Numerical comparison between the theoretical $\hbar$ corrections $\mathcal{C}_l$ for the quantum Green's function $G(\mathbf{q},\mathbf{q}_0,2)$ of the 2D hydrogen atom in a magnetic field, for the case $\mathbf{q}=\mathbf{q}_0=\mathbf{0}$ and the numerical coefficients $\mathcal{C}_l^{HI}$ extracted from exact quantum function $g_1(\zeta)$ [Eq. (104)] using harmonic inversion (taking into account multiplicity). The agreement is excellent for the amplitudes and rather nice on the phases, thus emphasizing the validity of the present theory. That the agreement becomes less good for the last orbit only shows the limitations of the harmonic inversion method, which usually appear on the phase.

Code	$\mathcal{C}_l$	$\lvert\mathcal{C}_l^{HI}\rvert$	Rel. error	$\arg \mathcal{C}_l^{HI}$
$\overline{13}$	−0.186 230 5	0.1864	$\approx 8\times10^{-4}$	$1.002\times\pi$
$\overline{1243}$	−0.099 668 1	0.0995	$\approx 2\times10^{-3}$	$1.01\times\pi$
$\overline{121343}$	−0.107 106 7	0.1072	$\approx 9\times10^{-4}$	$1.02\times\pi$
$\overline{12124343}$	−0.101 242 7	0.1016	$\approx 4\times10^{-3}$	$1.04\times\pi$
$\overline{1212134343}$	−0.075 439 8	0.0761	$\approx 9\times10^{-3}$	$1.14\times\pi$

TABLE III. Classical properties of periodic orbits involved in the semiclassical expansion of the trace of the quantum Green's function $\mathrm{Tr}\, G(\mathbf{q},\mathbf{q},2)$ of the 2D hydrogen atom in a magnetic field. Their trajectories in the (u,v) plane are shown in Fig. 4. S_l^{tr} is the reduced action (i.e., $\oint \mathbf{p}\, d\mathbf{q}/2\pi$), T_l is the period, $\mathcal{A}_l^{\mathrm{tr}}$ is the leading semiclassical amplitude, μ_l is the Maslov index, $\mathcal{C}_l^{\mathrm{tr}}$ is the first order $\hbar$ correction, given by the sum $C_1(T_l)+C_1^{T\to E}(T_l)$, see Eq. (98).

Code	S_l^{tr}	T_l^{tr}	$\mathcal{A}_l^{\mathrm{tr}}$	μ_l
$\overline{1234}$	2.709 851 3	6.204 155 6	0.827 881 4	4
$\overline{1243}$	3.129 996 4	7.200 274 7	0.616 496 8	4
$\overline{12434}$	3.227 168 1	7.541 640 6	0.548 479 1	5
$\overline{123434}$	3.272 238 1	7.748 406 8	0.555 880 6	6

Code	$C_1(T_l)$	$C_1^{T\to E}(T_l)$	$\mathcal{C}_l^{\mathrm{tr}}$
$\overline{1234}$	−0.622 577	0.026 912	−0.595 665
$\overline{1243}$	0.166 821	0.051 665	0.218 486
$\overline{12434}$	−0.203 536	0.058 541	−0.144 995
$\overline{123434}$	−1.417 05	0.072 41	−1.344 64

VII. CONCLUSION

In summary, we have explained in this paper how to effectively compute $\hbar$ corrections in the semiclassical expansions of the propagator $K(\mathbf{q},\mathbf{q}_0,T)$, its trace $K(T)$, the quantum Green's function $G(\mathbf{q},\mathbf{q}_0,E)$ and its trace $G(E)$ for chaotic systems with smooth potential. The method is based on the classical Green's functions associated to the relevant trajectories, that is either going from $\mathbf{q}$ to $\mathbf{q}_0$ in the propagator case or periodic orbits for $K(T)$, together with adapted boundary conditions. We have shown how all quantities can be obtained by integrating, using the standard Runge-Kutta method, sets of differential equations. We have also shown

TABLE IV. Numerical comparison between the theoretical $\hbar$ corrections $\mathcal{C}_l^{\mathrm{tr}}$ for the trace of the quantum Green's function $\mathrm{Tr}\, G(\mathbf{q},\mathbf{q},2)$ of the 2D hydrogen atom in a magnetic field and the numerical coefficients $\mathcal{C}_l^{HI}$ extracted from exact quantum function $g_1^{\mathrm{tr}}(\zeta)$ [Eq. (104)] using harmonic inversion (taking into account multiplicity). The agreement is excellent for the amplitudes and rather nice on the phases, thus emphasizing the validity of the present theory, especially the additional term due to the transformation from the Cartesian coordinates to the local frame along the periodic orbit [see Eq. (48)].

Code	$\mathcal{C}_l^{\mathrm{tr}}$	$\lvert\mathcal{C}_l^{HI}\rvert$	Rel. Error	$\arg \mathcal{C}_l^{HI}$
$\overline{1234}$	−0.595 665	0.5958	$\approx 2\times10^{-4}$	$1.005\times\pi$
$\overline{1243}$	0.218 486	0.2178	$\approx 3\times10^{-3}$	$0.04\times\pi$
$\overline{12434}$	−0.144 995	0.147	$\approx 1\times10^{-2}$	$0.93\times\pi$
$\overline{123434}$	−1.344 64	1.347	$\approx 2\times10^{-3}$	$0.98\times\pi$

that in the derivation of the semiclassical expansion for $K(T)$ [and thus $G(E)$], starting from the Feynman path integral, one must take into account additional terms, which affect only $\hbar$ correction coefficients. This is emphasized by the excellent agreement observed when comparing, in the case of the 2D hydrogen atom in a magnetic field, our theoretical results with the numerical coefficients extracted from exact quantum data, using the harmonic inversion. Obviously, there are still many points to be developed. Besides the few cases, such as self-retracing orbits or continuous families of orbits, needing specific extensions, it would be very interesting to understand how to include continuous and discrete symmetries. Also, going into the extended phase space $(\mathbf{q},t,\mathbf{p},-E)$ [22], it would be possible to get a better understanding of similarities observed between the differential sets leading, on one side to the $\hbar$ corrections for the propagator and its trace and, on the other side to the additional terms arising in the $\hbar$ corrections for the quantum Green's function and its trace.

ACKNOWLEDGMENTS

The author thanks D. Delande for fruitful discussions and for his kind support during this work, especially for numerous suggestions which led to the present form. The author also thanks M. Kuś for useful discussions. Laboratoire Kastler Brossel is laboratoire de l'Université Pierre et Marie Curie et de l'Ecole Normale Supérieure, Unité Mixte de Recherche 8552 du CNRS.

APPENDIX: FEW PROPERTIES OF $M(T)$

In this Appendix, we consider an isolated unstable periodic orbit of period T. We shall use the notations $\mathbf{e}_\parallel$ and $\mathbf{e}_\perp$ for the units vectors, which are, respectively, parallel to the flow and perpendicular to the energy shell at the initial point. From Hamilton's equations, we have that $M(T)\cdot\mathbf{e}_\parallel=\mathbf{e}_\parallel$, i.e., $\mathbf{e}_\parallel$ is an eigenvector of the matrix $M(T)$ for the eigenvalue 1. The symplectic equation fulfilled by $M(T)$, namely, $M(T)^\top\cdot\Sigma\cdot M(T)=\Sigma$, implies that, if $\mathbf{e}_i$ and $\mathbf{e}_j$ are two eigenvectors for the eigenvalues λ_i and λ_j, we have the following properties:

$$M(T)^\top\cdot(\Sigma\mathbf{e}_i)=\frac{1}{\lambda_i}(\Sigma\mathbf{e}_i),$$
$$(\lambda_i\lambda_j-1)\mathbf{e}_i^\top\Sigma\mathbf{e}_j=0, \tag{A1}$$

showing thus that $1/\lambda_i$ is an eigenvalue of $M(T)^\top$ and, from that, of $M(T)$. In addition, $M(T)$ being a real matrix, $\overline{\lambda_j}$ and $1/\overline{\lambda_j}$ are also eigenvalues of $M(T)$, so that the nontrivial eigenvalues (i.e., $\neq 1$) either fall in the $(\lambda,1/\lambda)$ pair or in quadruplet $(\lambda,1/\lambda,\overline{\lambda},1/\overline{\lambda})$.

In the case of $\mathbf{e}_i=\mathbf{e}_\parallel$, the two preceding equations (A1) imply that $\mathbf{e}_\perp$ is an eigenvector of $M(T)^\top$ [but not necessarily of $M(T)$] for the eigenvalue 1 and that for every $\lambda_j\neq 1$, $\mathbf{e}_j$ is an orthogonal to $\mathbf{e}_\perp$. In the basis $(\mathbf{e}_\parallel,\mathbf{e}_\perp,\mathbf{e}_1,\ldots,\mathbf{e}_{2f-2})$, $M(T)$ entries then read

$$M(T)=\begin{bmatrix} 1 & \alpha_\parallel & 0 & 0 & \cdots & 0 \\ 0 & 1 & 0 & 0 & \cdots & 0 \\ 0 & \alpha_1 & \lambda_1 & 0 & \cdots & 0 \\ 0 & \alpha_2 & 0 & \lambda_2 & \cdots & 0 \\ \vdots & \vdots & \vdots & \vdots & \ddots & \vdots \\ 0 & \alpha_{2f-2} & 0 & 0 & \cdots & \lambda_{2f-2} \end{bmatrix}, \tag{A2}$$

where we have supposed that all eigenvalues are simple. For degenerated eigenvalues, $M(T)$ would be block diagonal. For a generic periodic orbit, $\alpha_\parallel$ and α_i are nonvanishing emphasizing thus that $\mathbf{e}_\perp$ is not an eigenvector of $M(T)$. Introducing the vector $\tilde{\mathbf{e}}_\perp$ defined as follows:

$$\tilde{\mathbf{e}}_\perp=\mathbf{e}_\perp+\sum_{j=1}^{2f-2}\beta_j\mathbf{e}_j \quad \text{with} \quad \beta_j=\frac{\alpha_j}{1-\lambda_j} \tag{A3}$$

one immediately gets that

$$M(T)\tilde{\mathbf{e}}_\perp=\tilde{\mathbf{e}}_\perp+\alpha_\parallel\mathbf{e}_\parallel. \tag{A4}$$

In the case $\alpha_\parallel=0$, we have thus found another eigenvector for the eigenvalue 1, which means that a small displacement of initial conditions in the $\tilde{\mathbf{e}}_\perp$ direction leads to another periodic motion with the same period T, and thus that the periodic orbit is actually embedded in a continuous family. Indeed, using notations from Sec. V, one can show that

$$\mathbf{X}^{(1)}(0)=-\frac{\|\dot{\mathbf{X}}\|}{\alpha_\parallel}\tilde{\mathbf{e}}_\perp \tag{A5}$$

so that we have

$$\alpha_\parallel=\|\dot{\mathbf{X}}\|^2\partial_E T. \tag{A6}$$

In Sec. V, one needs to compute derivatives with respect to the period T of $\det[m(T)-1]$, whose expression in terms of the nontrivial eigenvalues of the monodromy matrix reads

$$\det[m(T)-1]=\prod_{j=1}^{2f-2}(\lambda_j-1). \tag{A7}$$

Introducing $\mathcal{P}_\parallel$ and $\mathcal{P}_\perp$ the projectors on the directions $\mathbf{e}_\parallel$ and $\mathbf{e}_\perp$, more precisely,

$$\mathcal{P}_\parallel=\mathbf{e}_\parallel\cdot\mathbf{e}_\parallel^\top \quad \text{and} \quad \mathcal{P}_\perp=\mathbf{e}_\perp\cdot\mathbf{e}_\perp^\top \tag{A8}$$

ones defines the matrix $N(T)$ as follows:

$$N(T)=M(T)-(1-\mathcal{P}_\parallel-\mathcal{P}_\perp). \tag{A9}$$

In the basis $(\mathbf{e}_\parallel,\mathbf{e}_\perp,\mathbf{e}_1,\ldots,\mathbf{e}_{2f-2})$, using orthogonality between $\mathbf{e}_\perp$ and $\mathbf{e}_j$, entries of $N(T)$ read

$$N(T)=\begin{bmatrix} 1 & \alpha_{\parallel} & \gamma_1 & \gamma_2 & \cdots & \gamma_{2f-2} \\ 0 & 1 & 0 & 0 & \cdots & 0 \\ 0 & \alpha_1 & \lambda_1-1 & 0 & \cdots & 0 \\ 0 & \alpha_2 & 0 & \lambda_2-1 & \cdots & 0 \\ \vdots & \vdots & \vdots & \vdots & \ddots & \vdots \\ 0 & \alpha_{2f-2} & 0 & 0 & \cdots & \lambda_{2f-2}-1 \end{bmatrix}, \tag{A10}$$

where $\gamma_j=\mathbf{e}_{\parallel}^{\top}\cdot\mathbf{e}_j$, which actually could be related to the α_j, but this is not necessary in our case. This shows that the determinant of $N(T)$ is exactly $\Pi_{j=1}^{2f-2}(\lambda_j-1)$. The main advantage of the matrix $N(T)$ is that its expression (A9) does not involve the eigenvectors or the eigenvalues of $M(T)$, so that its determinant can be directly computed, without the diagonalization stage required when getting $\det[m(T)-1]$ through the eigenvalues λ_j. Furthermore, derivatives of $\ln\det N(T)$ with respect to the period T are also straightforward to obtain, knowing derivatives of $M(T)$ and of $\dot{\mathbf{X}}(T)$, whereas derivatives of λ_j would require the knowledge of those of the eigenvectors $\mathbf{e}_j$.

[1] M. C. Gutzwiller, *Chaos in Classical and Quantum Mechanics* (Springer-Verlag, New York, 1990).
[2] J. H. Van Vleck, Proc. Natl. Acad. Sci. U.S.A. **14**, 178 (1928).
[3] M. Brack and R. K. Bhaduri, *Semiclassical Physics* (Addison-Wesley, Reading, MA, 1997).
[4] H. Friedrich and D. Wintgen, Phys. Rep. **183**, 37 (1989).
[5] D. Delande, in *Chaos and Quantum Physics*, edited by M.-J. Giannoni, A. Voros and J. Zinn-Justin, Les Houches Summer School, Session LII (North-Holland, Amsterdam, 1991).
[6] G. S. Ezra, K. Richter, G. Tanner, and D. Wintgen, J. Phys. B **24**, L413 (1991).
[7] P. Gaspard and S. A. Rice, Phys. Rev. A **48**, 54 (1993).
[8] B. Grémaud and P. Gaspard, J. Phys. B **31**, 1671 (1998).
[9] D. S. Saraga and T. S. Monteiro, Phys. Rev. Lett. **81**, 5796 (1998).
[10] L. A. Bunimovitch, Commun. Math. Phys. **65**, 295 (1979).
[11] P. Cvitanović and B. Eckhardt, Phys. Rev. Lett. **63**, 823 (1989).
[12] P. Gaspard and D. Alonso, Phys. Rev. A **47**, R3468 (1993).
[13] P. Gaspard, D. Alonso, and I. Burghardt, Adv. Chem. Phys. **90**, 105 (1995).
[14] E. B. Bogomolny, U. Gerland, and C. Schmidt, Phys. Rev. E **59**, R1315 (1999).
[15] S. C. Creagh and R. G. Littlejohn, Phys. Rev. A **44**, 836 (1991).
[16] S. C. Creagh and R. G. Littlejohn, J. Phys. A **25**, 1643 (1992).
[17] G. Vattay and P. E. Rosenqvist, Phys. Rev. Lett. **76**, 335 (1996).
[18] B. Eckhardt and D. Wintgen, J. Phys. A **24**, 4335 (1991).
[19] J. Main, K. Weibert, and G. Wunner, Phys. Rev. E **58**, 4436 (1998).
[20] J. Main, Phys. Rep. **316**, 233 (1999).
[21] K. Weibert, J. Main, and G. Wunner, Eur. Phys. J. D **12**, 381 (2000).
[22] R. G. Littlejohn, J. Math. Phys. **31**, 2952 (1990).
[23] R. Marcinek and D. Delande, Phys. Rev. A **62**, 062704 (2000).
[24] T. Jonckheere, B. Grémaud, and D. Delande, Phys. Rev. Lett. **81**, 2442 (1998).
[25] E. P. Bogomolny, Zh. Éksp. Teor. Fiz. **96**, 487 (1989) [Sov. Phys. JETP **69**, 275 (1989)].
[26] M. J. Englefield, *Group Theory and the Coulomb Problem* (Wiley, New York, 1972).
[27] C. C. Martens, R. L. Waterland, and W. P. Reinhardt, J. Chem. Phys. **90**, 2328 (1989).
[28] J. M. Robbins, Phys. Rev. A **40**, 2128 (1989).
[29] J. Gao and J. B. Delos, Phys. Rev. A **46**, 1455 (1992).
[30] A. Holle, J. Main, G. Wiebusch, H. Rottke, and K. H. Welge, Phys. Rev. Lett. **61**, 161 (1988).
[31] J. Main, G. Wiebusch, K. Welge, J. Shaw, and J. B. Delos, Phys. Rev. A **49**, 847 (1994).
[32] B. Eckhardt and D. Wintgen, J. Phys. B **23**, 355 (1990).
[33] K. T. Hansen, Phys. Rev. E **51**, 1838 (1995).

2.3.3 Prendre en compte les symétries

En outre, pour pouvoir établir des comparaisons avec des résultats expérimentaux, j'ai été amené à prendre en compte l'effet des symétries, quelles soient discrètes (parité) ou continues (invariance par rotation). Dans le premier cas, la théorie des groupes fournit directement les modifications à apporter pour calculer les corrections en $\hbar$ aux formules de traces restreintes à des états appartenant à une des représentations du groupe de symétrie. Le cas de l'invariance par rotation est plus délicat puisque, pour une valeur donnée du moment angulaire, il faut prendre en compte l'effet des termes centrifuges dans le hamiltonien, typiquement $\hbar^2 L^2/2/r^2$, qui dans la limite $\hbar \to 0$ ne modifient pas la dynamique classique, mais contribuent aux corrections. Là encore, j'ai montré comment prendre proprement en compte ces termes, en particulier leur singularité en $r = 0$, pour calculer leur contribution aux corrections au premier ordre en $\hbar$ aux formules de trace. Les comparaisons numériques, dans le cas de l'hydrogène en champ magnétique, ont montré l'excellent accord entre ces prédictions et les calculs quantiques exacts.

Semiclassical analysis of real atomic spectra beyond Gutzwiller's approximation

Benoît Grémaud*
Laboratoire Kastler Brossel, Université Pierre et Marie Curie, Case 74, 4, place Jussieu, 75252 Paris Cedex 05, France
(Received 24 January 2005; published 13 October 2005)

Real atomic systems, like the hydrogen atom in a magnetic field or the helium atom, whose classical dynamics are chaotic, generally present both discrete and continuous symmetries. In this paper, we explain how these properties must be taken into account in order to obtain the proper (i.e., symmetry projected) $\hbar$ expansion of semiclassical expressions like the Gutzwiller trace formula. In the case of the hydrogen atom in a magnetic field, we shed light on the excellent agreement between present theory and exact quantum results.

DOI: 10.1103/PhysRevE.72.046208 PACS number(s): 05.45.Mt, 03.65.Sq, 32.30.−r

In the studies of the quantum properties of systems whose classical counterparts depict chaotic behavior, semiclassical formulas are essential links between the two worlds, emphasized by Gutzwiller's work [1]. More specifically, starting from Feynman's path formulation of quantum mechanics, he has been able to express the quantum density of states as a sum over all (isolated) periodic orbits of the classical dynamics. This formula, and extensions of it, have been widely used to understand and obtain properties of the energy levels of many classically chaotic systems, among which is the hydrogen atom in a magnetic field [2,3], the helium atom [4–6], or billiards [7–10].

At the same time, because the trace formula (and its variations) as derived by Gutzwiller only contained the leading term of the asymptotic expansion of the quantum level density, the systematic expansion of the semiclassical propagator in powers of $\hbar$ has been the purpose of several studies [9–12], but which focused on billiards, for which both classical and quantum properties are easier to calculate.

In a recent paper [13], general equations for efficient computation of $\hbar$ corrections in semiclassical formulas for a chaotic system with smooth dynamics were presented, together with explicit calculations for the hydrogen atom in a magnetic field. However, only the two-dimensional case was considered, because for the three-dimensional (3D) case, discrete symmetries and centrifugal terms had to be taken into account. Actually, this situation occurs in almost all real atomic systems depicting a chaotic behavior (molecules, two electron atoms…), for which experimental data involve levels having well defined parity, total angular momentum, and, if relevant, exchange between particles. In particular, semiclassical estimations of experimental signals like photoionization cross sections are calculated with closed orbits with vanishing total angular momentum, whereas they usually involve P ($L=1$) quantum states, whose positions in energy are shifted with respect to S ($L=0$) states. Furthermore, in recent years, the development of the harmonic inversion method makes it possible to extract the relevant quantities (position of peaks, complex amplitudes) from both theoretical and experimental data with a much higher accuracy than with the conventional Fourier transform [14]. In particular, it becomes possible to measure the deviation of the exact quantum results from the semiclassical leading order predictions. Thus a detailed semiclassical analysis of experimental results, beyond the leading order in $\hbar$, requires the understanding and the calculation of corrections due to both the discrete symmetries and centrifugal terms. In addition, we would like to stress that even if the present analysis is made with the density of states, it can also be made with the quantum Green function, which leads to expressions and numerical computations of the first order $\hbar$ corrections for physical quantities like the photoionization cross section [15,16], which could either be compared to available experimental data [17,18], or become a starting point for refined experimental tests of the quantum-classical correspondence in the chaotic regime.

$\hbar$ corrections and discrete symmetries have already been discussed, but only for billiards [9,10,12], whereas in the case of systems with smooth dynamics a detailed study is still lacking. Also, centrifugal terms and/or rotational symmetries have been considered by many authors, but either in the case of integrable systems [19,20], or for values of the angular momentum comparable to the action of classical orbits [1,21,22]. From this point of view, the present study, which focuses on fixed values of the quantum angular momentum and the effect of the centrifugal terms on $\hbar$ corrections for systems with smooth chaotic dynamics, goes beyond the preceding considerations. More precisely, in this paper, we explain how to take into account both discrete symmetries and centrifugal terms in order to obtain a full semiclassical description of the first order $\hbar$ corrections for the 3D hydrogen atom in a magnetic field.

At first, in the case of a chaotic system, whose Hamiltonian $H=\mathbf{p}^2/2+V(\mathbf{q})$ is invariant under a group $\mathcal{S}$ of discrete transformations σ, the leading order of semiclassical approximation for the trace of the Green function $G(E)=1/(E-H)$, restricted to the mth irreducible representation is given by [23]

$$g_m^{\mathrm{sc}}(E)=\frac{d_m}{i\hbar}\sum_l \frac{T_l}{|K_l|}\sum_n \chi_m(\sigma_l^n)g_{(l,n)}^{(0)}(E) \tag{1}$$

with

$$g_{(l,n)}^{(0)}(E)=\frac{1}{|\det(A_l^n-1)|^{1/2}}\exp\left[\frac{i}{\hbar}nS_l-in\mu_l\frac{\pi}{2}\right], \tag{2}$$

where the l sum is taken over all primitive (isolated) orbits which become periodic through the symmetry operation σ_l

*Electronic address: Benoit.Gremaud@spectro.jussieu.fr

[i.e., final position (respectively, velocity) is mapped back to initial position (respectively, velocity) by σ_l]. $\chi_m(\sigma_l^n)$ is the character of σ_l^n in the mth irreducible representation of dimension d_m. S_l is the action of the orbit l, μ_l is the Maslov index, T_l is the "period," A_l^n represents the Poincaré surface-of-section map linearized around the orbit, and K_l is the subgroup of $\mathcal{S}$ leaving each point of the orbit l invariant. Adding first order $\hbar$ corrections, the preceding equation (1) becomes

$$g_m^{\mathrm{sc}}(E) = \frac{d_m}{i\hbar}\sum_l \frac{T_l}{|K_l|}\sum_n \chi_m(\sigma_l^n) g_{(l,n)}^{(0)}(E)\left(1 + i\hbar \mathcal{C}_{(l,n)}^{\mathrm{tr}}\right). \quad (3)$$

$\mathcal{C}_{l,n}^{\mathrm{tr}}$ can be derived by a detailed analysis of the stationary phase approximations starting from the Feynman path integral, following the same steps as in Refs. [10,13] and reads as follows:

$$\mathcal{C}_{l,n}^{\mathrm{tr}} = C_{l,n}^{T\to E} + \frac{1}{nT_l}\int_0^{nT_l} dt_0 C_{l,n}(t_0), \quad (4)$$

where $C_{l,n}^{T\to E}$ arises from the time to energy domain transformation. $C_{l,n}(t_0)$ (see Ref. [13] for the expressions) involves the classical Green functions $\mathcal{G}_{l,n}(t,t')$, i.e., the solutions of the equations controlling the linear stability around the classical trajectory $\mathbf{q}_{l,n}^{\mathrm{cl}}(t)$:

$$\left(-\frac{d^2}{dt^2}\mathbb{1} - \frac{\partial^2 V}{\partial \mathbf{q}\,\partial \mathbf{q}}[\mathbf{q}_{l,n}^{\mathrm{cl}}(t)]\right)\mathcal{G}_{l,n}(t,t') = \mathbb{1}\,\delta(t-t'). \quad (5)$$

The fact that the orbits are periodic after the symmetry transformation σ_l^n determines the boundary conditions that the classical Green functions $\mathcal{G}_{l,n}(t,t')$ must fulfill, namely,

$$\begin{cases} \sigma_l^{-n}\mathcal{G}_{l,n}(nT_l,t') = \mathcal{G}_{l,n}(0,t') \\ \mathcal{P}_{t_0}\mathcal{G}_{l,n}(0,t') = 0 \qquad\qquad \forall\ t' \in [0,nT_l], \\ \mathcal{Q}_{t_0}\sigma_l^{-n}\dot{\mathcal{G}}_{l,n}(nT_l,t') = \mathcal{Q}_{t_0}\dot{\mathcal{G}}_{l,n}(0,t') \end{cases} \quad (6)$$

where $\mathcal{P}_{t_0}$ is the projector along the "periodic" orbit at the position depicted by time t_0 and $\mathcal{Q}_{t_0}=\mathbb{1}-\mathcal{P}_{t_0}$. Of course, for $\sigma_l=\mathbb{1}$, one recovers the boundary conditions given in Ref. [13]. Finally, all technical steps of Ref. [13] leading to efficient computation of $\mathcal{G}_{l,n}(t,t')$ and $\hbar$ corrections, that is, solutions of sets of first order differential equations, can easily be adapted to take into account these modified boundary conditions.

As a numerical example, we have considered the 2D hydrogen atom in a magnetic field, at scaled energy $\epsilon=-0.1$ [2]. More precisely, we have computed the trace of the quantum Green function, using roughly 8000 states belonging to the *EEE* representation [24] of the group D_4, corresponding to effective $1/\hbar$ values ranging from 0 to 124 (see Ref. [13] for further details). In that case, the periodic orbit $\overline{1234}$ [25,26] (see inset of the top of Fig. 1 for the trajectory in semiparabolic coordinates), being (globally) invariant under a rotation of angle $\pi/2$, gives rise to contributions in the semiclassical approximation of the trace at all multiples of $S_{\overline{1234}}/4$. In the same way, the periodic orbit $\overline{1243}$ (see middle inset of Fig. 1) being invariant under a rotation of angle π, contributions are present at all multiples of $S_{\overline{1243}}/2$. For both these orbits, Table I displays the comparison of the present theoretical calculation and the numerical coefficient $\mathcal{C}_{l,n}^{HI}$, extracted from the exact quantum Green function, using harmonic inversion [13,14]. As one can notice, the agreement is excellent for the amplitudes and rather good for the phases, which is the usual behavior of harmonic inversion. Furthermore, the same agreement has also been found for the other representations, thus emphasizing the present approach for the calculation of the first order $\hbar$ corrections when taking into account discrete symmetries.

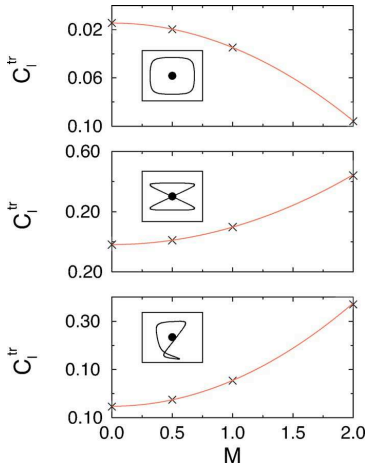

FIG. 1. (Color online) First order $\hbar$ correction to the semiclassical approximation of the trace of the quantum Green function for the hydrogen atom in a magnetic field for different values of the magnetic number M, $M=1/2$ corresponding to the 2D case [13]. Crosses depict the values extracted from the exact quantum function using harmonic inversion, whereas the solid line corresponds to the classical results given by Eq. (10). For the three different periodic orbits, whose trajectories in the (u,v) plane are plotted (the nucleus being depicted by the black dot), the agreement is excellent, thus emphasizing the validity of Eqs. (9) and (10).

Contrary to the preceding, calculating first order $\hbar$ corrections due to centrifugal terms is more complicated and is best explained in the case of the 3D hydrogen atom in a magnetic

TABLE I. Numerical comparison between the theoretical $\hbar$ corrections $\mathcal{C}_l^{\mathrm{tr}}$ for the trace of the quantum Green function, restricted to the *EEE* representation, of the 2D hydrogen atom in a magnetic field and the numerical coefficients $\mathcal{C}_l^{HI}$ extracted from exact quantum function using harmonic inversion. The agreement is excellent for the amplitudes and rather good on the phases, thus emphasizing the validity of the present approach.

Code	$\mathcal{C}_l^{\mathrm{tr}}$	$\lvert\mathcal{C}_l^{HI}\rvert$	Rel. error	$\arg \mathcal{C}_l^{HI}$
$\frac{1}{4}\overline{1234}$	−0.094 430	0.09445	$\approx 2\times10^{-4}$	$0.9996\times\pi$
$\frac{1}{2}\overline{1234}$	−0.361 689	0.3611	$\approx 2\times10^{-3}$	$0.996\times\pi$
$\frac{3}{4}\overline{1234}$	−0.400 555	0.3992	$\approx 3\times10^{-3}$	$1.005\times\pi$
$\frac{1}{2}\overline{1243}$	0.049 399	0.0493	$\approx 8\times10^{-4}$	$-0.075\times\pi$

field. The regularized Hamiltonian in semiparabolic coordinates, for fixed value M of the projection of the angular momentum along the field axis, is given by [2]

$$H = -\frac{\hbar^2}{2}\left\{\frac{\partial^2}{\partial u^2}+\frac{\partial^2}{\partial v^2}+\left(\frac{1}{4}-|M|^2\right)\left[\frac{1}{u^2}+\frac{1}{v^2}\right]\right\} - \epsilon(u^2+v^2)+\frac{1}{8}u^2v^2(u^2+v^2)$$
$$= H_0 + \frac{\hbar^2}{2}\left(|M|^2-\frac{1}{4}\right)U(u,v). \quad (7)$$

H_0 is then the Hamiltonian of the 2D hydrogen atom in a magnetic field. If $U(u,v)$ was regular, then the additional first order $\hbar$ correction for the orbit l would simply be

$$-\frac{1}{2}\left(|M|^2-\frac{1}{4}\right)\int_0^{T_l} dt\, U(u_l(t),v_l(t)). \quad (8)$$

One must mention that in this case, the Langer transformation [27] of the coordinates $(u,v)\rightarrow(\exp(-x),\exp(-y))$ gives rise to a Hamiltonian which does not separate into kinetic and potential energies and for which no expressions for $\hbar$ corrections are available.

On the other hand, the fact that $U(u,v)$ is singular imposes boundary conditions on both classical and quantum dynamics. The classical trajectories have to make (smooth) bounces near $u=0$ and $v=0$ and for vanishing values of $\hbar$, we expect the trajectories of H to be those of H_0, but mapped onto the reduced phase space $(u>0,v>0)$, i.e., making hard bounces on the (u,v) axis. From the quantum point of view, depending on the parity of M, only wave functions belonging to given representations of D_4 are allowed. Thus first order $\hbar$ corrections due to the singular part of the potential U, are given by the preceding considerations on the symmetries, whereas remaining corrections are given by Eq. (8), where U has to be replaced by a smooth counterpart, namely,

$$\tilde{U} = \lim_{\epsilon\rightarrow 0^+}\frac{1}{2}\left(\frac{1}{(u+i\epsilon)^2}+\frac{1}{(u-i\epsilon)^2}+\frac{1}{(v+i\epsilon)^2}+\frac{1}{(v-i\epsilon)^2}\right). \quad (9)$$

Actually, one can show that the preceding equation gives the right answers for $\hbar$ expansion of the propagator of the free particle (up to $\hbar^3$) and the harmonic oscillator (up to $\hbar^2$), for which analytical expressions for classical trajectories, classical Green functions, and quantum propagators exist (higher orders have not been checked yet). However, even if a detailed analysis of the derivation of the trace formula in presence of centrifugal terms seems to show that the preceding approach works in general cases, rigorous proof of Eq. (9) is lacking.

Nevertheless, in the case of the 3D hydrogen atom in a magnetic field, we have compared the first order $\hbar$ corrections, for different periodic orbits and for different values of the magnetic number M, with the present prediction, namely,

$$C_l^{\mathrm{tr}}(M) = C_l^{\mathrm{tr}}(2D) - \frac{1}{8}(4|M|^2-1)\int_0^{T_l} dt\tilde{U}(u_l(t),v_l(t)). \quad (10)$$

The results are displayed in Fig. 1 for $M=0,1,2$ and for three different orbits, namely 1234, 1243, and 12343, whose trajectories in the (u,v) plane are plotted. The solid line is the theoretical result given by Eq. (10), whereas the crosses are the values extracted from the trace of the exact quantum Green function, using harmonic inversion (for scaled energy $\epsilon=-0.1$, roughly 8000 effective $1/\hbar$ values ranging from 0 to 124). As one can notice the agreement is excellent, thus giving strong support for the validity of Eqs. (9) and (10). Furthermore, the simplicity of the replacement $\tilde{U}$ may serve as a guideline for a rigorous treatment of the $\hbar$ corrections arising from the centrifugal terms. In particular, the calculation of higher orders involves products of the derivatives of these centrifugal terms and those of the potential V_0, giving rise to nontrivial mixing between centrifugal and standard $\hbar$ corrections.

In conclusion, we have presented a semiclassical analysis, beyond the usual Gutzwiller approximation, including first order $\hbar$ corrections, of the quantum properties of real chaotic systems. More specifically, we have explained the additional corrections arising when taking into account both discrete symmetries and centrifugal terms. In the case of the (3D) hydrogen in a magnetic field, the agreement between the theory and the numerical data extracted from exact quantum results is excellent, emphasizing the validity of the analysis, especially of Eqs. (9) and (10).

Finally, since we know how to compute the $\hbar$ corrections, it would be very interesting to work the other way around, that is, to perform the semiclassical quantization, thus getting $\hbar$ corrections in the semiclassical estimations of the quantum quantities, like the eigenenergies. Of course, this represents a more considerable amount of work, since the $C_{l,n}^{\mathrm{tr}}$ coefficients must be computed for all relevant orbits and then included in standard semiclassical quantization schemes, like the cycle expansion [5,11,28].

The author thanks D. Delande for his kind support during this work. Laboratoire Kastler Brossel is Laboratoire de l'Université Pierre et Marie Curie et de l'Ecole Normale Supérieure, unité mixte de recherche 8552 du CNRS.

[1] M. C. Gutzwiller, *Chaos in Classical and Quantum Mechanics* (Springer, New York, 1990).
[2] H. Friedrich and D. Wintgen, Phys. Rep. **183**, 37 (1989).
[3] D. Delande, in *Chaos and Quantum Physics*, edited by M.-J. Giannoni, A. Voros, and J. Zinn-Justin, Les Houches Summer School, Session LII (North-Holland, Amsterdam, 1991).
[4] G. S. Ezra, K. Richter, G. Tanner, and D. Wintgen, J. Phys. B **24**, L413 (1991).

[5] P. Gaspard and S. A. Rice, Phys. Rev. A **48**, 54 (1993).
[6] B. Grémaud and P. Gaspard, J. Phys. B **31**, 1671 (1998).
[7] L. A. Bunimovitch, Commun. Math. Phys. **65**, 295 (1979).
[8] P. Cvitanović and B. Eckhardt, Phys. Rev. Lett. **63**, 823 (1989).
[9] P. Gaspard and D. Alonso, Phys. Rev. A **47**, R3468 (1993).
[10] P. Gaspard, D. Alonso, and I. Burghardt, Adv. Chem. Phys. **90**, 105 (1995).
[11] G. Vattay and P. E. Rosenqvist, Phys. Rev. Lett. **76**, 335 (1996).
[12] K. Weibert, J. Main, and G. Wunner, Eur. Phys. J. D **19**, 379 (2002).
[13] B. Grémaud, Phys. Rev. E **65**, 056207 (2002).
[14] J. Main, Phys. Rep. **316**, 233 (1999).
[15] E. P. Bogomolny, Zh. Eksp. Teor. Fiz. **96**, 487 (1989) [Sov. Phys. JETP **69**, 275 (1989)].
[16] J. Gao and J. B. Delos, Phys. Rev. A **46**, 1455 (1992).
[17] A. Holle, J. Main, G. Wiebusch, H. Rottke, and K. H. Welge, Phys. Rev. Lett. **61**, 161 (1988).
[18] J. Main, G. Wiebusch, K. Welge, J. Shaw, and J. B. Delos, Phys. Rev. A **49**, 847 (1994).
[19] L. S. Schulmann, *Techniques and Applications of Path Integration* (Wiley, New York, 1981).
[20] K. C. Khandekar and S. V. Lawande, J. Math. Phys. **16**, 384 (1975).
[21] S. C. Creagh and R. G. Littlejohn, Phys. Rev. A **44**, 836 (1991).
[22] S. C. Creagh and R. G. Littlejohn, J. Phys. A **25**, 1643 (1992).
[23] J. M. Robbins, Phys. Rev. A **40**, 2128 (1989).
[24] C. C. Martens, R. L. Waterland, and W. P. Reinhardt, J. Chem. Phys. **90**, 2328 (1989).
[25] B. Eckhardt and D. Wintgen, J. Phys. B **23**, 355 (1990).
[26] K. T. Hansen, Phys. Rev. E **51**, 1838 (1995).
[27] R. E. Langer, Phys. Rev. **51**, 669 (1937).
[28] P. Cvitanović and B. Eckhardt, Phys. Rev. Lett. **63**, 823 (1989).

Chapitre 3

Milieux désordonnés et effets non-linéaires

3.1 Cadre général

L'étude de la propagation d'ondes dans les milieux désordonnés est un sujet de recherche actif depuis une centaine d'années environ. Si la motivation première a été d'ordre astrophysique, les concepts et outils qui ont été développés ont eu depuis des applications dans bien d'autres domaines de la physique (optique, acoustique, sismologie, conduction électronique, imagerie médicale, *etc*). Pendant longtemps on a cru que la moyenne sur le désordre détruisait *tous* les effets d'interférence. Sous cette hypothèse de phase aléatoire, le transport est alors décrit à l'échelle mésoscopique par une succession de diffusions espacées par une propagation dans un milieu moyen (théorie du transfert radiatif) . Cette marche au hasard induit, dans les cas les plus simples, un processus de diffusion à l'échelle macroscopique.

En 1958, dans le contexte du transport électronique, Anderson a réfuté cette hypothèse en mettant théoriquement en évidence la possibilité d'une transition métal-isolant induite par le désordre, c'est à dire la suppression complète du transport diffusif par effet d'interférences destructives (localisation forte). Vingt ans plus tard, l'hypothèse du 'scaling' montrait que le transport dans les systèmes 1D et 2D se faisaient toujours en régime localisé, alors qu'à 3D il fallait franchir un certain seuil de désordre pour pouvoir atteindre le régime de localisation forte (critère de Ioffe-Regel). Durant toutes ces années, il est également apparu que certaines interférences survivent au désordre et altèrent le transport même loin du régime localisé. C'est le cas en particulier de l'interférence associée aux ondes partielles se propageant en sens opposé le long de *boucles* de diffusion. Ces interférences conduisent à des effets macroscopiques observables comme la réduction interférentielle de la constante de diffusion (localisation faible), les fluctuations universelles de conductance et le phénomène de rétro-diffusion cohérente.

Dans ce type d'expériences, les atomes froids jouent le rôle de diffuseurs pour de la lumière éclairant le nuage, qui forme un milieu complexe et désordonné. Les effets de diffusion multiple peuvent se voir par exemple sur les propriétés de la lumière diffusée vers l'arrière : la rétro-diffusion cohérente. On l'observe quand on éclaire un échantillon diffuseur épais par une lumière cohérente (laser) : l'intensité moyenne réfléchie présente un pic centré dans la direction arrière. Ce pic est dû à l'interférence qui existe entre ondes partielles se propageant en sens opposé le long des chemins de diffusion multiple. Néanmoins ces prédictions sont faites sur la base d'approximations fortes (diffuseurs ponctuels et immobiles), qui ne sont pas nécessairement valides dans le cas d'atomes froids. L'enjeu de ce thème de recherche est donc de comprendre dans quelle mesure sont modifiées les propriétés de la lumière diffusée. Les atomes peuvent être des diffuseurs très résonants avec des sections efficaces énormes par rapport à leur taille, ce qui augmente considérablement les effets de diffusion et donc paraît favorable à la localisation. Mais l'atome est un objet quantique qui ne peut être décrit comme un diffuseur classique, car la diffusion d'un seul photon modifie notablement son état interne et externe. Ce problème avait été clarifié, au cours de leur thèse, conjointement par T .Jonckheere (LKB) et C. Müller (LOD, Nice) qui, en utilisant les symétries du système ont montré le rôle essentiel de la structure interne des atomes. L'effet de rétrodiffusion cohérente calculé pour des atomes froids correspond

d'ailleurs bien à l'observation expérimentale effectuée dans le groupe de C. Miniatura et R. Kaiser à Sophia-Antipolis.

Les résultats numériques (facteur d'amplification, forme du cône...) avaient été obtenus en utilisant des calculs du types monte-carlo. Or, dans la géométrie particulière du milieu semi-infini, il est possible de calculer analytiquement les résultats, par la méthode de Wiener-Hopf. Cette méthode se base sur des propriétés d'analyticité des équations du transfert radiatif, et avait déjà été employée dans le cas des diffuseurs dipolaires classiques. À partir des résultats théoriques développés dans la thèse de C. Müller, qui tient compte explicitement de la structure interne des diffuseurs atomiques (sous-niveaux Zeeman dégénérés), j'ai pu mettre en évidence le changement qualitatif des propriétés dans le plan complexe des différentes fonctions en jeu : les pôles deviennent des singularités essentielles entraînant la présence de coupures. De là, j'ai montré comment il était possible d'appliquer la méthode de Wiener-Hopf pour obtenir les différentes quantités physiques[1]. Les résultats sont en parfait accord avec les simulations numériques, en particulier cela a permis de confirmer et calibrer les estimations des erreurs inhérentes à la méthode monte-carlo. Cela permet ainsi, lors des comparaisons avec les résultats expérimentaux, de préciser si les déviations observées sont pertinentes ou non.

Tous ces travaux supposent l'hypothèse d'un faisceau lumineux incident faible, (i.e. ne saturant pas la transition atomique), ce qui permet d'utiliser des méthodes perturbatives pour calculer les propriétés de la lumière diffusée. Or, une autre différence fondamentale entre un diffuseur classique et un atome est la possibilité d'observer facilement des effets non-linéaires de la réponse atomique à un faisceau lumineux intense : l'intensité de la lumière diffusée n'est plus proportionelle à la lumière incidente. De plus, la fréquence de la lumière diffusée n'est plus nécessairement conservée puisque la saturation (via les 'fluctuations du vide') induit de la *diffusion inélastique*. De manière intuitive, on s'attend à ce que la diffusion inélastique réduit les effets d'interférence en diffusion multiple. Et en effet, une réduction de la hauteur du cône de rétrodiffusion a été mise en évidence dans l'expérience. Cependant, l'absence d'une description théorique appropriée ne permet pas de comprendre quantitativement la dépendance du signal interférentiel en fonction des paramètres du système (paramètre de saturation s et désaccord laser δ). En d'autres termes, le mécanisme physique à l'origine de cette perte de cohérence de phase n'était pas bien compris.

Au-delà, l'enjeu est de comprendre et de décrire les effets ondulatoires sur le transport dans les milieux désordonnés et non-linéaires. A cause des fluctuations locales de speckle, il n'est pas du tout évident que le transfert radiatif puisse être décrit par une équation intégrale fermée, comme c'est le cas du régime linéaire. De plus, ces fluctuations induisent des fluctuations fortes de l'indice de réfraction du milieu qu'il faut savoir prendre en compte pour une description correcte de la propagation moyenne entre deux événements de diffusion. D'autres phénomènes complexes d'optique non linéaire (d'ordinaire étudiés dans les milieux homogènes) devraient se manifester, comme le mélange à quatre ondes, la

[1]Evidemment, je ne vais pas détailler la méthode utilisée, même si, personnellement, je trouve ça extrêmement élégant...

génération d'harmoniques, l'auto-focalisation et la filamentation, la formation de structures spatiales, instabilités temporelles, *etc.* Leur impact sur le transport et les corrections interférentielles au transport est tout simplement inconnu à ce jour. Il faut noter que ces phénomènes non-linéaires concernent également les effets de localisation observés dans des expériences faites à l'aide de condensats de Bose-Einstein dans des potentiels lumineux aléatoires (speckle). Enfin, dans le cas de milieux amplificateurs, la compréhension de ces effets non-linéaires sont importants pour obtenir une meilleure description qualitative et quantitative des lasers aléatoires.

3.2 Approche perturbative

La première approche possible consiste à étendre l'approche diagrammatique au delà du cas linéaire en incluant les évènements où deux photons peuvent être diffusés simultanément par un atome. L'avantage de cette approche est de donner une interprétation simple de la diminution de la sur-intensité observée dans la direction arrière ; lorsque l'on envoie deux photons sur deux atomes, deux diagrammes contribuent au champ diffusé vers l'arrière, dans un cas (fig. 3.1, à droite) les deux photons laser sont d'abord diffusés inélastiquement par l'atome 1, puis un des deux photons inélastiques est diffusé par l'atome 2 ; dans l'autre cas (fig. 3.1, à gauche) un des photons laser est d'abord diffusé élastiquement par l'atome 2, puis est diffusé inélastiquement avec l'autre photon sur l'atome 1 (voir figure 3.1). La différence entre ces deux diagrammes est la donc fréquence du photon "intermédiaire" (spectre inélastique dans le premier cas, fréquence du laser dans le deuxième), ce qui fait que les amplitudes associées, a_1 et a_2, sont, a priori, différentes. L'intensité totale étant donnée par $|a_1 + a_2|^2 = |a_1|^2 + |a_2|^2 + 2\Re(a_1 a_2^*)$, le déséquilibre entre les deux amplitudes empêche l'égalité entre le terme direct $|a_1|^2 + |a_2|^2$ et croisé $2\Re(a_1 a_2^*)$. On voit donc le rôle primordial joué à la fois par le spectre inélastique et la réponse atomique[2].

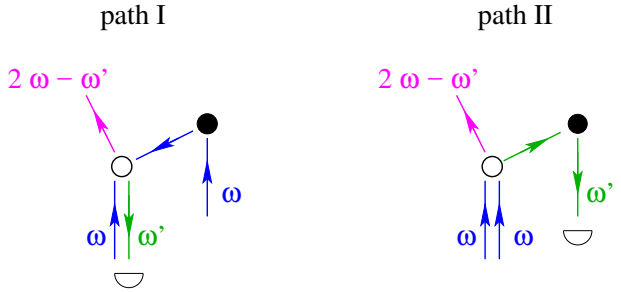

FIG. 3.1 –

L'approche précédente peut-être étendue au cas d'un milieu désordonné composé d'un nombre quelconque d'atomes. La seule restriction importante est de se limiter au régime perturbatif de la diffusion à deux photons pour lequel un chemin de diffusion multiple possède *au plus* un événement de diffusion inélastique et un nombre quelconque de diffusions linéaires. Ainsi, nous restreignons notre étude aux processus montrés dans la fig. 3.2. Ceci est justifié lorsque $sb^2 \ll 1$, où b est l'épaisseur optique du milieu. Le traitement théorique de cette situation exige de combiner la matrice de diffusion à deux photons avec les techniques habituelles de la théorie du transfert radiatif linéaire. Un ingrédient important à ne pas oublier est évidemment l'interférence qui existe entre paires de chemins parcourus en sens *inverse* et qui explique les phénomènes de rétro-diffusion cohérente et de localisation faible.

Or l'ajout *d'un seul* événement de diffusion à deux photons n'est absolument pas anodin. La non linéarité transforme les *paires* de chemins renversés en *triplets*, voir fig. 3.2.

[2]T. Wellens, B. Grémaud, D. Delande and C. Miniatura, "Coherent backscattering of light by two atoms in the saturated regime", Phys. Rev. A **70**, 023817 (2004)

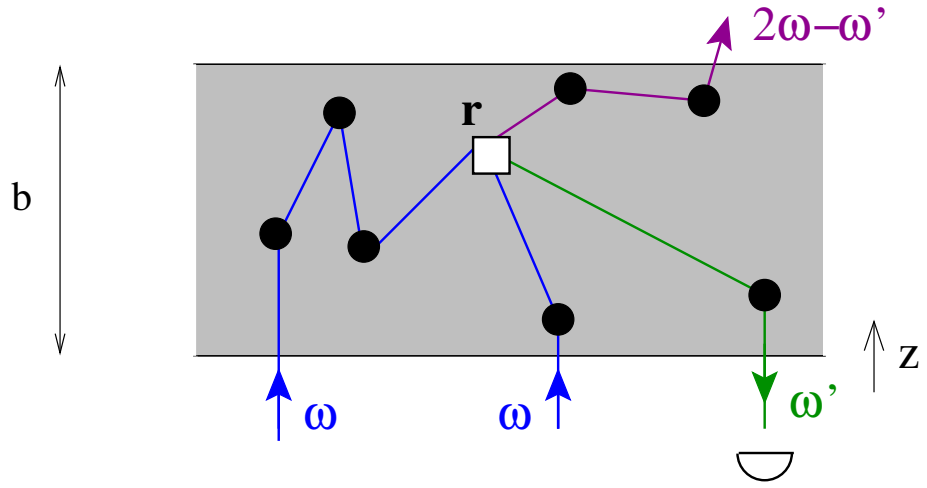

FIG. 3.2 – Diagrammes de diffusion représentant la rétro-diffusion de la lumière par un milieu désordonné dans le régime de faible non linéarité, avec au plus un événement de diffusion à deux photons (□) et un nombre quelconque des diffusions à un photon (•) par chemin de diffusion. Dans ce régime, il y a en général *trois* amplitudes différentes dont l'interférence contribue au signal interférentiel.

Cette interférence à trois amplitudes existe aussi bien pour la *diffusion* non linéaire (décrite par une section efficace non linéaire) que pour la *propagation* non linéaire (décrite par l'indice non linéaire du milieu effectif dans lequel se propage le photon entre les événements de diffusion). Ainsi la hauteur du cône de rétro-diffusion peut *en principe* atteindre la valeur maximale 3 tandis que la valeur 2 n'est jamais dépassée dans le cas linéaire. Bien que cet effet se manifeste dans n'importe quel milieu désordonné présentant une non linéarité de type $\chi^{(3)}$, il n'avait jamais été correctement décrit dans la littérature sur le sujet, antérieure à nos articles[3]. Ces résultats ont été confirmés en les confrontant à des calculs numériques dans un modèle de non-linéarité de type $\chi^{(3)}$ purement élastique. Dans ce cas, pour une configuration fixe (mais aléatoire) des diffuseurs, on se ramène à la résolution d'un systèmes d'équations non-linéaires où les inconnues sont les valeurs du champ électromagnétique à la position de chaque diffuseur. J'ai mis au point des programmes basés sur des méthodes du type Newton-Krylov pour résoudre de manière efficace et rapide ces équations. On résout typiquement un système de quelques milliers d'équations non-linéaires couplées en quelques minutes sur une station de travail. De ces solutions, on déduit l'intensité émise dans toutes les directions par ces atomes. En réitérant la procédure pour d'autres configurations, on peut ainsi obtenir les valeurs moyennées sur le désordre. En particulier, nous avons pu montrer la pertinence des différents diagrammes impliqués dans soit dans la diffusion (voir figure 3.3), soit dans la propagation (voir figure 3.4)[4].

[3] T. Wellens, B. Grémaud, D. Delande et C. Miniatura, "Coherent Backscattering of Light by Nonlinear Scatterers", Phys. Rev. E **71**, R055603-(1-4) (2005)

[4] T. Wellens and B. Grémaud, "Observation of coherent backscattering 'factor three' in a numerical experiment" J. Phys. B : At. Mol. Opt. Phys. **39** (2006) 4719-4731

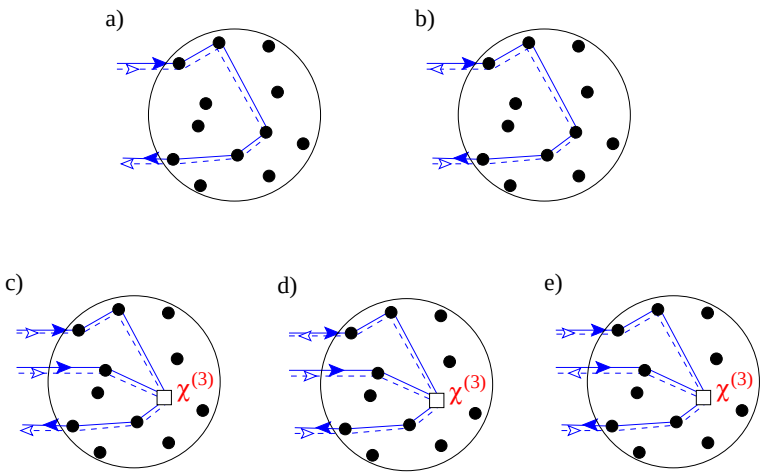

FIG. 3.3 – Diagrammes de diffusion représentant les différentes contribution à la rétro-diffusion de la lumière par un milieu désordonné. Dans un milieu linéaire usuel, pour chaque diagramme "Ladder" (a), correspondant à l'intensité moyenne diffusée, il correspond un diagramme "Crossed" (b) donnant la surintensité dans la direction arrière. Au contraire, dans le régime de faible non linéarité, c'est-à-dire, avec au plus un événement de diffusion à deux photons (□) et un nombre quelconque des diffusions à un photon (•) par chemin de diffusion, pour chaque diagramme "Ladder" (c), il existe deux diagrammes "crossed" (d) et (e).

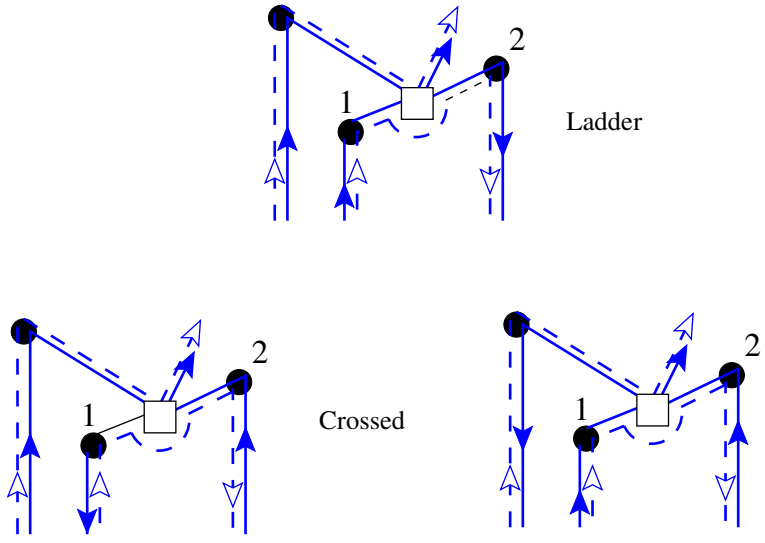

FIG. 3.4 – Diagrammes de diffusion représentant les différentes contribution à la rétro-diffusion de la lumière résultant de la modification de l'indice de réfraction due à la non-linéarité (effet Kerr). Ici encore, pour chaque diagramme "Ladder" (en haut), il existe deux diagrammes "crossed" (en bas).

Il convient toutefois de signaler que cette prédiction du 'facteur 3' ne s'applique qu'à la contribution *non linéaire* du signal de détection. Finalement, une amplification de la rétrodiffusion par rapport au cas linéaire n'apparaît que pour un milieu à non linéarité 'positive' pour lequel la section efficace *augmente* quand s augmente. Un tel milieu pourrait être produit en utilisant des diffuseurs plongés dans un milieu à absorption saturable. Malheureusement, dans notre milieu atomique, la non linéarité est 'négative' (la section efficace *diminue* quand s augmente). Dans ce cas, l'effet global d'interférence à trois amplitudes est de réduire le cône de rétrodiffusion. Pour pouvoir observer un contraste supérieur à 2 dans un milieu atomique, il faut d'abord exclure, par filtrage adéquat, la contribution élastique du signal de rétro-diffusion. La prise en compte précise, dans le calcul du signal, de la polarisation des photons diffusés montre alors qu'on obtient dans ce cas un contraste égal à 2.5 au lieu de 3, donc bien au-delà de la borne supérieure linéaire[5].

[5]T. Wellens, B. Grémaud, D. Delande et C. Miniatura, "Coherent Backscattering of Light with Nonlinear Atomic Scatterers", Phys. Rev. A **73**, 013802-(1-17) (2006)

3.3 Approche non-perturbative, régime stable

3.3.1 cas simple : deux atomes dans le vide

Pour aller au-delà des faibles non-linéarités, les méthodes basées sur les équations de type Bloch-optique semblaient bien adaptées. L'idée était la suivante : traiter de manière non-linéaire la propagation du laser incident dans le milieu atomique, puis d'en déduire à l'aide des équations de Bloch-optique les susceptibilités non-linéaires. De là, on déduit l'indice effectif du milieu pour les champs multiplement diffusés. En fait cette approche s'est révélée insuffisante notamment parce que de cette façon on n'obtient que les susceptibilités à la fréquence du laser incident. Or, des atomes dont la transition atomique est saturée émettent également un spectre inélastique (triplet de Mollow), qui se propage également dans le milieu. La bonne approche consiste à travailler, non plus avec les équations de Bloch-optique, mais avec les équations de Langevin qui décrivent entièrement les opérateurs atomiques couplés à la fois aux champs incidents et aux fluctuations quantiques (les équations de Bloch-optique étant déduites des équations de Langevin par moyennage sur les fluctuations quantiques). On obtient ainsi facilement à la fois la réponse atomique à toutes les fréquences et les parties inélastiques du spectre.

Une autre difficulté est survenue quand on a voulu comparer, dans le cas de deux atomes sans milieu, les résultats donnés par les équations de bloch-optique à deux atomes et ceux donnés par l'approche Langevin. Dans l'hypothèse de milieu dilué (distance entre atomes très grande devant la longueur d'onde optique), l'approche naïve consisterait à supposer que les fluctuations quantiques pour chaque atome sont totalement décorrélées. En fait, même si ces corrélations sont très faibles, de l'ordre de $1/kd$, où d est la distance entre les deux atomes) elles sont du même ordre de grandeur que le champ rayonné par un atome vers l'autre. Elles ne peuvent donc pas être négligées. Plus précisément, j'ai montré comment les prendre en compte de manière exacte pour retrouver les résultats donnés par les équations de Bloch-optique[6] dans le cas d'une transition $J_g = 0 \rightarrow J_e = 1$. Une grande différence avec le cas linéaire tient donc dans le fait que, même en milieu dilué, on ne peut plus considérer les atomes individuellement pour calculer le champ et l'intensité diffusés : du fait des non-linéarités, il s'établit des corrélations quantiques entre les atomes.

Avec cette méthode, on a ainsi pu mettre en évidence le rôle fondamental joué par le spectre inélastique (voir figure 3.5). Les courbes montrent le spectre inélastique (triplet de Mollow) de l'intensité rayonnée collectivement par les deux atomes. La courbe noire correspond à la partie isotrope (Ladder term), tandis que la courbe rouge correspond à la partie dépendant de l'angle entre la direction d'observation et celle du laser incident (Crossed term). Cette dernière est à l'origine de l'augmentation d'intensité dans la direction arrière : la rétrodiffusion cohérente. La fréquence du laser correspond à $\Delta = 0$ et les pointillés vert dénotent la fréquence de résonance de la transition. Les quatre figures correspondent aux valeurs suivantes de la saturation et du désaccord : a) $s = 0.02, \quad \delta = \omega_L - \omega_0 = 0$, b)

[6] B. Grémaud, T. Wellens, D. Delande et C. Miniatura, "Coherent backscattering in nonlinear atomic media : Quantum Langevin approach", Phys. Rev. A 74, 033808 (2006)

$s = 2, \quad \delta = 0$, c) $s = 0.02, \quad \delta = 5\Gamma$ et d) $s = 50, \quad \delta = 0$. Si l'on compare a) et c), pour lesquels la valeur de la saturation est la même, on voit immédiatement que le spectre inélastique est dominé par les photons émis à la fréquence de la résonance atomique et que la symétrie du triplet de Mollow émis par un atome unique est profondément modifiée. On comprend bien dans ce cas que la partie inélastique du terme Crossed va être bien plus faible que celle du terme Ladder. Il s'ensuit que le facteur de sur-intensité dans la direction arrière est nettement diminué dans le cas c) : 1.67 au lieu du facteur 2.

3.3.2 Cas d'un milieu atomique

Le but ultime serait de combiner les effets non-linéaires atomiques (incluant les effets inélastiques et les corrélations quantiques) dans les méthodes diagrammatiques développées plus haut. Ce travail est toujours en cours, la difficulté principale venant en fait des corrélations quantiques. Néanmoins, si on se limite à des diffuseurs "classiques" (i.e. pour lesquels on néglige les effets quantiques en ne prenant en compte que la partie élastique), on a pu étendre les méthodes diagrammatiques à la fois pour une non-linéarité arbitrairement grande (i.e., incluant tous les ordres $\chi^{(n)}$) et pour un nombre quelconque d'évènements non-linéaires. L'idée est que dans le régime de localisation faible, d'une part, on peut toujours séparer les évènements de diffusion et la propagation et, d'autre part, les effets d'interférences restent des corrections par rapport à l'intensité moyenne dans le milieu. Dans ce cas, le calcul du cône de rétrodiffusion cohérente se fait en deux étapes.

Dans un premier temps, on écrit une théorie du transport radiatif non-linéaire, c'est-à-dire décrivant l'intensité lumineuse, moyennée sur le désordre, à l'intérieur d'un nuage de diffuseurs non-linéaires. Dans cette approche, la description du milieu se fait à l'aide de grandeurs locales (libre parcours moyen, section efficace de diffusion) qui dépendent de manière non-linéaire de l'intensité. Comme en chaque point, le champ est simplement la somme du champ entrant et de tout ce qui est rayonné par le reste du milieu, on se ramène ainsi à une description auto-consistante de l'intensité en chaque point. Un point important est de tenir compte proprement du caractère aléatoire du champ diffusé, c'est-à-dire que localement, il présente des fluctuations gaussienne caractéristiques d'un speckle. Par exemple, comme le libre parcours moyen $\ell(I)$ en un point dépend de manière non-linéaire l'intensité I en ce point, la valeur moyenne (i.e. sur les différentes réalisations du speckle) du libre parcours moyen $\langle \ell(I) \rangle$ en ce point est très différente de la valeur $\ell(\langle I \rangle)$. En pratique, on obtient alors un système d'équations non-linéaires couplées pour l'intensité cohérente et l'intensité diffuse en chaque point du milieu. La figure 3.6 montre la comparaison entre cette théorie effective et le résultat des simulations de type brute-force (i.e. calcul du champ pour chaque configuration aléatoire des diffuseurs et moyennage sur différentes configurations). La situation (figure de gauche) correspond à un nuage de diffuseurs éclairés par une onde plane et la figure de droite montre différentes quantités calculées dans le milieu le long de l'axe du nuage (-1 correspond à la face d'entrée et +1 à la face de sortie). Le paramètre de saturation est 0.5. Les courbes continues verte et bleue correspondent aux simulations numériques (1500 diffuseurs, 5000 configurations

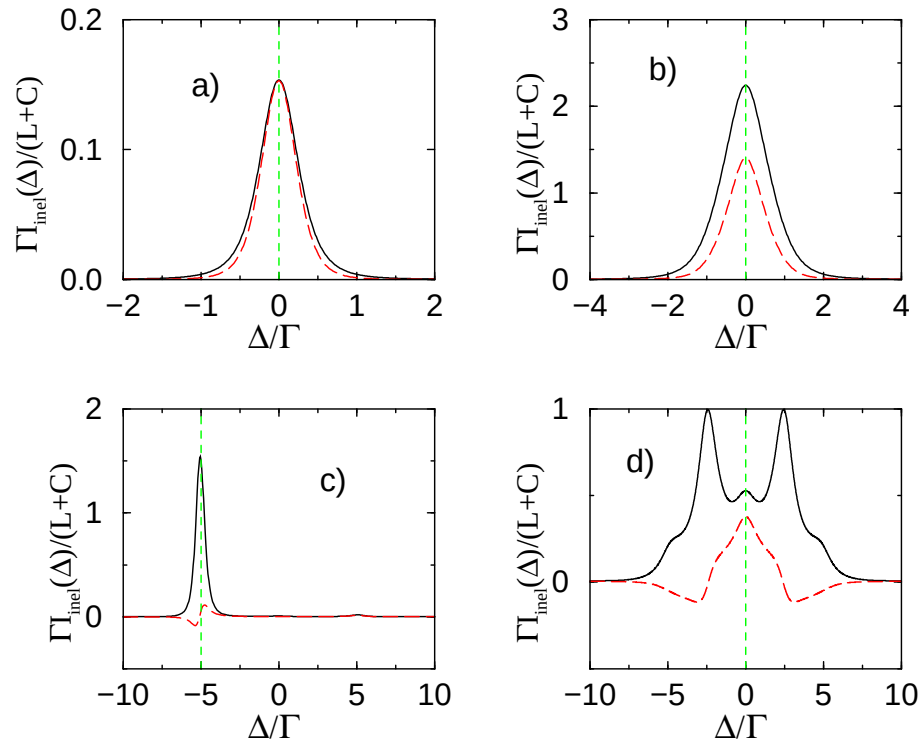

FIG. 3.5 – Les courbes montrent le spectre inélastique (triplet de Mollow) de l'intensité rayonnée collectivement par les deux atomes. La courbe noire correspond à la partie isotrope (Ladder term), tandis que la courbe rouge correspond à la partie dépendant de l'angle entre la direction d'observation et celle du laser incident (Crossed term). Cette dernière est à l'origine de l'augmentation d'intensité dans la direction arrière : la rétrodiffusion cohérente. La fréquence du laser correspond à $\Delta = 0$ et les pointillés vert dénotent la fréquence de résonance de la transition. Les quatre figures correspondent aux valeurs suivantes de la saturation et du désaccord : a) $s = 0.02, \quad \delta = \omega_L - \omega_0 = 0$, b) $s = 2, \quad \delta = 0$, c) $s = 0.02, \quad \delta = 5\Gamma$ et d) $s = 50, \quad \delta = 0$. Si l'on compare a) et c), pour lesquels la valeur de la saturation est la même, on voit immédiatement que le spectre inélastique est dominé par les photons émis à la fréquence de la résonance atomique et que la symétrie du triplet de Mollow émis par un atome unique est profondément modifiée. On comprend bien dans ce cas que la partie inélastique du terme Crossed va être bien plus faible que celle du terme Ladder. Il s'ensuit que le facteur de sur-intensité dans la direction arrière est nettement diminué dans le cas c) : 1.67 au lieu du facteur 2.

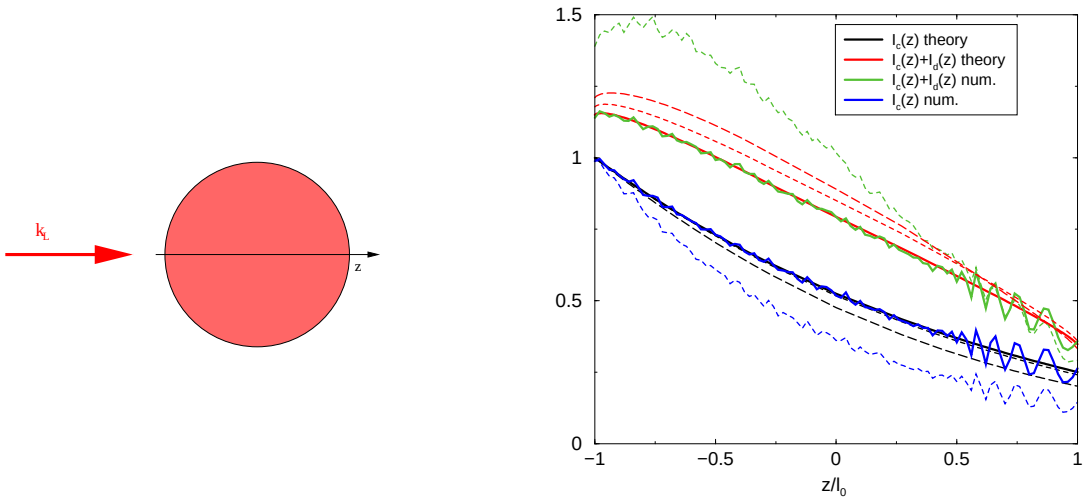

FIG. 3.6 – Comparaison entre la théorie effective et le résultat des simulations de type brute-force (i.e. calcul du champ pour chaque configuration aléatoire des diffuseurs et moyennage sur différentes configurations). La situation (figure de gauche) correspond à un nuage de diffuseurs éclairés par une onde plane et la figure de droite montre différentes quantités calculées dans le milieu le long de l'axe du nuage (-1 correspond à la face d'entrée et +1 à la face de sortie). Le paramètre de saturation est 0.5. Les courbes continues verte et bleue correspondent aux simulations numériques (1500 diffuseurs, 5000 configurations différentes). La courbe bleue est l'intensité cohérente ($| < E > |^2$) tandis que la courbe verte est l'intensité totale ($< |E|^2 >$). Les courbes noires et rouges sont le résultat de la théorie auto-consistante. On voit que l'accord est très bon, alors que l'on est déjà dans un régime fortement non-perturbatif (le résultat linéaire est donné par les courbes tiretées bleues et vertes). Les courbes tiretées court noires et rouges montrent les mêmes résultats si on n'avait pas pris en compte le caractère aléatoire du champ local.

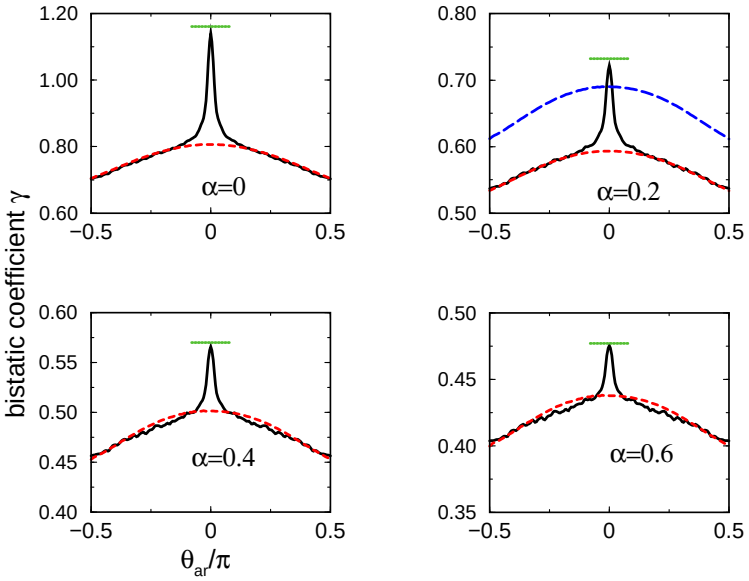

FIG. 3.7 – Cônes de rétrodiffusion non-linéaire obtenus par calcul numérique exact comparés à la théorie effective pour différentes valeurs de la non-linéarité α. La ligne pleine donne les résultats exacts, la ligne tiretée donne l'intensité moyenne "Ladder" rayonnée dans la direction θ ($\theta = 0$ correspondant à la direction de rétrodiffusion). La ligne ligne pointillée donne l'intensité totale dans la direction arrière (i.e. "Ladder"+"Crossed"). La courbe supplémentaire pour $\alpha = 0.2$ correspond à l'intensité moyenne obtenue sans prendre en compte le caractère aléatoire (i.e. du speckle) du champ diffus.

différentes). La courbe bleue est l'intensité cohérente ($| < E > |^2$) tandis que la courbe verte est l'intensité totale ($< |E|^2 >$). Les courbes noires et rouges sont le résultat de la théorie auto-consistante. On voit que l'accord est très bon, alors que l'on est déjà dans un régime fortement non-perturbatif (le résultat linéaire est donné par les courbes tiretées bleues et vertes). Les courbes tiretées court noires et rouges montrent les mêmes résultats si on n'avait pas pris en compte le caractère aléatoire du champ local. L'effet est important, ce qui renforce la solidité de notre description effective.

Dans un deuxième temps, on peut calculer les corrections de localisation faible à cette intensité moyenne. Du fait du caractère non-linéaire du milieu, il y a un plus grand nombre de blocs élémentaires permettant de calculer les termes du type "crossed". De plus, on a pu montrer que l'on ne peut pas enchaîner ces blocs de manière arbitraire, certaines combinaisons sont interdites car ne correspondant pas à des processus physiques[7]. Le résultat est montré par la figure 3.7.

En conclusion, il faut noter que l'approche développée ne s'applique pas seulement au cas des diffuseurs ponctuels non-linéaires, mais aussi au cas de diffuseurs linéaires dans un milieu homogène non-linéaire et également aux ondes de matières dans des potentiels

[7]T. Wellens and B. Grémaud, "Nonlinear coherent transport of waves in disordered media", Phys. Rev. Lett. **100** 033902 (2008)

désordonnés. Dans ce dernier cas, l'interaction entre atomes, dans une approche type champ moyen (équation de Gross-Pitaesvskii), donne lieu à un terme non-linéaire.

3.4 Régimes instables

3.4.1 Instabilités de speckle

Pour des milieux homogènes avec une non-linéarité du type $\chi^{(3)}$, à l'intérieur d'une cavité, on peut observer des effets de multistabilité dus à la coexistence de plusieurs solutions pour l'intensité à l'intérieure de la cavité pour une même intensité entrante. Ce même genre de phénomène a été prédit dans le cas de diffuseurs linéaires plongés dans milieu non-linéaire. Le rôle des miroirs est alors assumé par la diffusion multiple qui permet des chemins extrêmement longs à l'intérieur du milieu.

On s'attend également au même type de comportement dans le cas de diffuseurs ponctuels non-linéaires. Néanmoins, si on garde le modèle "classique" atomique, on n'observe pas de multistabilité, ce que l'on peut relier au fait qu'un atome à deux niveaux dont la transition est saturée devient un très mauvais diffuseur : on dégrade la qualité des miroirs de la cavité faite par la diffusion multiple. On a donc considéré un autre type de non-linéarité décrite par déphasage non-linéaire, i.e. le dipôle induit s'écrit

$$-i\frac{e^{i\delta(|E|^2)}-1}{2}E \text{ avec } \delta(I) = 2\delta_0 + \alpha I$$

Dans ce cas, on peut observer de la multistabilité, comme le montre la figure 3.8. Ces résultats proviennent de la résolution d'un système couplé de N équations (complexes) non-linéaires où N est le nombre de diffuseurs, les inconnues étant le champ sur chaque diffuseur :

$$\mathbf{F}(\mathbf{X}, \alpha) = \mathbf{0} \text{ où } \mathbf{X} = (E_1, E_2, \cdots, E_N)$$

A chaque point de rebroussement (voir figure 3.9), les quantités $\frac{\partial \mathbf{X}_i}{\partial \alpha}$ sont infinies. Or, le long de la solution on a :

$$\mathbf{M}\frac{\partial \mathbf{X}}{\partial \alpha} + \frac{\partial \mathbf{F}}{\partial \alpha} = 0 \text{ avec } \mathbf{M} = \frac{\partial \mathbf{F}}{\partial \mathbf{X}}$$

Comme $\frac{\partial \mathbf{F}}{\partial \alpha}$ est finie, on déduit donc que la matrice M a nécessairement une valeur propre nulle. C'est bien ce que l'on voit sur la figure 3.10 qui montre l'évolution du module de la plus petite valeur propre de M en fonction de α.

Pour savoir si la solution stationnaire est instable, il faut considérer la dynamique autour de cette solution. Pour cela, on modélise la dynamique du système comme il suit :

$$E_i(t) = E_i^{\text{in}} - \sum_{j \neq i} \frac{e^{ikr_{ij}}}{kr_{ij}} d_j(t)$$

$$\dot{d}_j = -\Gamma \left(d_j(t) - (-i\frac{e^{i\delta(|E_j|^2)}-1}{2}E_j) \right)$$

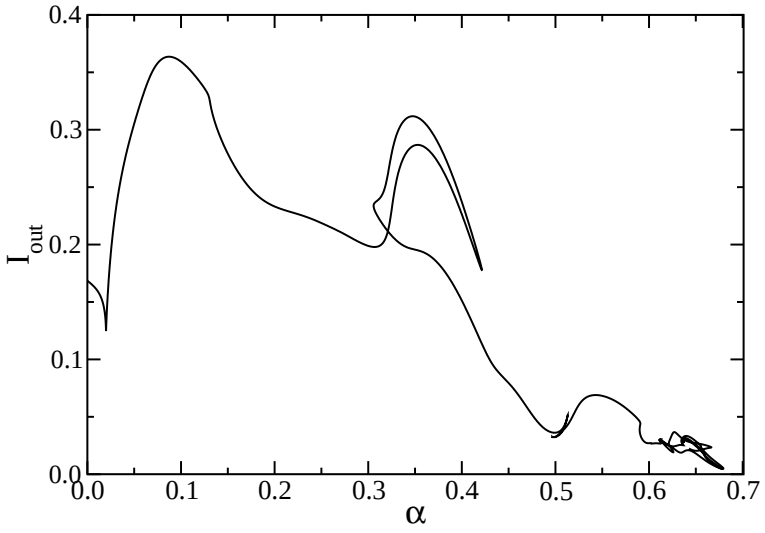

FIG. 3.8 – Intensité diffusé vers l'arrière par un ensemble de diffuseurs ponctuels non-linéaires en fonction de la non-linéarité α, l'intensité entrante étant normalisée à 1. On voit très clairement la présence de solutions multiples au-delà d'un certain seuil. Pour des raisons pratiques, on ne montre qu'une partie de la courbe. Paramètres : 1000 atomes, densité : $n\lambda^3 = 1$.

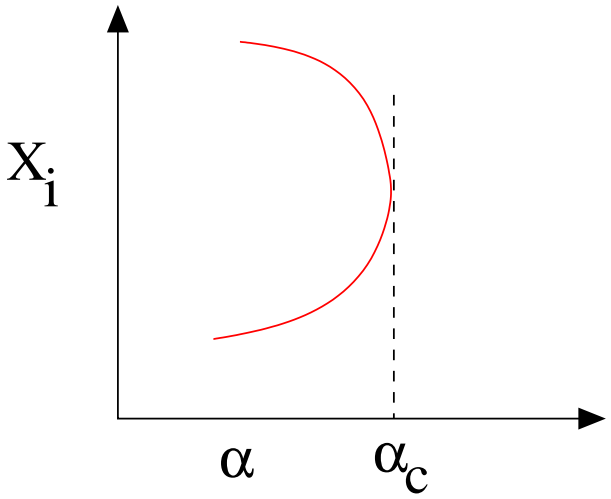

FIG. 3.9 – Point de rebroussement en α_c, engendrant une multistabilité pour les valeurs de α inférieures. Au point de rebroussement, la matrice jacobienne $\frac{\partial \mathbf{F}}{\partial \mathbf{X}}$ a nécessairement une valeur propre nulle.

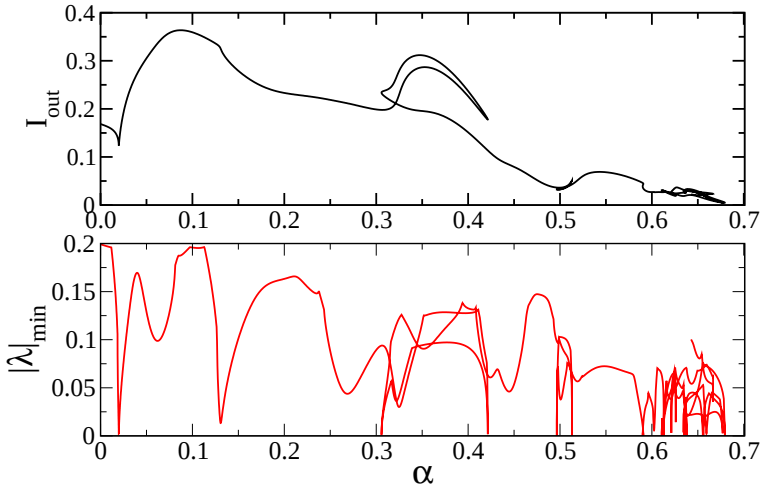

FIG. 3.10 – En haut : intensité rayonnée vers l'arrière par un ensemble diffuseurs ponctuels en fonction de la force de la non-linéarité α. A chaque point de rebroussement, une des valeurs propres de la matrice jacobienne M s'annule, comme le montre la figure du bas, montrant le plus petit module des valeurs propres de M.

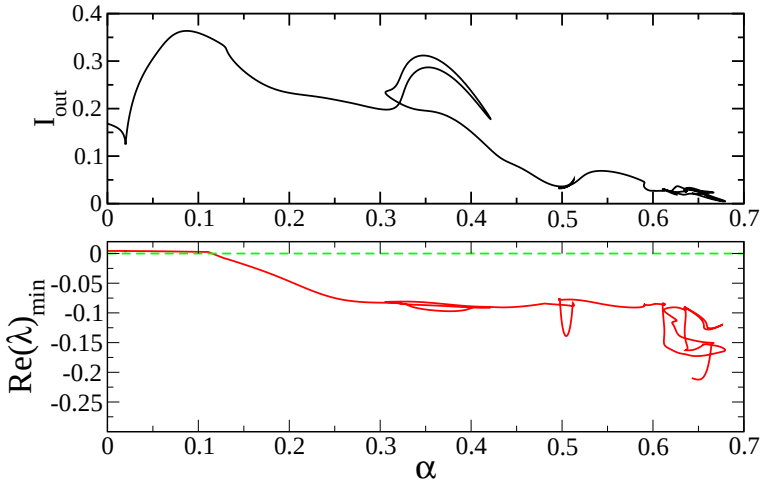

FIG. 3.11 – En haut : intensité rayonnée vers l'arrière par un ensemble diffuseurs ponctuels en fonction de la force de la non-linéarité α. En bas : plus petite partie réelle des valeurs propres de M. Une partie réelle négative indique une solution stationnaire instable.

$1/\Gamma$ donne le temps typique de réponse du dipôle. Dans ce cas, on voit que les écarts $x_i = E_i(t) - E_i^{\text{st}}$ à la solution stationnaire sont gouvernés par l'équation linéaire :

$$\dot{x}_i = -\Gamma \sum_j \frac{\partial F_i}{\partial X_j} x_i(t)$$

et donc que la solution est stable si toutes les valeurs propres λ_i de M ont une partie réelle positive. La figure 3.11 montre l'évolution de la plus petite partie réelle des valeurs propres

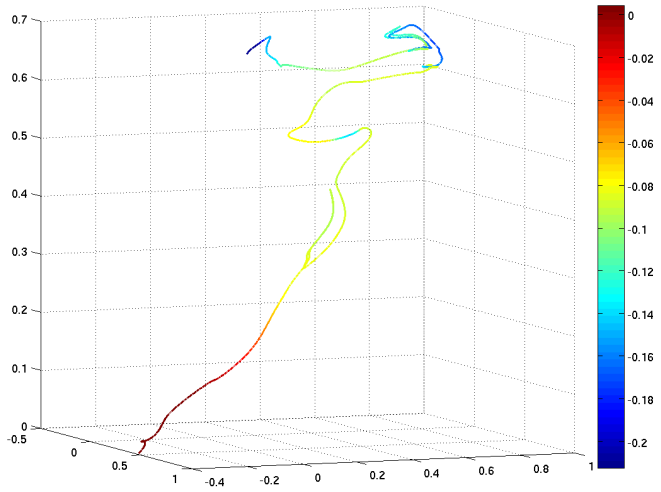

FIG. 3.12 – Evolution du champ $(Re(E), Im(E))$ sur un des diffuseurs en fonction de la non-linéarité (axe vertical), la couleur indique de degré d'instabilité. On voit que pour $\alpha \approx 0.7$, le nombre de solutions coexistantes s'est accru et sont toutes instables. On peut raisonnablement penser que la figure de speckle à cette non-linéarité est instable et qu'on va plutôt observer un comportement fluctuant

de M, en fonction de α. La figure 3.12 montre l'évolution du champ $(Re(E), Im(E))$ sur un des diffuseurs en fonction de la non-linéarité (axe vertical), la couleur indique de degré d'instabilité. On voit que pour $\alpha \approx 0.7$, le nombre de solutions coexistantes s'est accru et sont toutes instables. On peut raisonnablement penser que la figure de speckle à cette non-linéarité est instable et qu'on va plutôt observer un comportement fluctuant (voir plus loin).

Pour chaque configuration, on peut donc estimer le seuil d'instabilité et regarder ensuite la distribution de probabilité de ces seuils. La figure 3.13 montre, en fonction de α, le nombre de configurations dont le seuil d'instabilité est plus petit que α. Chaque configuration comporte 1000 diffuseurs pour une densité $n\lambda^3 = 1$. En comparant ces statistiques pour différentes valeurs de la densité et du nombre d'atomes (et donc de l'épaisseur optique b du milieu), on observe une loi d'échelle : la distribution ne dépend que du produit $N \times n\lambda^3$ soit encore $b^3 \times k\ell_0$ où ℓ_0 est le libre parcours moyen linéaire (voir figure 3.14). Cette loi d'échelle est différente de celle prédite pour des diffuseurs linéaires dans un milieu non-linéaire homogène : $b^2 \times (b + k\ell_0)$. Ceci est probablement dû au fait que, dans le cas présent, la non-linéarité est corrélée au désordre local. Finalement, on peut s'intéresser à la dépendance de quantités en fonction du paramètre $b^3 \times k\ell_0$. Pour le seuil moyen, la figure 3.15 montre très clairement une variation linéaire : $\langle \alpha_{\text{seuil}} \rangle \simeq (b^3 \times k\ell_0)^{-1}$.

C'est un résultat surprenant puisque si l'on fixe l'épaisseur optique b, le seuil moyen diminue quand on augmente $k\ell$, c'est-à-dire si on diminue la force du désordre. Bien sûr,

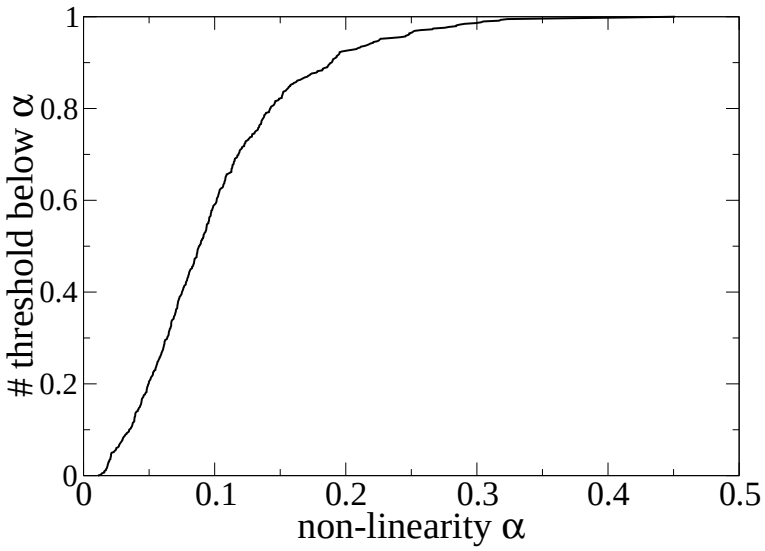

FIG. 3.13 – Nombre de configurations dont le seuil d'instabilité est plus petit que α. 1000 diffuseurs, $n\lambda^3 = 1$, $b \approx 4$

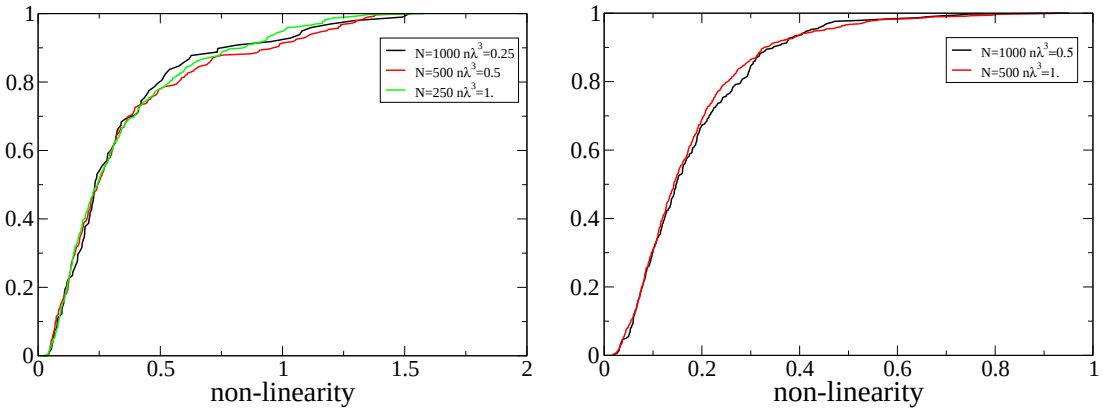

FIG. 3.14 – Nombre de configurations dont le seuil d'instabilité est plus petit que α pour différentes valeurs de la densité et de l'épaisseur optique. On observe une loi d'échelle : la distribution ne dépend que du produit $N \times n\lambda^3$ soit encore $b^3 \times k\ell_0$ où ℓ_0 est le libre parcours moyen linéaire

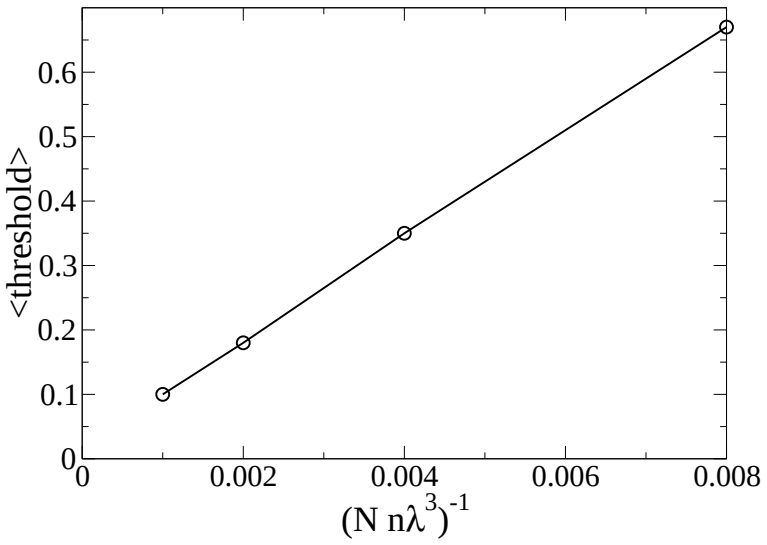

FIG. 3.15 – Valeur moyenne du seuil d'instabilité en fonction de $(b^3 \times k\ell_0)^{-1}$. La courbe semble clairement montrer un comportement linéaire.

si on diminue la force du désordre, on doit augmenter la taille physique du système (i.e. le nombre diffuseurs) pour obtenir la même épaisseur optique. Néanmoins, ceci tend à montrer que ces instabilités résultent de phénomènes interférentiels et impliquent donc la structure sous-jacente des modes du champ dans le nuage. Dans cet esprit, on peut imaginer que le mode pour lequel les effets non-linéaires sont les plus importants est celui qui est le plus localisé, c'est-à-dire dont la largeur est la plus faible. Pour des petites valeurs de la non-linéarité, on peut supposer avoir une bonne idée de la physique en regardant les propriétés du système linéaire. On s'est donc intéressé aux distributions statistiques de la largeur Γ^s du mode le plus localisé pour $\alpha = 0$. Le résultat est donné par la figure 3.16. On retrouve clairement la loi d'échelle en $p = N \times n\lambda^3$, ce qui tend à corroborer l'idée que c'est le mode le plus localisé qui devient instable et démontre l'importance des effets des interférences dans les instabilités de speckle. De plus, une analyse (rapide) de la dépendance de la moyenne de ces largeurs donne $< 1/\Gamma^s > \propto N^{2/3}(n\lambda^3)^{2/3}$, à comparer au temps de Thouless (i.e. le temps caractéristique que met un photon pour diffuser hors du nuage) qui ne croît qu'en b^2, c'est-à-dire $N^{2/3}(n\lambda^3)^{4/3}$.

On peut alors se poser la question des effets de ces instabilités sur les effets cohérents comme le cône de rétrodiffusion cohérente. La figure 3.17 montre, pour une même configuration (1000 diffuseurs, $n\lambda^3 = 1$), l'évolution temporelle de l'intensité diffusée vers l'arrière et pour différente valeurs de la non-linéarité. On évolue clairement d'un régime stationnaire dans le cas linéaire ($\alpha = 0$) vers un régime probablement chaotique ($\alpha = 1$) en passant par un régime instable, mais périodique. On remarquera que cette figure est cohérente avec la figure 3.13, puisque pour $\alpha = 0.3$, on prédit que la plupart des configurations sont instables. Néanmoins, quand on moyenne sur un nombre important de configurations, on retrouve un effet cohérent vers l'arrière comme le montre la figures 3.18 : on trace en fonction du temps

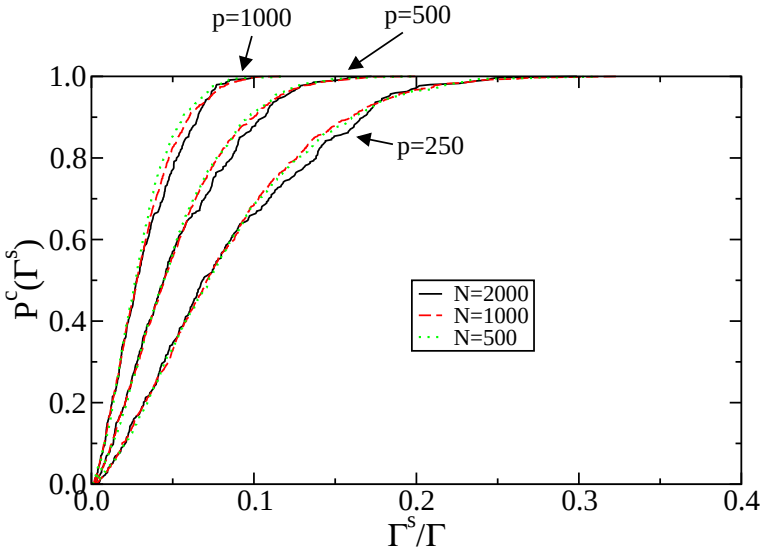

FIG. 3.16 – Distribution statistiques de la largeur Γ^s du mode le plus localisé. On retrouve bien la loi d'échelle en $p = N \times n\lambda^3$. De plus, on trouve que la valeur moyenne $< 1/\Gamma^s >$ évolue comme $N^{2/3}(n\lambda^3)^{2/3}$, à comparer au temps de Thouless $\propto b^2 = N^{2/3}(n\lambda^3)^{4/3}$.

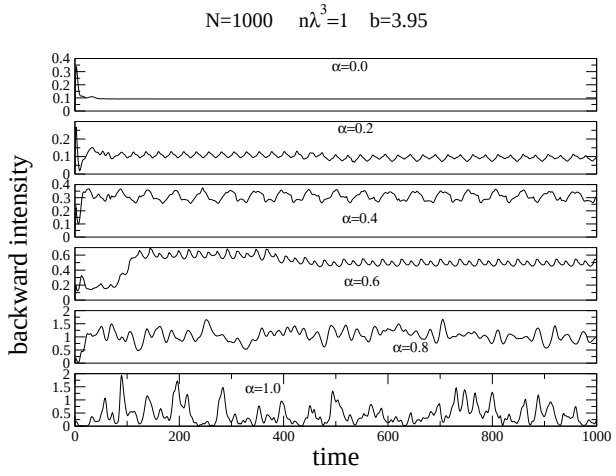

FIG. 3.17 – Intensité rayonnée vers l'arrière par un ensemble de diffuseurs non-linéaires en fonction du temps et pour différentes valeurs de la non-linéarité. On évolue clairement d'un régime stationnaire dans le cas linéaire ($\alpha = 0$) vers un régime probablement chaotique ($\alpha = 1$) en passant par un régime instable, mais périodique

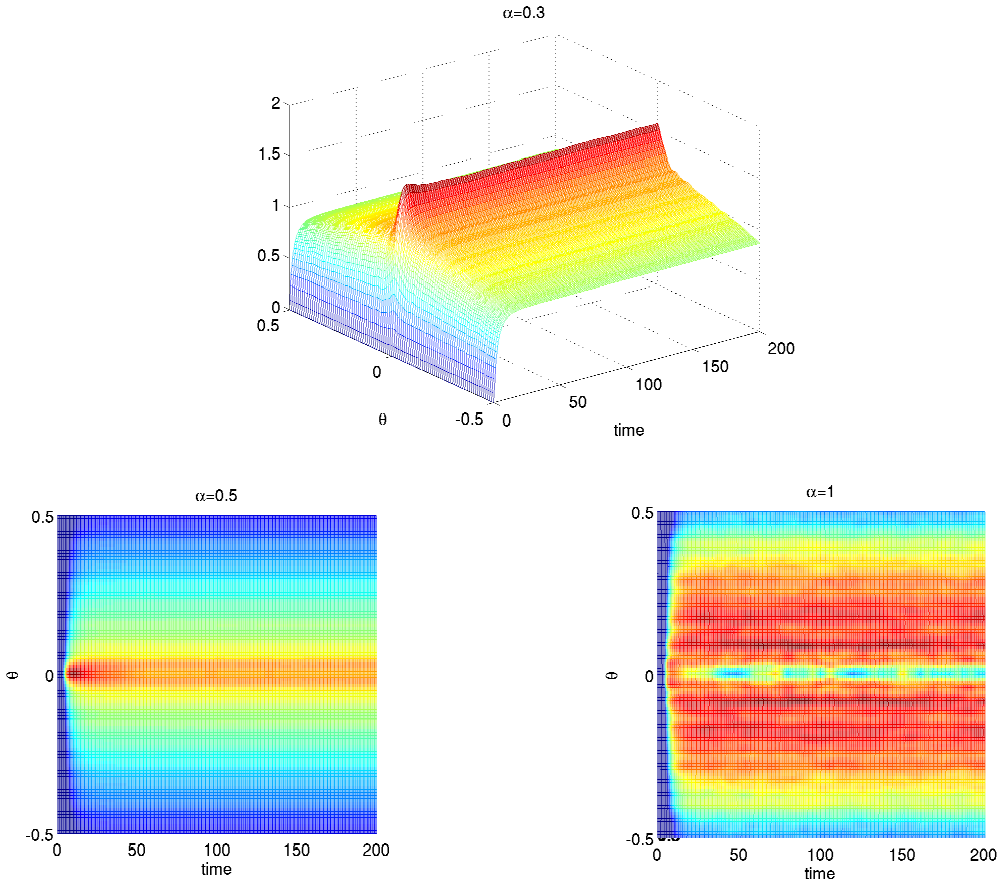

FIG. 3.18 – Intensité rayonnée dans la direction θ ($\theta = 0$ correspondant à la rétrodiffusion) en fonction du temps. L'intensité a été moyennée sur 1000 configurations différentes. Non seulement dans le régime instable (figure du haut $\alpha = 0.3$ et figure en bas à gauche $\alpha = 0.5$), mais aussi dans le régime chaotique (figure en bas à droite $\alpha = 1$), il reste un effet cohérent vers l'arrière.

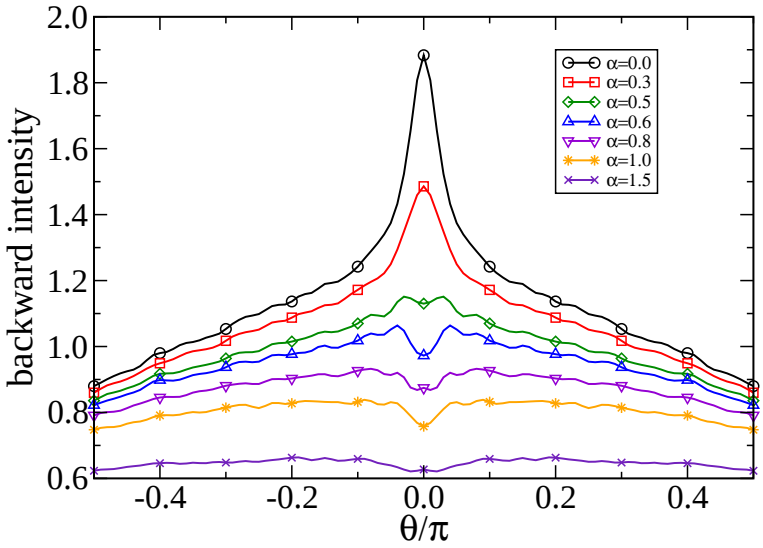

FIG. 3.19 – Intensité rayonnée dans la direction θ ($\theta = 0$ correspondant à la rétrodiffusion) au temps $200\Gamma^{-1}$. L'intensité a été moyennée sur 1000 configurations différentes. Même dans le régime chaotique $\alpha \gtrsim 0.8$, il reste un effet cohérent vers l'arrière. Le fait que le cône s'inverse vient du fait de la non-linéarité, produit un déphasage entre les deux chemins du "crossed" qui produit une interférence destructive.

l'intensité diffusée dans la direction θ par rapport à la direction arrière. Si on se reporte à la figure 3.13 et 3.17, on se rend compte que non seulement dans le régime instable (figure du haut $\alpha = 0.3$ et figure en bas à gauche $\alpha = 0.5$), mais aussi dans le régime chaotique (figure en bas à droite $\alpha = 1$), il reste un effet cohérent vers l'arrière. Cet effet est résumé par la figure 3.19, qui montre l'intensité diffusé vers l'arrière au temps $t = 1000\Gamma^{-1}$. Le fait que le cône s'inverse vient du fait de la non-linéarité, produit un déphasage entre les deux chemins du "crossed" qui produit une interférence destructive. Ce genre de comportement est prédit qualitativement par notre approche diagrammatique (voir plus haut) et a également été observé dans des calculs numériques de condensat de Bose-Einstein (2D) dans des potentiels aléatoires.

3.4.2 Laser aléatoires

Enfin, dans le cas de milieu actifs, le phénomène du laser aléatoire ou encore laser sans cavité est maintenant bien établi expérimentalement. Au niveau théorique, il reste de nombreuses questions ouvertes : dans le régime de la localisation faible pour lequel il n'y a plus, en moyenne, de modes localisés, quelle est la structure sous-jacente du mode du laser ? Au-dessus du seuil, quelle est la dynamique du système ? Peut-on prédire les modes du laser à partir des modes de la cavité passive (i.e. les modes de la diffusion multiple) ? Quelle est leur statistique ? La question de savoir si on pourrait observer cet effet avec des atomes froids (à deux ou trois niveaux) fait également partie des questions ouvertes. A titre d'exemple, voici les résultats de simulations numériques dans le cas de nuages d'atomes à trois niveaux, dans le régime de localisation forte. La figure 3.20 montre le spectre de la lumière émise par 250 atomes. A gauche pour $n\lambda^3 = 30$ et à droite pour $n\lambda^3 = 40$. Les deux figures du haut sont dans le régime non-lasant. On voit néanmoins des pics correspondants aux modes localisés au milieu de la la lorenztienne donnant l'émission spontanée. Les deux figures du bas sont dans le régime laser au-dessus du seuil. A gauche, on voit bien qu'il y a déjà plusieurs modes en compétition, tandis qu'à droite un seul mode semble dominer. La transition laser est clairement montrée par la figure 3.21, montrant l'évolution du spectre (en échelle logarithmique) en fonction delà puissance de pompe W. On voit bien la transition juste au-dessus de $W = 1$, puis l'apparition de nouveaux pics. Enfin la figure 3.22 montre le nombre de seuils laser plus petit que W. Bien sûr tous ces résultats sont préliminaires et nécessitent une étude plus approfondie pour en faire ressortir les propriétés importantes, non seulement statiques (seuils) mais aussi dynamiques (compétition de modes).

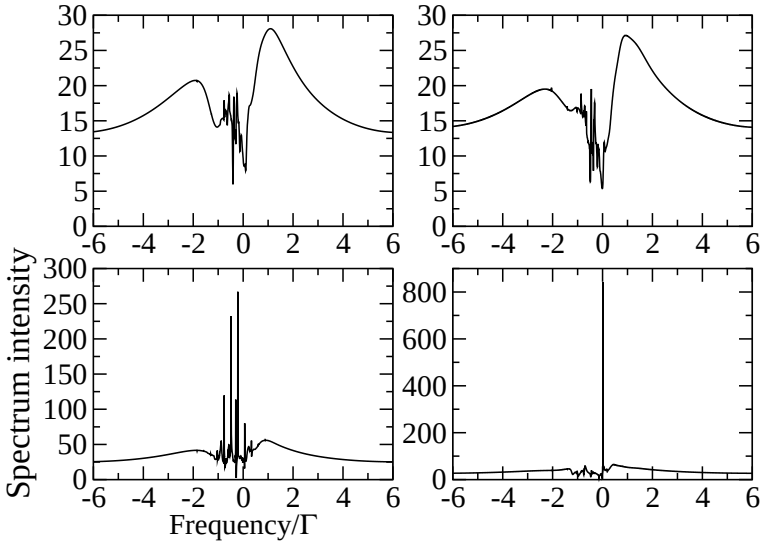

FIG. 3.20 – Spectre de la lumière émise par 250 atomes à trois niveaux. A gauche pour $n\lambda^3 = 30$ et à droite pour $n\lambda^3 = 40$. Les deux figures du haut sont dans le régime non-lasant. On voit néanmoins des pics correspondants aux modes localisés au milieu de la la lorenztienne donnant l'émission spontanée. Les deux figures du bas sont dans le régime laser au-dessus du seuil. A gauche, on voit bien qu'il y a plusieurs modes en compétition, tandis qu'à droite un seul mode semble dominer.

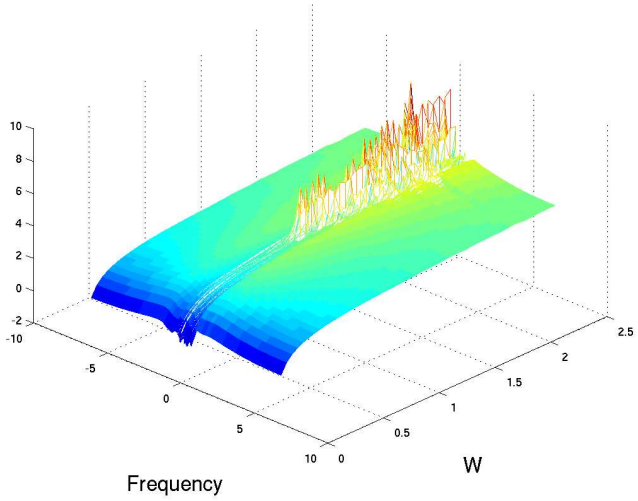

FIG. 3.21 – Spectre (en échelle logarithmique) de la lumière émise par 250 atomes à trois niveaux en fonction de la puissance de pompe W. On voit bien la transition laser juste au-dessus de $W = 1$, puis l'apparition de nouveaux pics.

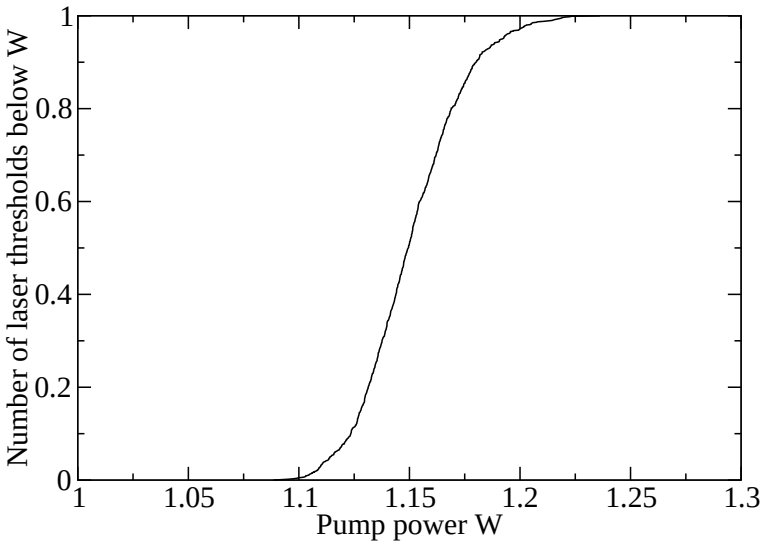

FIG. 3.22 – Exemple de distribution statistique des seuils de transition laser.

3.5 Sélection d'articles

Coherent backscattering of light by two atoms in the saturated regime

T. Wellens,[1,2] B. Grémaud,[2] D. Delande,[2] and C. Miniatura[1]
[1]*Institut Non Linéaire de Nice, 1361 route des Lucioles, F-06560 Valbonne, France*
[2]*Laboratoire Kastler Brossel, Université Pierre et Marie Curie, 4 Place Jussieu, F-75005 Paris, France*
(Received 23 February 2004; published 26 August 2004)

We present a calculation of coherent backscattering with inelastic scattering by saturated atoms. We consider the scattering of a quasimonochromatic laser pulse by two distant atoms in free space. By restricting ourselves to scattering of two photons, we employ a perturbative approach, valid up to second order in the incident laser intensity. The backscattering enhancement factor is found to be smaller than two (after excluding single scattering), indicating a loss of coherence between the doubly scattered light emitted by both atoms. Since the undetected photon carries information about the path of the detected photon, the coherence loss can be explained by a which-path argument, in analogy with a double-slit experiment.

DOI: 10.1103/PhysRevA.70.023817 PACS number(s): 42.50.Ar, 32.80.−t

I. INTRODUCTION

Weak localization of light in random media was demonstrated for the first time in the 1980s [1–3]. Here, constructive interference between two waves which interact with the same particles, but in reversed order, enhances, in average, scattering in the direction opposite to the incident light. For systems obeying the reciprocity symmetry [4], the *backscattering enhancement factor*, i.e., the light intensity detected in exact backscattering direction divided by the background intensity, is exactly two, provided single scattering can be neglected. If the reversed paths are not linked by the reciprocity symmetry, however, the enhancement factor will be strictly smaller than two. This is known to occur, e.g., when detecting the backscattered light with linear polarization orthogonal to the initial one, in the presence of a magnetic field leading to a rotation of the polarization (Faraday effect), or in the case of a random motion of the scatterers [5–9].

Similar interference effects between multiply scattered waves also affect the properties of transport through disordered media. If the mean free path can be sufficiently reduced, the transport is even expected to come to a complete standstill [10]. In experiments on strong localization of light [11], however, the role of absorption is discussed controversially [12,13].

One may wonder whether a medium consisting of individual atoms would constitute a good candidate for strong localization. In contrast to the classical scenario (Maxwell's equations in a medium with random dielectric constant), the quantum-mechanical atom-photon interaction exhibits some characteristic features, which may affect the coherence between multiply scattered waves. First, the resonance may be extremely sharp, corresponding to a very narrow linewidth Γ of the excited state. On the one hand, this leads to a large atom-photon scattering cross section and slow diffusion of light [14], properties in favor of localization. On the other hand, it implies that the atoms have to be cooled to very low temperatures. Only if the Doppler shift induced by a moving atom is much smaller than Γ, the interference between two counterpropagating waves is preserved [15]. Typically, this regime is reached at about a few mK, which is, however, still high enough to neglect the thermal de-Broglie wavelength of the atoms, i.e., to treat their external motion classically. Furthermore, atoms usually have an internal quantum structure, which may have a strong impact on coherent backscattering [16–19]. If necessary, this can be circumvented by using atoms with a nondegenerate ground state ($J=0$) [20].

Another property of the atom-light interaction, whose impact on coherent backscattering has so far remained almost unexplored, is the strongly nonlinear response of an atom to incoming radiation. Since already a single photon is sufficient to bring the atom to the excited state, where it rests for quite a long time Γ^{-1} without being able to scatter other photons, a saturation of the atomic medium can be induced already with rather moderate laser intensities. Not only the atom-photon cross section, but also the spectrum of the light is affected by saturation. With increasing saturation, it becomes more and more probable that an atom scatters inelastically, i.e., that it emits photons at a frequency different from the one of the incident laser. As we will show in this paper, this implies a loss of coherence between two reversed scattering paths. Similarly, a recent experiment showed coherent backscattering by a cloud of cold strontium atoms to be reduced when increasing the saturation induced by the probe laser [21].

In order to expose the physical mechanism responsible for the loss of coherence as clearly as possible, we will consider in this paper two two-level atoms in free space, the simplest system exhibiting coherent backscattering. Effects which arise in the presence of a larger number of atoms, such as the nonlinear index of refraction of an atomic medium, will be relegated to future publications. With view at the experiment [21] performed with a dilute medium, we are interested in the case where the distance r_{12} between the two atoms is *much* larger than the optical wavelength λ. In this regime, both atoms exchange at most one photon, quite contrary to the "Dicke limit" $r_{12} \ll \lambda$, where, due to recurrent exchange of photons, the atoms may form collective states, leading to super- or subradiance [22,23]. Nevertheless, collective effects, such as coherent backscattering, are also observed in the dilute limit $r_{12} \gg \lambda$, provided that the single scattering contribution (arising from two independent atoms) is filtered

out by using a suitable polarization channel (see Sec. III B). In contrast to the case of two independently radiating atoms [24,25], we will see that the *doubly* scattered light emitted by both atoms remains partially coherent even in the presence of inelastic scattering. Moreover, the ensuing constructive interference in backscattering direction occurs independently of the positions of the atoms.

To calculate the photodetection signal of the light emitted by the two atoms, we use scattering theory. Generally, the higher the intensity of the incoming light, the more photons are scattered inelastically. In the present paper, we restrict ourselves to two-photon scattering. Thereby, we employ a perturbative approach, valid up to second order in the incident intensity.

The paper is organized as follows. In Sec. II, we summarize known results about the scattering of two photons by a single atom. After introducing the scattering operator in Sec. II B, we obtain the corresponding photodetection signal in Sec. II C, thereby recovering the resonance fluorescence spectrum in second order of the intensity. In Sec. III, we add a second atom to our model. We proceed in a similar way as in Sec. II, using the results of the single-atom case as a building block of the two-atom solution. After deriving the scattering operator in Sec. III A, we calculate the photodetection signal in Sec. III B. In contrast to the single-atom case, the latter contains interference between the light emitted by the two atoms, enhancing the detection signal in the backscattering direction. In this way, we obtain the main result of the present paper, the backscattering enhancement factor, which is found to be smaller than two, due to inelastic scattering. This fact is interpreted in Sec. III C as a loss of coherence between the light scattered by both atoms in opposite order. Regarding the undetected photon as a path detector for the detected photon, we can explain the loss of coherence by an analogy to the double-slit experiment, where the interference pattern is washed out if we try to observe which slit the particle has passed through. Finally, Sec. III D concludes the paper.

II. SINGLE ATOM

Let us start with discussing the scattering of two photons by a single atom. This is useful since we will assume later that the second atom is far away from the first one. The two-atom scattering process can then be viewed as a succession of two single-atom scattering processes.

A. Approximations and Hamiltonian

We assume a two-level atom located at a fixed position $\mathbf{r}$. As already mentioned above, neglecting the external atomic motion is justified at very low temperatures, where the Doppler shift induced by the atomic motion is small enough. Also the recoil effect, i.e., the change of the atomic velocity when scattering a photon, can be neglected, provided that the number of scattering events is not too large. On the other hand, the temperature should still be high enough such that the external atomic motion need not to be treated quantum mechanically. Furthermore, let us stress that we consider an *undegenerate* atomic ground state ($J=0$). This is important since coherent backscattering may be severely affected by degeneracy [16–19]. The excited state is then threefold degenerate ($J=1$). Which one of the three excited states is populated depends on the polarization of the absorbed photon.

With the approximations mentioned above, our Hamiltonian reads as follows:

$$H = H_0 + V, \tag{1}$$

where

$$H_0 = \tilde{\omega}_{\mathrm{at}}\sigma^\dagger\sigma + \sum_{\mathbf{k},s} \omega_{\mathbf{k}} a^\dagger_{\mathbf{k}s} a_{\mathbf{k}s}, \tag{2}$$

$$V = \sum_{\mathbf{k},s} \left(ige^{i\mathbf{k}\cdot\mathbf{r}}(\sigma^\dagger \boldsymbol{\epsilon}_{\mathbf{k}s}) a_{\mathbf{k}s} - ige^{-i\mathbf{k}\cdot\mathbf{r}}(\sigma \boldsymbol{\epsilon}^*_{\mathbf{k}s}) a^\dagger_{\mathbf{k}s} \right) \tag{3}$$

denote the free evolution and the interaction, respectively (in units where $\hbar=1$). Here, the operators $\sigma^\dagger$ and σ describe transitions between the atomic ground and excited states, with energy difference $\tilde{\omega}_{\mathrm{at}}$ (in the case of an isolated atom), whereas $a^\dagger_{\mathbf{k}s}$ and $a_{\mathbf{k}s}$ create and annihilate a photon in mode $\mathbf{k}$ (a plane wave with wave vector $\mathbf{k}$) and polarization $\boldsymbol{\epsilon}_{\mathbf{k}s}$ (perpendicular to $\mathbf{k}$). The coupling constant

$$g = d\left(\frac{\omega_{\mathbf{k}}}{2\epsilon_0 L^3}\right)^{1/2} \simeq d\left(\frac{\omega_{\mathrm{at}}}{2\epsilon_0 L^3}\right)^{1/2}, \tag{4}$$

with L^3 the quantization volume (which will finally drop out of the equations, when taking the limit $L\to\infty$) and d the magnitude of the atomic dipole, determines the strength of the atom-field coupling.

In Eq. (3), we have employed the so-called "rotating wave approximation": a transition from one of the excited states to the ground state is only possible by emitting a photon, and vice versa by absorption. This is justified since we will restrict ourselves to near-resonant processes, where only photons with frequencies close to the atomic resonance are important (i.e., $|\omega_{\mathbf{k}}-\omega_{\mathrm{at}}| \ll \omega_{\mathrm{at}}$). For the same reason, we may assume a constant value of g in Eq. (4), i.e., neglect its dependence on $\omega_{\mathbf{k}}$.

Due to the coupling to the electromagnetic vacuum, the state $|e\rangle$ is unstable: after an average lifetime given by

$$\Gamma = \frac{d^2\omega_{\mathrm{at}}^3}{3\pi\epsilon_0} = \frac{2g^2\omega_{\mathrm{at}}^2 L^3}{3\pi}, \tag{5}$$

an excited atom decays into the ground state, through spontaneous emission of a photon. This gives rise to an effective, complex atomic resonance frequency

$$\omega_0 = \omega_{\mathrm{at}} - i\frac{\Gamma}{2}, \tag{6}$$

where also the real part ω_{at} is shifted, as compared to the isolated atom, Eq. (2).

B. Scattering matrix

In the following, we make use of scattering theory in order to calculate the properties of the light emitted by the

atoms. Here, the object of interest is the scattering operator S, which connects the initial and final photon states $|i\rangle$ and $|f\rangle$:

$$|f\rangle = S|i\rangle. \tag{7}$$

The initial and final state of the atom is always the ground state $|g\rangle$, which we do not explicitly write in the following. Furthermore, we will restrict ourselves to the scattering of two photons, thereby employing a perturbative approach, valid up to second order in the incident intensity.

Since, as we will see below, the two photons may be scattered independently from each other, we consider first the scattering of a single photon. In order to distinguish between the scattered and nonscattered part of the photon wave packet, the transition operator T_1 is introduced as follows:

$$S_1 = 1 - 2\pi i \delta(\omega_f - \omega_i) T_1, \tag{8}$$

where the δ function implies conservation of the photon's frequency (which follows from energy conservation, since the state of the atom is the same before and after scattering). For one-photon states, its matrix elements read [26]:

$$\langle \mathbf{k}_f \boldsymbol{\epsilon}_f | T_1 | \mathbf{k}_i \boldsymbol{\epsilon}_i \rangle = \frac{g^2}{\omega_i - \omega_0} (\boldsymbol{\epsilon}_i \boldsymbol{\epsilon}_f^*) e^{i(\mathbf{k}_i - \mathbf{k}_f)\mathbf{r}}. \tag{9}$$

The situation changes when considering a second photon. It is convenient to write the matrix elements in the following form:[1]

$$\langle \mathbf{k_3}\boldsymbol{\epsilon}_3, \mathbf{k_4}\boldsymbol{\epsilon}_4 | S_2 | \mathbf{k_1}\boldsymbol{\epsilon}_1, \mathbf{k_2}\boldsymbol{\epsilon}_2 \rangle$$

$$= \langle \mathbf{k_3}\boldsymbol{\epsilon}_3 | S_1 | \mathbf{k_1}\boldsymbol{\epsilon}_1 \rangle \langle \mathbf{k_4}\boldsymbol{\epsilon}_4 | S_1 | \mathbf{k_2}\boldsymbol{\epsilon}_2 \rangle + \langle \mathbf{k_3}\boldsymbol{\epsilon}_3 | S_1 | \mathbf{k_2}\boldsymbol{\epsilon}_2 \rangle \langle \mathbf{k_4}\boldsymbol{\epsilon}_4 | S_1 | \mathbf{k_1}\boldsymbol{\epsilon}_1 \rangle$$
$$+ \langle \mathbf{k_3}\boldsymbol{\epsilon}_3, \mathbf{k_4}\boldsymbol{\epsilon}_4 | T_2 | \mathbf{k_1}\boldsymbol{\epsilon}_1, \mathbf{k_2}\boldsymbol{\epsilon}_2 \rangle. \tag{10}$$

Here, the first two terms scatter the two photons independently from each other. (There are two terms since the photons are indistinguishable: the final photon $|\mathbf{k_3}\boldsymbol{\epsilon}_3\rangle$, for example, may correspond either to the initial photon $|\mathbf{k_1}\boldsymbol{\epsilon}_1\rangle$ or $|\mathbf{k_2}\boldsymbol{\epsilon}_2\rangle$.) Since, however, the atom cannot interact with the second photon while it is excited by the first one, the photons are in fact not completely independent. This gives rise to the second term [27]:

$$\langle \mathbf{k_3}\boldsymbol{\epsilon}_3, \mathbf{k_4}\boldsymbol{\epsilon}_4 | T_2 | \mathbf{k_1}\boldsymbol{\epsilon}_1, \mathbf{k_2}\boldsymbol{\epsilon}_2 \rangle$$
$$= 2\pi i \frac{g^4 \delta(\omega_1 + \omega_2 - \omega_3 - \omega_4)}{(\omega_1 - \omega_0)(\omega_2 - \omega_0)} \left(\frac{1}{\omega_3 - \omega_0} + \frac{1}{\omega_4 - \omega_0} \right)$$
$$\times [(\boldsymbol{\epsilon}_1 \boldsymbol{\epsilon}_3^*)(\boldsymbol{\epsilon}_2 \boldsymbol{\epsilon}_4^*) + (\boldsymbol{\epsilon}_2 \boldsymbol{\epsilon}_3^*)(\boldsymbol{\epsilon}_1 \boldsymbol{\epsilon}_4^*)] e^{i(\mathbf{k}_1 + \mathbf{k}_2 - \mathbf{k}_3 - \mathbf{k}_4)\mathbf{r}}. \tag{11}$$

Although their sum is conserved, the individual frequencies of both photons may be changed by T_2, for that reason we call it "inelastic" scattering.

[1]Equation (10) is valid only if $\mathbf{k}_1\boldsymbol{\epsilon}_1 \neq \mathbf{k}_2\boldsymbol{\epsilon}_2$ and $\mathbf{k}_3\boldsymbol{\epsilon}_3 \neq \mathbf{k}_4\boldsymbol{\epsilon}_4$. We will not consider double occupancy of modes in the following, since it can be neglected in the continuous limit of infinite mode density. In other words: two photons are never exactly in the same mode, although they may be infinitesimally close to each other.

C. Photodetection signal

Given the final photon state $|f\rangle$, the intensity of the photodetection signal, as measured by a broadband detector (polarization $\boldsymbol{\epsilon}_D$) located at $\mathbf{R}$ at time t, reads [26]:

$$I = \langle f | E^{(-)}(\mathbf{R}, t) E^{(+)}(\mathbf{R}, t) | f \rangle. \tag{12}$$

Here, the detection of the photon is described by the electric field operator

$$E^{(+)}(\mathbf{R}, t) = \frac{g}{d} \sum_{\mathbf{k},s} (\boldsymbol{\epsilon}_{\mathbf{k}s} \boldsymbol{\epsilon}_D^*) e^{i(\mathbf{k}\cdot\mathbf{R} - \omega t)} a_{\mathbf{k}s}, \tag{13}$$

which annihilates a photon at position $\mathbf{R}$.

As initial state, we consider a state of N photons

$$|i_N\rangle = \sqrt{N!} \sum_{(\mathbf{k}_1 \cdots \mathbf{k}_N)} h(\mathbf{k}_1) \cdots h(\mathbf{k}_N) |\mathbf{k}_1 \boldsymbol{\epsilon}_L, \ldots, \mathbf{k}_N \boldsymbol{\epsilon}_L\rangle, \tag{14}$$

where all photons are described by the same single-photon wave packet

$$|i_1\rangle = \sum_{\mathbf{k}} h(\mathbf{k}) |\mathbf{k}\boldsymbol{\epsilon}_L\rangle. \tag{15}$$

The factor $\sqrt{N!}$ in Eq. (14) arises from the symmetry under exchange of photons as bosonic particles and is required to obtain the correct normalization

$$\langle i_N | i_N \rangle = N! \sum_{(\mathbf{k}_1 \cdots \mathbf{k}_N)} |h(\mathbf{k}_1)|^2 \cdots |h(\mathbf{k}_N)|^2 = \left(\sum_{\mathbf{k}} |h(\mathbf{k})|^2 \right)^N$$
$$= |\langle i_1 | i_1 \rangle|^N = 1. \tag{16}$$

Since, due to symmetrization, the sum in Eq. (14) does not include permutations of $(\mathbf{k}_1 \cdots \mathbf{k}_N)$, the factor $N!$ is needed for the transformation into N independent sums $\Sigma_{\mathbf{k}_1} \cdots \Sigma_{\mathbf{k}_N}$. We assume that the wave packet describes an almost plane wave, i.e., $h(\mathbf{k})$ is sharply peaked around its center $\mathbf{k}_L$ ("sharply" means much narrower than Γ). For this reason, we may also neglect in Eq. (14) the dependence of the initial polarization vector $\boldsymbol{\epsilon}_L$ on $\mathbf{k}$.

The initial state $|i_N\rangle$ corresponds to the following incident intensity seen by the atom at position $\mathbf{r}$ and time $t=0$, obtained by inserting $|i_N\rangle$ instead of $|f\rangle$ in Eq. (12), and summing over the detector polarization $\boldsymbol{\epsilon}_D$:

$$I_{\text{in}} = N \frac{g^2}{d^2} \left| \sum_{\mathbf{k}} e^{i\mathbf{k}\cdot\mathbf{r}} h(\mathbf{k}) \right|^2. \tag{17}$$

In the following, we will use a dimensionless quantity, the so-called "saturation parameter"

$$s = \frac{2d^2 I_{\text{in}}}{|\omega_L - \omega_0|^2} = \frac{2Ng^2}{|\omega_L - \omega_0|^2} \left| \sum_{\mathbf{k}} e^{i\mathbf{k}\cdot\mathbf{r}} h(\mathbf{k}) \right|^2. \tag{18}$$

It accounts for the fact that photons interact less strongly with the atom if they are far detuned from the atomic resonance (i.e., if $|\omega_L - \omega_0|$ is large). From the solution of the optical Bloch equations [26], it is known that s determines the ratio between inelastic and elastic scattering, see Eq. (38) below.

We are interested in the photodetection signal measured at position $\mathbf{R}$ at time $t = |\mathbf{R} - \mathbf{r}|$ (the time needed for the scattered

light to reach the detector, in units where $c=1$). We assume that the detector is placed far away from the atom, such that $t=|\mathbf{R}-\mathbf{r}|$ is long enough for the scattering approach to be valid. Furthermore, the detector should not be placed in the direction of the initial wave vector $\mathbf{k}_L$, such that only scattered photons are detected [i.e., $E^{(+)}(\mathbf{R},t)|i_1\rangle=0$].

In order to proceed, we have to generalize the scattering operator for two photons, Eq. (10), to the case of N photons. For this purpose, we assume that the saturation parameter s is so small that at most one photon pair is scattered inelastically. This yields the photodetection signal up to second order in s, see below. Summing over the different pairs (i,j), and taking into account all possible permutations of the N photons, we obtain:

$$\begin{aligned}\langle \mathbf{k}_1' \cdots \mathbf{k}_N'|S_N|\mathbf{k}_1 \cdots \mathbf{k}_N\rangle = &\sum_{P_N}\prod_{l=1}^{N}\langle \mathbf{k}_l'|S_1|\mathbf{k}_{P_N(l)}\rangle \\ &+\sum_{\substack{i,j=1\\ i<j}}^{N}\sum_{P_N/P_2}\langle \mathbf{k}_i'\mathbf{k}_j'|T_2|\mathbf{k}_{P_N(i)}\mathbf{k}_{P_N(j)}\rangle \\ &\times\prod_{\substack{l=1\\ l\neq i,j}}^{N}\langle \mathbf{k}_l'|S_1|\mathbf{k}_{P_N(l)}\rangle. \end{aligned} \tag{19}$$

(In the following, we do not write explicitly the polarization vectors.) Equation (19) contains a sum over all permutations P_N of the N indices $\{1\cdots N\}$, modulo a permutation of the two indices $P_N(i)$ and $P_N(j)$ in the second term, where the latter permutation is included in the two-photon operator T_2, see Eq. (11). In the case $N=2$, the above expression agrees with the one of the previous section, Eq. (10). According to Eq. (19), the final photon state $|f_N\rangle=S_N|i_N\rangle$ can be expressed as follows:

$$\begin{aligned}\langle \mathbf{k}_1 \cdots \mathbf{k}_N|f_N\rangle = &\sqrt{N!}\prod_{l=1}^{N}\langle \mathbf{k}_l|f_1\rangle \\ &+\sqrt{\frac{N!}{2}}\sum_{\substack{i,j=1\\ i<j}}^{N}\langle \mathbf{k}_i\mathbf{k}_j|g_2\rangle\prod_{\substack{l=1\\ l\neq i,j}}^{N}\langle \mathbf{k}_l|f_1\rangle, \end{aligned} \tag{20}$$

in terms of the one- and two-photon states

$$|f_1\rangle = S_1|i_1\rangle, \tag{21}$$

$$|g_2\rangle = T_2|i_2\rangle. \tag{22}$$

Following Eq. (12), we now apply the electric field operator on the final photon state. It may annihilate either an elastically or an inelastically scattered photon. Correspondingly, we obtain the following three contributions:

$$|\psi\rangle = E^{(+)}(\mathbf{R},t)|f\rangle = \sum_{i=1}^{3}|\psi_i\rangle, \tag{23}$$

with

$$\langle \mathbf{k}_1 \cdots \mathbf{k}_{N-1}|\psi_1\rangle = \sqrt{N!}E\prod_{l=1}^{N-1}\langle \mathbf{k}_l|f_1\rangle, \tag{24}$$

$$\langle \mathbf{k}_1 \cdots \mathbf{k}_{N-1}|\psi_2\rangle = \sqrt{\frac{N!}{2}}\sum_{i=1}^{N-1}\langle \mathbf{k}_i|g_1\rangle\prod_{\substack{l=1\\ l\neq i}}^{N-1}\langle \mathbf{k}_l|f_1\rangle, \tag{25}$$

$$\langle \mathbf{k}_1 \cdots \mathbf{k}_{N-1}|\psi_3\rangle = \sqrt{\frac{N!}{2}}E\sum_{\substack{i,j=1\\ i<j}}^{N-1}\langle \mathbf{k}_i\mathbf{k}_j|g_2\rangle\prod_{\substack{l=1\\ l\neq i,j}}^{N-1}\langle \mathbf{k}_l|f_1\rangle, \tag{26}$$

and

$$E = \langle 0|E^{(+)}(\mathbf{R},t)|f_1\rangle, \tag{27}$$

$$|g_1\rangle = E^{(+)}(\mathbf{R},t)|g_2\rangle. \tag{28}$$

According to Eq. (12), the norm $I=\langle\psi|\psi\rangle$ gives the total intensity. Let us first concentrate on the contributions from $|\psi_1\rangle$ and $|\psi_2\rangle$. (As we will argue later, $|\psi_3\rangle$ can be neglected.) We obtain a sum of three terms, from elastic and inelastic scattering, and their interference. Using $\langle f_1|f_1\rangle=1$ (since S_1 is unitary), we obtain

$$I_{\mathrm{el}}^{(1)} = \langle\psi_1|\psi_1\rangle = N|E|^2, \tag{29}$$

$$I_{\mathrm{el}}^{(2)} = \langle\psi_1|\psi_2\rangle + \langle\psi_2|\psi_1\rangle = N(N-1)\mathrm{Re}\{\sqrt{2}E\langle g_1|f_1\rangle\}, \tag{30}$$

$$I_{\mathrm{in}} = \langle\psi_2|\psi_2\rangle = \frac{N(N-1)}{2}\langle g_1|g_1\rangle + \frac{N(N-1)(N-2)}{2}|\langle f_1|g_1\rangle|^2. \tag{31}$$

Whereas in $I_{\mathrm{el}}^{(1,2)}$, the frequency of the detected photon is fixed to $\omega=\omega_L$ (since one-photon scattering is elastic), this is not the case for I_{in}, where the overlap $\langle g_1|g_1\rangle$ implies an integral over ω. Thereby, we obtain an elastic and inelastic component of the detection signal.

To complete the calculation, we insert the one- and two-photon scattering matrices given in Sec. II B. Using Eqs. (8) and (9), the final one-photon state reads

$$|f_1\rangle = |i_1\rangle - \frac{2\pi i g^2}{\omega_L-\omega_0}\sum_{\mathbf{k}_i,\mathbf{k}_f\epsilon_f} h(\mathbf{k}_i)\,\delta(\omega_i-\omega_f)(\boldsymbol{\epsilon}_L\boldsymbol{\epsilon}_f^*)e^{i(\mathbf{k}_i-\mathbf{k}_f)\mathbf{r}}|\mathbf{k}_f\boldsymbol{\epsilon}_f\rangle. \tag{32}$$

Since the wave packet $h(\mathbf{k}_i)$ is quasimonochromatic, we may replace the argument of functions which vary slowly (i.e., on the scale of Γ) as a function of ω_i by the constant value ω_L. Applying the electric field operator on $|f_1\rangle$, see Eq. (27), yields, under the assumptions given above:

$$E = \frac{-3\Gamma(\boldsymbol{\epsilon}_L\boldsymbol{\epsilon}_D^*)g}{4\omega_L dR(\omega_L-\omega_0)}\sum_{\mathbf{k}_i} e^{i\mathbf{k}_i\cdot\mathbf{r}}h(\mathbf{k}_i). \tag{33}$$

Similarly, we obtain for the inelastic part, see Eqs. (11), (22), and (28),

$$|g_1\rangle = -2Eg^2 \sum_{\mathbf{k}_i,\mathbf{k}_f\epsilon_f} \frac{\sqrt{2}e^{i(\mathbf{k}_i-\mathbf{k}_f)\mathbf{r}}h(\mathbf{k}_i)(\boldsymbol{\epsilon}_L\boldsymbol{\epsilon}_f^*)}{(\omega_f-\omega_0)(2\omega_L-\omega_f-\omega_0)}|\mathbf{k}_f\boldsymbol{\epsilon}_f\rangle. \tag{34}$$

According to Eqs. (29)–(31), we obtain the following intensity $I=I_{\rm el}^{(1)}+I_{\rm el}^{(2)}+I_{\rm in}$ of the photodetection signal:

$$I_{\rm el}^{(1)} = \eta\frac{s}{2}, \quad I_{\rm el}^{(2)} = -\eta\frac{N-1}{N}s^2, \tag{35}$$

$$I_{\rm in} = \eta\frac{N-1}{N}\frac{s^2}{2} + o(s^3), \tag{36}$$

with the prefactor

$$\eta = \left(\frac{3\Gamma|\boldsymbol{\epsilon}_L\boldsymbol{\epsilon}_D^*|}{4d\omega_L R}\right)^2. \tag{37}$$

The term proportional to $|\langle f_1|g_1\rangle|^2$ in Eq. (31) gives a contribution to the inelastic component in third order of s, which can be neglected. As it should be, for large N—such that the first photon can be absorbed without significantly changing the saturation induced by the remaining $(N-1)$ photons—the above result agrees with the elastic and inelastic components

$$I_{\rm el} = \eta\frac{s}{2(1+s)^2}, \quad I_{\rm in} = \eta\frac{s^2}{2(1+s)^2} \tag{38}$$

of the resonance fluorescence as predicted by the Bloch equations [26], expanded up to second order in s.

However, we have not yet accounted for the third term $|\psi_3\rangle$ in Eq. (23). If we compare Eqs. (20), (24), and (26), we note that $|\psi_1\rangle+|\psi_3\rangle=\sqrt{NE}|f_{N-1}\rangle$, and hence the norm of $|\psi_1\rangle+|\psi_3\rangle$ equals the norm of $|\psi_1\rangle$, Eq. (29), provided that the norm of $|f_{N-1}\rangle$ is 1. Although the latter condition is not necessarily fulfilled if the scattering operator is truncated as in Eq. (19), its unitarity will be recovered when including higher scattering orders. Similarly, it can be shown that contributions from $\langle\psi_2|\psi_3\rangle$—if they are not of third order in s—are exactly canceled by other terms which appear in $\langle\psi_2|\psi_1\rangle$ when including into $\langle\psi_2|$ another inelastically scattered photon pair. Hence the term $|\psi_3\rangle$ does not contribute to the photodetection signal up to second order in the saturation parameter s.

By putting a spectral filter in front of the detector, we can resolve the power spectrum $P(\omega)$ of the detection signal, i.e., the probability of detecting a photon of a definite frequency ω. Since elastic scattering conserves the frequency, the spectrum exhibits a sharp peak at ω_L (almost a δ function for our quasimonochromatic initial wave packet f),

$$P(\omega) = I^{(\rm el)}\delta_f(\omega-\omega_L) + P^{(\rm in)}(\omega), \tag{39}$$

whereas the inelastic component depends smoothly on ω. The latter is proportional to the absolute square of the inelastic transition amplitude, Eq. (11) (with $\omega_1=\omega_2=\omega_L$ the initial frequency, $\omega_3=\omega$ the frequency of the detected photon, and $\omega_4=2\omega_L-\omega$). With the correct normalization,

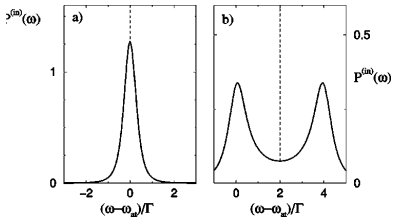

FIG. 1. Inelastic resonance fluorescence spectrum $P^{(\rm in)}(\omega)$ (in units of $I^{(\rm in)}/\Gamma$), Eq. (41), for small saturation, $s\ll 1$, (a) zero detuning $\delta=\omega_L-\omega_{\rm at}=0$, and (b) $\delta=2\Gamma$. The dashed lines indicate the position of the elastic peak at ω_L, see Eq. (39).

$$I^{(\rm in)} = \int d\omega\, P^{(\rm in)}(\omega), \tag{40}$$

we obtain

$$P^{(\rm in)}(\omega) = \frac{\Gamma I^{(\rm in)}}{4\pi}\left|\frac{1}{\omega-\omega_0}+\frac{1}{2\omega_L-\omega-\omega_0}\right|^2. \tag{41}$$

For zero detuning, $\omega_L=\omega_{\rm at}$, the inelastic spectrum consists of a peak of width 0.64Γ, whereas for large detuning $\delta=\omega_L-\omega_{\rm at}$ (i.e., if $4\delta^2\gg\Gamma^2$), there are two peaks of width Γ at $\omega=\omega_L\pm\delta$, see Fig. 1.[2] Note that one of them is centered exactly at the atomic resonance. Evidently, this will be important if we allow the scattered photons to interact with a second atom, as we will do now.

III. TWO ATOMS

A. Scattering matrix

Let us now turn to the case of two atoms alone in vacuum. We assume that the second atom is far away from the first one, compared to the optical wavelength. This means that we may restrict ourselves to processes where at most one of the two photons is scattered by both atoms. As shown in Appendix A, the corresponding scattering matrix can then be obtained in a simple way from the single-atom scattering matrix, see Eqs. (A9) and (A10): apart from the geometrical phase factors $e^{\pm i\mathbf{k}\cdot\mathbf{r}_{1,2}}$ for absorption or emission of a photon $|\mathbf{k}\rangle$ by atom 1 or 2, and the terms depending on the polarization, we only have to take into account the "photon exchange factor"

$$B(\omega) = -\frac{3\Gamma e^{i\omega r_{12}}}{4\omega r_{12}(\omega-\omega_0)}, \tag{42}$$

depending on the frequency ω of the doubly scattered photon. In Eq. (42), we recognize the propagation of a spherical wave from one atom to the other one (inversely proportional to their distance r_{12}), and the amplitude $(\omega-\omega_0)^{-1}$ describing scattering by a single atom, see Eq. (9).

[2]The reader may have in mind that the resonance fluorescence actually exhibits *three* peaks [28]. However, the one at $\omega=\omega_L$ is of higher order in s, since it arises from three-photon scattering.

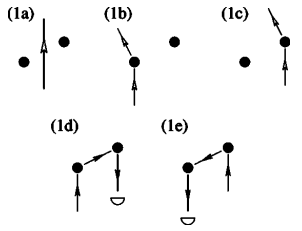

FIG. 2. Scattering of a single photon by two distant atoms. In the coherent backscattering experiment, only the doubly scattered photon is detected, see diagrams (1d) and (1e). Consequently, the diagrams (1a)–(1c), with single or no scattering, describe the undetected photon.

In particular, the structure of the scattering operator as a sum of an elastic single-photon and an inelastic two-photon component is the same as before, compare Eqs. (8) and (10):

$$\langle \mathbf{k_3}\boldsymbol{\epsilon}_3, \mathbf{K_4}\boldsymbol{\epsilon}_4 | S_2^{(2)} | \mathbf{k_1}\boldsymbol{\epsilon}_1, \mathbf{k_2}\boldsymbol{\epsilon}_2 \rangle$$

$$= \langle \mathbf{k_3}\boldsymbol{\epsilon}_3 | S_1^{(2)} | \mathbf{k_1}\boldsymbol{\epsilon}_1 \rangle \langle \mathbf{k_4}\boldsymbol{\epsilon}_4 | S_1^{(2)} | \mathbf{k_2}\boldsymbol{\epsilon}_2 \rangle + \langle \mathbf{k_3}\boldsymbol{\epsilon}_3 | S_1^{(2)} | \mathbf{k_2}\boldsymbol{\epsilon}_2 \rangle$$
$$\times \langle \mathbf{k_4}\boldsymbol{\epsilon}_4 | S_1^{(2)} | \mathbf{k_1}\boldsymbol{\epsilon}_1 \rangle + \langle \mathbf{k_3}\boldsymbol{\epsilon}_3, \mathbf{k_4}\boldsymbol{\epsilon}_4 | T_2^{(2)} | \mathbf{k_1}\boldsymbol{\epsilon}_1, \mathbf{k_2}\boldsymbol{\epsilon}_2 \rangle, \quad (43)$$

where the single-photon component of $S^{(2)}$ contains also the nonscattered wave, see diagram (1a) in Fig. 2:

$$S_1^{(2)} = 1 - 2\pi i \delta(\omega_f - \omega_i) T_1^{(2)}. \quad (44)$$

The remaining single-photon processes are also shown in Fig. 2. The photon may be scattered by only one atom (1 or 2), or by both (first 1, then 2, and vice versa). Correspondingly, the single-photon transition operator reads:

$$\langle \mathbf{k}_f \boldsymbol{\epsilon}_f | T_1^{(2)} | \mathbf{k}_i \boldsymbol{\epsilon}_i \rangle = \frac{g^2}{\omega_i - \omega_0}$$
$$\times \{ e^{i(\mathbf{k}_i - \mathbf{k}_f)\mathbf{r}_1} [(\boldsymbol{\epsilon}_i \boldsymbol{\epsilon}_f^*) + B(\omega_i)$$
$$\times (\boldsymbol{\epsilon}_i \Delta_{12} \boldsymbol{\epsilon}_f^*) e^{i\mathbf{k}_i(\mathbf{r}_2 - \mathbf{r}_1)}] + e^{i(\mathbf{k}_i - \mathbf{k}_f)\mathbf{r}_2} [(\boldsymbol{\epsilon}_i \boldsymbol{\epsilon}_f^*)$$
$$+ B(\omega_i) (\boldsymbol{\epsilon}_i \Delta_{12} \boldsymbol{\epsilon}_f^*) e^{i\mathbf{k}_i(\mathbf{r}_2 - \mathbf{r}_1)}] \}. \quad (45)$$

As mentioned above, for the two double-scattering processes, see diagrams (1d) and (1e) in Fig. 2, we have to multiply the one-atom transition operator $\langle \mathbf{k}_f \boldsymbol{\epsilon}_f | T | \mathbf{k}_i \boldsymbol{\epsilon}_i \rangle$, Eq. (9), with the photon exchange factor $B(\omega_i)$, see Eq. (42), and to adjust the geometrical phase factor. Furthermore, the fact that the photon propagates in the direction $\mathbf{r}_2 - \mathbf{r}_1$ between the two scattering events implies a projection Δ_{12} of the polarization vector onto the plane perpendicular to $\mathbf{r}_2 - \mathbf{r}_1$. Thereby, the term $\boldsymbol{\epsilon}_i \boldsymbol{\epsilon}_f^*$ (for scattering by a single atom) is replaced by $\boldsymbol{\epsilon}_i \Delta_{12} \boldsymbol{\epsilon}_f^*$.

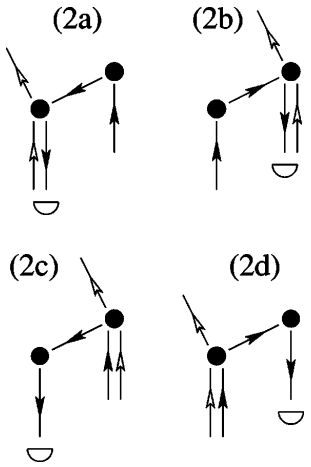

FIG. 3. Inelastic scattering of two photons by two distant atoms. Only the doubly scattered photon (full arrows) is detected. Since the photon frequencies are changed by the inelastic scattering event at the atom where both photons meet, the amplitude of the elastic scattering event at the second atom depends on whether the inelastic scattering occurs before the elastic one [(2c) and (2d)] or after [(2a) and (2b)].

In the case of inelastic two-photon scattering, the doubly scattered photon may be scattered first inelastically (by atom 1 or 2), and then elastically (by the other atom), or vice versa, compare, e.g., the diagrams (2a) and (2d) in Fig. 3. Correspondingly, the frequency to be inserted in the photon exchange factor $B(\omega)$, Eq. (42), is either the final or initial frequency of this photon, see Eq. (A9) or Eq. (A10). In total, we obtain:

$$\langle \mathbf{k}_3 \boldsymbol{\epsilon}_3, \mathbf{k}_4 \boldsymbol{\epsilon}_4 | T_2^{(2)} | \mathbf{k}_1 \boldsymbol{\epsilon}_1, \mathbf{k}_2 \boldsymbol{\epsilon}_2 \rangle = 2\pi i \frac{g^4 \delta(\omega_1 + \omega_2 - \omega_3 - \omega_4)}{(\omega_1 - \omega_0)(\omega_2 - \omega_0)} \left(\frac{1}{\omega_3 - \omega_0} + \frac{1}{\omega_4 - \omega_0} \right)$$
$$\times [e^{i(\mathbf{k}_1 + \mathbf{k}_2 - \mathbf{k}_3 - \mathbf{k}_4)\mathbf{r}_1} \{ (\boldsymbol{\epsilon}_1 \boldsymbol{\epsilon}_3^*)(\boldsymbol{\epsilon}_2 \boldsymbol{\epsilon}_4^*) + B(\omega_1)(\boldsymbol{\epsilon}_1 \Delta_{12} \boldsymbol{\epsilon}_3^*)(\boldsymbol{\epsilon}_2 \boldsymbol{\epsilon}_4^*) e^{i\mathbf{k}_1(\mathbf{r}_2 - \mathbf{r}_1)} + B(\omega_2)(\boldsymbol{\epsilon}_1 \boldsymbol{\epsilon}_3^*)(\boldsymbol{\epsilon}_2 \Delta_{12} \boldsymbol{\epsilon}_4^*) e^{i\mathbf{k}_2(\mathbf{r}_2 - \mathbf{r}_1)}$$
$$+ B(\omega_3)(\boldsymbol{\epsilon}_1 \Delta_{12} \boldsymbol{\epsilon}_3^*)(\boldsymbol{\epsilon}_2 \boldsymbol{\epsilon}_4^*) e^{-i\mathbf{k}_3(\mathbf{r}_2 - \mathbf{r}_1)} + B(\omega_4)(\boldsymbol{\epsilon}_1 \boldsymbol{\epsilon}_3^*)(\boldsymbol{\epsilon}_2 \Delta_{12} \boldsymbol{\epsilon}_4^*) e^{-i\mathbf{k}_4(\mathbf{r}_2 - \mathbf{r}_1)} \}$$
$$+ e^{i(\mathbf{k}_1 + \mathbf{k}_2 - \mathbf{k}_3 - \mathbf{k}_4)\mathbf{r}_2} \{ (\boldsymbol{\epsilon}_1 \boldsymbol{\epsilon}_3^*)(\boldsymbol{\epsilon}_2 \boldsymbol{\epsilon}_4^*) + B(\omega_1)(\boldsymbol{\epsilon}_1 \Delta_{12} \boldsymbol{\epsilon}_3^*)(\boldsymbol{\epsilon}_2 \boldsymbol{\epsilon}_4^*) e^{i\mathbf{k}_1(\mathbf{r}_1 - \mathbf{r}_2)} + B(\omega_2)(\boldsymbol{\epsilon}_1 \boldsymbol{\epsilon}_3^*)(\boldsymbol{\epsilon}_2 \Delta_{12} \boldsymbol{\epsilon}_4^*) e^{i\mathbf{k}_2(\mathbf{r}_1 - \mathbf{r}_2)}$$
$$+ B(\omega_3)(\boldsymbol{\epsilon}_1 \Delta_{12} \boldsymbol{\epsilon}_3^*)(\boldsymbol{\epsilon}_2 \boldsymbol{\epsilon}_4^*) e^{-i\mathbf{k}_3(\mathbf{r}_1 - \mathbf{r}_2)} + B(\omega_4)(\boldsymbol{\epsilon}_1 \boldsymbol{\epsilon}_3^*)(\boldsymbol{\epsilon}_2 \Delta_{12} \boldsymbol{\epsilon}_4^*) e^{-i\mathbf{k}_4(\mathbf{r}_1 - \mathbf{r}_2)} \}] + (\mathbf{k}_1 \boldsymbol{\epsilon}_1 \leftrightarrow \mathbf{k}_2 \boldsymbol{\epsilon}_2). \quad (46)$$

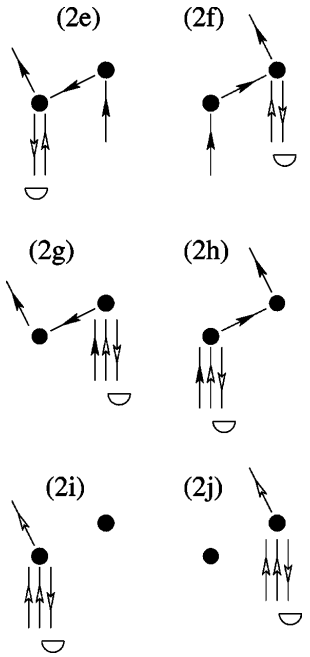

FIG. 4. Remaining diagrams describing inelastic scattering of two photons by two atoms. In the coherent backscattering experiment, they are filtered out by using the $h\|h$ polarization channel (see Sec. III B), in which a singly scattered photon (open arrows) cannot be detected.

Here, the last line denotes additional terms arising from exchanging the initial (or, equivalently, final) photons. We recognize two terms describing the scattering by atom 1 or 2 alone, see diagrams (2i) and (2j) in Fig. 4, and eight different terms describing the processes where both atoms are involved, see diagrams (2a)–(2h) in Figs. 3 and 4. Note that the terms depending on the polarization allow one to identify the photon which is scattered by both atoms. This photon is marked by full arrows in Figs. 2–4, whereas the open arrows denote the photon scattered by only one atom. If we assume that $|\mathbf{k}_4\boldsymbol{\epsilon}_4\rangle$ is the doubly scattered photon, the ten terms in Eq. (46) correspond (from top to bottom) to the diagrams (2i), (2e), (2a), (2h), (2d), (2j), (2f), (2b), (2g), and (2c), respectively.

B. Direct calculation of the enhancement factor

Having at hand the scattering matrix, we now determine the intensity of the photodetection signal. In principle, the calculation can be performed in the same way as in the single-atom case, Sec. II C. However, the detection signal will now depend nontrivially on the position of the atoms and the detector, due to the fact that the photons emitted by one atom interfere with the photons emitted by the other one. Even if we average over the positions $\mathbf{r}_1$ and $\mathbf{r}_2$ of the atoms, the interference is not completely washed out. There remains an enhanced probability to detect a photon in the direction opposite to the incident wave, an effect which is known as *coherent backscattering*. In the case of two atoms, it arises from double scattering: in the backscattering direction, a photon scattered first by atom 1, and then by atom 2, interferes constructively with the corresponding reversed path.

In order to examine cleanly this interference effect, we therefore assume that only doubly scattered photons are detected. Experimentally, this can be realized by using circularly polarized light $\boldsymbol{\epsilon}_L=(1,i,0)/\sqrt{2}$ (in Euclidean coordinates, where the z axis is parallel to $\mathbf{k}_L$), and detecting the scattered photons in the helicity preserving channel $\boldsymbol{\epsilon}_D=\boldsymbol{\epsilon}_L^*$. This implies $(\boldsymbol{\epsilon}_L\boldsymbol{\epsilon}_D^*)=0$, i.e., no singly scattered photons can be detected in the helicity preserving polarization channel. If we look at the inelastic part of the scattering matrix, Eq. (46), assuming (without loss of generality) that the photon $|\mathbf{k}_4\boldsymbol{\epsilon}_4\rangle$ is the detected one, this means that all terms with $(\boldsymbol{\epsilon}_1\boldsymbol{\epsilon}_4^*)$ or $(\boldsymbol{\epsilon}_2\boldsymbol{\epsilon}_4^*)$ are filtered out. These are the diagrams shown in Fig. 4, and only those of Fig. 3 remain.

Concerning the elastic single-photon scattering, see Fig. 2, we keep the single-scattering diagrams (1a)–(1c) to describe the undetected photon. For the sake of completeness, we will repeat in Appendix B the following calculation for the case of scalar photons, where, *a priori*, all the diagrams shown in Figs. 2–4 contribute.

1. Elastic contribution

Let us begin with the contribution $I_{\mathrm{el}}^{(1)}$ of one-photon scattering. According to Eqs. (27) and (29), it is obtained by applying the electric field on the final state $|f_1\rangle$ of single-photon scattering. As explained above, only the diagrams (1d) and (1e) in Fig. 2 contribute. At first, we concentrate on the phase factors depending on the position of the atoms. If $\mathbf{k}_L$ is the wave vector of the incident photon, and the detector is located in the direction $\mathbf{k}_D$ (with $|\mathbf{k}_D|=|\mathbf{k}_L|$, since one-photon scattering conserves the frequency), we obtain $\exp(i\mathbf{r}_1\cdot\mathbf{k}_L-i\mathbf{r}_2\cdot\mathbf{k}_D)$ for (1d) and $\exp(i\mathbf{r}_2\cdot\mathbf{k}_L-i\mathbf{r}_1\cdot\mathbf{k}_D)$ for (1e). Evidently, the phases are identical if $\mathbf{k}_D=-\mathbf{k}_L$, i.e., (1d) and (1e) interfere constructively in the backscattering direction. On the other hand, if $\mathbf{k}_L\neq\mathbf{k}_D$ (more precisely: if the angle between $\mathbf{k}_L$ and $\mathbf{k}_D$ is much larger than some characteristic quantity θ_C), the interference between (1d) and (1e) vanishes when averaging over the positions of the atoms. For simplicity, we fix the distance r_{12} and average only over the angular variables of $\mathbf{r}_1-\mathbf{r}_2$. In this case, the width of the enhanced backscattering signal (which is also called "the cone") is given by $\theta_C=1/(\omega r_{12})$. In total, we obtain both for the background intensity (known in the literature as the "ladder term" L), and the additional intensity in backscattering direction (the "crossed term" C) twice the result $\eta s/2$ of the single-atom case,

$$L^{(1)}=C^{(1)}=\tilde{\eta}s, \tag{47}$$

apart from a modification of the prefactor

$$\tilde{\eta}=\left(\frac{3\Gamma}{4d\omega_L R}\right)^2\langle|B(\omega_L)|^2|\boldsymbol{\epsilon}_L\Delta_{12}\boldsymbol{\epsilon}_D^*|^2\rangle_{\mathbf{r}_{1,2}} \tag{48}$$

$$= \frac{3}{8}\left(\frac{9\Gamma^2}{16 d\omega_L^2 R r_{12}|\omega_L - \omega_0|}\right)^2. \quad (49)$$

Here, Eq. (48) implies an average over the positions of the two atoms. The polarization-dependent term $|\boldsymbol{\epsilon}_L \Delta_{12} \boldsymbol{\epsilon}_D^*|^2 = \sin^4\theta/4$ is given by the angle θ between the incident laser $\mathbf{k}_L$ and the two atoms $\mathbf{r}_{12}=\mathbf{r}_1-\mathbf{r}_2$. Then, a spherical distribution of $\mathbf{r}_{12}$, at fixed distance r_{12}, yields the result given in Eq. (49). The fact that $L^{(1)}=C^{(1)}$ can be traced back to the reciprocity symmetry [4].

Next, we examine the interference between two-photon and one-photon scattering, which gives rise to the elastic component $I_{\mathrm{el}}^{(2)}$ of the intensity in second order of s, see Sec. II C. According to Eq. (30), $I_{\mathrm{el}}^{(2)}$ is given by the overlap of the respective quantum states $|f_1\rangle$ and $|g_1\rangle$ of the undetected photon, which amounts to a sum over the latter's state $|\mathbf{k}\boldsymbol{\epsilon}\rangle$ (i.e., $\langle g_1|f_1\rangle = \Sigma_{\mathbf{k},\boldsymbol{\epsilon}}\langle g_1|\mathbf{k}\boldsymbol{\epsilon}\rangle\langle\mathbf{k}\boldsymbol{\epsilon}|f_1\rangle$). First, we concentrate on the phase factor $\exp(-i\mathbf{k}\cdot\mathbf{r}_{1,2})$ of the undetected photon, depending on whether it is emitted by atom 1 or 2. Integrating over the angular variables $\Omega_{\mathbf{k}}$ of $\mathbf{k}$ (at fixed $|\mathbf{k}|=\omega_L$), we obtain, if $|\mathbf{k}\rangle$ is emitted by different atoms:

$$\int d\Omega_{\mathbf{k}} e^{\pm i\mathbf{k}(\mathbf{r}_1-\mathbf{r}_2)} = 4\pi \frac{\sin(\omega_L r_{12})}{\omega_L r_{12}} \ll 1. \quad (50)$$

Since we have assumed $\omega_L r_{12} \gg 1$, the above term can be neglected. In other words, diagrams where the undetected photon is emitted by different atoms do not interfere in leading order of $1/(\omega_L r_{12})$. If we now select one of the four diagrams (2a)–(2d) describing two-photon scattering, we can discard among the three one-photon diagrams (1a)–(1c), the one where the undetected photon is scattered by the "wrong" atom. The remaining two exactly give the final state of a photon scattered by a single atom, as described by Eq. (21). Concerning the detected photon of the one-photon scattering, we can choose either diagram (1d) or (1e). As already discussed above, one of them gives a contribution to the background L, and the other one to the enhanced backscattering signal C. As there are in total four diagrams (2a)–(2d), we obtain both for L and C four times the result $-\eta s^2$ of the single-atom case:

$$L^{(2,\mathrm{el})} = C^{(2,\mathrm{el})} = -4\tilde{\eta}s^2. \quad (51)$$

Note that the total elastic ladder term, Eq. (47) and Eq. (51), equals the total elastic crossed one, Eq. (47) and Eq. (51). This means interference with maximal contrast, corresponding to the maximal possible enhancement factor of two.

2. Inelastic contribution

The inelastic component I_{in} of the intensity, finally, arises from two-photon scattering. Here, the overlap $\langle g_1|g_1\rangle$, see Eq. (31), again implies a sum over the undetected photon, which now may have a frequency different from ω_L. With two atoms, $|g_1\rangle$ is a sum of four different contributions, corresponding to the diagrams (2a)–(2d). Correspondingly, we obtain diagonal terms $(|2\mathrm{a}|^2,\ldots,|2\mathrm{d}|^2)$, which contribute to the background signal, and interference terms, which may contribute to the backscattering cone, see below.

Let us examine first the diagrams (2a) and (2b), where the elastic scattering event occurs before the inelastic one. Here, the single-atom scattering amplitude is multiplied by a constant factor $B(\omega_L)$. This means that—apart from the modification of the prefactor η—both $|2\mathrm{a}|^2$ and $|2\mathrm{b}|^2$ give the same result as in the single-atom case, Eqs. (31) and (36),

$$I_{\mathrm{II}} = \frac{\tilde{\eta}}{\eta}\int d\omega P^{(\mathrm{in})}(\omega) = \tilde{\eta}\frac{s^2}{2}. \quad (52)$$

In the other two cases (2c) and (2d), the frequency to be inserted in the factor $B(\omega)$, Eq. (42), equals the final frequency of the detected photon (or, equivalently, of the undetected one, since $|B(\omega)|^2 = |B(2\omega_L-\omega)|^2$). Hence a factor $|B(\omega)|^2$ must be inserted in the integral over the inelastic power spectrum, Eq. (40). The resulting integral can be easily performed, and yields

$$I_{\mathrm{I}} = \frac{\tilde{\eta}}{\eta}\int d\omega \left|\frac{\omega_L-\omega_0}{\omega-\omega_0}\right|^2 P^{(\mathrm{in})}(\omega) = \tilde{\eta}\frac{s^2}{2}\left(\frac{3}{4}+\frac{\delta^2}{\Gamma^2}\right). \quad (53)$$

Hence the four diagonal terms $|2\mathrm{a}|^2,\ldots,|2\mathrm{d}|^2$, give the following contribution to the inelastic background intensity:

$$L^{(\mathrm{in})} = 2I_{\mathrm{I}} + 2I_{\mathrm{II}} = \tilde{\eta}\left(\frac{7}{4}+\frac{\delta^2}{\Gamma^2}\right)s^2. \quad (54)$$

Note that, for $\delta=0$, the contribution from Eq. (53) is smaller than the one from Eq. (52) (by a factor 3/4). This is due to the fact that, after the inelastic scattering event, the photon frequencies are no longer exactly on resonance, see Fig. 1(a), which reduces the cross section of the scattering by the other atom. The opposite is the case for large detuning δ: here, the inelastic scattering brings one of the two photons close to the atomic resonance, see Fig. 1(b), thereby increasing the corresponding contribution to the background signal.

The inelastic component of the enhanced backscattering signal arises from the interference of (2a) with (2d), and (2b) with (2c). (Remember that every diagram interferes only with those where the undetected photon is emitted by the same atom.) As argued above, equality of the corresponding geometrical phases, and thereby full constructive interference, is guaranteed if the wave vector of the detected photon is opposite to the incident wave vector, i.e., $\mathbf{k}_D=-\mathbf{k}_L$. Obviously, this condition will not be exactly fulfilled in the presence of inelastic scattering, even in exact backscattering direction (since in general $|\mathbf{k}_D| \neq |\mathbf{k}_L|$). The difference can be neglected, however, if we assume that the atomic linewidth Γ and the detuning $\delta=\omega_L-\omega_{\mathrm{at}}$, i.e., the parameters which determine the width of the power spectrum, see Fig. 1, are much smaller than the inverse of the distance r_{12} between the atoms:

$$\delta, \Gamma \ll \frac{c}{r_{12}}. \quad (55)$$

In other words: the propagation time r_{12}/c between the atoms is much smaller than the time scales associated with δ and Γ. This condition ensures a vanishing geometric phase difference, i.e., $\exp[(\mathbf{k}_L+\mathbf{k}_D)\cdot(\mathbf{r}_1-\mathbf{r}_2)] \simeq 1$, and is well fulfilled in the experiment [21]. What remains is the integration

over the inelastic spectrum, taking into account the photon exchange factors $B(\omega_L)$ or $B(\omega)$ in the cases (2a) and (2b) or (2c) and (2d), respectively:

$$2\int d\omega\,\mathrm{Re}\left\{\frac{\omega_L-\omega_0}{\omega-\omega_0}\right\}P^{(\mathrm{in})}(\omega)=\frac{3}{4}\eta s^2. \tag{56}$$

Here, we have neglected the exponential factor $e^{i(\omega-\omega_L)r_{12}}\simeq 1$ describing the propagation in the vacuum, the same approximation as above, see Eq. (55). From the two interfering pairs of diagrams, the inelastic contribution to the backscattering signal is obtained as twice the result of Eq. (56) with modified prefactor $\tilde{\eta}$:

$$C^{(\mathrm{in})}=\tilde{\eta}\frac{3}{2}s^2. \tag{57}$$

Note that $C^{(\mathrm{in})}$ is strictly smaller than the inelastic background, Eq. (54), which leads to a reduction of the backscattering enhancement factor, see below. This is consistent with the fact that two interfering diagrams, e.g., (2a) and (2d), are no more linked by the reciprocity symmetry: only diagrams with identical initial and final photon frequencies interfere with each other, whereas the reciprocity symmetry connects diagrams where initial and final frequencies are exchanged.

3. Double scattering enhancement factor

Adding all contributions, we have

$$L=L^{(1)}+L^{(2,\mathrm{el})}+L^{(\mathrm{in})}=\tilde{\eta}\left(s-\frac{9}{4}s^2+\frac{\delta^2}{\Gamma^2}s^2\right), \tag{58}$$

$$C=C^{(1)}+C^{(2,\mathrm{el})}+C^{(\mathrm{in})}=\tilde{\eta}\left(s-\frac{5}{2}s^2\right). \tag{59}$$

Finally, the double scattering enhancement factor reads:

$$\alpha=\frac{L+C}{L}=\frac{8-(19-4\delta^2/\Gamma^2)s}{4-(9-4\delta^2/\Gamma^2)s}. \tag{60}$$

Remember that single scattering has been removed by the helicity-preserving polarization channel.

At this stage, it is convenient to introduce the saturation parameter on resonance:

$$s_0=\frac{2d^2I_{\mathrm{in}}}{\Gamma^2/4}=\left(1+\frac{4\delta^2}{\Gamma^2}\right)s, \tag{61}$$

which depends only on the incident intensity I_{in} (and not on the detuning δ). Then, Eq. (60) can be rewritten:

$$\alpha=\frac{2+x}{1+x}, \tag{62}$$

with

$$x=\frac{s_0}{4-10s}\simeq\frac{s_0}{4}. \tag{63}$$

Here, we have used that s is small, otherwise our perturbative treatment (two-photon scattering) would be invalid. If the detuning δ is of the order of the linewidth Γ, this implies that s_0 must also be small. In this case, Eq. (62) yields

$$\alpha\simeq 2-\frac{s_0}{4}. \tag{64}$$

In principle, however, we may choose also a large value of the detuning δ, as long as we stay near resonant, and fulfill $(\delta/\Gamma)^2\ll 1/(\omega r_{12})^2$.[3] This means that s_0 may be large although s is small, see Eq. (61). In that case, the enhancement factor is given by Eq. (62), with $x=s_0/4$, see Fig. 5. This equation is valid for all values of s_0 corresponding to small s, i.e., $s_0\ll 1+4\delta^2/\Gamma^2$.

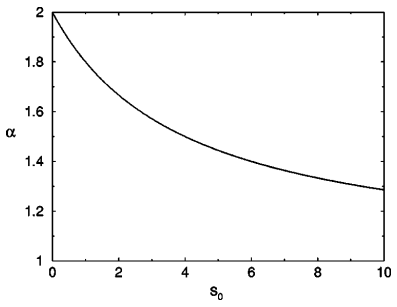

FIG. 5. The enhancement factor $\alpha=(8+s_0)/(4+s_0)$ as a function of the incident intensity s_0, and large detuning $\delta=\omega_L-\omega_{\mathrm{at}}$. If δ is not large, the displayed curve is valid only up to intensities $s_0\ll 1+4\delta^2/\Gamma^2$, corresponding to a small saturation parameter $s\ll 1$, cf. Eq. (61).

It may appear surprising that the enhancement factor α depends only on the intensity s_0 of the incident light, see Eqs. (62) and (63), whereas the intensity scattered by a *single* atom is determined by the saturation parameter s, see Sec. II C. This result is related to the form of the inelastic spectrum, see Fig. 1: since one of the two photons is always close to the atomic resonance after the inelastic scattering, the asymmetry between the reversed paths (see the following section) is larger for larger initial detuning δ, at a given value of s. Thereby, we can understand why, at a fixed s, the enhancement factor α decreases when increasing δ. However, we are not aware of an intuitive explanation why the relevant parameter turns out to be s_0, and not some other, similar combination of δ and s.

C. Interpretation

In this section, we discuss the physical mechanism responsible for the reduction of the backscattering enhancement factor. As we have seen above, it originates solely from inelastic scattering. For this reason, we will only consider inelastic scattering in the following.

[3]This condition implies $s_0|B(\omega_{\mathrm{at}})|^2\ll 1$, see Eqs. (42) and (61), and thereby suppresses exchange of more than one resonant photon between the two atoms, leading to terms proportional to s_0^2 (or higher order).

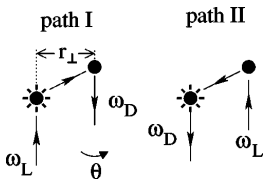

FIG. 6. Two reversed scattering paths, whose interference gives rise to enhanced backscattering. The left atom scatters inelastically, changing the photon frequency from ω_L to ω_D. Consequently, the amplitudes of the elastic scattering event by the right atom are different for both paths, see Eqs. (65) and (66), leading to a reduction of the backscattering enhancement factor.

1. Coherence loss

Generally, coherent backscattering arises from constructive interference between two scattering paths where the detected photon interacts with the respective scatterers in opposite order. The maximum enhancement factor of two is obtained if every path has a counterpropagating counterpart with the same amplitude. In the case of two photons, a "scattering path" in principle also specifies the final state $|\mathbf{k}\rangle$ of the undetected photon. As we have seen above, Eq. (50), the average over the angular variables of the undetected photon destroys interference between paths where the inelastic scattering occurs at different atoms (if the atoms are far away from each other). Consequently, if we concentrate on the detected photon, we should compare only the two reversed paths where the inelastic scattering occurs at the same atom, and the final frequency $\omega_D=2\omega_L-\omega_{\mathbf{k}}$ is the same (due to energy conservation), as shown in Fig. 6. Here, the left atom is marked as the one which scatters inelastically. Neglecting the propagation in the vacuum, see Eq. (55), the amplitudes $E_{\mathrm{I,II}}$ of the two reversed paths are obtained by multiplying the scattering amplitudes of the elastic and inelastic scattering event, Eqs. (9) and (11). Since the elastic scattering occurs at two different frequencies ω_L and ω_D, the amplitudes are not identical:

$$E_{\mathrm{I}}=\left(\frac{1}{\omega_D-\omega_0}+\frac{1}{2\omega_L-\omega_D-\omega_0}\right)\frac{e^{-ikr_\perp\theta/2}}{\omega_D-\omega_0}, \tag{65}$$

$$E_{\mathrm{II}}=\left(\frac{1}{\omega_D-\omega_0}+\frac{1}{2\omega_L-\omega_D-\omega_0}\right)\frac{e^{ikr_\perp\theta/2}}{\omega_L-\omega_0}, \tag{66}$$

where θ denotes the angle between the detector and backscattering direction, $r_\perp$ the perpendicular distance between the atoms, and prefactors not depending on ω_D or θ are ignored.

Equations (65) and (66) are valid for fixed final frequency ω_D. In reality, however, ω_D is a random variable, which implies that the ratio $E_{\mathrm{I}}/E_{\mathrm{II}}$ between the amplitudes of both paths fluctuates randomly. This leads to a loss of coherence between the two paths, i.e., a loss of contrast in the interference pattern $I(\theta)$.[4] A further loss of contrast originates from the fact that the inelastic scattering may take place either at atom 1 or 2. As discussed in the previous section, those two cases do not interfere with each other, i.e., they are added incoherently. For reasons of symmetry, the corresponding pairs of scattering amplitudes are identical, except for a change of sign of the detection angle θ. Hence we obtain the intensity $I(\theta)$ of the detection signal as follows:

$$I(\theta)=\int d\omega_D\big(|E_{\mathrm{I}}(\omega_D,\theta)+E_{\mathrm{II}}(\omega_D,\theta)|^2+|E_{\mathrm{II}}(\omega_D,-\theta)+E_{\mathrm{I}}(\omega_D,-\theta)|^2\big) \tag{67}$$

$$=2(I_{\mathrm{I}}+I_{\mathrm{II}})[1+\mathcal{V}\cos(kr_\perp\theta)], \tag{68}$$

with $I_{\mathrm{I,II}}$ the intensity of paths I and II, respectively, see Eqs. (52) and (53). Using Eqs. (65)–(68) yields the following interference contrast (also called "visibility"):

$$\mathcal{V}=\frac{6}{7+4\delta^2/\Gamma^2}. \tag{69}$$

Averaging over the positions $\mathbf{r}_1$ and $\mathbf{r}_2$ of the atoms does not affect the intensity observed at $\theta=0$; it only reduces the side maxima and determines the shape of the backscattering "cone." Thus the contrast $\mathcal{V}=C^{(\mathrm{in})}/L^{(\mathrm{in})}$ equals the ratio of the "ladder" and "crossed" term calculated in Sec. III B, see Eqs. (54) and (57), and is hence directly related to the backscattering enhancement factor. Remember, however, that we have considered only the *inelastic* component of the detection signal so far.

In general, a reduced contrast of two-wave interference originates either from a loss of coherence or from an asymmetry of the individual intensities of the two waves. More precisely, let us assume that the interference signal varies between $I_{\max}$ and $I_{\min}$. Since the mean value $(I_{\max}+I_{\min})/2=I_1+I_2$ equals the sum of the intensities $I_{1,2}$ of wave 1 and 2, the contrast is given by $\mathcal{V}=(I_{\max}-I_{\min})/(2I_1+2I_2)$. Then, the *degree of coherence* γ (see [30], pp. 499–503) is defined as

$$\mathcal{V}=\gamma\frac{2\sqrt{I_1I_2}}{I_1+I_2}. \tag{70}$$

In other words, in the asymmetric case $I_1\neq I_2$, the contrast is reduced (i.e., $\mathcal{V}<1$) even if the coherence is perfectly preserved (i.e., $\gamma=1$). This case is analogous to a double slit experiment performed with a perfect monochromatic plane wave, but different slit sizes.

In our case, we identify the two interfering waves as the light emitted by atom 1, on the one hand, and by atom 2, on the other one. Taking into account that the inelastic scattering event may take place either at atom 1 or 2, we see that the corresponding intensities are identical:

[4] In general, fluctuations of the phase and of the absolute value of $E_{\mathrm{I}}/E_{\mathrm{II}}$ both reduce the degree of coherence. In our case, the phase fluctuations have a stronger impact, at least for moderate values of the detuning δ (not much larger than Γ).

$$I_1 = I_2 = I_{\mathrm{I}} + I_{\mathrm{II}}, \tag{71}$$

i.e., both atoms emit the same intensity. Hence the reduction of contrast can be entirely attributed to a loss of coherence, i.e., $\mathcal{V}=\gamma$. As mentioned above, it originates both from the average over the spectrum of ω_D and from the random choice of the inelastically scattering event at atom 1 or 2. The relative importance of those two noise sources depends on the value of the detuning δ. Indeed, if we consider only one pair of the reversed paths I and II, i.e., if we fix atom 1 or 2 as the inelastically scattering one, we find a finite average phase difference

$$\phi = \arctan\left(\frac{2\delta}{3\Gamma}\right) \tag{72}$$

between the two paths, i.e., the maximum of the interference pattern is then shifted by an angle $\Delta\theta=\phi/(kr_\perp)$ away from the exact backscattering direction $\theta=0$. The second pair of reversed paths, where the inelastic scattering occurs at the other atom, leads to an identical shift, but in the opposite direction. Hence the random choice of the inelastically scattering atom reduces the contrast by a factor $\cos(\phi)=(1+4\delta^2/9\Gamma^2)^{-1/2}$, which is negligible only in the case of very small detuning, $\delta \ll \Gamma$.

2. Which-path information

An alternative physical explanation of the coherence loss can be obtained by an analogy to Young's famous double-slit experiment. As it is well known, interference is necessarily destroyed whenever we observe which slit the particle passes through (see, e.g., [31]). If $|D_1\rangle$ and $|D_2\rangle$ denote the quantum states of the which-path detector corresponding to slits 1 and 2, the degree of coherence is obtained as the overlap of the normalized detector states [29]:

$$\gamma = \frac{|\langle D_1|D_2\rangle|}{\sqrt{\langle D_1|D_1\rangle\langle D_2|D_2\rangle}}. \tag{73}$$

This implies perfect coherence, $\gamma=1$, if the paths are indistinguishable (i.e., if the detector states are identical), and total loss of coherence, $\gamma=0$, if the paths can be distinguished with certainty (i.e., if the detector states are orthogonal). The corresponding interference contrast follows via Eq. (70), with $I_1=\langle D_1|D_1\rangle$ and $I_2=\langle D_2|D_2\rangle$.

In our case, the path detector is given by the undetected photon. Remember that its frequency is correlated to the one of the detected photon, due to conservation of energy at the inelastic scattering event. Therefore the different dependence of the amplitudes $E_{\mathrm{I,II}}$ of paths I and II on the frequency of the detected photon, see Eqs. (65) and (66), reflects itself in the final state of the undetected photon:

$$|D_1\rangle = \sum_{\mathbf{k}\epsilon} \left(E_{\mathrm{I}}(2\omega_L - \omega_{\mathbf{k}}, \theta)e^{-i\mathbf{k}\cdot\mathbf{r}_1} + E_{\mathrm{II}}(2\omega_L - \omega_{\mathbf{k}}, -\theta)e^{-i\mathbf{k}\cdot\mathbf{r}_2}\right) \times|\mathbf{k}\epsilon\rangle, \tag{74}$$

$$|D_2\rangle = \sum_{\mathbf{k}\epsilon} \left(E_{\mathrm{II}}(2\omega_L - \omega_{\mathbf{k}}, \theta)e^{-i\mathbf{k}\cdot\mathbf{r}_1} + E_{\mathrm{I}}(2\omega_L - \omega_{\mathbf{k}}, -\theta)e^{-i\mathbf{k}\cdot\mathbf{r}_2}\right) \times|\mathbf{k}\epsilon\rangle. \tag{75}$$

Here, we have included the phase factors $e^{-i\mathbf{k}\cdot\mathbf{r}_{1,2}}$ indicating whether the inelastic scattering occurs at atom 1 or 2. As already mentioned, interference between those two cases does not contribute (in leading order of $1/\omega r_{12}$) to the overlap $\langle D_1|D_2\rangle$, see Eq. (50). Since $|D_1\rangle$ and $|D_2\rangle$ are not identical, the state of the undetected photon contains information about which path the first photon has taken. According to Eq. (73), this leads to a reduction of the degree of coherence γ, which, in our case, equals the contrast $\mathcal{V}$, since $I_1=I_2$, see Eqs. (70) and (71). Thereby, we can rederive the above result, Eq. (69).

Let us note that the interpretation in terms of a which-path experiment remains valid if we include the elastic component of the photodetection signal. Since, here, the undetected photon (described by the single-photon diagrams in Fig. 2) is not correlated with the detected photon, the elastic contributions to $|D_1\rangle$ and $|D_2\rangle$ are identical. This leads to a larger overlap $\langle D_1|D_2\rangle$ and, consequently, smaller loss of coherence than for the inelastic contribution alone. In total, we find the result $\mathcal{V}=C/L=\alpha-1$ of the previous section, see Eq. (60).

Finally, we want to stress that there is no loss of coherence associated with the inelastic scattering "on its own," but only in connection with the frequency filtering induced by the elastic scattering event. This can be demonstrated as follows: let us imagine that the response of the second atom is frequency-independent, i.e., $B(\omega)=\mathrm{const}$ in Eq. (42). Then, the amplitudes of two reversed paths, see Eqs. (65) and (66), are identical, the undetected photon does not carry any which-path information, and we recover the enhancement factor two, even in the presence of inelastic scattering. Such a situation can be realized, e.g., by choosing atoms with different linewidths $\Gamma_2 \gg \Gamma_1$, such that atom 2 cannot resolve the spectrum emitted by atom 1. In this case, a significant reduction of the enhancement factor is observed only if we increase the distance r_{12} between the atoms, such that the propagation in the vacuum becomes relevant.

D. Conclusion

In summary, we have presented a calculation of coherent backscattering in the presence of saturation. For two distant atoms, with single scattering excluded, the slope of the backscattering enhancement factor as a function of the incident intensity s_0 at $s_0=0$ equals $-1/4$, independently of the value of the detuning. The reduction of the enhancement factor can be traced back to the following two random processes: first, the frequency of the photons may be changed by the inelastic scattering event, which may, second, occur either at the first or at the second atom. Both processes [the latter one only for nonzero detuning, see Eq. (72)] lead to a random phase shift between the doubly scattered light emitted by the first atom, on the one hand, and by the second atom, on the other one, resulting in a loss of coherence. Alternatively, the coherence loss can be explained by regarding the undetected photon as

a which-path detector: its final state contains information about whether the detected photon has been emitted by the first or second atom, thereby partially destroying coherence between those paths.

Starting from the solution of our model, we can think of extending it to more general scenarios in two different directions, either increasing the number of photons, to reach higher values of the saturation parameter, or the number of atoms, to treat a disordered medium of atoms. Since the complexity of the scattering approach increases dramatically with the number of scattered particles, it may be more promising to use other methods, such as the optical Bloch equations [26], in the case of high saturation. The opposite is true for a large number of scatterers, where we can resort to known concepts from the theory of multiple scattering. An important question, which must be solved in order to interpret the results of the experiment [21], is how the average propagation of the two-photon state in the atomic medium affects the coherent backscattering signal.

ACKNOWLEDGMENTS

It is a pleasure to thank Cord Müller, Vyacheslav Shatokhin, David Wilkowski, Guillaume Labeyrie, and Andreas Buchleitner for fruitful discussions, critical remarks, and interest in our work. T.W. is indebted to the Deutsche Forschungsgemeinschaft for financial support within the Emmy Noether program. Laboratoire Kastler Brossel is Laboratoire de l'Université Pierre et Marie Curie et de l'Ecole Normale Supérieure, UMR 8552 du CNRS. CPU time on various computers has been provided by IDRIS.

APPENDIX A: TWO-ATOM SCATTERING MATRIX

In this appendix, we calculate the scattering of two photons by two atoms. For this purpose, we use the following expansion of the evolution operator $U(t_0,t)=\exp[-i(H_0+V)\times(t-t_0)]$:

$$U(t_0,t)=\sum_{n=0}^{\infty}\int_{t_0}^{t}dt_1\int_{t_1}^{t}dt_2\cdots\int_{t_{n-1}}^{t}dt_n\;U_0(t_0,t_1)\times VU_0(t_1,t_2)V\cdots VU_0(t_n,t), \tag{A1}$$

where $U_0(t_0,t)=\exp[-iH_0(t-t_0)]$ denotes the free evolution. With each interaction V, see Eq. (3), an atom may emit a photon or absorb one of the two photons. The corresponding "paths" connecting the initial and final two-photon state $|i\rangle=|\mathbf{k}_1\boldsymbol{\epsilon}_1,\mathbf{k}_2\boldsymbol{\epsilon}_2\rangle$ and $|f\rangle=|\mathbf{k}_3\boldsymbol{\epsilon}_3,\mathbf{k}_4\boldsymbol{\epsilon}_4\rangle$ can be represented diagrammatically, see Fig. 7.

Here, (Ia,b) describes the scattering of two photons by a single atom [27], and (IIa,b) and (IIIa,b) the scattering by two atoms. Let us first concentrate on (Ia,b) and (IIa,b), where the inelastic scattering event occurs before the elastic one. Note that in (IIa), we have not specified the order in which the photons are emitted or absorbed. What we mean by this is a sum over all possible orderings, as indicated in Fig. 8. As we will see below, however, the sum need not be explicitly evaluated.

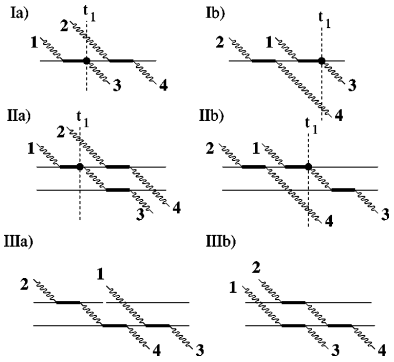

FIG. 7. Diagrams describing scattering of two photons by a single atom (Ia,b) and two atoms, (IIa,b) and (IIIa,b). The curly lines represent photons and thin or thick lines an atom in the ground or excited state. In order to simplify the comparison between (I) and (II), we split the diagrams into a right and a left half (see text).

Furthermore, we have selected one of the interaction operators V in the expansion (A1), at which we split the diagrams into a right and left half, denoted by $U^{(l,r)}$ in the following. According to Eq. (A1), we may write

$$U_{\mathrm{IIa}}(t_0,t)=\int_{t_0}^{t}dt_1 U_{\mathrm{IIa}}^{(l)}(t_0,t_1)VU_{\mathrm{IIa}}^{(r)}(t_1,t), \tag{A2}$$

and similarly for the other three diagrams (Ia), (Ib), and (IIb). Obviously, the left half is identical in the one- and two-atom cases I and II, respectively. In the right half, on the other hand, the two photons are always independent from each other, being scattered by different atoms (if at all). This means that the evolution operator is the product of the two single-photon evolution operators:

$$U_{\mathrm{IIa}}^{(r)}(t_1,t)=U_{\mathrm{II}}^{(r,1)}(t_1,t)U_{\mathrm{a}}^{(r,2)}(t_1,t), \tag{A3}$$

and likewise for (Ia), (Ib), and (IIb). Note that the evolution of the first photon $(1\rightarrow 3)$ depends only on (I) or (II), and not on (a) or (b), and vice versa for the second photon. Thereby, if we want to compare the one- and two-atom cases, we have to consider only the two single-photon diagrams $U_{\mathrm{I,II}}^{(r,1)}$, which are illustrated in Fig. 9.

The first one simply describes the emission of photon $|\mathbf{k}_3\boldsymbol{\epsilon}_3\rangle$ by an atom located at $\mathbf{r}_1$, followed by free evolution:

$$VU_{\mathrm{I}}^{(r,1)}(t_1,t)=-ig(\boldsymbol{\epsilon}_1\boldsymbol{\epsilon}_3^{*})e^{-i\mathbf{k}_3\cdot\mathbf{r}_1}e^{-i\omega_3(t-t_1)}. \tag{A4}$$

In the second case, the photon is scattered by the other atom. Here, we have to take the sum over its intermediate state. For the calculation, it is convenient to express the time evolution

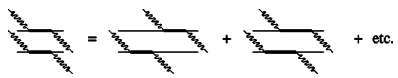

FIG. 8. Independent scattering of two photons by two different atoms. This diagram appears as a building block in (IIa) and (IIIb), Fig. 7.

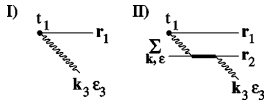

FIG. 9. (I) Emission of a photon $|\mathbf{k}_3\boldsymbol{\epsilon}_3\rangle$ at time t_1. (II) Photon emission and subsequent scattering by the second atom.

in terms of the corresponding Green's function:

$$VU_{\mathrm{II}}^{(r,1)}(t_1,t)=\int_{C^+}\frac{dz}{2\pi i}e^{-iz(t-t_1)}G_{\mathrm{II}}^{(r,1)}(z), \tag{A5}$$

where the contour C^+ runs just above the real axis, i.e., $z=x+i\epsilon$, $\epsilon>0$, from $x=+\infty$ to $-\infty$, and the Green's function of the above diagram (II) reads:

$$G_{\mathrm{II}}^{(r,1)}(z)=\sum_{\mathbf{k},\boldsymbol{\epsilon}}\frac{-ig^3(\boldsymbol{\epsilon}_1\boldsymbol{\epsilon}^*)(\boldsymbol{\epsilon}\boldsymbol{\epsilon}_3^*)e^{-i\mathbf{k}\cdot\mathbf{r}_1+i(\mathbf{k}-\mathbf{k}_3)\mathbf{r}_2}}{(z-\omega_k)(z-\omega_0)(z-\omega_3)}. \tag{A6}$$

In the continuous limit ($L\to\infty$), the sum is replaced by an integral [$\Sigma_k=(L/2\pi)^3\int dk$]. The result of the integral (A6), in leading order of $1/(\omega_3 r_{12})$, reads:

$$G_{\mathrm{II}}^{(r,1)}(z)=\frac{3i\Gamma g(\boldsymbol{\epsilon}_1\Delta_{12}\boldsymbol{\epsilon}_3^*)e^{-i\mathbf{k}_3\cdot\mathbf{r}_2}e^{izr_{12}}}{4\omega_3 r_{12}(z-\omega_0)(z-\omega_3)}. \tag{A7}$$

Here, Δ_{12} denotes the projection onto the plane orthogonal to $\mathbf{r}_2-\mathbf{r}_1$. Finally, in the contour integral (A5), only the pole at $z=\omega_3$ contributes (if $t-t_1\gg 1/\Gamma$):

$$VU_{\mathrm{II}}^{(r,1)}(t_1,t)=ig(\boldsymbol{\epsilon}_1\Delta_{12}\boldsymbol{\epsilon}_3^*)e^{-i\mathbf{k}_3\cdot\mathbf{r}_2}e^{-i\omega_3(t-t_1)}\times\frac{3\Gamma e^{i\omega_3 r_{12}}}{4\omega_3 r_{12}(\omega_3-\omega_0)}. \tag{A8}$$

Comparing Eqs. (A4) and (A8), we see that the contribution to the two-atom scattering matrix represented by (IIa,b) is given by the one-atom matrix S_{I}, times a correction of the geometrical phase and the polarization, times the photon exchange factor $B(\omega_3)$, see Eq. (42).

$$\langle\mathbf{k}_3\boldsymbol{\epsilon}_3,\mathbf{k}_4\boldsymbol{\epsilon}_4|S_{\mathrm{II}}|\mathbf{k}_1\boldsymbol{\epsilon}_1,\mathbf{k}_2\boldsymbol{\epsilon}_2\rangle=\langle\mathbf{k}_3\boldsymbol{\epsilon}_3,\mathbf{k}_4\boldsymbol{\epsilon}_4|S_{\mathrm{I}}|\mathbf{k}_1\boldsymbol{\epsilon}_1,\mathbf{k}_2\boldsymbol{\epsilon}_2\rangle\times e^{i\mathbf{k}_3(\mathbf{r}_1-\mathbf{r}_2)}\frac{(\boldsymbol{\epsilon}_1\Delta_{12}\boldsymbol{\epsilon}_3^*)}{(\boldsymbol{\epsilon}_1\boldsymbol{\epsilon}_3^*)}B(\omega_3). \tag{A9}$$

What remains is the contribution, where the elastic scattering occurs before the inelastic one, represented by diagrams (IIIa,b) in Fig. 7. The calculation can be repeated in almost the same way as above, or simply by noting that (IIIa,b) is related to (IIa,b) through time reversal, and the result is

$$\langle\mathbf{k}_3\boldsymbol{\epsilon}_3,\mathbf{k}_4\boldsymbol{\epsilon}_4|S_{\mathrm{III}}|\mathbf{k}_1\boldsymbol{\epsilon}_1,\mathbf{k}_2\boldsymbol{\epsilon}_2\rangle=\langle\mathbf{k}_3\boldsymbol{\epsilon}_3,\mathbf{k}_4\boldsymbol{\epsilon}_4|S_{\mathrm{I}}|\mathbf{k}_1\boldsymbol{\epsilon}_1,\mathbf{k}_2\boldsymbol{\epsilon}_2\rangle\times e^{-i\mathbf{k}_1(\mathbf{r}_1-\mathbf{r}_2)}\frac{(\boldsymbol{\epsilon}_1\Delta_{12}\boldsymbol{\epsilon}_3^*)}{(\boldsymbol{\epsilon}_1\boldsymbol{\epsilon}_3^*)}B(\omega_1). \tag{A10}$$

Here, the photon exchange factor $B(\omega)$ is evaluated at the frequency of the initial photon. The total scattering matrix is now readily obtained by adding S_{II} and S_{III}, and also including the diagrams where the two atoms and/or the two photons are exchanged.

APPENDIX B: THE SCALAR CASE

In this appendix, we calculate the photodetection signal for scalar photons. Although they are not suited for coherent backscattering, since single scattering cannot be excluded, the solution will be useful for a future comparison with the results obtained from the optical Bloch equations, which can be solved much more easily in the scalar case.

As in the vectorial case, we consider contributions to the detection signal up to second order in $1/(\omega_L r_{12})$. We neglect those terms whose order in $1/(\omega_L r_{12})$ is changed by the angular average over $\mathbf{r}_{12}$.[5] Furthermore, we consider only contributions which do not oscillate rapidly as a function of r_{12}, i.e., which survive an average over r_{12} over one wavelength.

First, since the two atoms may scatter independently from each other, we obtain two times the single-atom result, see Eqs. (35) and (36):

$$L^{(\mathrm{el},0)}=\eta_s(s-2s^2), \tag{B1}$$

$$L^{(\mathrm{in},0)}=\eta_s s^2, \tag{B2}$$

which contributes to the background intensity L. Here we have to take into account that the lifetime Γ, and the prefactor η, are different in the scalar and vectorial cases, respectively. Instead of Eqs. (5) and (37), the following expressions hold for scalar photons:

$$\Gamma_s=\frac{d^2\omega_{\mathrm{at}}^3}{2\pi\epsilon_0}, \tag{B3}$$

$$\eta_s=\left(\frac{\Gamma_s}{2d\omega_L R}\right)^2. \tag{B4}$$

Next, we consider the cases where one photon is exchanged between the two atoms. These contribute to the detection signal in second order of $1/(\omega_L r_{12})$. Concerning one-photon scattering, only the diagrams (1d) and (1e), Fig. 2, are relevant, and we obtain the same result as for the $h\|h$ channel in the vectorial case, see Eq. (47):

$$L^{(\mathrm{el},1)}=C^{(\mathrm{el},1)}=\eta_s|B|^2 s, \tag{B5}$$

but with modified "photon exchange factor"

$$B=\frac{\Gamma}{2\omega_L r_{12}(\omega_L-\omega_0)}, \tag{B6}$$

compare Eq. (42).

The elastic contribution quadratic in s arises from interference of two-photon and one-photon scattering. Let us first

[5]These terms give the corrections of the average photon propagation induced by a disordered medium consisting of only a single atom. In the case of many disordered atoms, they are taken into account by renormalizing the single-photon propagation, in order to describe the mean free path and refractive index of the atomic medium.

look at diagram (2a). As before in the $h\|h$ channel, it interferes with (1a)+(1b) for the undetected photon, and (1d) or (1e) for the detected photon, giving rise to $-\eta_s|B|^2s^2$ in background L and the cone C, respectively. Including single scattering, we obtain a contribution: the detected photon may be singly scattered (1b), and the undetected photon either doubly scattered (1e), or singly scattered by the other atom (1c). Here, the state (1e)+(1c) of the undetected photon exactly corresponds to the state (1a)+(1b), in the previous case. Consequently, we obtain another term $-\eta_s|B|^2s^2$ in the background.

With diagram (2b), the above considerations can be repeated in almost the same way. The difference from (2a) is only that the detected photon propagates in the opposite direction. Consequently, we obtain a term $-\eta_s|B|^2s^2$ in the cone C, instead of the background L.

Diagram (2e) is identical to diagram (2a), since we cannot distinguish between singly or doubly scattered photons (open or full arrows in Figs. 2–4) in the scalar case. (2c), (2d), and (2f), finally, are obtained by exchanging the atoms. Adding all contributions mentioned above, we get:

$$L^{(\mathrm{el},2)} = -10\,\eta_s|B|^2s^2, \tag{B7}$$

$$C^{(\mathrm{el},2)} = -8\,\eta_s|B|^2s^2. \tag{B8}$$

As for the inelastic component, we only have to include the new diagrams (2e,f), which—as already mentioned above—are identical to (2a,b). Hence, the background contribution $2I_{\mathrm{II}}$, see Eq. (52), is multiplied by a factor of 4, and the backscattering cone, Eq. (57), by a factor of 2. We obtain:

$$L^{(\mathrm{in},2)} = 2I_{\mathrm{I}} + 8I_{\mathrm{II}} = \left(\frac{19}{4} + \frac{\delta^2}{\Gamma^2}\right)\eta_s|B|^2s^2, \tag{B9}$$

$$C^{(\mathrm{in},2)} = 3\,\eta_s|B|^2s^2. \tag{B10}$$

What we have not taken into account so far is interference between two diagrams where the undetected photon is emitted by different atoms. According to Eq. (50), the angular integral over the undetected photon then yields $\sin(\omega r_{12})/(\omega r_{12})$. Hence if one of the two diagrams contains a photon exchange, we obtain a contribution proportional to $|B|^2$. However, it can be shown that these contributions are exactly canceled by other contributions originating from the diagrams (2g) and (2h), which also have been neglected so far. For example, the interference of (2g) with (1c) for the detected photon and (1c)+(1e) for the undetected one is canceled by the interference of (2j) with (1c) for the detected photon and (1e) for the undetected one. Similarly, the term $|2g|^2$ is canceled by the interference of (2g) with (2j). The underlying reason for all these cancelations is that which the undetected photon does after the inelastic scattering is irrelevant. We are only interested in its norm, which is not changed by subsequent scattering events (due to energy conservation). Hence the final result is given by Eqs. (B1)–(B10).

[1] Y. Kuga and A. Ishimaru, J. Opt. Soc. Am. A **1**, 831 (1984).
[2] M. P. van Albada and A. Lagendijk, Phys. Rev. Lett. **55**, 2692 (1985).
[3] P. E. Wolf and G. Maret, Phys. Rev. Lett. **55**, 2696 (1985).
[4] B. A. van Tiggelen and R. Maynard, in *Wave Propagation in Complex Media*, edited by G. Papanicolaou (Springer, Berlin, 1997).
[5] A. Akkermans, P. E. Wolf, R. Maynard, and G. Maret, J. Phys. (France) **49**, 77 (1988).
[6] A. A. Golubentsev, Sov. Phys. JETP **59**, 26 (1984).
[7] F. C. MacKintosh and S. John, Phys. Rev. B **37**, 1884 (1988).
[8] F. A. Erbacher, R. Lenke, and G. Maret, Europhys. Lett. **21**, 551 (1988).
[9] A. S. Martinez and R. Maynard, Phys. Rev. B **50**, 3714 (1994).
[10] A. A. Chabanov, M. Stoytchev, and A. Z. Genack, Nature (London) **404**, 850 (2000).
[11] D. S. Wiersma, P. Bartolini, A. Lagendijk, and R. Righini, Nature (London) **390**, 671 (1997).
[12] F. Scheffold, R. Lenke, R. Tweer, and G. Maret, Nature (London) **398**, 207 (1999).
[13] D. S. Wiersma, J. G. Rivas, P. Bartolini, A. Lagendijk, and R. Righini, Nature (London) **398**, 207 (1999).
[14] G. Labeyrie, E. Vaujour, C. A. Müller, D. Delande, C. Miniatura, D. Wilkowski, and R. Kaiser, Phys. Rev. Lett. **91**, 223904 (2003).
[15] D. Wilkowski *et al.*, Physica B **328**, 157 (2003).
[16] C. A. Müller, T. Jonckheere, C. Miniatura, and D. Delande, Phys. Rev. A **64**, 053804 (2001).
[17] C. A. Müller and C. Miniatura, J. Phys. A **35**, 10163 (2002).
[18] G. Labeyrie, F. de Tomasi, J.-C. Bernard, C. A. Müller, C. Miniatura, and R. Kaiser, Phys. Rev. Lett. **83**, 5266 (1999).
[19] T. Jonckheere, C. A. Müller, R. Kaiser, C. Miniatura, and D. Delande, Phys. Rev. Lett. **85**, 4269 (2000).
[20] Y. Bidel *et al.*, Phys. Rev. Lett. **88**, 203902 (2002).
[21] T. Chanelière, D. Wilkowski, Y. Bidel, R. Kaiser, and Ch. Miniatura, Phys. Rev. E (to be published).
[22] R. H. Dicke, Phys. Rev. **93**, 99 (1954).
[23] B. A. van Tiggelen, in *Coherent Atomic Matter Waves*, edited by R. Kaiser, C. Westbrook, and F. David (Springer, Berlin, 2001).
[24] U. Eichmann *et al.*, Phys. Rev. Lett. **70**, 2359 (1993).
[25] T. Wong, S. M. Tan, M. J. Collet, and D. F. Walls, Phys. Rev. A **55**, 1288 (1997).
[26] C. Cohen-Tannoudji, J. Dupont-Roc, and G. Grynberg, *Atom-Photon Interactions* (Wiley, New York, 1992).
[27] J. Dalibard and S. Reynaud, J. Phys. **12**, 1337 (1983).
[28] B. R. Mollow, Phys. Rev. **188**, 1969 (1969).
[29] S. M. Tan and D. F. Walls, Phys. Rev. A **47**, 4663 (1993).
[30] M. Born and E. Wolf, *Principles of Optics*, 6th ed. (Pergamon Press, Oxford, 1980).
[31] T. Pfau, S. Spälter, Ch. Kurtsiefer, C. R. Ekstrom, and J. Mlynek, Phys. Rev. Lett. **73**, 1223 (1994).

PHYSICAL REVIEW E **71**, 055603(R) (2005)

Coherent backscattering of light by nonlinear scatterers

T. Wellens,[1,2] B. Grémaud,[2] D. Delande,[2] and C. Miniatura[1]
[1]*Institut Non Linéaire de Nice, UMR 6618, 1361 route des Lucioles, F-06560 Valbonne, France*
[2]*Laboratoire Kastler Brossel, Université Pierre et Marie Curie, 4 Place Jussieu, F-75005 Paris, France*
(Received 22 November 2004; published 31 May 2005)

We theoretically study the propagation of light in a disordered medium with nonlinear scatterers. We especially focus on interference effects between reversed multiple scattering paths, which lead to weak localization and coherent backscattering. We show that, in the presence of weakly nonlinear scattering, constructive interferences exist in general between *three* different scattering amplitudes. This effect influences the nonlinear backscattering enhancement factor, which may thus exceed the linear barrier two.

DOI: 10.1103/PhysRevE.71.055603 PACS number(s): 42.25.Dd, 32.80.−t, 42.65.−k

Light transport inside a nonlinear medium gives rise to a wide variety of phenomena, such as pattern formation, four waves mixing, self-focusing effects, dynamical instabilities, etc. [1]. These effects are well described and understood with the help of an intensity dependent susceptibility, e.g., $\chi^{(3)}$ nonlinearity. However, in these approaches, one usually discards the fact that interference phenomena in disordered systems may significantly alter wave transport properties. Indeed, considering the return probability to a given point, all scattering paths are now closed loops. Then the *two-wave* interference between amplitudes contra-propagating along these loops typically increases the return probability by at most a factor of 2, inducing a decrease of the diffusion constant (the weak localization effect). How nonlinear effects affect weak localization is basically unknown and the present paper is aimed at showing that this could be more important than naively expected. Coherent random lasers [2] are probably the most striking systems intrinsically combining both nonlinear effects and disorder. Even if in this case one would require an active (i.e., amplifying) medium, a key point is the understanding of the mutual effects between multiple interferences and nonlinear scattering.

An effect similar to weak localization is *coherent backscattering* (CBS) where an enhancement of the average intensity scattered around the direction opposite to the incident wave is observed [3]. In the linear scattering regime, CBS also arises from a two-wave interference between amplitudes entering and leaving the medium in opposite directions and contrapropagating along all possible scattering paths. Thus both the CBS and the weak localization are described by the so-called "maximally crossed diagrams" [4]. The CBS enhancement factor, defined as the signal detected in the exact backscattering direction divided by the diffuse background, never exceeds two. This maximum value is reached if each pair of interfering waves has the same amplitude, and if single scattering can be suppressed. Previous studies of the nonlinear regime have been restricted to the case of linear scatterers embedded in a uniform nonlinear medium [5–7]. Here, it has been shown that the maximum enhancement factor remains two.

As we will show in this paper, however, the situation drastically changes in the presence of nonlinear scattering (in contrast to nonlinear propagation). In particular, in the perturbative regime of at most one scattering event with $\chi^{(3)}$ nonlinearity, CBS arises from interference between three amplitudes. Depending on the sign of the nonlinearity, this leads to an increase or decrease of the nonlinear CBS enhancement factor compared to the linear value two. Since the same physics is at work for weak localization corrections to transport, a corresponding change of the diffusion constant is expected, too. Because, for photons, CBS is easier to observe than weak localization, we specifically concentrate on the former.

In this paper, we calculate CBS by a dilute gas of nonlinear scatterers. We assume that the cross section of a single scatterer situated at position $\mathbf{r}$ inside the disordered medium depends on the local intensity $I(\mathbf{r})$ as follows:

$$\sigma(\mathbf{r}) = \sigma_0[1 + \alpha I(\mathbf{r})], \tag{1}$$

where σ_0 denotes the linear cross section, and α quantifies the strength of the nonlinearity, which is proportional to the $\chi^{(3)}$ coefficient of the scattering material. The local intensity $I(\mathbf{r})$ is the intensity due to all external sources, i.e., the light radiated by all other scatterers and the incident light penetrating the medium until $\mathbf{r}$ without being scattered. For future convenience, we measure $I(\mathbf{r})$ in units of the incident intensity I_{in} (before entrance into the medium). Thus, α is dimensionless and also proportional to I_{in}. The general form (1) of the nonlinear cross section is obtained under the assumption of small scatterers, i.e., constant local intensity inside the scatterer, weak $\chi^{(3)}$ nonlinearity (i.e., higher-order terms like I^2 negligible), and isotropic scattering. The following treatment can also be generalized to the nonisotropic case, however. At the end, we will present numerical results where we take into account the polarization state of the light field.

Besides the scattering cross section, the second ingredient needed for the description of a multiple scattering process is the propagation between two scattering events. Under the condition that no other scattering event occurs in between, the disorder averaged intensity propagator is given by an exponentially damped spherical wave

$$\overline{P(\mathbf{r},\mathbf{r}')} = \frac{e^{-|\mathbf{r}-\mathbf{r}'|\langle 1/\ell\rangle}}{4\pi|\mathbf{r}-\mathbf{r}'|^2}. \tag{2}$$

Here, $\langle 1/\ell\rangle$ denotes the mean value of the inverse mean free path along a straight line connecting the two scattering

events at $\mathbf{r}$ and $\mathbf{r}'$. In the linear case ($\alpha=0$), the mean-free-path ℓ_0 is constant, and is related via $1/\ell_0=\mathcal{N}\sigma_0$ to the linear cross section σ_0 and the scatterer density $\mathcal{N}$. This relation is a consequence of energy conservation, which ensures that the exponential attenuation of propagating field modes originates solely from scattering into other modes. Similarly, since we assume energy conservation for the nonlinear case, too (i.e., no absorbing or amplifying scatterers), we can also derive the nonlinear mean free path from the nonlinear scattering cross section, Eq. (1). Since the nonlinear contribution to the total intensity $\sigma(\mathbf{r})I(\mathbf{r})$ scattered from $\mathbf{r}$ is, according to Eq. (1), proportional to $\alpha I(\mathbf{r})^2$, we need to know the disorder-averaged *squared* intensity for this purpose. In a perturbative expansion up to first order in α, we can here replace $I(\mathbf{r})$ by its linear counterpart $I_0(\mathbf{r})$, whose fluctuation properties are well known [8]. By assuming uniformly distributed phases for the fields radiated by the other scatterers (which is valid in the case of a dilute medium), one obtains

$$\overline{I_0^2(\mathbf{r})} = 2\overline{I_0(\mathbf{r})}^2 - (e^{-z/\ell_0})^2. \tag{3}$$

The second term, with z the distance from the boundary of the medium to $\mathbf{r}$ along the incident direction, represents the squared intensity of the incident, coherent mode. It accounts for the fact that—in contrast to the diffuse light—the (linear) coherent mode intensity does not fluctuate for different realizations of the disorder. By equating the intensity loss due to propagation with the scattered intensity (i.e., employing energy conservation), we therefore obtain from Eq. (3) different expressions for the mean free paths for diffuse and coherent light

$$\frac{1}{\ell(\mathbf{r})} = \frac{1}{\ell_0}(1 + 2\alpha\overline{I_0(\mathbf{r})}), \tag{4}$$

$$\frac{1}{\ell_c(\mathbf{r})} = \frac{1}{\ell_0}(1 + 2\alpha\overline{I_0(\mathbf{r})} - \alpha e^{-z/\ell_0}). \tag{5}$$

We can now write down a nonlinear radiative transfer equation for the average intensity $\overline{I(\mathbf{r})}$ inside the disordered medium. Radiative transport is obtained by representing $\overline{I(\mathbf{r})}$ as the incoherent sum of the coherent incident field mode plus the diffuse light radiated from all individual scatterers

$$\overline{I(\mathbf{r})} = e^{-z\langle 1/\ell_c\rangle} + \mathcal{N}\int_V d\mathbf{r}'\overline{P(\mathbf{r},\mathbf{r}')} \times \overline{\sigma(\mathbf{r}')I(\mathbf{r}')}, \tag{6}$$

where $\langle 1/\ell_c\rangle$ denotes the mean value of the inverse coherent mean free path, Eq. (5), along the corresponding path of length z. In the second term, representing the diffuse light, the disorder average is decorrelated. This is justified by the fact that correlations between intensities at different positions (separated much further than the optical wavelength) can be neglected in the case of a dilute medium [4]. In the case $\alpha=0$, Eq. (6) reduces to the familiar linear radiative transfer equation [4], whose iterative solution yields $\overline{I_0(\mathbf{r})}$. To proceed, we expand Eq. (6) up to the first order in the nonlinearity parameter α. Introducing Eq. (3), we obtain a closed equation for the average intensity $\overline{I}$, which we solve by iteration. Finally, the average intensity of the backscattering signal follows via

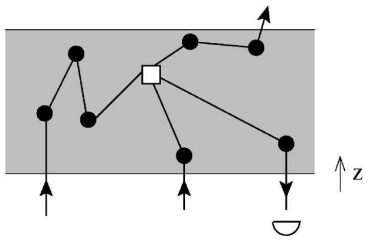

FIG. 1. In the perturbative approach, we assume a single nonlinear (□), but arbitrarily many linear scattering events (●). The nonlinear event symmetrically connects two linear propagators with each other. One of them finally reaches the detector placed in backscattering direction.

$$L = \mathcal{N}\int_V \frac{d\mathbf{r}}{A} e^{-z\langle 1/\ell\rangle} \times \overline{\sigma(\mathbf{r})I(\mathbf{r})}, \tag{7}$$

with A the transverse area of the medium. Expanding again to the first order in α, we identify the linear and nonlinear part, $L=L_0+L_1$, respectively. According to whether α originates from the cross section σ or the mean-free-path ℓ (or ℓ_c), the latter splits into a nonlinear scattering and nonlinear propagation component, i.e., $L_1=L_1^{(\mathrm{sc})}+L_1^{(\mathrm{pr})}$. For a slab geometry of length L, i.e., (linear) optical thickness $b=L/\ell_0$, we obtain

$$L_0 = \int_0^b d\zeta\overline{I_0}(\zeta)e^{-\zeta}, \tag{8}$$

$$L_1^{(\mathrm{sc})} = \alpha\int_0^b d\zeta\overline{I_0}(\zeta)[2\overline{I_0}^2(\zeta) - e^{-2\zeta}], \tag{9}$$

$$L_1^{(\mathrm{pr})} = -\alpha\int_0^b d\zeta\overline{I_0}(\zeta)[2\overline{I_0}^2(\zeta) - 2\overline{I_0}^2(b) - e^{-\zeta} + e^{-2\zeta}], \tag{10}$$

where we have introduced the (linear) optical depth $\zeta=z/\ell_0$. Note that the first terms in Eqs. (9) and (10) cancel each other. This is not surprising if one keeps in mind that energy conservation ensures the total outgoing flux to equal the incoming one. Thus, the nonlinear contribution vanishes even completely, if one considers the total detection signal, integrated over all directions in forward and backward direction. We have checked that Eqs. (8)–(10) are also obtained by using diagrammatic scattering theory [9], if only the so-called "ladder" diagrams are retained—thus neglecting recurrent scattering effects [10] and interferences between different scattering paths—and if, in addition, all diagrams with more than one nonlinear scattering event are discarded (see Fig. 1).

On top of the above background intensity, a narrow interference cone of height C is observed, originating from the interference between reversed scattering paths, which is de-

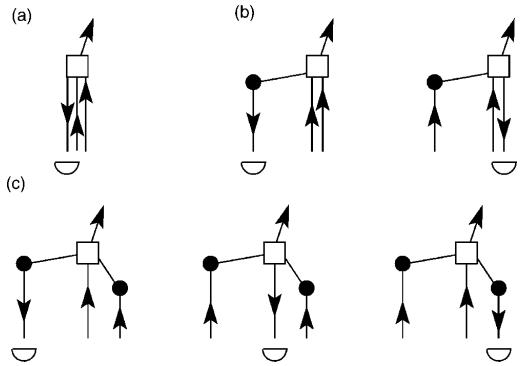

FIG. 2. In the presence of nonlinear scattering (□), there may be either (b) two, or (c) three interfering amplitudes contributing to enhanced backscattering, apart from single scattering (a), which only contributes to the background. In general, the case (c), which corresponds to the maximum enhancement factor three, is realized if either both incoming propagators, or one incoming and the outgoing detected propagator exhibit at least one linear scattering event (●) besides the nonlinear one.

scribed by the so-called maximally crossed diagrams. Due to time reversal symmetry, each maximally crossed diagram has the same value as the corresponding ladder diagram. In the linear case, there is exactly one reversed counterpart for each scattering path, except for those exhibiting only a single scattering event. Hence, the cone height equals the background, provided that single scattering is removed from the latter. In the presence of nonlinear scattering, however, there may be either two or three interfering amplitudes. As exemplified in Fig. 2, this is due to the fact that two linear propagators are symmetrically connected by the nonlinear event, which permits, in general, two different possibilities to reverse the propagator that finally reaches the detector. In the expression for the background component, Eq. (9), the three cases of Fig. 2 can be identified by writing the local intensity $\bar{I}_0 = \exp(-\zeta) + \bar{I}_d$ as a sum of the coherent and diffuse part, respectively. Then, all terms of at least second power in $\bar{I}_d$ correspond to the case (c), those linear in $\bar{I}_d$ to case (b), and the remaining ones to case (a). From this decomposition, C is easily obtained, since the ratio of the cone height to the background depends solely on the number of interfering amplitudes. In particular, the three-amplitudes case (c) contributes to the interference cone twice as much as to the background. In the two-amplitudes case (b), a small complication arises, since the right-hand amplitude of Fig. 2(b) is twice as large as the left-hand one [11]. Only in the latter one, both propagators arriving at the nonlinear scattering event originate from the coherent mode, and hence the asymmetry is related to the different fluctuation properties of diffuse and coherent light, expressed by Eq. (3). Here, the ratio between cone height and background is obtained as $(1\times2+2\times1)/(1\times1+2\times2)=4/5$. Finally, the single scattering terms (a) do not contribute to the cone, and must be removed from Eq. (9). Thereby, we obtain

$$C_1^{(\mathrm{sc})} = 4\alpha \int_0^L d\zeta [\bar{I}_0^3(\zeta) - 2\bar{I}_0(\zeta) e^{-2\zeta} + e^{-3\zeta}]. \qquad (11)$$

Concerning nonlinear propagation, interference between the three amplitudes does not occur [5–7]. Formally, the reason is that in this case the two incoming propagators are not connected symmetrically by the nonlinear scattering event. Instead, they can physically be distinguished from each other, as one of them (the "probe") keeps the direction of propagation, whereas the other one ("pump") is scattered. Hence, there are only two interfering amplitudes, obtained by reversing the path of the probe. Just as for the linear component, it is sufficient to remove single scattering contributions from the background, Eq. (10).

The perturbative results derived above allow us to calculate the CBS enhancement factor $\eta = 1 + C/L$ up to the first order in the nonlinearity coefficient α. In particular, we obtain the first derivative of $\eta(\alpha)$ at $\alpha = 0$, which quantifies the modification of CBS enhancement due to a small nonlinearity. In our case, the strength of the nonlinearity is limited by the perturbative assumption of at most one nonlinear scattering event. In order to estimate roughly its domain of validity, we have analyzed the statistical distribution of the number N of scattering events in linear backscattering paths, by numerical simulations with slab geometry. If we associate with each scattering event a constant probability proportional to α to be nonlinear (thereby neglecting the inhomogeneity of the local intensity), we find that the occurrence of two or more scattering events can be neglected provided that $\alpha b^2 \ll 1$. Let us note that a similar condition also ensures the stability of speckle fluctuations in a nonlinear medium [12].

We want to stress that the above treatment, valid for scalar point scatterers, can be extended to any kind of nonlinear scatterer with $\chi^{(3)}$ nonlinearity. Specifically, we have analyzed the vectorial case, where the polarization of the light field is taken into account. This case is especially interesting, since in the helicity preserving ($h\|h$) polarization channel single scattering contributions are filtered out, thus realizing the maximum linear enhancement factor two. Hence, any deviation of the enhancement factor from two can unambiguously be attributed to the nonlinear effect of interference between three amplitudes. Numerically, we have treated the vectorial case by using a Monte Carlo method, where the positions of the scattering events are randomly chosen.

The results for the scalar and vectorial ($h\|h$) case are shown in Fig. 3, as a function of the optical thickness b. Evidently, the slope $m = d\eta/d\alpha|_{\alpha=0}$ increases with b, since a nonlinear scattering event is more likely to occur at larger optical thickness. Thus, for large optical thickness, a significant change of η results already from a small nonlinearity α. In the vectorial case, the nonlinear influence on η is smaller. The main reason for this is the following: Due its explicit dependence on the polarization vectors attached to the two incoming and outgoing propagators, the nonlinear scattering amplitude does not remain invariant when exchanging a single incoming and outgoing propagator. (Only if *all* propagators are reversed, invariance is guaranteed by time-reversal symmetry.) This causes a polarization-induced loss of inter-

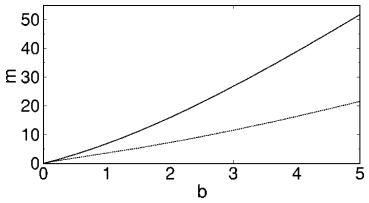

FIG. 3. Modification $m = d\eta/d\alpha|_{\alpha=0}$ of the CBS enhancement factor η induced by a small nonlinearity α, for backscattering from a slab of optical thickness b, in the scalar case (solid lines) and the $h\|h$ polarization channel (dotted lines). For a large optical thickness, already a small nonlinearity leads to a significant increase (or decrease, depending on the sign of α) of η. In the $h\|h$ channel, the nonlinear CBS modification is smaller than in the scalar case, as a consequence of decoherence due to polarization effects.

ference contrast, i.e., a reduction of the coherent nonlinear scattering component $C_1^{(sc)}$ (approximately by a factor $3/4$). Nevertheless, the effect of the three-amplitudes interference still prevails, such that in total a positive slope is observed. In particular, the CBS enhancement factor is predicted to exceed the linear barrier two, if the sign of the nonlinearity α is positive. Due to the close relation between CBS and weak localization mentioned above, we thus expect that weak localization—and possibly also strong localization—are facilitated by positive nonlinearities.

An alternative method to observe enhancement factors larger than two is provided by using atomic scatterers. As a specifically quantum mechanical property of the atom-photon interaction, nonlinearity is here intrinsically related to *inelastic* scattering, where the frequency of scattered photons changes. On the one hand, inelastic scattering acts as a source of decoherence between reversed scattering paths, with ensuing decrease of the CBS enhancement factor [11]. On the other hand, however, it allows to distinguish linearly and nonlinearly scattered light in terms of its frequency. Thereby, the linear components L_0 and C_0 can be filtered out from the detection signal, so that the nonlinear effect of interference between three amplitudes can manifest itself especially clearly, unspoiled by linear contributions. To minimize decoherence, the frequency filter must be sufficiently narrow and be put as close to the initial frequency as possible, but far enough to filter out elastically scattered light. In this limit, the backscattering enhancement factor is exclusively given by the nonlinear scattering components derived above, i.e., $\eta = 1 + C_1^{(sc)}/L_1^{(sc)}$. For sufficiently large optical thickness, we thereby predict maximum values of the CBS enhancement factor up to 3 (scalar case) or 2.5 ($h\|h$ channel).

It is a pleasure to thank Cord Müller for fruitful discussions. T.W. has been supported by the DFG Emmy Noether program. Laboratoire Kastler Brossel is laboratoire de l'Université Pierre et Marie Curie et de l'Ecole Normale Superieure, UMR 8552 du CNRS.

[1] R. W. Boyd, *Nonlinear Optics* (Academic, San Diego, 1992).
[2] H. Cao, Waves Random Media **13**, R1 (2003).
[3] M. P. van Albada and A. Lagendijk, Phys. Rev. Lett. **55**, 2692 (1985); P. E. Wolf and G. Maret, Phys. Rev. Lett. **55**, 2696 (1985).
[4] M. C. W. van Rossum and T. M. Nieuwenhuizen, Rev. Mod. Phys. **71**, 313 (1999).
[5] V. M. Agranovich and V. E. Kravtsov, Phys. Rev. B **43**, 13691 (1991).
[6] A. Heiderich, R. Maynard, and B. A. van Tiggelen, Opt. Commun. **115**, 392 (1995).
[7] R. Bressoux and R. Maynard, in *Waves and Imaging through Complex Media*, edited by P. Sebbah (Kluwer Academic Publishers, Dordrecht, 2001).
[8] J. W. Goodman, in *Laser Speckle and Related Phenomena*, edited by J. C. Dainty (Springer, Berlin, 1984).
[9] A. J. van Wonderen, Phys. Rev. B **50**, 2921 (1994).
[10] D. Wiersma, M. P. van Albada, B. A. van Tiggelen, and A. Lagendijk, Phys. Rev. Lett. **74**, 4193 (1995).
[11] T. Wellens, B. Grémaud, D. Delande, and C. Miniatura, Phys. Rev. A **70**, 023817 (2004).
[12] S. E. Skipetrov and R. Maynard, Phys. Rev. Lett. **85**, 736 (2000).

INSTITUTE OF PHYSICS PUBLISHING JOURNAL OF PHYSICS B: ATOMIC, MOLECULAR AND OPTICAL PHYSICS

J. Phys. B: At. Mol. Opt. Phys. **39** (2006) 4719–4731 doi:10.1088/0953-4075/39/22/015

Observation of coherent backscattering 'factor of three' in a numerical experiment

Thomas Wellens[1] **and Benoît Grémaud**[2]

[1] Institut für Theoretische Physik, Universität Erlangen-Nürnberg, Staudtstr. 7, 91058 Erlangen, Germany
[2] Laboratoire Kastler Brossel, Université Pierre et Marie Curie, 4 Place Jussieu, 75252 Paris Cedex 05, France

E-mail: Thomas.Wellens@physik.uni-erlangen.de

Received 25 July 2006, in final form 25 September 2006
Published 7 November 2006
Online at stacks.iop.org/JPhysB/39/4719

Abstract

We study coherent backscattering of light by nonlinear scatterers in the weakly nonlinear regime. We compare full numerical calculations with a diagrammatic approach; the validity of the latter is demonstrated by the excellent agreement between these two approaches. Especially it emphasizes the fact that, in the weakly nonlinear regime, the coherent backscattering phenomenon originates, in general, from the interference between *three* different scattering amplitudes. This effect reveals itself in the first nonlinear correction of the backscattered intensity, which is enhanced by almost a factor three as compared to the diffuse background.

1. Introduction

During the past ten years, many experiments studying localization effects in disordered media have been performed with cold atomic vapours, acting as dilute gases of randomly distributed atoms multiply scattering an incident monochromatic laser light [1–4]. In this case, the scattered light field exhibits a speckle-like structure due to (multiple) interference between all possible scattering paths. The key point is that the disorder average is insufficient to erase all interference effects. This gives rise to weak or strong localization effects in light transport depending on the strength of the disorder [5, 6]. A hallmark of this coherent transport regime is the coherent backscattering (CBS) phenomenon: the average intensity multiply scattered off an optically thick sample is up to two-times larger than the average background in a small angular range around the direction of backscattering, opposite to the incoming light [7, 8]. This effect in cold atomic gases has been the subject of extensive studies in the weak localization regime, both from theoretical [9–16] and experimental points of view [1–4], proving that these cold atoms provide a highly efficient and tuneable material.

0953-4075/06/224719+13$30.00

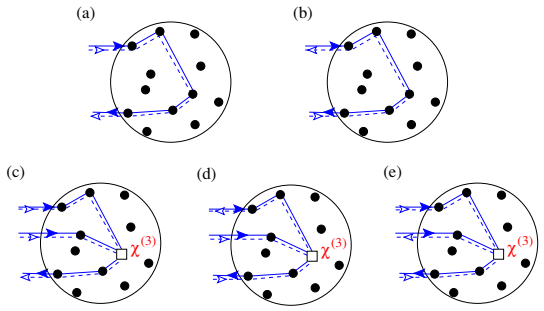

Figure 1. Top: in the linear regime, each 'ladder' diagram (a) has exactly one 'crossed' counterpart describing interference between reversed scattering paths (b). The coherent backscattering enhancement factor cannot exceed the maximum value 2. Bottom: nonlinearities lead to an effective 'interaction' between optical waves, which—in the lowest order of the nonlinearity constant $\chi^{(3)}$—is described by diagrams connecting two incoming and one outgoing intensity propagator (see section 3). This has an important impact on the phenomenon of coherent backscattering: for each ladder diagram (c), we now find two distinct pairs of reversed scattering paths, see diagrams (d) and (e), which both contribute to the detection signal in exact backscattering directions. Thus, the nonlinear component of the backscattering signal exhibits a backscattering cone up to two times larger than the diffuse background, corresponding to a maximum enhancement factor of three (see section 3.3 for details).

Quite naturally, the question of the possible observation of strong localization of light in these cold atomic clouds has been raised. For the transition to take place, the scatterers must be brought very close to each other, typically at a distance of the order of the wavelength. In these conditions, even if the incident light is very weak, the intensity of light scattered by one atom to one of its nearby neighbours may actually be very high. Then, one faces a peculiar feature of the atoms: their ability to depict nonlinear behaviour, even for moderate light intensity. The order of the magnitude of the required laser power is given by the so-called saturation intensity, whose values are 1.6 mW cm^{-2} for rubidium atoms and 42 mW cm^{-2} for strontium atoms, for their usual laser cooling transitions. For this reason, one must have a correct description and understanding of the impact of the nonlinear behaviour of the atoms on the coherence properties of the scattered light. A better understanding of the interplay between disorder and nonlinearity is also relevant for other subjects such as, e.g., the coherent random laser [17] or the propagation of Bose–Einstein condensates in disordered potentials [18–20].

In recent papers [13, 14], we have shown that, for moderate intensity, it is possible to use a scattering approach to describe the nonlinear corrections to all relevant quantities (scattered intensity, inelastic spectrum ...). In particular, we have predicted that the intensity scattered in the opposite direction to the incident laser beam is given by the (constructive) interference of three different amplitudes, allowing, in principle, a maximum enhancement factor equal to three, see figure 1. However, since this effect has not yet been experimentally observed, the purpose of the present paper is to confirm the validity of this prediction by numerical simulations, using a simplified 'classical' model for the nonlinear atomic scatterers.

This paper is divided as follows: in section 2, starting from the standard results for a single two-level atom, we explain the choice of our model. In section 3, the diagrammatic theory is derived, emphasizing the *factor of three* due to constructive interferences between three

different amplitudes in the backward direction. Comparison of these theoretical calculations and the numerical results is performed in section 4. Conclusions and possible continuations are given in section 5.

2. 'Classical' nonlinear scatterers

If one considers a two-level atom illuminated by a laser beam at the atomic frequency ω_0, the stationary quantities are given by the optical Bloch equations and read [21]

$$\langle \mathcal{D}^{\pm} \rangle = \mp \mathrm{i} \frac{\Gamma \Omega_{\mathrm{L}}}{\Gamma^2 + 2|\Omega_{\mathrm{L}}|^2} \tag{1a}$$

$$\langle \Pi^{\mathrm{e}} \rangle = \frac{|\Omega_{\mathrm{L}}|^2}{\Gamma^2 + 2|\Omega_{\mathrm{L}}|^2} \tag{1b}$$

where Γ is the spontaneous emission rate, Ω_{L} is the absorption rate induced by the laser (Ω_{L} is proportional to the laser field E_{L} and $|\Omega_{\mathrm{L}}|^2 \propto I_{\mathrm{L}}$). $\mathcal{D}^{\pm}$ are the raising and lowering dipole operators and Π^{e} is the population of the excited state. The brackets $\langle \cdots \rangle$ indicate the average over the quantum fluctuations. From these quantities, one can derive the average field and the average intensity radiated by the atom

$$\langle E(r) \rangle \propto \langle \mathcal{D}^{-} \rangle \tag{2a}$$

$$\langle I(r) \rangle = \langle |E(r)|^2 \rangle \propto \langle \Pi^{\mathrm{e}} \rangle \tag{2b}$$

where the proportionality factor depends on the distance r (see below). For low laser intensities ($|\Omega_{\mathrm{L}}| \ll \Gamma$), the scattered intensity is simply proportional to the incident one: we are in the linear regime. When increasing the laser intensity, the absorption rate eventually becomes comparable to the spontaneous emission rate, meaning that the atom is no longer able to scatter all the incident photons: the regime is then nonlinear. However, we also see that, in the nonlinear regime, $\langle I(r) \rangle \neq |\langle E(r) \rangle|^2$, which means that the light is not only elastically scattered. Actually, for large intensity, the majority of the scattered intensity is inelastic and the inelastic spectrum is usually derived using the quantum regression theorem.

However, in the case of many two-level atoms, the situation becomes incredibly complicated because of the nonlinear coupling between all the atoms. In principle, one would have to derive the optical Bloch equations for the whole density matrix, whose size exponentially grows with the number of atoms. On the other hand, the 'factor of three' (i.e., the interference between three amplitudes in the backscattering direction) does not rely on the exact description of the two-level atoms, but rather on the nonlinear relation between the scattered light and the incident light. In particular, even if one forgets the inelastic light and only takes into account the elastic scattering, the diagrammatic approach still involves the same diagrams (see below). For this reason, we will consider a simpler model—accessible to a direct numerical simulation—in which we will only take into account the elastic light, forgetting the quantum fluctuations (i.e., $\langle |E|^2 \rangle = |\langle E \rangle|^2$).

The disordered medium is thus built with a collection of N such 'classical' nonlinear scatterers located at randomly chosen positions $\mathbf{r}_i$, $i = 1, \ldots, N$, inside a sample volume V illuminated by a plane wave $\mathbf{k}_{\mathrm{L}}$. This point scatterer model is especially suitable for numerical implementation, since it yields a discrete system of equations for the field strengths E_i at the positions of the N scatterers

$$E^{(i)} = \mathrm{e}^{\mathrm{i}\mathbf{k}_{\mathrm{L}} \cdot \mathbf{r}_i} + \mathrm{i} \sum_{j \neq i} P^{(i,j)} \frac{E^{(j)}}{1 + \alpha |E^{(j)}|^2} \tag{3}$$

where α is proportional to the incoming intensity, and

$$P^{(i,j)} = \frac{\mathrm{e}^{\mathrm{i}kr_{ij}}}{kr_{ij}} \tag{4}$$

with $k = |\mathbf{k}_\mathrm{L}|$, is the propagator from j to i in the free space. For simplicity, we restrict ourselves to the case of a scalar wave within this paper.

In the small α limit, one can neglect the nonlinear behaviour and (3) simply becomes a linear system [24–26]

$$M\mathbf{E} = \mathbf{E}^\mathrm{L} \tag{5}$$

with

$$M_{ij} = \begin{cases} 1 & \text{for} \quad i = j \\ -\mathrm{i}P^{(i,j)} & \text{for} \quad i \neq j \end{cases} \tag{6}$$

and $\mathbf{E}_i^\mathrm{L} = \mathrm{e}^{\mathrm{i}\mathbf{k}_\mathrm{L}\cdot\mathbf{r}_i}$. For increasing (but still weak) incoming intensity α, (3) becomes

$$E^{(i)} = \mathrm{e}^{\mathrm{i}\mathbf{k}_\mathrm{l}\cdot\mathbf{r}_i} + \mathrm{i}\sum_{j\neq i} P^{(i,j)}(E^{(j)} - \alpha|E^{(j)}|^2 E^{(j)}) \tag{7}$$

describing thus a disordered Kerr medium with a nonlinearity of type $\chi^{(3)}$, the latter being proportional to the incident laser intensity.

3. Diagrammatic theory

In this section, we calculate the detection signal radiated by the system (3) of classical scatterers up to first order in α, using diagrammatic theory. The calculation follows closely the one presented in [14] for the case of quantum mechanical scatterers.

At first, we consider the linear regime, $\alpha = 0$. Here, the solution of (5) reads formally

$$E_0^{(i)} = \mathrm{e}^{\mathrm{i}\mathbf{k}_\mathrm{L}\cdot\mathbf{r}_i} + \sum_{n=1}^{\infty}\sum_{j_1,\ldots,j_n} \mathrm{e}^{\mathrm{i}\mathbf{k}_\mathrm{L}\cdot\mathbf{r}_{j_1}}(i)^n \left(\prod_{k=1}^{n-1} P^{(j_k,j_{k+1})}\right) P^{(j_n,i)}. \tag{8}$$

In the following, we will be interested in the next highest order of the perturbative expansion $E^{(i)} = \sum_n (-\alpha)^n E_n^{(i)}$ in α. From (7), we obtain

$$E_1^{(i)} = \mathrm{i}\sum_{j\neq i} P^{(i,j)}\left(E_1^{(j)} + E_0^{(j)}\left|E_0^{(j)}\right|^2\right) \tag{9}$$

with solution

$$E_1^{(i)} = \sum_{n=1}^{\infty}\sum_{j_1,\ldots,j_n} i^n E_0^{(j_1)}\left|E_0^{(j_1)}\right|^2 \left(\prod_{k=1}^{n-1} P^{(j_k,j_{k+1})}\right) P^{(j_n,i)}. \tag{10}$$

We note that the perturbative solution of (7) is unique, i.e. multiplicity or instability of solutions [22, 23] can only exist in the regime where the perturbative approach breaks down. (The validity of the perturbative approach will be discussed in section 4.)

A diagrammatic representation of the nonlinear field is shown in figure 2. The square (□) denotes the nonlinear scattering event, which, in (10), takes place at the scatterer j_1. The three incoming arrows represent the nonlinear source term $E_0^{(j_1)}\left|E_0^{(j_1)}\right|^2$, while the dashed arrow denotes the complex conjugate field $\left(E_0^{(j_1)}\right)^*$. According to (8), each of the three fields is obtained as a sum over all scattering paths ending at scatterer j_1. Correspondingly, each incoming arrow in figure 2 represents one such scattering path, whereas the outgoing arrow

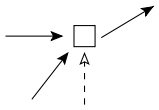

Figure 2. Diagrammatic representation of the nonlinear field, see equation (10).

represents a scattering path starting from j_1 and reaching finally the detector via $j_2, \ldots, j_n$, see (10).

Let us now consider the average *intensity*—the quantity which is measured in the end. The term of first order in α reads

$$I_1 = 2\,\mathrm{Re}\{E_1(E_0)^*\}. \tag{11}$$

This means that we have to add one dashed line to figure 2, which represents the *linear* field $(E_0)^*$. Now, we are ready to perform the ensemble average over the realization $\mathbf{r}_1, \ldots, \mathbf{r}_N$ of the disordered medium. For this purpose, we use the dilute medium approximation $\mathcal{N}\lambda^3 \ll 1$, where $\mathcal{N} = N/V$ is the density of scatterers. In this approximation, the only diagrams which survive the ensemble average are the 'ladder' and 'crossed' diagrams, i.e., those diagrams where the solid and dashed lines visit the same sequence of scatterers—either in the same (ladder) or reversed (crossed) order. Furthermore, recurrent scattering events, where a single scatterer is visited more than once, can be neglected.

In addition to washing out all except the ladder and crossed diagrams, the ensemble average leads to a homogeneous effective medium, which is characterized by its refractive index n. Its linear component reads

$$n_0 = 1 + \frac{\mathrm{i}}{2k\ell_0} \tag{12}$$

where the mean free path

$$\ell_0 = k^2/(4\pi\mathcal{N}) \tag{13}$$

depends on the density $\mathcal{N}$. The dilute medium approximation is thus valid provided that $k\ell_0 \gg 1$. Let us note that the real part of the refractive index is unchanged in our specific scattering model, defined by (3). This, however, presents no restriction since, in the case of a dilute medium, a small shift of the real part has no significant effect on the average intensity.

Due to the presence of the effective medium, the average field propagation (4) between two subsequent scattering events is replaced by

$$\tilde{P}_0^{(i,j)} = \frac{\mathrm{e}^{\mathrm{i}n_0 k r_{ij}}}{k r_{ij}}. \tag{14}$$

Remember that (14) describes *linear* propagation between i and j. Since we are dealing with nonlinear scatterers, the refractive index of the effective medium also has a nonlinear component, which will be calculated below.

3.1. Nonlinear scattering

Before turning to nonlinear propagation, however, we will first calculate the contribution from nonlinear scattering. In the ladder approximation, it is obtained as follows: (i) the incoming dashed line in figure 2 forms a ladder diagram (i.e., visiting the same sequence of scatterers) with one of the two incoming solid lines. (ii) The remaining solid lines form a ladder diagram

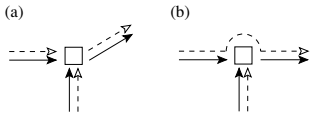

Figure 3. Ladder diagrams describing nonlinear scattering (a) and nonlinear propagation (b).

with the dashed line describing the additional linear field $(E_0)^*$ in (11). This leads us to the diagram shown in figure 3(a).

Note that each one of the three solid/dashed ladder pairs describes *linear* transport of the average intensity in a dilute medium. Let us hence briefly recall the calculation of linear transport. From (8), and employing the ladder approximation, the average linear intensity is found to fulfil the following integral equation:

$$\langle I_0(\mathbf{r})\rangle = \mathrm{e}^{-z/\ell_0} + \mathcal{N}\int_V \mathrm{d}\mathbf{r}' \left|\tilde{P}_0^{(\mathbf{r},\mathbf{r}')}\right|^2 \langle I_0(\mathbf{r}')\rangle. \tag{15}$$

Here, z denotes the distance from $\mathbf{r}$ to the surface of the volume V in the direction opposite to the incoming laser, $-\mathbf{k}_\mathrm{L}$. Diagrammatically, $\langle I_0(\mathbf{r})\rangle$ is represented as a solid/dashed ladder pair pointing to position $\mathbf{r}$. If we assume that the detector is placed in backscattering direction ($\mathbf{k}_\mathrm{D} \simeq -\mathbf{k}_\mathrm{L}$), the same function $\langle I_0(\mathbf{r})\rangle$ also describes an outgoing ladder pair, starting from $\mathbf{r}$ and pointing to the detector. From (15), the linear ladder component of the detected intensity results as

$$L_0 = \int_V \frac{\mathrm{d}\mathbf{r}}{A\ell_0}\langle I_0(\mathbf{r})\rangle\, \mathrm{e}^{-z/\ell_0} \tag{16}$$

where A denotes the transverse area of the scattering sample seen by the incident laser. (To obtain a dimensionless quantity, the 'bistatic coefficient' is defined such that $L_0 = 1$ corresponds to the case where all the incident intensity is scattered uniformly in all directions.)

To obtain the nonlinear scattering ladder component, we have to account for the fact that the two incoming solid/dashed ladder pairs can be grouped together in two different ways, see step (i) above. This leads to an additional factor 2 in the final result. An exception is the case where the four incoming arrows all originate from the same mode, i.e. the coherent incoming laser mode. With its intensity given by $\exp(-z/\ell_0)$, the average square of the linear intensity is obtained as

$$\langle I_0(\mathbf{r})^2\rangle = 2\langle I_0(\mathbf{r})\rangle^2 - \mathrm{e}^{-2z/\ell_0} \tag{17}$$

and the nonlinear scattering ladder component reads

$$L_1^{(\mathrm{sc})} = 2\int \frac{\mathrm{d}\mathbf{r}}{A\ell_0}\langle I_0(\mathbf{r})^2\rangle\langle I_0(\mathbf{r})\rangle. \tag{18}$$

Here, the factor 2 originates from equation (11), the average squared intensity $\langle I_0(\mathbf{r})^2\rangle$ describes the two incoming propagator pairs and $\langle I_0(\mathbf{r})\rangle$ the outgoing one.

3.2. Nonlinear propagation

The diagram describing nonlinear propagation differs from nonlinear scattering only in the fact that the additional dashed line does not take part in the nonlinear scattering event, see figure 3(b). Imagine that two linear scattering events take place at scatterers 1 and 2 just before and after the nonlinear event, respectively. The average propagation of the dashed line between 1 and 2 is then given by the linear expression $\left(\tilde{P}_0^{(1,2)}\right)^*$, see (14), since it does not

participate in the nonlinear event. The propagation of the solid lines forming ladder diagrams with the above dashed line, however, will be modified by the nonlinear event, depending on the local intensity represented by the remaining solid/dashed ladder pair. Integrating over the position $\mathbf{r}_3$ of the nonlinear event, we obtain for the nonlinear propagation in first order of the nonlinearity parameter α

$$\tilde{P}_1^{(1,2)} = 2\mathrm{i}\mathcal{N}\int \mathrm{d}\mathbf{r}_3\, \tilde{P}_0^{(1,3)}\, \tilde{P}_0^{(3,2)} \langle I_0(\mathbf{r}_3)\rangle \tag{19}$$

$$\simeq -\frac{r_{12}}{\ell_0}\langle I_0\rangle_{\mathbf{r}_1\to\mathbf{r}_2}\, \tilde{P}_0^{(1,2)}. \tag{20}$$

The factor 2 in (19) again accounts for the fact that the two incoming solid arrows can be exchanged. Evaluating the integral in leading order of the 'diluteness parameter' $1/(k\ell_0)$ (stationary phase approximation) yields (20). Only positions $\mathbf{r}_3$ located on a straight line connecting $\mathbf{r}_1$ and $\mathbf{r}_2$ give a significant contribution to the integral. Correspondingly, $\langle\cdots\rangle_{\mathbf{r}_1\to\mathbf{r}_2}$ denotes the average value along this line.

The same reasoning applies also if the wave propagates from scatterer 1 directly to the detector (i.e., without another linear event after the nonlinear one). In the linear case, this is described simply by $\exp(\mathrm{i}n_0 k z_1)$. For the nonlinear case, we obtain

$$\tilde{P}_1^{(1,\mathrm{det})} = -\frac{z_1}{\ell_0}\langle I_0\rangle_{\mathbf{r}_1\to\mathbf{r}_0}\, \mathrm{e}^{\mathrm{i}n_0 k z_1}. \tag{21}$$

Here, $\mathbf{r}_0$ denotes the intersection of the line from $\mathbf{r}_1$ to the detector with the boundary of the medium, and $z_1 = |\mathbf{r}_1 - \mathbf{r}_0|$.

A small complication arises for the propagation of the coherent mode, i.e., if the nonlinear event takes place before the first linear event at $\mathbf{r}_1$. As in the case of nonlinear scattering (see above), the exchange factor '2' vanishes if the 'pump intensity' represented by the solid/dashed ladder pair arriving at the nonlinear event also originates from the coherent mode. Thereby, we obtain

$$\tilde{P}_1^{(\mathrm{coh},1)} = -\frac{z_1}{2\ell_0}\big(2\langle I_0\rangle_{\mathbf{r}_0\to\mathbf{r}_1} - \mathrm{e}^{-z_1/\ell_0}\big)\, \mathrm{e}^{\mathrm{i}n_0 k z_1}. \tag{22}$$

For the sake of completeness, we also give here the expressions for the nonlinear correction (first order in α) of the refractive index, which result from (19)–(22), for diffuse and coherent light, respectively,

$$n_1(\mathbf{r}) = \frac{\mathrm{i}}{k\ell_0}\langle I_0(\mathbf{r})\rangle \tag{23}$$

$$n_1^{(\mathrm{coh})}(\mathbf{r}) = \frac{\mathrm{i}}{2k\ell_0}(2\langle I_0(\mathbf{r})\rangle - \mathrm{e}^{-z/\ell_0}). \tag{24}$$

Again, we note that our model exhibits no real part of the nonlinear index. We have checked that a non-vanishing real part would have no effect on the average intensity up to first order in α. (This might change for higher orders of α—a topic presently under investigation.)

What remains for the calculation of the total nonlinear average propagation ladder component is to add the above three cases (20), (21) and (22). The missing pieces of linear transport to or from position $\mathbf{r}_1$ or $\mathbf{r}_2$ are expressed by (15). This yields

$$L_1^{(\mathrm{prop})} = \mathcal{N}\int_V \frac{\mathrm{d}\mathbf{r}_1}{A\ell_0}\,\mathrm{d}\mathbf{r}_2 \langle I_0(\mathbf{r}_1)\rangle\langle I_0(\mathbf{r}_2)\rangle 2\,\mathrm{Re}\big\{\tilde{P}_1^{(1,2)}\big(\tilde{P}_0^{(1,2)}\big)^*\big\}$$
$$+\int_V \frac{\mathrm{d}\mathbf{r}_1}{A\ell_0}\langle I_0(\mathbf{r}_1)\rangle 2\,\mathrm{Re}\big\{\big(\tilde{P}_1^{(\mathrm{coh},1)} + \tilde{P}_1^{(1,\mathrm{det})}\big)\,\mathrm{e}^{-\mathrm{i}n_0^* k z_1}\big\}. \tag{25}$$

As in (11), the term $2\,\mathrm{Re}\{\cdots\}$ arises from adding the complex conjugate diagrams.

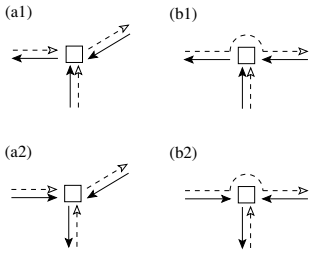

Figure 4. Crossed diagrams for nonlinear scattering (a1, a2) and nonlinear propagation (b1, b2). For each ladder diagram, see figures 3(a) and (b), there exist in general two different crossed diagrams contributing to the interference cone.

If the sample has slab geometry, with infinite length in the x and y directions and length L in the z direction, (25) can be simplified to

$$L_1^{(\mathrm{prop})} = -\int_0^L \frac{\mathrm{d}z}{\ell_0} \langle I_0(z)\rangle (2\langle I_0(z)\rangle^2 - 2\langle I_0(L)\rangle^2 + \mathrm{e}^{-2z/\ell_0} - \mathrm{e}^{-z/\ell_0}). \tag{26}$$

3.3. Interference cone

On top of the above ladder components, which define the weakly angle-dependent background of the average detection signal, one observes a narrow interference cone arising from the crossed diagrams. In the linear case, they describe the interference of each scattering path with its time-reversed counterpart. In our case, the two interfering amplitudes are equal in the exact backscattering direction due to time reversal symmetry. Hence, the height C_0 of the linear backscattering cone is equal to the background L_0—apart from the fact that single scattering contributions must be subtracted since they do not have a distinct, time-reversed counterpart

$$C_0 = L_0 - \int \frac{\mathrm{d}\mathbf{r}}{A\ell_0}\, \mathrm{e}^{-2z/\ell_0}. \tag{27}$$

The situation changes in the nonlinear regime. As is obvious from figure 4, there is in general more than one way to reverse a scattering path in the presence of a nonlinear event. We want to draw special attention to the nonlinear propagation diagram (b2), which appears somewhat counter-intuitive at first sight and does not have an easy interpretation. Here, one of the dashed arrows propagates from left to right, whereas the other one (from below) contributes to the 'pump intensity' for the nonlinear event. Concerning the solid lines, one could say that the left one is scattered downwards, whereas the right one contributes to the pump or vice versa (these two interpretations cannot be distinguished).

We note that the same diagram (b2) also applies to the case of a *homogeneous* nonlinear $\chi^{(3)}$ medium, into which linear scatterers are randomly embedded. (In fact, all results presented in this section concerning nonlinear propagation are equally valid in this case; only nonlinear scattering does not occur.) This is the situation examined in [27, 28], where, however, the diagram (b2) has not been taken into account. Consequently, [27, 28] predict that only the shape, but not the height of the backscattering cone is modified by the nonlinearity, whereas, according to our theory, also the cone height (i.e., the backscattering enhancement factor) is modified. Hence, one of the main motivations for the present paper was to demonstrate the importance of diagram (b2) by an independent method, i.e. by numerical simulation.

Due to time reversal symmetry, each of the crossed diagrams in figure 4 gives in general the same value as the corresponding ladder diagram in figure 3. Thus, the crossed is twice as large as the ladder contribution, yielding the nonlinear backscattering factor of three. However, the following special cases must be considered.

(i) As in the linear case, single scattering contributions must be subtracted. These are the cases where one of the two crossed diagrams is identical to the corresponding ladder or the two crossed diagrams are identical.
(ii) If both incoming solid lines originate from the coherent mode, the exchange factor of two (see above) must be removed (if present in the corresponding ladder diagram).
(iii) If only one of the incoming solid lines originates from the coherent mode, and the outgoing solid line propagates from the nonlinear event directly to the detector, the exchange factor of two must be taken into account (if absent in the corresponding ladder diagram).

Thereby, we find

$$C_1^{(\mathrm{sc})} = 2L_1^{(\mathrm{sc})} - 4\int_V \frac{\mathrm{d}\mathbf{r}}{A\ell_0}(3\langle I_0(\mathbf{r})\rangle - 2\mathrm{e}^{-z/\ell_0})\,\mathrm{e}^{-2z/\ell_0} \tag{28}$$

$$C_1^{(\mathrm{pr})} = 2L_1^{(\mathrm{pr})} + 3\int_V \frac{\mathrm{d}\mathbf{r}_1}{A\ell_0}\,\mathrm{e}^{-z_1/\ell_0}\left[\langle I_0(\mathbf{r}_1)\rangle(1-\mathrm{e}^{-z_1/\ell_0}) + 2\,\mathrm{Re}\left\{\tilde{P}_1^{(\mathrm{coh},1)}\,\mathrm{e}^{-\mathrm{i}n_0^* k z_1}\right\}\right]. \tag{29}$$

For a slab geometry, we obtain

$$C_1^{(\mathrm{pr})} = 2L_1^{(\mathrm{pr})} + 3\int_0^L \frac{\mathrm{d}z}{\ell_0}\langle I_0(z)\rangle(\mathrm{e}^{-z/\ell_0} - \mathrm{e}^{-2L/\ell_0}) - \left(\frac{1}{2} - \frac{3}{2}\,\mathrm{e}^{-2L/\ell_0} + \mathrm{e}^{-3L/\ell_0}\right). \tag{30}$$

4. Numerical results

For the numerical comparison, we will consider the case where the nonlinear scatterers are randomly distributed inside a sphere, with a homogeneous density. We have two parameters in our simulations, namely, the number of scatterers N and the radius of the sphere R. The (linear) optical thickness b along the diameter of the sphere being $2R/\ell_0$, we get the following relations:

$$k\ell_0 = \frac{(kR)^3}{3N} \tag{31a}$$

$$b = 2\frac{kR}{k\ell_0}. \tag{31b}$$

Typically, we have worked with several thousand scatterers, for optical thickness ranging from 1 to 3 and $k\ell_0$ between 50 and 100. For each configuration, the nonlinear set of equations (3) is solved using a Newton–Krylov method. Only a few iterations are needed to get a converged solution with a residual error smaller than 10^{-12}. From the solution, we calculate the radiated field and intensity outside the cloud in different directions. This procedure is then repeated with many different configurations (typically 1000) giving us the disorder averaged field and intensity. More precisely, the nonlinear system is solved for different values of the parameter α ranging from 0 to 10^{-3}, and the first nonlinear corrections to the averaged quantities are obtained as follows:

$$I_1(\mathbf{n}) = \frac{\overline{I(\mathbf{n},\alpha)} - \overline{I(\mathbf{n},0)}}{\alpha} \tag{32}$$

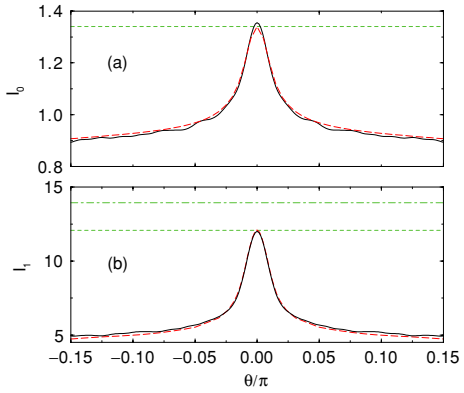

Figure 5. Linear intensity I_0 (top) and nonlinear correction I_1 (bottom) averaged over 1000 configurations, in the case of 2500 scatterers in a sphere of optical thickness $b = 2.45$ with $k\ell_0 \approx 64$. The solid curves are the numerical results, whereas the long dashed ones are the theoretical calculations. As one can see, the agreement is rather excellent. In particular, the nonlinear cone clearly exhibits an enhancement factor larger than two, due to the effect of interference between three amplitudes. The horizontal dashed lines correspond to the intensity in the exact backward direction, and the dot-dashed line on the bottom plot would be the same result without taking into account the diagram (b2) of figure 4 contributing to the nonlinear propagation of the crossed intensity, thus emphasizing its importance.

where $\mathbf{n}$ represents the direction of observation and $\overline{I}$ means configuration average. We have checked that I_1 is independent of the value of α. We have also checked that we recover the same results, if, for each configuration, we first solve the linear system (5) and then get the first-order nonlinear correction to the field from the linear system (10); from this solution, we calculate the outgoing intensity and then perform the configuration average.

In the case of 2500 scatterers in a sphere of optical thickness $b = 2.45$ with $k\ell_0 \approx 64$, the linear intensity I_0 and nonlinear correction I_1 averaged over 1000 configurations are compared with the theoretical predictions in figure 5. The top plot depicts the linear results and the bottom one the nonlinear corrections. The solid curves are the numerical results, whereas the long dashed ones are the theoretical calculations according to the method presented in section 3 (with some straightforward extensions to account for the precise angle dependence of the backscattered intensity). As one can see, the agreement is rather excellent. The horizontal dashed lines correspond to the intensity in the exact backward direction and the dot-dashed line on the bottom plot would be the same result without taking into account the diagram (b2) of figure 4 contributing to the nonlinear propagation of the crossed intensity. Thus, even if at first glance, the contribution of this diagram to the backscattered intensity seemed not to be obvious and, for this reason, was not mentioned in earlier papers on nonlinear effects in coherent backscattering [13, 27, 28], the comparison with the present numerical simulations really emphasizes its importance. Finally, the numerical values of the nonlinear ladder and crossed term are in this case $L_1 = 4.85$ and $C_1 = 7.22$. Obviously C_1 is larger than L_1, emphasizing the fact that for each ladder diagram there correspond, in general, two crossed diagrams. The fact that the nonlinear enhancement factor of three, corresponding to $C_1 = 2L_1$, is not precisely realized in figure 5(b) can be traced back to single scattering and similar processes, see the discussion before equation (29).

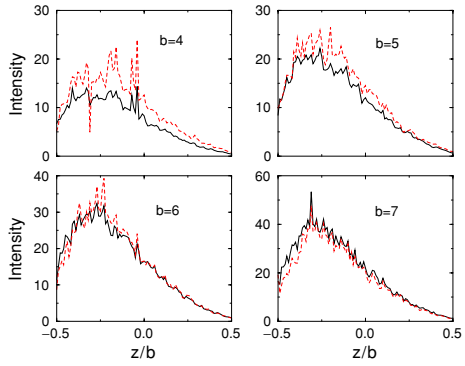

Figure 6. Comparison between the first and second order in the nonlinearity strength α for the intensity inside the bulk for different values of the optical thickness b. More precisely, we plot the intensity along the diameter of the sphere parallel to the incident laser beam. The horizontal axis is thus the position on the diameter in units of optical thickness b ($z = 0$ is the centre of the sphere, $z = -\frac{1}{2}$ corresponds to the illuminated surface and $z = \frac{1}{2}$ corresponds to the opposite surface). The solid lines denote $I_1(b, z)$, whereas the dashed lines correspond to $I_2(b, z)/b^2$. One can clearly see that for increasing optical thickness b, the two curves are getting closer to each other, thus emphasizing that, in the large b limit, one has $I_2(b, z) \approx b^2 I_1(b, z)$ and, thus, that the relevant perturbation parameter is $b^2\alpha$.

We note that the angular width of the backscattering cone is roughly the same in the linear and the nonlinear case, in both cases being mainly determined by the optical thickness ($b = 2.45$) and the geometry (sphere) of the scattering medium. For larger values of the optical thickness, the nonlinear cone is expected to become narrower than the linear one, since longer light paths are more probably affected by a nonlinear event than shorter ones. This may eventually lead to the appearance of a 'dip' in the total (linear plus nonlinear) backscattering cone [27, 28].

Finally, we want to discuss the validity of the present approach. Formally, the present approach is an expansion in powers of α, the strength of the nonlinearity, but the coefficients of this series depend on the geometry of the medium, especially on the optical thickness b (omitting bordering effects):

$$I(\alpha, b) = I_0(b) + \alpha I_1(b) + \alpha^2 I_2(b) + \cdots. \tag{33}$$

For the present approach to be valid, each term in this series must be much smaller than the preceding one, that is $\alpha I_{n+1}(b) \ll I_n(b)$. In a preceding paper [14], we gave a rough quantitative estimation, based on the distribution of the number N of scattering events which a backscattered photon undergoes in a linear random walk. If we assign to each scattering event the same probability $\alpha \ll 1$ to be nonlinear, the ratio p_2/p_1 of the probabilities for two and one nonlinear events, respectively, follows as $p_2/p_1 = \alpha\langle N^2\rangle/2\langle N\rangle$. Since, as we have checked numerically, $\langle N\rangle \propto b$ and $\langle N^2\rangle \propto b^3$ (in the limit of large b), the criterion $p_2 \ll p_1$ for the validity of the perturbative treatment turns out to be $\alpha b^2 \ll 1$.

This is confirmed by the present numerical simulations. In figure 6, we compared the first and second order for the intensity inside the bulk for different values of the optical thickness b. More precisely, we plot the intensity along the diameter of the sphere parallel to the incident laser beam. The horizontal axis is thus the position on the diameter in units of

optical thickness b ($z = 0$ is the centre of the sphere, $z = -\frac{1}{2}$ corresponds to the illuminated surface and $z = \frac{1}{2}$ corresponds to the opposite surface). The fluctuations in the signals originate from the exceptional presence, in a given configuration, of a scatterer very close to the diameter (smaller than the wavelength λ), resulting in a large local intensity. These fluctuations are also present in the linear case and their sizes decrease when increasing the number of configurations. The solid lines denote $I_1(b, z)$, whereas the dashed lines correspond to $I_2(b, z)/b^2$. For these numerical computations, in order to achieve larger optical thickness, we have lowered the value $k\ell_0$ down to $\approx$30, which still leads to correct linear results (i.e., the dilute medium approximation $k\ell_0 \gg 1$ is still valid). The number of scatterers is $N = 2048$ (4000, 6390 and 10 976) for an optical thickness $b = 4$ (5, 6 and 7). The final quantities results from the average over 1000 different configurations. One sees that in all the four cases $I_2(b, z) \approx b^2 I_1(b, z)$ and, thus, that the relevant perturbation parameter is $b^2\alpha$. The small change in the ratio between $I_2(b, z)/b^2$ and $I_1(b, z)$, which is observed from $b = 4$, where $I_2(b, z)/b^2$ is slightly larger than $I_1(b, z)$, to $b = 7$, where $I_2(b, z)/b^2$ is equal to $I_1(b, z)$, shows that the large b limit is not yet reached at $b = 4$.

5. Conclusion

In summary, we have presented a numerical study of nonlinear effects on the coherent backscattering cone. More precisely, we have considered a simplified model of 'classical' two-level atoms, in which the inelastic scattering was removed, only keeping the nonlinear elastic scattering events. This allowed us to write a closed set of nonlinear equations describing the electromagnetic field in a cloud of such nonlinear scatterers illuminated by a laser beam. From its exact numerical solution, we computed the first-order nonlinear corrections C_1 and L_1 to the backscattering cone, which we compared with a diagrammatic approach. The validity of the latter is proved by the excellent agreement between the two approaches. In particular, it emphasizes the fact that, in general, the nonlinear scattered intensity results from the interferences between *three* amplitudes leading to a nonlinear correction C_1 of the interference cone up to two times larger than the nonlinear correction L_1 of the diffuse intensity. Finally, when comparing the first- and second-order term in α for the intensity inside the bulk, we have shown that the relevant perturbation parameter is $b^2\alpha$, where b is the optical thickness.

A natural way to extend this work is to relax the perturbative assumption and admit more than one nonlinear scattering event. Since the number of interfering amplitudes increases if more than two photons are connected by nonlinear scattering events, we expect the occurrence of even larger enhancement factors in the nonperturbative regime—especially in the case of scatterers with positive nonlinearity, i.e. for scatterers whose cross section *increases* with increasing intensity.

Furthermore, the relation between coherent backscattering and weak localization in the presence of nonlinear scattering remains to be explored. Does a large nonlinear enhancement of coherent backscattering also imply a strong reduction of nonlinear diffusive transport? The answer to this question could shed new light onto the problem of wave localization in nonlinear media.

Acknowledgments

We would like to thank Dominique Delande and Christian Miniatura for stimulating discussions. TW was supported by the DFG. Laboratoire Kastler Brossel is laboratoire de l'Université Pierre et Marie Curie et de l'Ecole Normale Superieure, UMR 8552 du CNRS.

References

[1] Labeyrie G, de Tomasi F, Bernard J C, Müller C A, Miniatura C and Kaiser R 1999 *Phys. Rev. Lett.* **83** 5266
[2] Wilkowski D *et al* 2004 *J. Opt. Soc. Am.* B **21** 183 and references therein
[3] Sigwarth O, Labeyrie G, Jonckheere T, Delande D, Kaiser R and Miniatura C 2004 *Phys. Rev. Lett.* **93** 143906
[4] Chanelière T, Wilkowski D, Bidel Y, Kaiser R and Miniatura C 2004 *Phys. Rev.* E **70** 036602
[5] Akkermans E and Montambaux G 1995 *Mesoscopic Quantum Physics* ed J L Pichard and J Zinn-Justin (Amsterdam: North-Holland)
[6] Akkermans E and Montambaux G 2004 *Physique mésoscopique des électrons et des photons* (Paris: EDP Sciences/CNRS Editions) (an english translation is in preparation)
[7] van Albada M P and Lagendijk A 1985 *Phys. Rev. Lett.* **55** 2692
[8] Wolf P E and Maret G 1985 *Phys. Rev. Lett.* **55** 2696
[9] Jonckheere T, Müller C A, Kaiser R, Miniatura C and Delande D 2000 *Phys. Rev. Lett.* **85** 4269
[10] Müller C A, Jonckheere T, Miniatura C and Delande D 2001 *Phys. Rev.* A **64** 053804
[11] Müller C A and Miniatura C 2002 *J. Phys. A: Math. Gen.* **35** 10163
[12] Wellens T, Grémaud B, Delande D and Miniatura C 2004 *Phys. Rev.* A **70** 023817
[13] Wellens T, Grémaud B, Delande D and Miniatura C 2005 *Phys. Rev.* E **71** R055603
[14] Wellens T, Grémaud B, Delande D and Miniatura C 2006 *Phys. Rev.* A **73** 013802
[15] Shatokhin V, Müller C A and Buchleitner A 2005 *Phys. Rev. Lett.* **94** 043603
[16] Grémaud B, Wellens T, Delande D and Miniatura C 2006 *Phys. Rev.* A **74** 033808
[17] Cao H 2003 *Waves Random Media* **13** R1
[18] Clément D, Varón A F, Hugbart M, Retter J A, Bouyer P, Sanchez-Palencia L, Gangardt D M, Shlyapnikov G V and Apect A 2005 *Phys. Rev. Lett.* **95** 170409
[19] Fort C, Fallani L, Guarrera V, Lye J E, Modugno M, Wiersma D S and Inguscio M 2005 *Phys. Rev. Lett.* **95** 170410
[20] Schulte T, Drenkelforth S, Kruse J, Ertmer W, Arlt J, Sacha K, Zakrzewski J and Lewenstein M 2005 *Phys. Rev. Lett.* **95** 170411
[21] Cohen-Tannoudji C, Dupont-Roc J and Grynberg G 1992 *Atom–Photon Interactions* (New York: Wiley)
[22] Spivak B and Zyuzin A 2000 *Phys. Rev. Lett.* **84** 1970
[23] Skipetrov S and Maynard R 2000 *Phys. Rev. Lett.* **85** 736
[24] Rusek M, Orłowski A and Mostowski J 1996 *Phys. Rev.* E **53** 4122
[25] Rusek M, Mostowski J and Orłowski A 1999 *Phys. Rev.* A **61** 022704
[26] Pinheiro F A, Rusek M, Orłowski A and van Tiggelen B A 2004 *Phys. Rev.* E **69** 026605
[27] Agranovich V M and Kravtsov V E 1991 *Phys. Rev.* B **43** 13691
[28] Heiderich A, Maynard R and van Tiggelen B A 1995 *Opt. Commun.* **115** 392

Coherent backscattering in nonlinear atomic media: Quantum Langevin approach

Benoît Grémaud,[1,*] Thomas Wellens,[1,2] Dominique Delande,[1] and Christian Miniatura[2]
[1]*Laboratoire Kastler Brossel, Université Pierre et Marie Curie, 4, place Jussieu, 75252 Paris Cedex 05, France*
[2]*Institut Non Linéaire de Nice, UMR 6618, 1361 route des Lucioles, F-06560 Valbonne, France*
(Received 1 June 2005; revised manuscript received 24 May 2006; published 12 September 2006)

In this theoretical paper, we investigate coherence properties of the near-resonant light scattered by two atoms exposed to a strong monochromatic field. To properly incorporate saturation effects, we use a quantum Langevin approach. In contrast to the standard optical Bloch equations, this method naturally provides the inelastic spectrum of the radiated light induced by the quantum electromagnetic vacuum fluctuations. However, to get the right spectral properties of the scattered light, it is essential to correctly describe the statistical properties of these vacuum fluctuations. Because of the presence of the two atoms, these statistical properties are not Gaussian: (i) the spatial two-points correlation function displays a specklelike behavior and (ii) the three-points correlation function does not vanish. We also explain how to incorporate in a simple way propagation with a frequency-dependent scattering mean-free path, meaning that the two atoms are embedded in an average scattering dispersive medium. Finally we show that saturation-induced nonlinearities strongly modify the atomic scattering properties and, as a consequence, provide a source of decoherence in multiple scattering. This is exemplified by considering the coherent backscattering configuration where interference effects are blurred by this decoherence mechanism. This leads to a decrease of the so-called coherent backscattering enhancement factor.

DOI: 10.1103/PhysRevA.74.033808 PACS number(s): 42.50.Lc, 42.65.−k, 42.50.Ar, 42.25.Dd

I. INTRODUCTION

Over the past ten years, cold atomic gases have gradually become a widely employed and highly tunable tool for testing new ideas in many areas of quantum physics: quantum phase transitions (Bose-Einstein condensation, Fermi degenerate gases, Mott-Hubbard transition) [1–3], quantum chaos [4], applications in metrology [5], and disordered systems [6–8] to cite a few. In the latter case, cold atomic vapors act as dilute gases of randomly distributed atoms multiply scattering an incident monochromatic laser light. In this case, the scattered light field exhibits a specklelike structure due to (multiple) interference between all possible scattering paths. The key point is that the disorder average is insufficient to erase all interference effects. This gives rise to weak or strong localization effects in light transport depending on the strength of disorder [9,10]. A hallmark of this coherent transport regime is the coherent backscattering (CBS) phenomenon: the average intensity multiply scattered off an optically thick sample is up to twice larger than the average background in a small angular range around the direction of backscattering, opposite to the incoming light [11]. This interference enhancement of the diffuse reflection off the sample is a manifestation of a two-wave interference. As such, it probes the coherence properties of the outgoing light [12]. The CBS effect in cold atomic gases has been the subject of extensive studies in the weak localization regime, both from theoretical and experimental points of view [13]. In particular, modifications brought by atoms, as compared to classical scatterers, for light transport properties (mean-free path, coherence length, CBS enhancement factor) have been highlighted. They are essentially due to the quantum internal atomic structure [14,15].

Another interesting feature of atoms is their ability to display a nonlinear behavior: the scattered light is no more proportional to the incident one. This leads to a wide variety of phenomena, like pattern formation, four-wave mixing, self-focusing effects, dynamical instabilities, etc. [16–19]. For a weak nonlinearity, introducing an intensity-dependent susceptibility is enough to properly describe these effects, including quantum properties [16,20,21], e.g., the Kerr effect (intensity dependence of the refractive index) can be obtained with a $\chi^{(3)}$ nonlinearity. However, when the incident intensity is large enough, and this is easily achieved with atoms, perturbation theories eventually fail and a full nonlinear treatment is required. For a single two-level atom, the solution is usually given by the so-called optical Bloch (OB) equations. Together with the quantum regression theorem, they allow for a complete description of the spectral properties of the fluorescence light [23]. In particular, these equations show that the atomic nonlinear behavior is intrinsically linked to the quantum nature of the electromagnetic field. More specifically, as opposed to classical nonlinear scatterers, the radiated light exhibits quantum fluctuations characterized by peculiar time correlation properties. They define a power spectrum, known as the Mollow triplet, emphasizing inelastic scattering processes at work in the emission process [23–25].

However, even if all these aspects are well understood in the case of a *single* atom exposed to a strong monochromatic field [23], the situation changes dramatically in the case of a large number of atoms where a detailed analysis including both quantum nonlinear properties and coherence effects is still lacking. Until now, the nonlinear coupling between the atoms and the quantum vacuum fluctuations is either included in a perturbative scheme [21,22] or simply described by a classical noise [26–30]. In the dilute regime $\lambda \ll R$ where the light wavelength λ is much less than the average particle separation R, one expects the quantum fluctuations to

*Electronic address: Benoit.Gremaud@spectro.jussieu.fr

reduce the degree of coherence of the scattered light. This will alter not only propagation parameters (mean-free path, refraction index), but also weak localization corrections to transport, and the CBS enhancement factor, which is related to the coherence properties of the scattered light field [7,8,12]. We want here to stress that, even beyond interference and weak localization phenomena, any transport property which may be influenced by saturating the atomic transition deserves a special and necessary study on its own. The most striking systems falling in this category where both nonlinear and disordered descriptions are intimately interwoven are coherent random lasers [31], where interference effects lead to localized light modes inside the disordered medium, comparable to resonator eigenmodes in chaotic lasers [32–35]. Even if, in this case, one would require an active (i.e., amplifying) medium, a key point is the understanding of the mutual effects between multiple interference and nonlinear scattering.

In the present paper, we will focus on the rather simple case of two atoms in vacuum. Our aim is threefold. (i) First to properly calculate quantum correlations between pairs of atoms as a crucial step towards a better understanding of the physical mechanisms at work, (ii) second to implement a method allowing for a simple incorporation of frequency-dependent propagation effects, and (iii) finally to understand, in the CBS situation, the modifications brought by the (quantum) nonlinearity to the interference properties. We hope that these points, once mastered, can provide an efficient way to produce realistic computer models to simulate real experiments. Point (i) alone could easily be solved using the standard OB method [36,37]. But the latter almost becomes useless regarding point (ii), since frequency-dependent propagation leads to complicated time-correlation functions. From a numerical point of view, it also leads to such large linear systems of coupled equations that its practical use is limited up to only a few atoms, very far from a real experimental situation. For these reasons, we will rather use the quantum Langevin method for our purposes. This method not only solves points (i) and (ii), but also leads to a simple explanation of point (iii), through a direct evaluation of the quantum noise spectrum. Note however that, in the absence of any effective medium surrounding the two atoms, and as long as only the numerical results are concerned (but not the physical interpretation), the quantum Langevin approach is completely equivalent to solving the multiatom optical Bloch equations as in Refs. [36,37].

This paper divides as follows. In Sec. II, the notations are defined and the quantum Langevin approach is explained for the single atom case. In Sec. III, the method is adapted to the case where two atoms are weakly coupled by the dipole interaction. The validity and relevance of the method is controlled by a comparison with a direct calculation using OB equations. Then, in the CBS configuration, numerical results for different values of the laser intensity and detuning are presented and discussed in Sec. IV. In particular, possible reasons for the reduction of the enhancement factor are put forward. Conclusions and possible continuations are given in Sec. V.

II. SINGLE TWO-LEVEL ATOM CASE

A. Time-domain approach

We consider an atom with a zero angular momentum electronic ground state ($J_g=0$) exposed to a monochromatic light field. The light field frequency ω_L is near-resonant with an optical dipole transition connecting this ground state to an excited state with angular momentum $J_e=1$. The angular frequency separation between these two states is ω_0 and the natural linewidth of the excited state is Γ. We will denote hereafter by $\delta_L=\omega_L-\omega_0$ the laser detuning. The ground state is denoted by $|00\rangle$ while the excited states are denoted by $|1m_e\rangle$, with $m_e=-1,0,1$ the Zeeman magnetic quantum number. As we assume no magnetic field to be present throughout this paper, the excited state is triply degenerate.

In the Heisenberg picture, this two-level atom is entirely characterized by the following set of 16 time-dependent operators:

$$\Pi^g = |00\rangle\langle 00|, \quad \Pi^e_{m_e m'_e} = |1m_e\rangle\langle 1m'_e|,$$

$$\mathcal{D}^+_{m_e} = |1m_e\rangle\langle 00|, \quad \mathcal{D}^-_{m_e} = |00\rangle\langle 1m_e|. \tag{1}$$

The atomic operators obey the completeness constraint

$$1 = \Pi^g + \Pi^e, \tag{2}$$

where Π^g and $\Pi^e=\Sigma_{m_e}\Pi^e_{m_e m_e}$ are the ground and excited state atomic population operators.

The full atom-field Hamiltonian $\mathcal{H}$ is the sum of the free atom Hamiltonian $\mathcal{H}_A=\hbar\omega_0\Pi^e$, of the free quantized field Hamiltonian $\mathcal{H}_F=\Sigma_{\mathbf{k},\boldsymbol{\epsilon}\perp\mathbf{k}}\hbar\omega_{\mathbf{k}}a^\dagger_{\mathbf{k}\boldsymbol{\epsilon}}a_{\mathbf{k}\boldsymbol{\epsilon}}$ and of the dipolar interaction $\mathcal{V}=-\mathbf{d}\cdot(\mathbf{E}_L+\mathbf{E}_V)$ between the atomic dipole $\mathbf{d}$, the classical laser field $\mathbf{E}_L$, and the quantum electromagnetic vacuum field $\mathbf{E}_V$. Performing the usual approximations of quantum optics, i.e., neglecting nonresonant terms (rotating wave approximation) and assuming Markov-type correlations between the atomic operators and the vacuum field, one obtains the quantum Langevin equations controlling the time evolution of any atomic operator $\mathcal{O}$ in the rotating frame [23,26]:

$$\frac{d\mathcal{O}}{dt} = i\delta_L[\mathcal{O},\Pi^e] - \frac{i}{2}\sum_q (-1)^q[\mathcal{O},\mathcal{D}^+_q]\Omega^{L+}_{-q}(\mathbf{R}) - \frac{i}{2}\sum_q [\mathcal{O},\mathcal{D}^-_q]\Omega^{L-}_q(\mathbf{R}) - \frac{\Gamma}{2}(\mathcal{O}\Pi^e + \Pi^e\mathcal{O}) + \Gamma\sum_q \mathcal{D}^+_q\mathcal{O}\mathcal{D}^-_q + \mathcal{F}_\mathcal{O}(\mathbf{R},t), \tag{3}$$

where Ω^{L+}_q (Ω^{L-}_q) are the components of the Rabi frequency of the positive (negative) frequency parts of the incident laser beam, i.e., $\hbar\boldsymbol{\Omega}=-d\mathbf{E}$ where d is the dipole strength. Finally $\mathcal{F}_\mathcal{O}(t)$ is the Langevin force depicting the effects of the quantum fluctuations of the vacuum electromagnetic field and reads

$$\mathcal{F}_{\mathcal{O}}(t) = -\frac{i}{2}\sum_q (-1)^q [\mathcal{O}, \mathcal{D}_q^+]\Omega_{-q}^{0+}(\mathbf{R},t) - \frac{i}{2}\sum_q \Omega_q^{0-}(\mathbf{R},t)[\mathcal{O}, \mathcal{D}_q^-], \tag{4}$$

where $\Omega^{0+}(\mathbf{R},t)$ is the vacuum Rabi field operator

$$\mathbf{\Omega}^{0+}(\mathbf{R},t) = -\frac{2id}{\hbar}\sum_{\mathbf{k},\boldsymbol{\epsilon}\perp\mathbf{k}} \mathcal{E}(\omega)\boldsymbol{\epsilon} a_{\mathbf{k}\boldsymbol{\epsilon}}(t_0) e^{i\mathbf{k}\cdot\mathbf{R}-i(\omega-\omega_L)(t-t_0)} \tag{5}$$

with t_0 an initial time far in the past. In the case of a surrounding cavity, one would expand the vacuum Rabi field onto the cavity modes [34] instead of the free space modes $\boldsymbol{\epsilon} a_{\mathbf{k}\boldsymbol{\epsilon}}(t_0)e^{i\mathbf{k}\cdot\mathbf{R}-i(\omega-\omega_L)(t-t_0)}$. From the preceding expression, one can calculate the time correlation functions of the vacuum field [38]

$$(-1)^q[\Omega_{-q}^{0+}(\mathbf{R},t), \Omega_{q'}^{0-}(\mathbf{R},t')] = 4\Gamma\delta_{qq'}f(t-t'), \tag{6}$$

where $f(\tau)$ is a function centered around $\tau=0$, whose width τ_c is much smaller than any characteristic atomic time scale (i.e., $\tau_c \ll \omega_0^{-1} \ll \Gamma^{-1}$) and whose time integral is equal to unity. Thus, hereafter, $f(\tau)$ will be safely replaced by a δ function $f(\tau)\to\delta(\tau)$.

The time evolution for the expectation values is obtained by averaging over the initial density matrix $\sigma(t_0)$, i.e., $\langle\mathcal{O}(t)\rangle = \mathrm{Tr}[\mathcal{O}(t)\sigma(t_0)]$. Since the atom and the vacuum field are supposed to be decoupled initially, $\sigma(t_0)$ is simply $\sigma_{\mathrm{at}}(t_0)\otimes|0\rangle\langle 0|$ ($|0\rangle$ being the vacuum field state). Because of the normal ordering, one immediately gets

$$\langle\mathcal{F}_{\mathcal{O}}(t)\rangle = 0, \tag{7}$$

and the time correlation functions of the Langevin forces

$$\langle\mathcal{F}_{\mathcal{O}}(t)\mathcal{F}_{\mathcal{O}'}(t')\rangle = -\Gamma\left\langle\sum_q [\mathcal{O}(t), \mathcal{D}_q^+(t)][\mathcal{O}'(t'), \mathcal{D}_q^-(t')]\right\rangle\delta(t-t'). \tag{8}$$

The physical picture of the quantum Langevin approach is to represent quantum fluctuations by a fluctuating force acting on the system, in analogy with the usual Brownian motion. Not surprisingly, this leads to a diffusivelike behavior of expectation values. More precisely, because of the δ function in Eq. (8), we can set $t'=t$ for the atomic operators and we finally obtain in the stationary regime $t \gg t_0$:

$$\langle\mathcal{F}_{\mathcal{O}}(t)\mathcal{F}_{\mathcal{O}'}(t')\rangle = \frac{\Gamma}{4}D_{\mathcal{O}\mathcal{O}'}\delta(t-t'), \tag{9}$$

where D is a matrix of diffusion constants depending only on the stationary values of the atomic operators. The stationary hypothesis also results from the fact that these correlation functions only depend on the time difference $t-t'$.

From this, it is possible to prove that the quantum regression theorem applies [23,39], allowing for the calculation of two-times correlation functions of the atomic operators and of their expectation values. From their Fourier transforms, one can obtain the spectrum of the radiated light. But, for the reasons mentioned in the Introduction, we will explain how these properties can be obtained in a much simpler way by directly translating the Langevin equations in the Fourier domain [39].

B. Frequency-domain approach

First, because of the constraint (2), only 15 atomic operators are actually independent. More specifically, we will use the following set, denoted by the column vector $\mathbf{X}$:

$$\begin{aligned} \Pi_{m_e}^z &= \frac{1}{2}[\Pi_{m_e m_e}^e - \Pi^g], \\ \Pi_{m_e m_e'}^e &= |1m_e\rangle\langle 1m_e'|, \quad m_e \neq m_e', \\ \mathcal{D}_{m_e}^+ &= |1m_e\rangle\langle 00|, \\ \mathcal{D}_{m_e}^- &= |00\rangle\langle 1m_e|. \end{aligned} \tag{10}$$

The Langevin equations for $\mathbf{X}$ then formally read as follows

$$\frac{d}{dt}\mathbf{X}(t) = M\mathbf{X}(t) + \mathbf{L} + \mathbf{F}(t), \tag{11}$$

where M is a time-independent matrix depending on the laser Rabi frequency $\Omega^{L\pm}$, $\mathbf{L}$ is a constant vector scaling with Γ and $\mathbf{F}(t)$ is a vector characterizing the Langevin forces at work on the atom (for simplicity, we have dropped the explicit position dependence). The stationary expectation values are then simply given by

$$\langle\mathbf{X}\rangle = -M^{-1}\mathbf{L}. \tag{12}$$

The Fourier transforms of the different quantities are defined as follows:

$$f(\Delta) = \int dt f(t)e^{i\Delta t}, \qquad f(t) = \int \frac{d\Delta}{2\pi} f(\Delta)e^{-i\Delta t}, \tag{13}$$

leading to the Langevin equations in the frequency domain

$$(-i\Delta 1 - M)\mathbf{X}(\Delta) = 2\pi\delta(\Delta)\mathbf{L} + \mathbf{F}(\Delta). \tag{14}$$

Introducing the Green's function $G(\Delta)=(-i\Delta 1 - M)^{-1}$, the solution of the preceding equations simply reads

$$\mathbf{X}(\Delta) = G(\Delta)[2\pi\delta(\Delta)\mathbf{L} + \mathbf{F}(\Delta)]. \tag{15}$$

Using $G(0)=-M^{-1}$ and Eq. (12), this solution separates into a nonfluctuating part $\mathbf{X}_L(\Delta)$ and a fluctuating (frequency-dependent) part $\mathbf{X}_F(\Delta)$:

$$\mathbf{X}_L(\Delta) = 2\pi\delta(\Delta)\langle\mathbf{X}\rangle, \qquad \mathbf{X}_F(\Delta) = G(\Delta)\mathbf{F}(\Delta). \tag{16}$$

From the linearity of the Fourier transform, we still have $\langle\mathbf{F}(\Delta)\rangle=\mathbf{0}$ implying $\langle\mathbf{X}_F(\Delta)\rangle=\mathbf{0}$. The time correlation functions for the Langevin force components, Eq. (8), become

$$\langle \mathbf{F}_i(\Delta')\mathbf{F}_j(\Delta)\rangle = 2\pi\delta(\Delta'+\Delta)\Gamma D_{ij}, \tag{17}$$

where the $2\pi\delta(\Delta'+\Delta)$ function is a direct consequence of the time-translation invariance, i.e., that we calculate the correlation functions in the stationary regime. This implies that the correlation function for the components of $\mathbf{X}_F$ in the frequency domain are

$$\langle (\mathbf{X}_F(\Delta'))_i (\mathbf{X}_F(\Delta))_j\rangle = 2\pi\delta(\Delta+\Delta')(GD^tG)_{ij}, \tag{18}$$

where the superscript t means matrix transposition.

The field radiated at frequency Δ by the atom at a distance $r \gg \lambda$ (far-field regime) reads as follows:

$$(-1)^q \Omega^+_{-q}(\Delta) = -\frac{3}{2}\Gamma \mathcal{P}^{\mathbf{r}}_{qq'} \mathcal{D}^-_{q'}(\Delta)\frac{e^{ikr}}{kr}, \tag{19}$$

where we use implicit sum over repeated indices. $\mathcal{P}^{\mathbf{r}}$ is the projector onto the plane perpendicular to vector $\mathbf{r}$:

$$\mathcal{P}^{\mathbf{r}}_{qq'} = \bar{\boldsymbol{\epsilon}}_q \mathcal{P}^{\mathbf{r}} \boldsymbol{\epsilon}_{q'} = \bar{\boldsymbol{\epsilon}}_q \left(1 - \frac{\mathbf{r}\,{}^t\mathbf{r}}{r^2}\right)\boldsymbol{\epsilon}_{q'} = \delta_{qq'} - (-1)^q \frac{\mathbf{r}_{-q}\mathbf{r}_{q'}}{r^2}, \tag{20}$$

where the overbar denotes complex conjugation and where $(\mathbf{r}\,{}^t\mathbf{r})$ is a dyadic tensor.

The correlation functions $\langle \Omega^-_{q'}(\Delta')\Omega^+_q(\Delta)\rangle$ of the light emitted by the atom is then proportional to $\langle \mathcal{D}^+_{q'}(\Delta')\mathcal{D}^-_q(\Delta)\rangle$ and read

$$\langle \Omega^-_{q'}(\Delta')\Omega^+_q(\Delta)\rangle \propto (2\pi)^2\delta(\Delta)\delta(\Delta')\langle \mathcal{D}^+_{q'}\rangle\langle \mathcal{D}^-_q\rangle + 2\pi\delta(\Delta'+\Delta)\sum_{j'j} G_{i'j'}(\Delta')G_{ij}(\Delta)D_{j'j}, \tag{21}$$

where the index i (i') corresponds to $\mathcal{D}^-_q$ ($\mathcal{D}^+_{q'}$). The nonfluctuating part gives rise to a spectral component of the emitted light at exactly the incident laser frequency and is thus naturally called the elastic part. The fluctuating part gives rise to the inelastic Mollow triplet spectrum [41], whose properties (position and width of the peaks) are given by the poles of $G(\Delta)$, i.e., by the complex eigenvalues of M. Actually, we simply recover the results of the quantum regression theorem, which states that the atomic time correlation functions evolve with the same equations than the expectation values $\langle \dot{\mathbf{X}}\rangle = M\langle \mathbf{X}\rangle + \mathbf{L}$ [23,24].

III. TWO-ATOM CASE

A. Optical Bloch equations

We now consider two isolated atoms, located at fixed positions $\mathbf{R}_1$ and $\mathbf{R}_2$. Defining $\mathbf{R} = \mathbf{R}_2 - \mathbf{R}_1 = R\mathbf{u}$ (with $R = |\mathbf{R}|$ and $\mathbf{u}$ the unit vector joining atom 1 to atom 2), we assume the far-field condition $R \gg \lambda$ to hold. We also assume that R is sufficiently small for the light propagation time R/c to be much smaller than any typical atomic time scales $(\Gamma^{-1}, \delta^{-1}, \Omega_L^{-1})$. In this regime, all quantities involving the two atoms are to be computed at the same time t. The contribution of the atom-atom dipole interaction in the Langevin equation for any atomic operator $\mathcal{O}$ reads

$$\left.\frac{d\mathcal{O}}{dt}\right|_{\text{dip.}} = i\frac{3\Gamma}{4}\left\{([\mathcal{O},\mathcal{D}^{1+}_q]\mathcal{P}^{\mathbf{R}}_{qq'}\mathcal{D}^{2-}_{q'} + [\mathcal{O},\mathcal{D}^{2+}_q]\mathcal{P}^{\mathbf{R}}_{qq'}\mathcal{D}^{1-}_{q'})\frac{e^{ikR}}{kR} + (\mathcal{D}^{1+}_q\mathcal{P}^{\mathbf{R}}_{qq'}[\mathcal{O},\mathcal{D}^{2-}_{q'}] + \mathcal{D}^{2+}_q\mathcal{P}^{\mathbf{R}}_{qq'}[\mathcal{O},\mathcal{D}^{1-}_{q'}])\frac{e^{-ikR}}{kR}\right\}. \tag{22}$$

In the OB equations, the two-atom system is entirely described by the set of 256 operators X_{ij} made of all possible products $X^1_i X^2_j$. The stationary expectation values $\langle X_{ij}\rangle$ are then obtained as solutions of a linear system resembling Eq. (12). This is the approach used in Ref. [37], where such optical Bloch equations are solved.

Since the two atoms are far enough from each other, the electromagnetic field radiated by one atom onto the other can be treated as a perturbation with respect to the incident laser field. More precisely, the solutions $\langle X_{ij}\rangle$ can be expanded up to second order in powers of g and $\bar{g}$:

$$\langle X_{ij}\rangle = \langle X_{ij}\rangle^{(0)} + g\langle X_{ij}\rangle^{(g)} + \bar{g}\langle X_{ij}\rangle^{(\bar{g})} + g\bar{g}\langle X_{ij}\rangle^{(g\bar{g})} + g^2\langle X_{ij}\rangle^{(gg)} + \bar{g}^2\langle X_{ij}\rangle^{(\bar{g}\bar{g})}, \tag{23}$$

where the complex coupling constant g is

$$g = i\frac{3\Gamma}{2}\frac{\exp(ikR)}{kR}. \tag{24}$$

In fact, it will be shown below that both terms in g^2 and $\bar{g}^2$ give a vanishing contribution to the coherent backscattering signal.

As explained in the Introduction, this approach has two drawbacks: (i) the solutions obtained in this way are global and, thus, do not provide a simple understanding of the properties of the emitted light and (ii) when the two atoms are embedded in a medium whose susceptibility strongly depends on the frequency, the field radiated by one atom onto the other at a given time t now depends on the atomic operators of the first atom at earlier times (since retardation effects become frequency dependent). Time correlation functions in the dipole interaction then explicitly show up.

B. Langevin approach

The Langevin equations for the two sets of atomic operators $\mathbf{X}^\alpha$, with $\alpha = 1,2$, formally read

$$\dot{\mathbf{X}}^\alpha = M^\alpha\mathbf{X}^\alpha + \mathbf{L} + \mathbf{F}^\alpha + gT^{q+}\mathbf{X}^\alpha\mathcal{P}^{\mathbf{R}}_{qq'}\mathcal{D}^{\beta-}_{q'} + \bar{g}\mathcal{D}^{\beta+}_q\mathcal{P}^{\mathbf{R}}_{qq'}T^{q'-}\mathbf{X}^\alpha, \tag{25}$$

where β denotes the other atom and where $T^{q\pm}$ are 15×15 matrices defined by $[X_i, \mathcal{D}^\pm_q] = \pm 2T^{q\pm}_{ij}X_j$. Taking the Fourier transform of these equations, one gets

$$\mathbf{X}^\alpha(\Delta) = G^\alpha(\Delta)[2\pi\delta(\Delta)\mathbf{L} + \mathbf{F}^\alpha(\Delta)] + gG^\alpha(\Delta)T^{q+}\mathcal{P}^{\mathbf{R}}_{qq'}(\mathbf{X}^\alpha \otimes \mathcal{D}^{\beta-}_{q'})(\Delta) - \bar{g}G^\alpha(\Delta)\mathcal{P}^{\mathbf{R}}_{qq'}T^{q'-}(\mathcal{D}^{\beta+}_q \otimes \mathbf{X}^\alpha)(\Delta), \tag{26}$$

where $\otimes$ is the convolution operator

$$(A \otimes B)(\Delta) = \frac{1}{2\pi} \int \int d\Delta_1 d\Delta_2 \delta(\Delta_1 + \Delta_2 - \Delta) A(\Delta_1) B(\Delta_2). \tag{27}$$

Introducing, for simplicity, the following notations:

$$\mathbf{X}^{\alpha^{(0)}}(\Delta) = G^{\alpha}(\Delta)[2\pi\delta(\Delta)\mathbf{L} + \mathbf{F}^{\alpha}(\Delta)],$$

$$G^{\alpha^+_q}(\Delta) = G^{\alpha}(\Delta) T^{q'+} \mathcal{P}^{\mathbf{R}}_{q'q},$$

$$G^{\alpha^-_q}(\Delta) = G^{\alpha}(\Delta) T^{q'-} \mathcal{P}^{\mathbf{R}}_{qq'}, \tag{28}$$

Eq. (26) becomes

$$\mathbf{X}^{\alpha}(\Delta) = \mathbf{X}^{\alpha^{(0)}}(\Delta) + g G^{\alpha^+_q}(\Delta)(\mathbf{X}^{\alpha} \otimes \mathcal{D}^{\beta-}_q)(\Delta) - \bar{g} G^{\alpha^-_q}(\Delta)(\mathcal{D}^{\beta+}_q \otimes \mathbf{X}^{\alpha})(\Delta), \tag{29}$$

from which one gets the expansion in power of g and $\bar{g}$ (up to $g\bar{g}$) for the atomic operators:

$$\begin{aligned} X^{\alpha}_i(\Delta) = {} & X^{\alpha^{(0)}}_i(\Delta) + g G^{\alpha^+_q}_{ij}(\Delta)(X^{\alpha^{(0)}}_j \otimes \mathcal{D}^{\beta-(0)}_q)(\Delta) \\ & - \bar{g} G^{\alpha^-_q}_{ij}(\Delta)(\mathcal{D}^{\beta+(0)}_q \otimes X^{\alpha^{(0)}}_j)(\Delta) \\ & - g\bar{g}\{G^{\alpha^+_q}_{ij}(\Delta)[X^{\alpha^{(0)}}_j \otimes G^{\beta^-_p}_{\mathcal{D}^-_{q'j'}}(\mathcal{D}^{\alpha+(0)}_p \otimes X^{\beta^{(0)}}_{j'})](\Delta) \\ & + G^{\alpha^+_q}_{ij}(\Delta)[G^{\alpha^-_p}_{jj'}(\mathcal{D}^{\beta+(0)}_p \otimes X^{\alpha^{(0)}}_{j'}) \otimes \mathcal{D}^{\beta-(0)}_q](\Delta) \\ & + G^{\alpha^-_q}_{ij}(\Delta)[\mathcal{D}^{\beta+(0)}_q \otimes G^{\alpha^+_p}_{jj'}(X^{\alpha^{(0)}}_{j'} \otimes \mathcal{D}^{\beta-(0)}_p)](\Delta) \\ & + G^{\alpha^-_q}_{ij}(\Delta)[G^{\beta^+_p}_{\mathcal{D}^-_{q'j'}}(X^{\beta^{(0)}}_{j'} \otimes \mathcal{D}^{\alpha-(0)}_p) \otimes X^{\alpha^{(0)}}_j](\Delta)\}, \end{aligned} \tag{30}$$

where the notation $G^{\beta^-_p}_{\mathcal{D}^-_{q'j'}}$ means the matrix element $G_{i'j'}$ with i' such that $X_{i'} = \mathcal{D}^-_q$. A schematic representation of the preceding equation is shown in Fig. 1. The thick arrows depict the incident laser intensity (the pump field). The continuous arrows depict the propagation of the components of the positive frequency part of electromagnetic field (i.e., Ω^+), whereas the dashed arrows correspond to the negative frequency part (i.e., Ω^-). Figure 1(a) represents thus the g coefficient in Eq. (30): the atom β is pumped by the incident laser field and thus emits light (elastic and inelastic) (dipole operator $\mathcal{D}^{\beta-(0)}_q$), which is then scattered by the atom α (nonlinear susceptibilities $G^{\alpha^+_q}_{ij} X^{\alpha^{(0)}}_j$). Figure 1(b) depicts the $\bar{g}$ coefficient corresponding to the case where a forward four-wave mixing (FFWM) process occurs at the atom α; i.e., the components of the negative frequency part of the electromagnetic field emitted by the atom β and the components of the positive frequency part of the incident laser field are nonlinearly mixed at the atom α resulting in a radiated field with a positive frequency part (see Sec. IV C for more details). Figure 2(a) corresponds to the first $g\bar{g}$ coefficient and must be read as follows: the atom α emits light (the negative frequency components $\mathcal{D}^{\alpha+(0)}_p$), which undergoes a FFWM process at the atom β (term $G^{\beta^-_p}_{\mathcal{D}^-_{q'j'}} X^{\beta^{(0)}}_{j'}$), the resulting field is then scattered by the atom α (term $G^{\alpha^+_q}_{ij} X^{\alpha^{(0)}}_j$). Figure 2(b) corresponds to the second $g\bar{g}$ coefficient and depicts the following process: the positive frequency components of the light emitted by the atom β (term $\mathcal{D}^{\beta-(0)}_q$) are scattered by the atom α with nonlinear susceptibilities which are modified by the negative frequency components emitted by the atom β (term $G^{\alpha^+_q}_{ij} G^{\alpha^-_p}_{jj'} \mathcal{D}^{\beta+(0)}_p X^{\alpha^{(0)}}_{j'}$). Finally the (c) (third $g\bar{g}$ coefficient) is analog to Fig. 2(b) with an additional FFWM process at the atom α and Fig. 2(d) (fourth $g\bar{g}$ coefficient) is analog to Fig. 2(a) with a FFWM process also at the atom α.

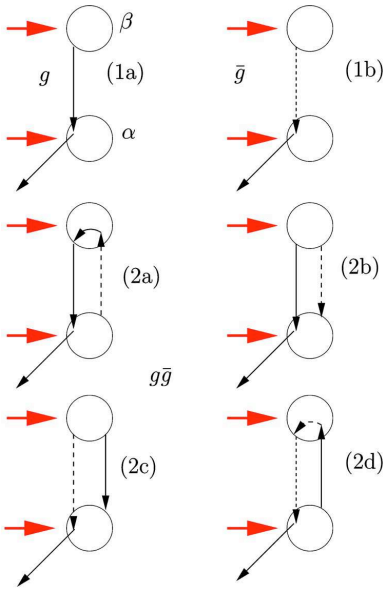

FIG. 1. (Color online) A schematic representation of Eq. (30). The thick arrows depict the incident laser intensity (the pump field). The continuous arrows depict the propagation of the components of the positive frequency part of electromagnetic field (i.e., Ω^+), whereas the dashed arrows correspond to the negative frequency part (i.e., Ω^-). (a) represents thus the g coefficient in Eq. (30): the atom β is pumped by the incident laser field and thus emits light (elastic and inelastic) (dipole operator $\mathcal{D}^{\beta-(0)}_q$), which is then scattered by the atom α (nonlinear susceptibilities $G^{\alpha^+_q}_{ij} X^{\alpha^{(0)}}_j$). The diagram (b) depicts the $\bar{g}$ coefficient corresponding to the case where a forward four-wave mixing (FFWM) process occurs at the atom α; i.e., the components of the negative frequency part of the electromagnetic field emitted by the atom β and the components of the positive frequency part of the incident laser field are non-linearly mixed at the atom α, resulting in a radiated field with a positive frequency part (see Sec. IV C for more details). Figure 2(a) corresponds to the first $g\bar{g}$ coefficient and must be read as follows: the atom α emits light (the negative frequency components $\mathcal{D}^{\alpha+(0)}_p$), which undergoes a FFWM process at the atom β (term $G^{\beta^-_p}_{\mathcal{D}^-_{q'j'}} X^{\beta^{(0)}}_{j'}$); the resulting field is then scattered by the atom α (term $G^{\alpha^+_q}_{ij} X^{\alpha^{(0)}}_j$). Figure 2(b) corresponds to the second $g\bar{g}$ coefficient and depicts the following process: the positive frequency components of the light emitted by the atom β (term $\mathcal{D}^{\beta-(0)}_q$) are scattered by the atom α with nonlinear susceptibilities which are modified by the negative frequency components emitted by the atom β (term $G^{\alpha^+_q}_{ij} G^{\alpha^-_p}_{jj'} \mathcal{D}^{\beta+(0)}_p X^{\alpha^{(0)}}_{j'}$). Finally the (c) (third $g\bar{g}$ coefficient) is analog to Fig. 2(b) with an additional FFWM process at the atom α and Fig. 2(d) (fourth $g\bar{g}$ coefficient) is analog to Fig. 2(a) with a FFWM process also at the atom α.

light emitted by the atom β (term $\mathcal{D}_q^{\beta-(0)}$) are scattered by the atom α with nonlinear susceptibilities which are modified by the negative frequency components emitted by the atom β (term $G_{ij}^{\alpha_q^+}G_{jj'}^{\alpha_p^-}\mathcal{D}_p^{\beta+(0)}X_{j'}^{\alpha(0)}$). Finally, Fig. 2(c) (third $g\bar{g}$ coefficient) is analog to Fig. 2(b) with an additional FFWM process at the atom α and Fig. 2(d) (fourth $g\bar{g}$ coefficient) is analog to Fig. 2(a) with also a FFWM process at the atom α. For all these figures, one must notice that the regular nonlinear susceptibilities only depend on the intensity of the incident laser field, whereas the FFWM processes also depend on the phase of the laser. These properties will play a crucial role for the calculation of the CBS signal (see Sec. IV C).

Two-body term expansions, obtained from Eq. (30), read as follows:

$$\begin{aligned}
X_{i'}^{\beta}(\Delta')X_i^{\alpha}(\Delta) &= X_{i'}^{\beta(0)}(\Delta')X_i^{\alpha(0)}(\Delta) \\
&+ g\{X_{i'}^{\beta(0)}(\Delta')G_{ij}^{\alpha_q^+}(\Delta)(X_j^{\alpha(0)}\otimes\mathcal{D}_q^{\beta-(0)})(\Delta) \\
&+ G_{i'j'}^{\beta_q^+}(\Delta')(X_{j'}^{\beta(0)}\otimes\mathcal{D}_q^{\alpha-(0)})(\Delta')X_i^{\alpha(0)}(\Delta)\} \\
&- \bar{g}\{X_{i'}^{\beta(0)}(\Delta')G_{ij}^{\alpha_q^-}(\Delta)(\mathcal{D}_q^{\beta+(0)}\otimes X_j^{\alpha(0)})(\Delta) \\
&+ G_{i'j'}^{\beta_q^-}(\Delta')(\mathcal{D}_q^{\alpha+(0)}\otimes X_{j'}^{\beta(0)})(\Delta')X_i^{\alpha(0)}(\Delta)\} \\
&- g\bar{g}\ \{\text{see Eq. (A1)}\},
\end{aligned}$$

$$\begin{aligned}
X_{i'}^{\alpha}(\Delta')X_i^{\alpha}(\Delta) &= X_{i'}^{\alpha(0)}(\Delta')X_i^{\alpha(0)}(\Delta) \\
&+ g\{X_{i'}^{\alpha(0)}(\Delta')G_{ij}^{\alpha_q^+}(\Delta)(X_j^{\alpha(0)}\otimes\mathcal{D}_q^{\beta-(0)})(\Delta) \\
&+ G_{i'j'}^{\alpha_q^+}(\Delta')(X_{j'}^{\alpha(0)}\otimes\mathcal{D}_q^{\beta-(0)})(\Delta')X_i^{\alpha(0)}(\Delta)\} \\
&- \bar{g}\{X_{i'}^{\alpha(0)}(\Delta')G_{ij}^{\alpha_q^-}(\Delta)(\mathcal{D}_q^{\beta+(0)}\otimes X_j^{\alpha(0)})(\Delta) \\
&+ G_{i'j'}^{\alpha_q^-}(\Delta')(\mathcal{D}_q^{\beta+(0)}\otimes X_{j'}^{\alpha(0)})(\Delta')X_i^{\alpha(0)}(\Delta)\} \\
&- g\bar{g}\ \{\text{see Eq. (A2)}\}. \qquad (31)
\end{aligned}$$

The quantities involved in the preceding equations are operators acting on both atomic and electromagnetic field spaces. In particular, the quantum fluctuations due to the vacuum electromagnetic field still appear through the Langevin terms. A full numerical simulation of these equations would then take place in the framework of the quantum stochastic calculus [40]. However, as in the one atom case, we will show that, from these equations, one can *directly* obtain the power expansion of the expectation values (i.e., quantities averaged over the quantum fluctuations). The latter can be derived from the quantum average of the preceding equations, but not as easily as it seems. Indeed, if one formally writes

$$X_{i'}^{\alpha'}(\Delta')X_i^{\alpha}(\Delta) = \sum_{ab} O(a,b)g^a\bar{g}^b,$$

$$\langle X_{i'}^{\alpha'}(\Delta')X_i^{\alpha}(\Delta)\rangle = \sum_{ab} C(a,b)g^a\bar{g}^b, \qquad (32)$$

then $C(a,b)$ is not simply equal to $\langle O(a,b)\rangle$. Actually, $C(a,b)$ depends on all $\langle O(a',b')\rangle$ for $(a',b')\leq(a,b)$, and this for two reasons.

For a given atom α, the frequency correlation functions $\langle F_p^{\alpha}(\Delta')F_q^{\alpha}(\Delta)\rangle$ are given by $2\pi\delta(\Delta'+\Delta)D_{pq}$, where D_{pq} depends on the stationary values. But the latter are modified by the second atom and, thus, must also be expanded in power of g and $\bar{g}$. This implies, for example, that the first term $X_{i'}^{\alpha(0)}(\Delta')X_i^{\alpha(0)}(\Delta)$ in the expansion of $X_{i'}^{\alpha}(\Delta')X_i^{\alpha}(\Delta)$ [Eq. (31)] will contribute to all coefficients of $\langle X_{i'}^{\alpha}(\Delta')X_i^{\alpha}(\Delta)\rangle$.

The Langevin forces acting on two different atoms are correlated since they both originate from the vacuum quantum field. More precisely, their frequency correlation functions depend on their relative distance. This dependence is analogous to the correlation function of a speckle pattern (resulting from the random superposition of plane waves with the same wavelength but arbitrary directions):

$$\begin{aligned}
\langle F_{i'}^{\beta}(\Delta')F_i^{\alpha}(\Delta)\rangle &= 2\pi\delta(\Delta'+\Delta)\frac{3}{2}\Gamma\frac{\sin kR}{kR}T_{i'j'}^{q'+}\mathcal{P}_{q'q}^{\mathbf{R}}T_{ij}^{q-}\langle X_{j'}^{\beta}X_j^{\alpha}\rangle \\
&= -\frac{1}{2}(g+\bar{g})2\pi\delta(\Delta'+\Delta)T_{i'j'}^{q'+}\mathcal{P}_{q'q}^{\mathbf{R}}T_{ij}^{q-}\langle X_{j'}^{\beta}X_j^{\alpha}\rangle \\
&= -\frac{1}{2}(g+\bar{g})2\pi\delta(\Delta'+\Delta)D_{i'i}^{\beta\alpha}. \qquad (33)
\end{aligned}$$

Thus, terms such as $X_{i'}^{\beta(0)}(\Delta')(X_j^{\alpha(0)}\otimes\mathcal{D}_q^{\beta-(0)})(\Delta)$ appearing in Eq. (31) will also contribute to higher-order coefficients in the power expansion of $\langle X_{i'}^{\beta}(\Delta')X_i^{\alpha}(\Delta)\rangle$. One must note that, when $R\to 0$, $\mathcal{P}_{q'q}^{\mathbf{R}}\to\frac{2}{3}\delta_{q'q}$ and one recovers the single atom correlation functions given by Eq. (17), which emphasizes the consistency of the present approach.

C. Comparison with optical Bloch results

Despite these subtleties, it is nevertheless possible to calculate power expansions of the atomic correlation functions. More precisely, in order to emphasize the validity of the present approach, we will compare the results obtained from the OB equations and from the Langevin approach. Indeed from the atomic correlation functions, the stationary solutions can be calculated by inverse Fourier transform as follows:

$$\langle X_{i'}^{\alpha}X_i^{\alpha'}\rangle = \frac{1}{(2\pi)^2}\int\int d\Delta' d\Delta\langle X_{i'}^{\alpha}(\Delta')X_i^{\alpha'}(\Delta)\rangle. \qquad (34)$$

As a specific example, the coefficient proportional to g in the perturbative expansion of $\langle X_{i'}^{\beta}(\Delta')X_i^{\alpha}(\Delta)\rangle$ is given by

$$\begin{aligned}\langle X_{i'}^{\beta}(\Delta')X_i^{\alpha}(\Delta)\rangle^{(g)} &= \underline{\langle X_{i'}^{\beta^{(0)}}(\Delta')X_i^{\alpha^{(0)}}(\Delta)\rangle^{(g)}} \\ &+ \langle X_{i'}^{\beta^{(0)}}(\Delta')G_{ij}^{\alpha_g^+}(\Delta)(X_j^{\alpha^{(0)}} \otimes \mathcal{D}_q^{\beta_-^{(0)}})(\Delta)\rangle^{(0)} \\ &+ \langle G_{i'j'}^{\beta_q^+}(\Delta')(X_{j'}^{\beta^{(0)}} \otimes \mathcal{D}_q^{\alpha_-^{(0)}})(\Delta')X_i^{\alpha^{(0)}}(\Delta)\rangle^{(0)} \\ &= \underline{G_{i'j'}^{\beta}(\Delta')G_{ij}^{\alpha}(\Delta)\langle F_{j'}^{\beta}(\Delta')F_j^{\alpha}(\Delta)\rangle^{(g)}} \\ &+ G_{ij}^{\alpha_g^+}(\Delta)\langle X_j^{\alpha^{(0)}}\rangle\langle X_{i'}^{\beta^{(0)}}(\Delta')\mathcal{D}_q^{\beta_-^{(0)}}(\Delta)\rangle^{(0)} \\ &+ G_{i'j'}^{\beta_q^+}(\Delta')\langle X_{j'}^{\beta^{(0)}}\rangle\langle \mathcal{D}_q^{\alpha_-^{(0)}}(\Delta')X_i^{\alpha^{(0)}}(\Delta)\rangle^{(0)}, \end{aligned} \tag{35}$$

where we have used the fact that terms such as $\langle X^{\alpha^{(0)}}X^{\beta^{(0)}}\rangle^{(0)}$ (i.e., zeroth order) actually factorize into $\langle X^{\alpha}\rangle\langle X^{\beta}\rangle$ since their fluctuating parts necessarily give rise to higher orders in g and $\bar{g}$, see Eq. (33). The underlined terms correspond to the nonvanishing correlations of the quantum vacuum fluctuations evaluated at the two atom positions.

Finally, separating elastic and inelastic part, one gets

$$\begin{aligned}\langle X_{i'}^{\beta}(\Delta')X_i^{\alpha}(\Delta)\rangle^{(g)} &= (2\pi)^2\delta(\Delta')\delta(\Delta)(G_{ij}^{\alpha_g^+}(0)\langle X_j^{\alpha^{(0)}}\rangle\langle X_{i'}^{\beta^{(0)}}\rangle\langle \mathcal{D}_q^{\beta_-^{(0)}}\rangle \\ &+ G_{i'j'}^{\beta_q^+}(0)\langle X_{j'}^{\beta^{(0)}}\rangle\langle \mathcal{D}_q^{\alpha_-^{(0)}}\rangle\langle X_i^{\alpha^{(0)}}\rangle) \\ &+ 2\pi\delta(\Delta'+\Delta)\Bigg(-\frac{1}{2}\underline{G_{i'j'}^{\beta}(\Delta')G_{ij}^{\alpha}(\Delta)D_{j'j}^{\beta\alpha^{(0)}}} \\ &+ G_{ij}^{\alpha_g^+}(\Delta)G_{i'j'}^{\beta}(\Delta')G_{\mathcal{D}_q^-k'}^{\beta}(\Delta)D_{j'k'}^{\beta\beta^{(0)}}\langle X_j^{\alpha^{(0)}}\rangle \\ &\times G_{i'j'}^{\beta_q^+}(\Delta')G_{\mathcal{D}_q^-k}^{\alpha}(\Delta')G_{ij}^{\alpha}(\Delta)D_{kj}^{\alpha\alpha^{(0)}}\langle X_{j'}^{\beta^{(0)}}\rangle\Bigg). \end{aligned} \tag{36}$$

The corresponding stationary solution then reads

$$\begin{aligned}\langle X_{i'}^{\beta}X_i^{\alpha}\rangle^{(g)} &= G_{ij}^{\alpha_g^+}(0)\langle X_j^{\alpha^{(0)}}\rangle\langle X_{i'}^{\beta^{(0)}}\rangle\langle \mathcal{D}_q^{\beta_-^{(0)}}\rangle \\ &+ G_{i'j'}^{\beta_q^+}(0)\langle X_{j'}^{\beta^{(0)}}\rangle\langle \mathcal{D}_q^{\alpha_-^{(0)}}\rangle\langle X_i^{\alpha^{(0)}}\rangle \\ &+ \frac{1}{2\pi}\int d\Delta\Bigg(-\frac{1}{2}\underline{G_{i'j'}^{\beta}(-\Delta)G_{ij}^{\alpha}(\Delta)D_{j'j}^{\beta\alpha^{(0)}}} \\ &+ G_{ij}^{\alpha_g^+}(\Delta)G_{i'j'}^{\beta}(-\Delta)G_{\mathcal{D}_q^-k'}^{\beta}(\Delta)D_{j'k'}^{\beta\beta^{(0)}}\langle X_j^{\alpha^{(0)}}\rangle \\ &\times G_{i'j'}^{\beta_q^+}(-\Delta)G_{\mathcal{D}_q^-k}^{\alpha}(-\Delta)G_{ij}^{\alpha}(\Delta)D_{kj}^{\alpha\alpha^{(0)}}\langle X_{j'}^{\beta^{(0)}}\rangle\Bigg). \end{aligned} \tag{37}$$

All quantities above only depend on the stationary values without coupling between the atoms and thus can be calculated from the single atom solutions. Furthermore, the integration over Δ can be performed either numerically or analytically by the theorem of residues once the poles of G (i.e., the complex eigenvalues of M) are known. Because of causality, they all lie in the lower-half of the complex plane. In practice, we have checked that we effectively recover, from the preceding expressions, the results obtained from the full OB equations. In particular, the contribution of the correlations of the quantum vacuum fluctuations evaluated at the two atom positions (the underlined term) is essential to get the correct results.

The same kind of expressions can be derived for $g\bar{g}$ terms, but they are slightly more complicated, since they explicitly involve three-body correlation functions, more precisely terms like

$$G_{ij}^{\alpha_g^+}(\Delta)\langle X_{i'}^{\beta^{(0)}}(\Delta')(X_j^{\alpha^{(0)}} \otimes \mathcal{D}_q^{\beta_-^{(0)}})(\Delta)\rangle^{(\bar{g})},$$

$$G_{ij}^{\alpha_g^+}(\Delta)\langle X_{i'}^{\beta}(\Delta')[G_{jj'}^{\alpha_p^-}(\mathcal{D}_p^{\beta+^{(0)}} \otimes X_{j'}^{\alpha^{(0)}}) \otimes \mathcal{D}_q^{\beta_-^{(0)}}](\Delta)\rangle^{(0)} \tag{38}$$

which require the calculation of three-points Langevin force correlation functions like

$$\begin{aligned} G_{ij}^{\alpha_g^+}(\Delta)G_{i'j'}^{\beta}(\Delta')\frac{1}{2\pi}\int\int d\Delta_1 d\Delta_2\delta(\Delta_1+\Delta_2-\Delta) \\ \times G_{jk}^{\alpha}(\Delta_1)G_{\mathcal{D}_q^-k'}^{\beta}(\Delta_2)\langle F_{j'}^{\beta}(\Delta')F_k^{\alpha}(\Delta_1)F_{k'}^{\beta}(\Delta_2)\rangle^{(\bar{g})}, \end{aligned}$$

$$\begin{aligned} G_{ij}^{\alpha_g^+}(\Delta)G_{i'k'}^{\beta}(\Delta')\frac{1}{2\pi}\int\int d\Delta_1 d\Delta_2\delta(\Delta_1+\Delta_2-\Delta) \\ \times G_{jj'}^{\alpha_p^-}(\Delta_1)G_{\mathcal{D}_p^+k}^{\beta}(\Delta_1)G_{\mathcal{D}_p^+k''}^{\beta}(\Delta_2)\langle F_{k'}^{\beta}(\Delta')F_k^{\beta}(\Delta_1)F_{k''}^{\beta}(\Delta_2)\rangle^{(0)}. \end{aligned} \tag{39}$$

These correlation functions are nonzero even if they involve an odd number of Langevin forces, emphasizing that the statistical properties of the vacuum field fluctuations are far from Gaussian. Nevertheless, the explicit expressions of the above quantities can be derived (see Appendix B). They lead to rather complicated and tedious formulas for the atomic correlation functions at order $g\bar{g}$. From that, we get the corresponding stationary expectations values. Again, we have checked that we indeed recover the OB results.

D. Incorporation of an effective medium

Finally, and in sharp contrast to optical Bloch equations, it is very easy to adapt all the preceding results to the case of propagation in a medium with a frequency-dependent complex susceptibility. Indeed, the quantization of the electromagnetic field in dielectrics involves the tensor-valued Green's function of the classical problem [42,43], from which all possible commutation relations of the field operators can be derived. In particular, for a homogeneous medium, this Green's function involves the complex-valued permittivity $\epsilon(\omega_L+\Delta)=1+\chi(\omega_L+\Delta)$. Its real part is responsible for dispersion and its imaginary part for absorption. In the dilute regime, this allows us to write the field radiated by an atom at a distance R and at frequency Δ as follows:

$$(-1)^q \Omega_{-q}^{+}(\Delta) = ig\mathcal{P}_{qq'}^{\mathbf{R}} \mathcal{D}_{q'}^{-}(\Delta) \exp\left(-\frac{1}{2}\frac{R}{l^{+}(\Delta)}\right), \quad (40)$$

where $l^{+}(\Delta)$ is the (complex) scattering mean-free path, defined by $1/kl^{+}(\Delta) = i\chi(\omega_L + \Delta)$ with the dilute regime condition $k|l^{+}(\Delta)| \gg 1$.

The real part of $1/l^{+}(\Delta)$ describes thus the exponential attenuation of the field during its propagation in the medium while the imaginary part describes the additional dephasing induced by the medium. More complicated formulas, accounting for possible variations of l with position, birefringence effects, or even nonlinearities in propagation, can be derived in the same spirit. In all preceding equations, leading to the calculation of the correlation functions, any occurrence of the dipole operators must then simply be replaced by

$$\mathcal{D}^{\mp} \to \mathcal{D}^{\mp} \exp\left(-\frac{R}{2l^{\pm}(\Delta)}\right) \quad (41)$$

while keeping the same "medium-free" coupling constant g. In this way, the present approach can be easily extended to the situation where the two atoms are embedded in a medium. In the case of a nonlinear medium, this could lead to a self-consistent set of nonlinear equations.

It is important to stress that accounting for the effective medium is rather straightforward in this frequency-domain approach but is a much more difficult task in the temporal-domain approach. Indeed, one basic hypothesis for deducing OB equations from the Langevin approach—see Sec. III A—is that the light propagation time between the two atoms is much shorter than any typical atomic time scale. When this condition is fulfilled, it is possible to evaluate expectation values at equal times for both atoms, producing the set of closed OB equations. In the presence of a surrounding medium, propagation between the two atoms is affected and this basic assumption may fail. If the refraction index of the dilute medium is smoothly varying with frequency, then the corresponding propagation term is also smoothly varying with frequency and can be factored out. Thus, except for the exponential attenuation, one may recover the OB equations where equal times must be used for atoms 1 and 2. On the contrary, if the propagation term has a complicated frequency dependence, the problem cannot be simply reduced to OB equations. It will rather involve operators evaluated at the other atom, but at different times, thus leading to a much more complicated structure. This difficulty may even take place in a dilute medium with refraction index close to unity. Indeed, the important parameter is the time delay induced by the medium, itself related to the derivative of the index of refraction with respect to frequency. If the medium is composed of atoms having sharp resonances, the effective group velocity can be reduced by several orders of magnitude, consequently increasing by the same amount the propagation time between the two atoms. Around the atomic resonance line, the typical propagation time delay induced by the medium over one mean-free path depends on the laser detuning but is of the order of the atomic timescale for the internal dynamics, namely, Γ^{-1} [47]. In this case, only the full Langevin treatment developed in this paper can properly account for the effect of the average atomic medium. Its practical implementation calls for an investigation on its own and is thus postponed to a future paper. We must also note that, if the surrounding medium is composed of the same atoms than the scatterers, it is not completely clear that propagation in the medium can be described "classically," i.e., that the correlation between the Langevin forces acting on the scatterers and the Langevin forces acting on the medium can be safely neglected. For the rest of this paper, we will consider two isolated atoms in vacuum.

IV. MAIN RESULTS

A. Scattered field correlation functions in the CBS configuration

In the case of a large number of atoms and for a given configuration, the interference between all possible multiple scattering paths gives rise to a speckle pattern. When averaging the intensity scattered off the sample over all possible positions of the atoms, one recovers the CBS phenomenon: the intensity radiated in the direction opposite to the incident beam is up to twice larger than the background intensity and gradually decreases to the background value over an angular range $\Delta\theta$ scaling essentially as $(kl)^{-1}$, with l the scattering mean-free path. In the present case, the averaging procedure is performed numerically by integrating over the relative positions of the two atoms. As will be seen below, the far-field condition $kR \gg 1$ allows for an *a priori* selection of the dominant terms contributing to the CBS signal.

The field radiated by the two atoms in the direction $\mathbf{n}$ at a distance $r \gg R \gg \lambda$, in the polarization channel $\boldsymbol{\epsilon}^{\text{out}}$ orthogonal to $\mathbf{n}$ ($\boldsymbol{\epsilon}^{\text{out}} \cdot \mathbf{n} = 0$), is given by

$$\Omega_{\text{out}}^{+}(\mathbf{n}, \Delta) = -\frac{3}{2}\Gamma \epsilon_q^{\text{out}} [\mathcal{D}_q^{1-}(\Delta) e^{-ik\mathbf{n}\cdot\mathbf{R}_1} + \mathcal{D}_q^{2-}(\Delta) e^{-ik\mathbf{n}\cdot\mathbf{R}_2}) \frac{e^{ikr}}{kr}, \quad (42)$$

so that the field correlation function in this channel reads

$$\begin{aligned}\langle \Omega_{\text{out}}^{-}(\mathbf{n}, \Delta') \Omega_{\text{out}}^{+}(\mathbf{n}, \Delta) \rangle &= \left(\frac{3\Gamma}{2kr}\right)^2 \epsilon_q^{\text{out}} \epsilon_p^{\text{out}} \{\langle \mathcal{D}_p^{1+}(\Delta') \mathcal{D}_q^{1-}(\Delta) \rangle + \langle \mathcal{D}_p^{2+}(\Delta') \mathcal{D}_q^{2-}(\Delta) \rangle \\ &\quad + e^{ik\mathbf{n}\cdot\mathbf{R}} \langle \mathcal{D}_p^{2+}(\Delta') \mathcal{D}_q^{1-}(\Delta) \rangle + e^{-ik\mathbf{n}\cdot\mathbf{R}} \langle \mathcal{D}_p^{1+}(\Delta') \mathcal{D}_q^{2-}(\Delta) \rangle \}. \end{aligned} \quad (43)$$

The CBS effect occurs when the total phase in the interference terms in the preceding expression becomes independent of the positions of the atom. This phase accumulates during the propagation of the incident laser beam to the atoms and during the propagation of the radiated field between the two atoms. The phase factor due to the incoming laser beam (a plane wave with wave number $\mathbf{k}_L = k\mathbf{n}_L$) can be explicitly factorized out of the atomic operators as follows

$$\tilde{\mathcal{D}}_q^{\alpha\pm} = \mathcal{D}_q^{\alpha\pm} e^{\pm i\mathbf{k}_L\cdot\mathbf{R}_\alpha}. \tag{44}$$

The other components of $\tilde{X}$, see Eq. (10), are populations and are not affected by this phase factor. In the single atom case, the expectation values of the hereby defined operators $\tilde{\mathcal{D}}_q^{\alpha\pm}$ are independent of the positions of the atoms. Defining $\phi = \mathbf{k}_L\cdot\mathbf{R}$ and

$$g_1 = ge^{i\phi}, \quad g_2 = ge^{-i\phi}, \tag{45}$$

the Langevin equations (29) then become

$$\tilde{\mathbf{X}}^\alpha(\Delta) = \tilde{\mathbf{X}}^{\alpha^{(0)}}(\Delta) + g_\alpha \tilde{G}^{\alpha^+_q}(\Delta)(\tilde{\mathbf{X}}^\alpha \otimes \tilde{\mathcal{D}}_q^{\beta-})(\Delta) + \bar{g}_\alpha \tilde{G}^{\alpha^-_q}(\Delta)(\tilde{\mathcal{D}}_q^{\beta+} \otimes \tilde{\mathbf{X}}^\alpha)(\Delta). \tag{46}$$

In the preceding equation, the Green's functions $\tilde{G}$ are now independent of the position of the atoms, so that the phase information due to the incident laser beam is entirely contained in the coefficients g_α.

Frequency correlation functions of the Langevin forces (33) must also be modified accordingly:

$$\langle \tilde{F}_{i'}^\beta(\Delta')\tilde{F}_i^\alpha(\Delta)\rangle = -\frac{1}{2}(g_\beta + \bar{g}_\alpha)2\pi\delta(\Delta'+\Delta)\tilde{D}_{i'i}^{\beta\alpha}. \tag{47}$$

Dropping for simplicity the tilde notation, the field correlation function (43), in the backward direction $\mathbf{n}=-\mathbf{n}_L$, becomes

$$\langle \Omega_{\text{out}}^-(-\mathbf{n}_L,\Delta')\Omega_{\text{out}}^+(-\mathbf{n}_L,\Delta)\rangle = \left(\frac{\Gamma}{kr}\right)^2 \epsilon_q^{\text{out}}\epsilon_p^{\text{out}}\{\langle \mathcal{D}_p^{1+}(\Delta')\mathcal{D}_q^{1-}(\Delta)\rangle + \langle \mathcal{D}_p^{2+}(\Delta')\mathcal{D}_q^{2-}(\Delta)\rangle + e^{-2i\phi}\langle \mathcal{D}_p^{2+}(\Delta')\mathcal{D}_q^{1-}(\Delta)\rangle + e^{2i\phi}\langle \mathcal{D}_p^{1+}(\Delta')\mathcal{D}_q^{2-}(\Delta)\rangle\}. \tag{48}$$

The configuration average is then performed in two steps. Since we are working in the limit $kR \gg 1$, the first one is to keep only terms with a total phase independent of kR. In the power expansion with respect to the four parameters g_1, g_2, $\bar{g}_1$, and $\bar{g}_2$, this simply amounts to keep terms with even powers of $g_\alpha\bar{g}_{\alpha'}$. This obviously cancels any ϕ dependence. More precisely, the field correlation function in the backward direction, beside the trivial zeroth order (in g) term, is given by

$$\begin{aligned}\langle \Omega_{\text{out}}^-(-\mathbf{n}_L,\Delta')\Omega_{\text{out}}^+(-\mathbf{n}_L,\Delta)\rangle^{(2)} &= \left(\frac{\Gamma}{kr}\right)^2 \epsilon_q^{\text{out}}\epsilon_p^{\text{out}}\{\langle \mathcal{D}_p^{1+}(\Delta')\mathcal{D}_q^{1-}(\Delta)\rangle^{(g_1\bar{g}_1)} \\ &+ \langle \mathcal{D}_p^{2+}(\Delta')\mathcal{D}_q^{2-}(\Delta)\rangle^{(g_2\bar{g}_2)} + \langle \mathcal{D}_p^{2+}(\Delta')\mathcal{D}_q^{1-}(\Delta)\rangle^{(g_1\bar{g}_2)} \\ &+ \langle \mathcal{D}_p^{1+}(\Delta')\mathcal{D}_q^{2-}(\Delta)\rangle^{(g_2\bar{g}_1)}\} \\ &= \left(\frac{\Gamma}{kr}\right)^2 (L(\Delta',\Delta) + C(\Delta',\Delta)).\end{aligned} \tag{49}$$

The preceding field correlation function still depends on the relative orientation of the atoms through the projector $\mathcal{P}^{\mathbf{R}}$, so that, in a second step, an additional average over $\mathbf{R}$ must be performed. In the preceding equation, the first two terms correspond to the usual "ladder" terms $L(\Delta',\Delta)$ (they are actually independent of the direction of observation), whereas the two other terms correspond to the usual "maximally crossed" terms $C(\Delta',\Delta)$:

$$\begin{aligned}L(\Delta',\Delta) &= \frac{9}{4}\epsilon_q^{\text{out}}\epsilon_p^{\text{out}}\{\langle \mathcal{D}_p^{1+}(\Delta')\mathcal{D}_q^{1-}(\Delta)\rangle^{(g_1\bar{g}_1)} + \langle \mathcal{D}_p^{2+}(\Delta')\mathcal{D}_q^{2-}(\Delta)\rangle^{(g_2\bar{g}_2)}\}, \\ C(\Delta',\Delta) &= \frac{9}{4}\epsilon_q^{\text{out}}\epsilon_p^{\text{out}}\{\langle \mathcal{D}_p^{2+}(\Delta')\mathcal{D}_q^{1-}(\Delta)\rangle^{(g_1\bar{g}_2)} + \langle \mathcal{D}_p^{1+}(\Delta')\mathcal{D}_q^{2-}(\Delta)\rangle^{(g_2\bar{g}_1)}\}.\end{aligned} \tag{50}$$

B. CBS enhancement factor

In the case of linear scatterers, the CBS enhancement factor achieves its maximal value 2 (recall that the CBS phenomenon is an incoherent sum of two-wave interference patterns all starting with a bright fringe at exact backscattering) if the single scattering contribution can be removed from the total signal and provided reciprocity holds. This is the case for scatterers with spherical symmetry in the so-called polarization preserving channel $h\|h$ [44].

In this polarization channel, we have calculated the relevant quantities for an evaluation of the CBS enhancement factor when no frequency filtering of the outgoing signal is made. We have thus derived the elastic and inelastic ladder terms and the elastic and inelastic crossed terms, together with their corresponding frequency spectra, for different values of the on-resonance saturation parameter $s_0 = 2|\Omega_L|^2/\Gamma^2$. This parameter measures the intensity strength of the incident laser beam in units of the natural atomic transition line width Γ, i.e., it compares the on-resonance transition rate induced by the laser to the atomic spontaneous emission rate. For a detuned laser beam, the saturation parameter is $s(\delta_L)$ and is defined as

$$s(\delta_L) = \frac{s_0}{1+(2\delta_L/\Gamma)^2}. \tag{51}$$

In the following, different values of the laser detuning have also been considered:

(a) $\delta_L = 0$, $s = s_0 = 0.02$, (b) $\delta_L = 0$, $s = s_0 = 2.00$,
(c) $\delta_L = 5\Gamma$, $s_0 = 2.00$, $s = 0.02$, (d) $\delta_L = 0$, $s = s_0 = 50.0$.

The ladder and crossed terms (49) are separated into their elastic and inelastic parts according to

$$\begin{aligned}L(\Delta',\Delta) &= 2\pi\delta(\Delta+\Delta')\{2\pi\delta(\Delta)L_{\text{el}} + L_{\text{inel}}(\Delta)\}, \\ C(\Delta',\Delta) &= 2\pi\delta(\Delta+\Delta')\{2\pi\delta(\Delta)C_{\text{el}} + C_{\text{inel}}(\Delta)\}.\end{aligned} \tag{52}$$

The corresponding inelastic spectra $L_{\text{inel}}(\Delta)$ and $C_{\text{inel}}(\Delta)$ are displayed in Fig. 2. For a sufficiently low saturation parameter s_0, the inelastic contribution to the total intensity is small and the crossed intensity is almost equal to the ladder one [see graph 2(a)]. For larger saturation parameters [see graphs 2(b) and 2(d)], there are two effects: first, the inelastic

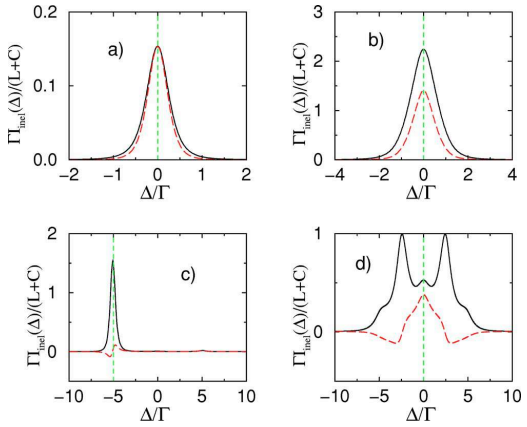

FIG. 2. (Color online) Backscattered light spectrum in the helicity-preserving polarization channel $h\|h$. The solid lines represent the ladder term (average background intensity value) and the long-dashed lines represent the crossed (interference) term. For both terms, the plotted values correspond to $\Gamma I_{\rm inel}(\Delta)/(C^{\rm tot}+L^{\rm tot})$, see Eq. (52), where $C^{\rm tot}+L^{\rm tot}$ is the total (elastic *plus* inelastic) intensity scattered in the backward direction. The vertical dashed lines indicate the atomic transition frequency. Δ corresponds to the scattered light angular frequency change with respect to the initial laser angular frequency ($\Delta=0$ means thus that light is radiated at ω_L). Graph (a) corresponds to an on-resonance saturation parameter $s_0=0.02$ and a laser detuning $\delta_L=0$, graph (b) to $(s_0=2, \delta_L=0)$, graph (c) to $(s_0=2, \delta_L=5\Gamma)$, and graph (d) to $(s_0=50, \delta_L=0)$. At low s_0, the inelastic contribution to the total intensity is small and the ladder intensity is almost equal to the crossed one. For a larger saturation parameter, first the inelastic contribution becomes comparable to the elastic one and second, the crossed term becomes smaller than the ladder one. For a nonzero detuning, see graph (c), one clearly observes an asymmetry in the inelastic spectrum, which reflects the fact that the scattering cross section of the atomic transition is maximal for resonant light: the symmetric inelastic spectrum emitted by a single atom is filtered out when scattered by the other one. At very large saturation (d), the structure of the radiated spectrum becomes rather complicated.

contribution becomes comparable to the elastic one and second, the crossed term is smaller than the ladder one. For a nonzero detuning [see graph 2(c)], one clearly observes an asymmetry in the inelastic spectrum, which reflects that the scattering cross section of the atomic transition is maximal for resonant light (indicated by the vertical dashed line): the symmetric inelastic spectrum emitted by a single atom is filtered out when scattered by the other one. We also observe that the crossed spectrum is much more reduced than the ladder term, highlighting the nonlinear effects in the quantum correlations between the two atoms. Finally, for much larger saturation parameters [see graph 2(d)], the scattered light almost entirely originates from the inelastic spectrum, as for a single atom. However, contrary to the single atom case (for which the scattered intensity reaches a constant value), the total intensity scattered by the two atoms decreases when increasing the incoming intensity. Indeed, since the atomic transitions become fully saturated, the nonlinear scattering cross section of each atom is decreasing, resulting in a smaller total intensity scattered by the two atoms compared to the one scattered by a single atom.

The CBS enhancement factor η is defined as the peak to background ratio. It thus reads

$$\eta = 1 + \frac{C^{\rm tot}}{L^{\rm tot}} \tag{53}$$

with

$$L^{\rm tot} = L_{\rm el} + L^{\rm tot}_{\rm inel} = L_{\rm el} + \int \frac{d\Delta}{2\pi} L_{\rm inel}(\Delta),$$

$$C^{\rm tot} = C_{\rm el} + C^{\rm tot}_{\rm inel} = C_{\rm el} + \int \frac{d\Delta}{2\pi} C_{\rm inel}(\Delta). \tag{54}$$

If the CBS phenomenon is reducible to a two-wave interference, as it is the case here, then the enhancement factor η is simply related to the degree of coherence γ of the scattered light [45]. If the single scattering contribution can be removed from the detected signal, and this is the case in the $h\|h$ channel, one has simply $\eta=1+\gamma$ and consequently $\gamma = C^{\rm tot}/L^{\rm tot}$. The maximal value for η is 2, meaning that full coherence $\gamma=1$ is maintained for the scattered field since then $C^{\rm tot}=L^{\rm tot}$. If all interference effects disappear, meaning $C^{\rm tot}=0$, η reaches its minimal value 1 and correspondingly coherence is fully lost $\gamma=0$. Furthermore, one can show that in the $h\|h$ polarization channel $L_{\rm el}=C_{\rm el}$ [37]. Consequently, as soon as $C^{\rm tot}_{\rm inel}<L^{\rm tot}_{\rm inel}$ in this channel, the coherence of the scattered light field is partially destroyed, since then $\eta<2$ and $\gamma<1$.

Our results are summarized in Table I. At low saturation parameter s_0, η reaches its maximal value 2 and $\gamma=1$. This is so because the ladder and crossed inelastic components are almost equal as evidenced in Fig. 2(a). Increasing s_0 reduces further $C^{\rm tot}_{\rm inel}$ with respect to $L^{\rm tot}_{\rm inel}$, thus decreasing η and γ. In the strongly saturated regime, one thus expects γ to decrease. However, there is no reason for the ratio $C^{\rm tot}_{\rm inel}/L^{\rm tot}_{\rm inel}$ to tend to zero as $s_0\to\infty$. It rather tends to a finite value, which depends on the detuning, in agreement with the results published in Ref. [37]. Furthermore, keeping s_0 fixed and decreasing the saturation parameter s, situation (c), η increases, as expected, but to a value which strongly depends on s_0. In other words, contrary to the single atom case, the properties of the scattered light are not only determined by the saturation parameter s [20], highlighting the crucial role of the inelastic processes. Indeed, in both situations (a) and (c), s has the same (small) value, but the enhancement factor strongly differs, mainly because the relative contribution of the inelastic ladder term has increased. A qualitative understanding of this behavior can be obtained from the diagrammatic approach: Fig. 3 displays the basic processes contributing to the ladder and crossed terms. In the small s regime, only one nonlinear event is necessary to calculate the first correction to the linear regime [20], so that we can assume that inelastic processes occur only at atom 1, whereas atom 2 behaves similar to a linear scatterer. In the case of the ladder term [Fig. 3(a)], the inelastic light is thus emitted by atom 1 and then (elastically) scattered by atom 2. The crucial point

TABLE I. Ladder (average background) and crossed (interference) terms, see Eq. (52), contributing to the light scattered in the backward direction in the helicity-preserving polarization channel $h\|h$. The given values are relative to the incoming saturation parameter s. At low s_0, the inelastic contributions are small and almost equal. Thus $C^{\mathrm{tot}} \approx L^{\mathrm{tot}}$ and the maximum enhancement factor 2 of the linear case is thus recovered, meaning that full coherence $\gamma=1$ is maintained. At larger s_0, elastic and inelastic terms become comparable. For very large s_0, the contributions from the elastic terms vanish, as in the single atom case. The inelastic contributions are also decreasing, reflecting the fact that the probability for the light to be scattered by a saturated atom becomes smaller with increasing saturation. Furthermore, the inelastic crossed term is *always* smaller than the inelastic ladder one. This is a signature of a coherence loss $\gamma<1$ induced by the quantum vacuum fluctuations. However, the ratio $C^{\mathrm{tot}}_{\mathrm{inel}}/L^{\mathrm{tot}}_{\mathrm{inel}}$ does not go to zero as $s_0 \to \infty$ but reaches the limit value 0.096 (for $\delta_L=0$). Also, contrary to the single atom case, the properties of the scattered light are not solely determined by the saturation parameter s, but additionally depend on the detuning δ_L, as exemplified by cases (a) and (c), highlighting the role of the inelastic processes.

	(a) $s=s_0=0.02, \delta_L=0$	(b) $s=s_0=2.00, \delta_L=0$	(c) $s=0.02, s_0=2.00, \delta_L=5\Gamma$	(d) $s=s_0=50.0, \delta_L=0$
L_{el}	0.624	0.833×10^{-2}	0.618×10^{-2}	0.998×10^{-7}
$L^{\mathrm{tot}}_{\mathrm{inel}}$	0.220×10^{-1}	0.573×10^{-1}	0.328×10^{-2}	0.487×10^{-3}
L^{tot}	0.646	0.656×10^{-1}	0.946×10^{-2}	0.487×10^{-3}
C_{el}	0.624	0.833×10^{-2}	0.618×10^{-2}	0.998×10^{-7}
$C^{\mathrm{tot}}_{\mathrm{inel}}$	0.188×10^{-1}	0.295×10^{-1}	0.157×10^{-3}	0.466×10^{-4}
C^{tot}	0.642	0.378×10^{-1}	0.634×10^{-2}	0.467×10^{-4}
$\eta=1+\gamma$	1.994	1.576	1.670	1.096

is that one peak of the inelastic light spectrum is exactly at the atomic frequency ω_0 (i.e., corresponding to $\Delta=-\delta_L$) for which the scattering cross section of atom 2 is maximum. More precisely, the inelastic spectrum scattered $I(\Delta)$ by atom 1 is multiplied by the factor

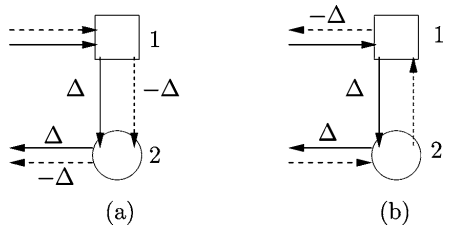

FIG. 3. A schematic approach of the basic processes contributing to the inelastic ladder and crossed spectrum, in the small saturation regime [20]. Nonlinear behavior only occurs at the atom 1, whereas only elastic scattering events take place at the atom 2. In the case of the ladder term (a), the inelastic light is thus emitted by atom 1 and then scattered by the atom 2. For nonzero detuning δ_L of the incident light, one peak of the inelastic light spectrum is exactly at the atomic frequency ω_0 (i.e., corresponding to $\Delta=-\delta_L$) for which the scattering cross section of atom 2 is maximum. This results in the ladder spectrum depicted by Fig. 2(c). In the case of the crossed term (b), the main difference is that the atom 2 scatters fields at different frequencies: one still corresponds to the inelastic light emitted by atom 1 (frequency $\omega_L+\Delta$) whereas the other corresponds to the incident light (frequency ω_L), which for large detuning δ_L results in a smaller crossed inelastic spectrum; furthermore, this also explains the dispersive behavior around $\Delta=-\delta_L$ depicted by Fig. 2(c).

$$\frac{\Gamma^2}{\Gamma^2+4(\Delta+\delta_L)^2} \tag{55}$$

which is maximum for $\Delta=-\delta_L$. This results in the ladder spectrum depicted by Fig. 2(c). In the case of the crossed term [Fig. 2(b)], the main difference is that atom 2 scatters fields at different frequencies: one still corresponds to the inelastic light emitted by atom 1 (frequency $\omega_L+\Delta$) whereas the other corresponds to the incident light (frequency ω_L). This leads to a new factor [20]

$$\mathrm{Re}\left(\frac{\Gamma^2}{[i\Gamma+2(\Delta+\delta_L)][i\Gamma+2(\delta_L)]}\right), \tag{56}$$

where $\mathrm{Re}(z)$ is the real part of z. For large detuning δ_L, this factor is then much smaller than the factor for the ladder case; furthermore, this also explains the dispersive behavior around $\Delta=-\delta_L$ depicted by Fig. 2(c).

Finally, depending on the values of the s and δ_L parameters, a rich variety of situations can be observed, with various physical interpretations. These are beyond the scope of this paper, which instead concentrate on the basic ingredients of the quantum Langevin approach and will be published elsewhere.

C. Linear response model

Some insight on the relative behavior of $C_{\mathrm{inel}}(\Delta)$ and $L_{\mathrm{inel}}(\Delta)$ can be found by comparing the respective formulas from which these quantities are extracted:

$$\langle X_{i'}^{\beta}(\Delta')X_i^{\alpha}(\Delta)\rangle^{(\bar{g}_\beta g_\alpha)} = g_\alpha\langle X_{i'}^{\beta^{(0)}}(\Delta')G_{ij}^{\alpha^+_q}(\Delta)(X_j^{\alpha^{(0)}}\otimes\mathcal{D}_q^{\beta-(0)})(\Delta)\rangle^{(\bar{g}_\beta)} - \bar{g}_\beta\langle G_{i'j'}^{\beta^-_q}(\Delta')(\mathcal{D}_q^{\alpha+(0)}\otimes X_{j'}^{\beta^{(0)}})(\Delta')X_i^{\alpha^{(0)}}(\Delta)\rangle^{(g_\alpha)}$$
$$- g_\alpha\bar{g}_\beta\{\langle X_{i'}^{\beta}(\Delta')G_{ij}^{\alpha^+_q}(\Delta)[X_j^{\alpha^{(0)}}\otimes G_{\mathcal{D}_q^-j'}^{\beta^-_p}(\mathcal{D}_p^{\alpha+(0)}\otimes X_{j'}^{\beta^{(0)}})](\Delta)\rangle^{(0)}$$
$$+\langle G_{i'j'}^{\beta^-_q}(\Delta')[G_{\mathcal{D}_q^-j}^{\alpha^+_p}(X_j^{\alpha^{(0)}}\otimes\mathcal{D}_p^{\beta-(0)})\otimes X_{j'}^{\beta^{(0)}}](\Delta')X_i^{\alpha^{(0)}}(\Delta)\rangle^{(0)}$$
$$+\langle[G_{i'j'}^{\beta^-_p}(\Delta')(\mathcal{D}_p^{\alpha+(0)}\otimes X_{j'}^{\beta^{(0)}})(\Delta')][G_{ij}^{\alpha^+_q}(\Delta)(X_j^{\alpha^{(0)}}\otimes\mathcal{D}_q^{\beta-(0)})(\Delta)]\rangle^{(0)}\} \tag{57}$$

and

$$\langle X_{i'}^{\alpha}(\Delta')X_i^{\alpha}(\Delta)\rangle^{(\bar{g}_\alpha g_\alpha)}$$
$$= \langle X_{i'}^{\alpha^{(0)}}(\Delta')X_i^{\alpha^{(0)}}(\Delta)\rangle^{(\bar{g}_\alpha g_\alpha)} + g_\alpha\{\langle X_{i'}^{\alpha^{(0)}}(\Delta')G_{ij}^{\alpha^+_q}(\Delta)(X_j^{\alpha^{(0)}}\otimes\mathcal{D}_q^{\beta-(0)})(\Delta)\rangle^{(\bar{g}_\alpha)}$$
$$+\langle G_{i'j'}^{\alpha^+_q}(\Delta')(X_{j'}^{\alpha^{(0)}}\otimes\mathcal{D}_q^{\beta-(0)})(\Delta')X_i^{\alpha^{(0)}}(\Delta)\rangle^{(\bar{g}_\alpha)}\} - \bar{g}_\alpha\{\langle X_{i'}^{\alpha^{(0)}}(\Delta')G_{ij}^{\alpha^-_q}(\Delta)(\mathcal{D}_q^{\beta+(0)}\otimes X_j^{\alpha^{(0)}})(\Delta)\rangle^{(g_\alpha)}$$
$$+\langle G_{i'j'}^{\alpha^-_q}(\Delta')(\mathcal{D}_q^{\beta+(0)}\otimes X_{j'}^{\alpha^{(0)}})(\Delta')X_i^{\alpha^{(0)}}(\Delta)\rangle^{(g_\alpha)}\} - \bar{g}_\alpha g_\alpha\{\langle X_{i'}^{\alpha}(\Delta')G_{ij}^{\alpha^+_q}(\Delta)[G_{jj'}^{\alpha^-_p}(\mathcal{D}_p^{\beta+(0)}\otimes X_{j'}^{\alpha^{(0)}})\otimes\mathcal{D}_q^{\beta-(0)}](\Delta)\rangle^{(0)}$$
$$+\langle X_{i'}^{\alpha}(\Delta')G_{ij}^{\alpha^-_q}(\Delta)[\mathcal{D}_q^{\beta+(0)}\otimes G_{jj'}^{\alpha^+_p}(X_{j'}^{\alpha^{(0)}}\otimes\mathcal{D}_p^{\beta-(0)})](\Delta)\rangle^{(0)} + \langle G_{i'j'}^{\alpha^+_q}(\Delta')[G_{jj'}^{\alpha^-_p}(\mathcal{D}_p^{\beta+(0)}\otimes X_j^{\alpha^{(0)}})\otimes\mathcal{D}_q^{\beta-(0)}](\Delta')X_i^{\alpha^{(0)}}(\Delta)\rangle^{(0)}$$
$$+\langle G_{i'j'}^{\alpha^-_q}(\Delta')[\mathcal{D}_q^{\beta+(0)}\otimes G_{jj'}^{\alpha^+_p}(X_j^{\alpha^{(0)}}\otimes\mathcal{D}_p^{\beta-(0)})](\Delta')X_i^{\alpha^{(0)}}(\Delta)\rangle^{(0)}$$
$$+\langle[G_{i'j'}^{\alpha^+_p}(\Delta')(X_{j'}^{\alpha^{(0)}}\otimes\mathcal{D}_p^{\beta-(0)})(\Delta')][G_{ij}^{\alpha^-_q}(\Delta)(\mathcal{D}_q^{\beta+(0)}\otimes X_j^{\alpha^{(0)}})(\Delta)]\rangle^{(0)}$$
$$+\langle[G_{i'j'}^{\alpha^-_p}(\Delta')(\mathcal{D}_p^{\beta+(0)}\otimes X_{j'}^{\alpha^{(0)}})(\Delta')][G_{ij}^{\alpha^+_q}(\Delta)(X_j^{\alpha^{(0)}}\otimes\mathcal{D}_q^{\beta-(0)})(\Delta)]\rangle^{(0)}\}. \tag{58}$$

There are twice as many terms contributing to the ladder terms as to the crossed terms. A rather simple explanation of this fact is borrowed from the usual linear response theory. Indeed, each atom is exposed to two fields: the incoming monochromatic field (angular frequency ω_L, wave vector $\mathbf{k}_L$) and the field scattered by the other atom (angular frequency $\omega_L+\Delta$, wave vector $\mathbf{k}_p$). In the far-field regime $R\gg\lambda$, the incoming field is more intense than the scattered field. It thus plays the role of a pump beam with angular Rabi frequency Ω_L, while the second weaker field plays the role of a probe beam with angular Rabi frequency Ω_p. In this case, the response of each atom is simply described by its nonlinear susceptibility [16,23]. More precisely, forgetting about polarization effects, we have

$$\delta\mathcal{D}^+(\Delta) = e^{-i(2\mathbf{k}_L-\mathbf{k}_p)\cdot\mathbf{R}_\alpha}\chi_{++}(\Delta)\Omega_p^+ + e^{-i\mathbf{k}_p\cdot\mathbf{R}_\alpha}\chi_{+-}(\Delta)\Omega_p^-,$$
$$\delta\mathcal{D}^-(\Delta) = e^{i\mathbf{k}_p\cdot\mathbf{R}_\alpha}\chi_{-+}(\Delta)\Omega_p^+ + e^{i(2\mathbf{k}_L-\mathbf{k}_p)\cdot\mathbf{R}_\alpha}\chi_{--}(\Delta)\Omega_p^-, \tag{59}$$

where the phases due to the light fields have been explicitly factorized.

As obviously seen, the two terms χ_{+-} and χ_{-+} generate the forward propagation of the probe whereas the two other terms χ_{++} and χ_{--} can generate an additional field in the direction $2\mathbf{k}_L-\mathbf{k}_p$ provided phase-matching conditions are fulfilled. This corresponds to the usual forward four-wave mixing mechanism (FFWM) [16,23]. In the low saturation regime, this corresponds to the following multiphotonic process: the atom first absorbs a photon from the pump; then the probe induces a stimulated emission; finally, another photon from the pump is absorbed, followed by a final spontaneous emission at frequency $2\omega_L-\omega_p=\omega_L-\Delta$. If we now replace the probe field by the field radiated by the other atom β, we get

$$\delta\mathcal{D}_{\beta\to\alpha}^+(\Delta) = \frac{1}{kR}\{e^{-i(kR+2\mathbf{k}_L\cdot\mathbf{R}_\alpha-\mathbf{k}_L\cdot\mathbf{R}_\beta)}\chi_{++}(\Delta)\mathcal{D}_\beta^-$$
$$+ e^{i(kR-\mathbf{k}_L\cdot\mathbf{R}_\beta)}\chi_{+-}(\Delta)\mathcal{D}_\beta^+\},$$

$$\delta\mathcal{D}_{\beta\to\alpha}^-(\Delta) = \frac{1}{kR}\{e^{-i(kR-\mathbf{k}_L\cdot\mathbf{R}_\beta)}\chi_{-+}(\Delta)\mathcal{D}_\beta^-$$
$$+ e^{i(2\mathbf{k}_L\cdot\mathbf{R}_\alpha+kR-\mathbf{k}_L\cdot\mathbf{R}_\beta)}\chi_{--}(\Delta)\mathcal{D}_\beta^+\}. \tag{60}$$

Hence the ladder and crossed contributions are given by (dropping for sake of clarity any frequency dependence)

$$C^{(2)} \approx \delta\mathcal{D}_{\alpha\to\beta}^+\delta\mathcal{D}_{\beta\to\alpha}^- e^{i(-\mathbf{k}_L\cdot\mathbf{R}_\beta+\mathbf{k}_L\cdot\mathbf{R}_\alpha)}$$
$$\approx e^{i[2\mathbf{k}_L\cdot(\mathbf{R}_\alpha-\mathbf{R}_\beta)-2kR]}\chi_{++}\chi_{-+}\mathcal{D}_\alpha^-\mathcal{D}_\beta^-$$
$$+ e^{4i\mathbf{k}_L\cdot(\mathbf{R}_\alpha-\mathbf{R}_\beta)}\chi_{++}\chi_{--}\mathcal{D}_\alpha^-\mathcal{D}_\beta^+ + \chi_{+-}\chi_{-+}\mathcal{D}_\alpha^+\mathcal{D}_\beta^-$$
$$+ e^{i[2\mathbf{k}_L\cdot(\mathbf{R}_\alpha-\mathbf{R}_\beta)+2kR]}\chi_{+-}\chi_{--}\mathcal{D}_\alpha^+\mathcal{D}_\beta^+,$$

$$L^{(2)} \approx \delta\mathcal{D}^{+}_{\beta\to\alpha}\delta\mathcal{D}^{-}_{\beta\to\alpha}$$
$$\approx e^{i[2\mathbf{k}_L\cdot(\mathbf{R}_\beta-\mathbf{R}_\alpha)-2kR]}\chi_{++}\chi_{-+}\mathcal{D}^{-}_{\beta}\mathcal{D}^{-}_{\beta}+\chi_{++}\chi_{--}\mathcal{D}^{-}_{\beta}\mathcal{D}^{+}_{\beta}$$
$$+\chi_{+-}\chi_{-+}\mathcal{D}^{+}_{\beta}\mathcal{D}^{-}_{\beta}+e^{i[2\mathbf{k}_L\cdot(\mathbf{R}_\alpha-\mathbf{R}_\beta)+2kR]}\chi_{+-}\chi_{--}\mathcal{D}^{+}_{\beta}\mathcal{D}^{+}_{\beta}. \quad (61)$$

Averaging these expressions over the positions $\mathbf{R}_\alpha$ and $\mathbf{R}_\beta$ of the atoms while keeping $R\gg\lambda$ fixed, only terms with position-independent phases survive, giving rise to

$$C^{(2)} \approx \chi_{+-}\chi_{-+}\mathcal{D}^{+}_{\alpha}\mathcal{D}^{-}_{\beta},$$

$$L^{(2)} \approx \chi_{++}\chi_{--}\mathcal{D}^{-}_{\beta}\mathcal{D}^{+}_{\beta}+\chi_{+-}\chi_{-+}\mathcal{D}^{+}_{\beta}\mathcal{D}^{-}_{\beta}. \quad (62)$$

This simple model allows one to understand clearly why there are twice more terms in the ladder expression than in the crossed one. Fields generated in the FFWM process *always* interfere constructively in the case of the ladder, since they originate from the same atom. Of course, in the preceding explanation, we have discarded polarization effects and inelastic processes in the nonlinear susceptibilities. Nevertheless, even if in that case the situation becomes more involved, the differences between the ladder and crossed expressions still arise from this local four-wave mixing process. For example, in the last line of Eqs. (57) and (58), we see that the operator $[G^{\alpha_q^+}_{ij}(\Delta)X_j^{\alpha^{(0)}}\otimes]$ plays the role of a generalized nonlinear susceptibility (actually, the standard ones are recovered from the elastic part of $X_j^{\alpha^{(0)}}$). Thus we recover the same structure as previously depicted, which leads to similar conclusions.

Finally, as mentioned above, for large saturation parameters s_0, even if in that case the total scattered intensities (ladder and crossed) are dominated by the inelastic spectrum, we numerically observe that the enhancement factor does not vanish but rather goes to a finite limit 1.096 (for $\delta_L=0$). Field coherence is thus not fully erased, which, at first glance, could be surprising since the inelastic spectrum is a noise spectrum at the heart of the temporal decoherence of the radiated field. This only means that both crossed and ladder become vanishingly small relative to the incident intensity. Nevertheless, even if it would be hard to derive it analytically from Eqs. (57) and (58), they actually decrease at the same rate, resulting in a finite (but small) enhancement factor.

V. CONCLUSION

In the case of two atoms, even if the quantum Langevin approach leads to calculations more tedious and involved than the direct optical Bloch method, it nevertheless gives rise to an understanding closer to the usual scattering approach developed in the linear regime. In this way, one also gets direct information about the inelastic spectrum of the radiated light. In particular, it clearly outlines the crucial roles played by the inelastic nonlinear susceptibilities and by the quantum correlations of the vacuum fluctuations. Furthermore, since the framework of the quantum Langevin approach is set in the frequency domain, frequency-dependent propagation (i.e., frequency-dependent mean-free paths) between the atoms can be naturally included.

The next step would be to adapt the present approach to "macroscopic" configurations (i.e., at least many atoms), allowing for a more direct comparison with existing experiments [7,8], for which the observed behavior of the enhancement factor with the saturation parameter is not fully understood. Especially, in the latter experiment (using atoms with a degenerate ground level), it strongly depends on the laser polarization, which suggests that the optical pumping, whose rate increases with the saturation parameter, plays an important role. Finally, for given values of the incident laser intensity and detuning, the nonlinear mean-free path becomes negative in well-defined frequency windows. This means that light amplification can be achieved in these frequency windows [41,46]. The atomic media would then constitute a very simple realization of a coherent random laser.

ACKNOWLEDGMENTS

We would like to thank Cord Müller, Oliver Sigwarth, Andreas Buchleitner, Vyacheslav Shatokhin, Serge Reynaud, and Jean-Michel Courty for stimulating discussions. T.W. has been supported by the DFG Emmy Noether program. Laboratoire Kastler Brossel is laboratoire de l'Université Pierre et Marie Curie et de l'Ecole Normale Supérieure, Grant No. UMR 8552 du CNRS.

APPENDIX A

The $g\bar{g}$ terms in Eq. (31) read:

$$X^{\beta}_{i'}(\Delta')X^{\alpha}_{i}(\Delta) = \cdots - g\bar{g}\Big\{X^{\beta}_{i'}(\Delta')\Big(G^{\alpha_q^+}_{ij}(\Delta)[X_j^{\alpha^{(0)}}\otimes G^{\beta_p^-}_{\mathcal{D}^-_q j'}(\mathcal{D}_p^{\alpha+^{(0)}}\otimes X_{j'}^{\beta^{(0)}})](\Delta)$$
$$+G^{\alpha_q^+}_{ij}(\Delta)[G^{\alpha_p^-}_{jj'}(\mathcal{D}_p^{\beta+^{(0)}}\otimes X_{j'}^{\alpha^{(0)}})\otimes\mathcal{D}_q^{\beta-^{(0)}}](\Delta)+G^{\alpha_q^-}_{ij}(\Delta)[\mathcal{D}_q^{\beta+^{(0)}}\otimes G^{\alpha_p^+}_{jj'}(X_{j'}^{\alpha^{(0)}}\otimes\mathcal{D}_p^{\beta-^{(0)}})](\Delta)$$
$$+G^{\alpha_q^-}_{ij}(\Delta)[G^{\beta_p^+}_{\mathcal{D}^-_q j'}(X_{j'}^{\beta^{(0)}}\otimes\mathcal{D}_p^{\alpha-^{(0)}})\otimes X_j^{\alpha^{(0)}}](\Delta)\Big)+\Big(G^{\beta_q^+}_{i'j'}(\Delta')[X_{j'}^{\beta^{(0)}}\otimes G^{\alpha_p^-}_{\mathcal{D}^-_q j}(\mathcal{D}_p^{\beta+^{(0)}}\otimes X_j^{\alpha^{(0)}})](\Delta')$$
$$+G^{\beta_q^+}_{i'j'}(\Delta')[G^{\beta_p^-}_{j'j}(\mathcal{D}_p^{\alpha+^{(0)}}\otimes X_j^{\beta^{(0)}})\otimes\mathcal{D}_q^{\alpha-^{(0)}}](\Delta')+G^{\beta_q^-}_{i'j'}(\Delta')[\mathcal{D}_q^{\alpha+^{(0)}}\otimes G^{\beta_p^+}_{j'j}(X_j^{\beta^{(0)}}\otimes\mathcal{D}_p^{\alpha-^{(0)}})](\Delta')$$
$$+\ G^{\beta_q^-}_{i'j'}(\Delta')[G^{\alpha_p^+}_{\mathcal{D}^-_q j}(X_j^{\alpha^{(0)}}\otimes\mathcal{D}_p^{\beta-^{(0)}})\otimes X_{j'}^{\beta^{(0)}}](\Delta')\Big)X_i^{\alpha^{(0)}}(\Delta)+[G^{\beta_p^+}_{i'j'}(\Delta')(X_{j'}^{\beta^{(0)}}\otimes\mathcal{D}_p^{\alpha-^{(0)}})(\Delta')]$$

$$\times\ [G_{ij}^{\alpha_q^-}(\Delta)(\mathcal{D}_q^{\beta+(0)}\otimes X_j^{\alpha(0)})(\Delta)]+[G_{i'j'}^{\beta_p^-}(\Delta')(\mathcal{D}_p^{\alpha+(0)}\otimes X_{j'}^{\beta(0)})(\Delta')][G_{ij}^{\alpha_q^+}(\Delta)(X_j^{\alpha(0)}\otimes\mathcal{D}_q^{\beta-(0)})(\Delta)]\Big\}, \quad \text{(A1)}$$

$$\begin{aligned}
X_{i'}^{\alpha}(\Delta')X_i^{\alpha}(\Delta) = \cdots - g\bar{g}\Big\{ & X_{i'}^{\alpha}(\Delta')\Big(G_{ij}^{\alpha_q^+}(\Delta)[X_j^{\alpha(0)}\otimes G_{\mathcal{D}_{q'}^-j'}^{\beta_p^-}(\mathcal{D}_p^{\alpha+(0)}\otimes X_{j'}^{\beta(0)})](\Delta)\\
&+G_{ij}^{\alpha_q^+}(\Delta)[G_{jj'}^{\alpha_p^-}(\mathcal{D}_p^{\beta+(0)}\otimes X_{j'}^{\alpha(0)})\otimes\mathcal{D}_q^{\beta-(0)}](\Delta)\\
&+G_{ij}^{\alpha_q^-}(\Delta)[\mathcal{D}_q^{\beta+(0)}\otimes G_{jj'}^{\alpha_p^+}(X_{j'}^{\alpha(0)}\otimes\mathcal{D}_p^{\beta-(0)})](\Delta)+G_{ij}^{\alpha_q^-}(\Delta)[G_{\mathcal{D}_{q'}^-j'}^{\beta_p^+}(X_{j'}^{\beta(0)}\otimes\mathcal{D}_p^{\alpha-(0)})\otimes X_j^{\alpha(0)}](\Delta)\Big)\\
&+\Big(G_{i'j'}^{\alpha_q^+}(\Delta')[X_{j'}^{\alpha(0)}\otimes G_{\mathcal{D}_{q'}^-j}^{\beta_p^-}(\mathcal{D}_p^{\alpha+(0)}\otimes X_j^{\beta(0)})](\Delta')\\
&+G_{i'j'}^{\alpha_q^+}(\Delta')[G_{jj}^{\alpha_p^-}(\mathcal{D}_p^{\beta+(0)}\otimes X_j^{\alpha(0)})\otimes\mathcal{D}_q^{\beta-(0)}](\Delta')+G_{i'j'}^{\alpha_q^-}(\Delta')[\mathcal{D}_q^{\beta+(0)}\otimes G_{jj}^{\alpha_p^+}(X_j^{\alpha(0)}\otimes\mathcal{D}_p^{\beta-(0)})](\Delta')\\
&+G_{i'j'}^{\alpha_q^-}(\Delta')[G_{\mathcal{D}_{q'}^-j}^{\beta_p^+}(X_j^{\beta(0)}\otimes\mathcal{D}_p^{\alpha-(0)})\otimes X_{j'}^{\alpha(0)}](\Delta')\Big)X_i^{\alpha(0)}(\Delta)+[G_{i'j'}^{\alpha_p^+}(\Delta')(X_{j'}^{\alpha(0)}\otimes\mathcal{D}_p^{\beta-(0)})(\Delta')]\\
&\times\ [G_{ij}^{\alpha_q^-}(\Delta)(\mathcal{D}_q^{\beta+(0)}\otimes X_j^{\alpha(0)})(\Delta)]+[G_{i'j'}^{\alpha_p^-}(\Delta')(\mathcal{D}_p^{\beta+(0)}\otimes X_{j'}^{\alpha(0)})(\Delta')][G_{ij}^{\alpha_q^+}(\Delta)(X_j^{\alpha(0)}\otimes\mathcal{D}_q^{\beta-(0)})(\Delta)]\Big\}. \quad \text{(A2)}
\end{aligned}$$

APPENDIX B: THREE-BODY CORRELATION FUNCTIONS

1. Single atom case

The three-body correlation function for the Langevin force reads

$$C_{abc}(\Delta',\Delta)=\frac{1}{2\pi}\int\int d\Delta_1 d\Delta_2\,\delta(\Delta_1+\Delta_2-\Delta)f(\Delta_1)g(\Delta_2)\times\langle F_a^{\alpha}(\Delta')F_b^{\alpha}(\Delta_1)F_c^{\alpha}(\Delta_2)\rangle, \quad \text{(B1)}$$

where $f(\Delta)$ and $g(\Delta)$ are regular functions such that the preceding integral is well defined. Going back to the time domain, $C_{abc}(\Delta',\Delta)$ reads as follows:

$$C_{abc}(\Delta',\Delta)=\frac{1}{2\pi}\int\int dt dt' e^{i\Delta t}e^{i\Delta' t'}\int\int\int\int dt_1 dt_2 dt_3 dt_4\times\delta(t_1+t_2-t)\delta(t_3+t_4-t)f(t_1)g(t_3)\times\langle F_a^{\alpha}(t')F_b^{\alpha}(t_2)F_c^{\alpha}(t_4)\rangle. \quad \text{(B2)}$$

Then, from the time correlation properties of the vacuum field, one can show that

$$\begin{aligned}
\langle F_a^{\alpha}(t')F_b^{\alpha}(t_2)F_c^{\alpha}(t_4)\rangle &= 4T_{aa'}^{q+}T_{bb'}^{q-}\delta(t'-t_2)\langle X_{a'}^{\alpha}(t')X_{b'}^{\alpha}(t')F_c^{\alpha}(t_4)\rangle\\
&+4T_{aa'}^{q+}T_{cc'}^{q-}\delta(t'-t_4)\langle X_{a'}^{\alpha}(t')F_b^{\alpha}(t_2)X_{c'}^{\alpha}(t_4)\rangle\\
&+4T_{bb'}^{q+}T_{cc'}^{q-}\delta(t_2-t_4)\langle F_a^{\alpha}(t')X_{b'}^{\alpha}(t_2)X_{c'}^{\alpha}(t_2)\rangle, \quad \text{(B3)}
\end{aligned}$$

where the $T^{q\pm}$ are 15×15 matrices defined by $[X_i,\mathcal{D}_q^{\pm}]=\pm2T_{ij}^{q\pm}X_j$.

When taken at the same time, the atomic operators (including the identity 1) define a group entirely characterized by the group structure constants ϵ_{ij}^k, i.e.,

$$X_i(t)X_j(t)=\sum_k\epsilon_{ij}^k X_k(t), \quad \text{(B4)}$$

so that the preceding equation becomes

$$\begin{aligned}
\langle F_a^{\alpha}(t')F_b^{\alpha}(t_2)F_c^{\alpha}(t_4)\rangle &= 4T_{aa'}^{q+}T_{bb'}^{q-}\delta(t'-t_2)\epsilon_{a'b'}{}^{u}\langle X_u^{\alpha}(t')F_c^{\alpha}(t_4)\rangle\\
&+4T_{aa'}^{q+}T_{cc'}^{q-}\delta(t'-t_4)\langle X_{a'}^{\alpha}(t')F_b^{\alpha}(t_2)X_{c'}^{\alpha}(t_4)\rangle\\
&+4T_{bb'}^{q+}T_{cc'}^{q-}\delta(t_2-t_4)\epsilon_{a'b'}{}^{u}F_a^{\alpha}(t')X_u^{\alpha}(t_2). \quad \text{(B5)}
\end{aligned}$$

Injecting the preceding relations in $C(a,b,c)$ and going back to the frequency domain, we get

$$\begin{aligned}
C_{abc}(\Delta',\Delta) = {} & 4T_{aa'}^{q+}T_{bb'}^{q-}\epsilon_{a'b'}{}^{u}\frac{1}{2\pi}\int\int d\Delta_1 d\Delta_2\,\delta(\Delta_1+\Delta_2-\Delta)f(\Delta_1)g(\Delta_2)\langle X_u^{\alpha}(\Delta'+\Delta_1)F_c^{\alpha}(\Delta_2)\rangle\\
&+4T_{aa'}^{q+}T_{cc'}^{q-}\frac{1}{2\pi}\int d\Delta_3 g(\Delta_3)f(\Delta-\Delta_3)D_{a'c'}^{b,\alpha\alpha\alpha}(\Delta'+\Delta_3,\Delta-\Delta_3)\\
&+4T_{bb'}^{q+}T_{cc'}^{q-}\epsilon_{a'b'}{}^{u}\langle F_a^{\alpha}(\Delta')X_u^{\alpha}(\Delta)\rangle\frac{1}{2\pi}\int\int d\Delta_1 d\Delta_2\,\delta(\Delta_1+\Delta_2-\Delta)f(\Delta_1)g(\Delta_2)
\end{aligned}$$

$$
\begin{aligned}
&= 4T^{q+}_{aa'}T^{q-}_{bb'}\epsilon_{a'b'}{}^{u}\frac{1}{2\pi}\int\int d\Delta_1 d\Delta_2 \delta(\Delta_1+\Delta_2-\Delta) f(\Delta_1) g(\Delta_2) G^{\alpha}_{uv}(\Delta'+\Delta_1)\langle F^{\alpha}_{v}(\Delta'+\Delta_1)F^{\alpha}_{c}(\Delta_2)\rangle \\
&\quad + 4T^{q+}_{aa'}T^{q-}_{cc'}\frac{1}{2\pi}\int d\Delta_3 g(\Delta_3) f(\Delta-\Delta_3) D^{b,\alpha a\alpha}_{a'c'}(\Delta'+\Delta_3,\Delta-\Delta_3) \\
&\quad + 4T^{q+}_{bb'}T^{q-}_{cc'}\epsilon_{a'b'}{}^{u}G^{\alpha}_{uv}(\Delta)\langle F^{\alpha}_{a}(\Delta')F^{\alpha}_{v}(\Delta)\rangle\frac{1}{2\pi}\int\int d\Delta_1 d\Delta_2 \delta(\Delta_1+\Delta_2-\Delta) f(\Delta_1) g(\Delta_2) \\
&= 2\pi\delta(\Delta+\Delta')4T^{q+}_{aa'}T^{q-}_{bb'}\epsilon_{a'b'}{}^{u}D^{\alpha\alpha}_{vc}\frac{1}{2\pi}\int\int d\Delta_1 d\Delta_2 \delta(\Delta_1+\Delta_2-\Delta) f(\Delta_1) g(\Delta_2) G^{\alpha}_{uv}(-\Delta_2) \\
&\quad + 4T^{q+}_{aa'}T^{q-}_{cc'}\frac{1}{2\pi}\int d\Delta_3 g(\Delta_3) f(\Delta-\Delta_3) D^{b,\alpha a\alpha}_{a'c'}(\Delta'+\Delta_3,\Delta-\Delta_3) \\
&\quad + 2\pi\delta(\Delta+\Delta')4T^{q+}_{bb'}T^{q-}_{cc'}\epsilon_{a'b'}{}^{u}D^{\alpha\alpha}_{av}G^{\alpha}_{uv}(\Delta)\frac{1}{2\pi}\int\int d\Delta_1 d\Delta_2 \delta(\Delta_1+\Delta_2-\Delta) f(\Delta_1) g(\Delta_2),
\end{aligned}
\tag{B6}
$$

where we have introduced the matrix $D^{b,\alpha a\alpha}_{ik}(\Delta',\Delta)$ defined by

$$
D^{b,\alpha a\alpha}_{ik}(\Delta',\Delta) = \frac{1}{2\pi}\int\int d\Delta_1 d\Delta_2 \delta(\Delta_1+\Delta_2-\Delta')\langle X^{\alpha}_{i}(\Delta_1)F^{\alpha}_{b}(\Delta)X^{\alpha}_{k}(\Delta_2)\rangle. \tag{B7}
$$

This matrix is calculated using the same strategy (i.e., going back and forth to the time domain) and one finally gets

$$
\begin{aligned}
D^{b,\alpha a\alpha}_{ik}(\Delta',\Delta) &= 2\pi\delta(\Delta+\Delta')\Bigg\{ G^{\alpha}_{ia}(0)L^{\alpha}_{a}G^{\alpha}_{kc}(\Delta')\tilde{D}^{\alpha\alpha}_{bc} + G^{\alpha}_{ia}(\Delta')G^{\alpha}_{kc}(0)L^{\alpha}_{c}\tilde{D}^{\alpha\alpha}_{ab} \\
&\quad + 4T^{q+}_{bb'}T^{q-}_{cc'}\epsilon_{b'c'}{}^{v}\tilde{D}^{\alpha\alpha}_{au}\frac{1}{2\pi}\int\int d\Delta_1 d\Delta_2 \delta(\Delta_1+\Delta_2-\Delta') G^{\alpha}_{ia}(\Delta_1)G^{\alpha}_{kc}(\Delta_2)G^{\alpha}_{vu}(-\Delta_1) \\
&\quad + 4T^{+}_{aa'}T^{-}_{bb'}\epsilon_{a'b'}{}^{v}\tilde{D}^{\alpha\alpha}_{uc}\frac{1}{2\pi}\int\int d\Delta_1 d\Delta_2 \delta(\Delta_1+\Delta_2-\Delta') G^{\alpha}_{ia}(\Delta_1)G^{\alpha}_{kc}(\Delta_2)G^{\alpha}_{vu}(-\Delta_2)\Bigg\} \\
&\quad + 4T^{q+}_{aa'}T^{q-}_{cc'}\Bigg(\frac{1}{2\pi}\int\int d\Delta_3 d\Delta_4 \delta(\Delta_3+\Delta_4-\Delta') G^{\alpha}_{ia}(\Delta_3)G^{\alpha}_{kc}(\Delta_4)\Bigg) \\
&\quad \times\Bigg(\frac{1}{2\pi}\int\int d\Delta_1 d\Delta_2 \delta(\Delta_1+\Delta_2-\Delta')\langle X^{\alpha}_{a'}(\Delta_1)F^{\alpha}_{b}(\Delta)X^{\alpha}_{c'}(\Delta_2)\rangle\Bigg).
\end{aligned}
\tag{B8}
$$

It may seem that we have taken a loop path and that we are back to square one…. However, in the last line of the preceding formula, we immediately recognize the matrix $D^{b,\alpha a\alpha}_{a'b'}(\Delta',\Delta)$. Thus, the preceding equation is nothing else but a linear system for this matrix. More precisely, $D^{b,\alpha a\alpha}_{ik}(\Delta',\Delta)$ is the solution of the following linear system:

$$
D^{b,\alpha a\alpha}_{ik}(\Delta',\Delta) - I^{\alpha\alpha}_{ik,a'c'}(\Delta')D^{b,\alpha a\alpha}_{a'c'}(\Delta',\Delta) = J^{b,\alpha a\alpha}_{ik}(\Delta',\Delta), \tag{B9}
$$

with

$$
I^{\alpha\alpha}_{ik,a'c'}(\Delta') = 4T^{q+}_{aa'}T^{q-}_{cc'}\frac{1}{2\pi}\int\int d\Delta_3 d\Delta_4 \delta(\Delta_3+\Delta_4-\Delta')G^{\alpha}_{ia}(\Delta_3)G^{\alpha}_{kc}(\Delta_4),
$$

$$
\begin{aligned}
J^{b,\alpha a\alpha}_{ik}(\Delta',\Delta) &= 2\pi\delta(\Delta+\Delta')\Bigg\{ G^{\alpha}_{ia}(0)L^{\alpha}_{a}G^{\alpha}_{kc}(\Delta')\tilde{D}^{\alpha\alpha}_{bc} + G^{\alpha}_{ia}(\Delta')G^{\alpha}_{kc}(0)L^{\alpha}_{c}\tilde{D}^{\alpha\alpha}_{ab} \\
&\quad + 4T^{q+}_{bb'}T^{q-}_{cc'}\epsilon_{b'c'}{}^{v}\tilde{D}^{\alpha\alpha}_{au}\frac{1}{2\pi}\int\int d\Delta_1 d\Delta_2 \delta(\Delta_1+\Delta_2-\Delta') G^{\alpha}_{ia}(\Delta_1)G^{\alpha}_{kc}(\Delta_2)G^{\alpha}_{vu}(-\Delta_1) \\
&\quad + 4T^{+}_{aa'}T^{-}_{bb'}\epsilon_{a'b'}{}^{v}\tilde{D}^{\alpha\alpha}_{uc}\frac{1}{2\pi}\int\int d\Delta_1 d\Delta_2 \delta(\Delta_1+\Delta_2-\Delta') G^{\alpha}_{ia}(\Delta_1)G^{\alpha}_{kc}(\Delta_2)G^{\alpha}_{vu}(-\Delta_2)\Bigg\}.
\end{aligned}
\tag{B10}
$$

In the preceding equations, the Green's function $G(\Delta)$ and the diffusion matrix $D^{\alpha\alpha}$ only depend on the Rabi field Ω_L evaluated at the position of atom α. Thus, for *any* value of Δ, numerical values of I and J can be computed, allowing for a direct calculation of $D^{b,\alpha a\alpha}_{ik}(-\Delta,\Delta)$. Furthermore, it is not surprising that the matrix I shows up in the linear system. Indeed,

the Green's function $G(\Delta)$ governs the time evolution of $\mathbf{X}$ through a Fourier transform. Thus the time evolution of products of operators $\mathbf{X}_i(t)\mathbf{X}_j(t)$ will be simply governed by the Fourier transform of the product of two Green's functions $G(t)G(t)$, which is precisely the convolution product found in *I*. Finally, from the knowledge of the matrix D, we can calculate the value of $C_{abc}(\Delta',\Delta)$:

$$C_{abc}(\Delta',\Delta) = 2\pi\delta(\Delta+\Delta')\Bigg\{ 4T^{q+}_{aa'}T^{q-}_{bb'}\epsilon_{a'b'u}D^{\alpha\alpha}_{vc}\frac{1}{2\pi}\int\int d\Delta_1 d\Delta_2 \delta(\Delta_1+\Delta_2-\Delta) f(\Delta_1) g(\Delta_2) G^{\alpha}_{uv}(-\Delta_2)$$
$$+ 4T^{q+}_{aa'}T^{q-}_{cc'}\frac{1}{2\pi}\int\int d\Delta_1 d\Delta_2 \delta(\Delta_1+\Delta_2-\Delta) f(\Delta_1) g(\Delta_2) D^{b,\alpha\alpha\alpha}_{a'c'}(-\Delta_1,\Delta_1)$$
$$+ 4T^{q+}_{bb'}T^{q-}_{cc'}\epsilon_{a'b'u}D^{\alpha\alpha}_{av}G^{\alpha}_{uv}(\Delta)\frac{1}{2\pi}\int\int d\Delta_1 d\Delta_2 \delta(\Delta_1+\Delta_2-\Delta) f(\Delta_1) g(\Delta_2)\Bigg\}. \tag{B11}$$

Of course, we recover the global factor $2\pi\delta(\Delta+\Delta')$, showing that the time correlation function only depends on the time difference $t'-t$ (stationary condition).

2. Two-atom case

The calculation of quantities such as

$$C^{\alpha\beta}_{abc}(\Delta',\Delta) = \frac{1}{2\pi}\int\int d\Delta_1 d\Delta_2 \delta(\Delta_1+\Delta_2-\Delta) f(\Delta_1) g(\Delta_2) \langle F^{\alpha}_{j'}(\Delta') F^{\beta}_{k}(\Delta_1) F^{\alpha}_{k'}(\Delta_2)\rangle^{(\bar{g})} \tag{B12}$$

follows, more or less, the way described in the preceding section. In particular, it also involves the calculation of a matrix $D^{b,\alpha\beta\alpha^{(\bar{g})}}_{ik}(\Delta',\Delta)$ defined as

$$D^{b,\alpha\beta\alpha^{(\bar{g})}}_{ik}(\Delta',\Delta) = \frac{1}{2\pi}\int\int d\Delta_1 d\Delta_2 \delta(\Delta_1+\Delta_2-\Delta') \langle X^{\alpha}_{i}(\Delta_1) F^{\beta}_{b}(\Delta) X^{\alpha}_{k}(\Delta_2)\rangle^{(\bar{g})}. \tag{B13}$$

The latter is also found to be the solution of a linear system, resembling the preceding one [see Eq. (B9)]:

$$D^{b,\alpha\beta\alpha^{(\bar{g})}}_{ik}(\Delta',\Delta) - I^{\alpha\alpha}_{ik,a'c'}(\Delta') D^{b,\alpha\beta\alpha^{(\bar{g})}}_{a'c'}(\Delta',\Delta) = J^{b,\alpha\beta\alpha^{(\bar{g})}}_{ik}(\Delta',\Delta), \tag{B14}$$

with

$$J^{b,\alpha\beta\alpha^{(\bar{g})}}_{ik}(\Delta',\Delta) = -\left(\frac{1}{2}\right)2\pi\delta(\Delta+\Delta')\Bigg\{ G^{\alpha}_{ia}(0)L^{\alpha}_{a}G^{\alpha}_{kc}(\Delta')\tilde{D}^{\beta\alpha^{(0)}}_{bc} + G^{\alpha}_{ia}(\Delta')G^{\alpha}_{kc}(0)L^{\alpha}_{c}\tilde{D}^{\alpha\beta^{(0)}}_{ab}$$
$$+ 4T^{q+}_{bb'}\langle X^{\beta^{(0)}}_{b'}\rangle\frac{1}{2\pi}\int\int d\Delta_1 d\Delta_2 \delta(\Delta_1+\Delta_2-\Delta') G^{\alpha}_{ia}(\Delta_1) G^{\alpha^{-}_{q}}_{kc}(\Delta_2) G^{\alpha}_{cu}(-\Delta_1)\tilde{D}^{\alpha\alpha^{(0)}}_{au}$$
$$+ 4T^{q-}_{bb'}\langle X^{\beta^{(0)}}_{b'}\rangle\frac{1}{2\pi}\int\int d\Delta_1 d\Delta_2 \delta(\Delta_1+\Delta_2-\Delta') G^{\alpha^{+}_{q}}_{ia}(\Delta_1) G^{\alpha}_{kc}(\Delta_2) G^{\alpha}_{au}(-\Delta_2)\tilde{D}^{\alpha\alpha^{(0)}}_{uc}$$
$$- 2G^{\beta}_{\mathcal{D}^{+}_{q}u}(\Delta')\tilde{D}^{\beta\beta^{(0)}}_{ub}\frac{1}{2\pi}\int\int d\Delta_1 d\Delta_2 \delta(\Delta_1+\Delta_2-\Delta') G^{\alpha^{-}_{q}}_{ia}(\Delta_1)\langle\tilde{X}^{\alpha^{(0)}}_{a}(-\Delta_2)\tilde{X}^{\alpha^{(0)}}_{k}(\Delta_2)\rangle^{(0)}$$
$$- 2G^{\beta}_{\mathcal{D}^{+}_{q}u}(\Delta')\tilde{D}^{\beta\beta^{(0)}}_{bu}\frac{1}{2\pi}\int\int d\Delta_1 d\Delta_2 \delta(\Delta_1+\Delta_2-\Delta') G^{\alpha^{-}_{q}}_{kc}(\Delta_2)\langle\tilde{X}^{\alpha^{(0)}}_{i}(\Delta_1)\tilde{X}^{\alpha^{(0)}}_{c}(-\Delta_1)\rangle^{(0)}\Bigg\}. \tag{B15}$$

[1] C. J. Pethick and H. Smith, *Bose-Einstein Condensation in Dilute Gases* (Cambridge University Press, Cambridge, 2002); L. P. Pitaevskii and S. Stringari, *Bose-Einstein Condensation* (Clarendon, Oxford, 2003).

[2] M. Greiner, C. A. Regal, and D. S Jin, Nature (London) **426**, 537 (2003); S. Jochim *et al.*, Science **302**, 2101 (2003).

[3] M. Greiner, O. Mandel, T. Esslinger, T. W. Hnsch, and I. Bloch, Nature (London) **415**, 39 (2002).

[4] W. K. Hensinger, A. Mouchet, P. S. Julienne, D. Delande, N. R. Heckenberg, and H. Rubinsztein-Dunlop, Phys. Rev. A **70**, 013408 (2004); Z. Y. Ma, M. B. d'Arcy, and S. A. Gardiner, Phys. Rev. Lett. **93**, 164101 (2004).

[5] R. Battesti P. Cladé, S. Guellati-Khélifa, C. Schwob, B. Grémaud, F. Nez, L. Julien, and F. Biraben, Phys. Rev. Lett. **92**, 253001 (2004); M. Weitz, B. C. Young, and S. Chu, *ibid.* **73**, 2563 (1994).
[6] G. Labeyrie, F. de Tomasi, J. C. Bernard, C. A. Müller, C. Miniatura, and R. Kaiser, Phys. Rev. Lett. **83**, 5266 (1999).
[7] T. Chanelière, D. Wilkowski, Y. Bidel, R. Kaiser, and C. Miniatura, Phys. Rev. E **70**, 036602 (2004).
[8] S. Balik, P. Kulatunga, C. I. Sukenik, M. D. Havey, D. V. Kupriyanov, I. M. Solokov, J. Mod. Opt. **52**, 2269 (2005).
[9] *Mesoscopic Quantum Physics*, Proceedings of the Les Houches Summer School, Session LXI, edited by E. Akkermans, G. Montambaux, J. L. Pichard, and J. Zinn-Justin (North Holland, Elsevier Science, Amsterdam, 1995).
[10] E. Akkermans and G. Montambaux, *Physique Mésoscopique des Électrons et des Photons* (EDP Sciences, CNRS Editions, Paris 2004). An English translation is in preparation.
[11] M. P. Van Albada and A. Lagendijk, Phys. Rev. Lett. **55**, 2692 (1985); P. E. Wolf and G. Maret, *ibid.* **55**, 2696 (1985).
[12] A. Akkermans and G. Montambaux, J. Opt. Soc. Am. B **21**, 101 (2004).
[13] D. Wilkowski, Y. Bidel, T. Chaneliére, D. Delande, T. Jonckheere, B. Klappauf, G. Labeyrie, C. Miniatura, C. A. Müller, O. Sigwarth and R. KaiserJ. Opt. Soc. Am. B **21**, 183 (2004), and references therein.
[14] O. Sigwarth, G. Labeyrie, T. Jonckheere, D. Delande, R. Kaiser and C. Miniatura,Phys. Rev. Lett. **93**, 143906 (2004).
[15] C. A. Müller, T. Jonckheere, C. Miniatura, and D. Delande, Phys. Rev. A **64**, 053804 (2001).
[16] R. W. Boyd, *Nonlinear Optics* (Academic, San Diego, 1992).
[17] G. Grynberg, A. Maître, and A. Petrossian, Phys. Rev. Lett. **72**, 2379 (1994).
[18] M. L. Dowell, R. C. Hart, A. Gallagher, and J. Cooper, Phys. Rev. A **53**, 1775 (1996).
[19] S. E. Skipetrov and R. Maynard, Phys. Rev. Lett. **85**, 736 (2000).
[20] T. Wellens, B. Grémaud, D. Delande, and C. Miniatura, Phys. Rev. A **70**, 023817 (2004).
[21] T. Wellens, B. Grémaud, D. Delande, and C. Miniatura, Phys. Rev. E **71**, 055603(R) (2005).
[22] T. Wellens, B. Grémaud, D. Delande, and C. Miniatura, Phys. Rev. A **73**, 013802 (2006).
[23] C. Cohen-Tannoudji, J. Dupont-Roc, and G. Grynberg, *Atom-Photon Interactions* (Wiley, New York, 1992).
[24] B. R. Mollow, Phys. Rev. **188**, 1969 (1969).
[25] C. W. Gardiner and P. Zoller, *Quantum Noise*, 2nd ed. (Springer, Berlin, 1999).
[26] L. You, J. Mostowski, and J. Cooper, Phys. Rev. A **46**, 2903 (1992).
[27] L. You, J. Mostowski, and J. Cooper, Phys. Rev. A **46**, 2925 (1992).
[28] L. You and J. Cooper, Phys. Rev. A **51**, 4194 (1995).
[29] M. L. Dowell, B. D. Paul, A. Gallagher, and J. Cooper, Phys. Rev. A **52**, 3244 (1995).
[30] Y. Ben-Aryeh, Phys. Rev. A **56**, 854 (1997).
[31] H. Cao, Waves Random Media **13**, R1 (2003).
[32] V. M. Apalkov, M. E. Raikh, and B. Shapiro, Phys. Rev. Lett. **89**, 016802 (2002).
[33] V. A. Podolskiy, E. Narimanov, W. Fang, and H. Cao, Proc. Natl. Acad. Sci. U.S.A. **101**, 10498 (2004).
[34] G. Hackenbroich, C. Viviescas, and F. Haake, Phys. Rev. Lett. **89**, 083902 (2002).
[35] T. Harayama, P. Davis, and K. S. Ikeda, Phys. Rev. Lett. **90**, 063901 (2003).
[36] G. V. Varada and G. S. Agarwal, Phys. Rev. A **45**, 6721 (1992).
[37] V. Shatokhin, C. A. Müller, and A. Buchleitner, Phys. Rev. Lett. **94**, 043603 (2005).
[38] C. Cohen-Tannoudji, J. Dupont-Roc, and G. Grynberg, *Photons and Atoms, Introduction to Quantum Electrodynamics* (Wiley, New York, 1989).
[39] J. M. Courty and S. Reynaud, Phys. Rev. A **46**, 2766 (1992).
[40] C. W. Gardiner and P. Zoller, *Quantum Noise*, 2nd ed. (Springer-Verlag, New York, 2000).
[41] B. R. Mollow, Phys. Rev. A **5**, 2217 (1972).
[42] R. Matloob, R. Loudon, S. M. Barnett, and J. Jeffers, Phys. Rev. A **52**, 4823 (1995).
[43] S. Scheel, L. Knöll, and D. G. Welsch, Phys. Rev. A **58**, 700 (1998).
[44] B. van Tiggelen and R. Maynard, in *Waves in Random and Other Complex Media*, edited by L. Burridge, G. Papanicolaou, and L. Pastur (Springer, Berlin, 1997), Vol. 96, p. 247.
[45] Please note, however, that this result is no longer true as soon as inelastic scattering occurs in a medium: in this case, CBS can arise from a three-wave interference [21].
[46] F. Y. Wu, S. Ezekiel, M. Ducloy, and B. R. Mollow, Phys. Rev. Lett. **38**, 1077 (1977).
[47] G. Labeyrie, E. Vaujour, C. A. Müller, D. Delande, C. Miniatura, D. Wilkowski, and R. Kaiser, Phys. Rev. Lett. **91**, 223904 (2003).

Coherent backscattering of light with nonlinear atomic scatterers

T. Wellens,[1,2] B. Grémaud,[2] D. Delande,[2] and C. Miniatura[1]
[1]*Institut Non Linéaire de Nice, UMR 6618, 1361 route des Lucioles, F-06560 Valbonne, France*
[2]*Laboratoire Kastler Brossel, Université Pierre et Marie Curie, 4 Place Jussieu, F-75005 Paris, France*
(Received 16 September 2005; published 4 January 2006)

We study coherent backscattering of a monochromatic laser by a dilute gas of cold two-level atoms in the weakly nonlinear regime. The nonlinear response of the atoms results in a modification of both the average field propagation (nonlinear refractive index) and the scattering events. Using a perturbative approach, the nonlinear effects arise from inelastic two-photon scattering processes. We present a detailed diagrammatic derivation of the elastic and inelastic components of the backscattering signal for both scalar and vectorial photons. In particular, we show that the coherent backscattering phenomenon originates in some cases from the interference between *three* different scattering amplitudes. This is in marked contrast with the linear regime where it is due to the interference between two different scattering amplitudes. In particular we show that, if elastically scattered photons are filtered out from the photodetection signal, the nonlinear backscattering enhancement factor exceeds the linear barrier of 2, consistently with a three-amplitude interference effect.

DOI: 10.1103/PhysRevA.73.013802 PACS number(s): 42.65.−k, 32.80.−t, 42.25.Dd

I. INTRODUCTION

Propagation of light waves in disordered media is an active research area for 100 years now. The original scientific motivation came from astrophysical questions about properties of light radiated by interstellar atmospheres [1,2]. Then, within the first decades of the 20th century, the foundations of light transport in this regime were laid, leading to the radiative transfer equations [3–6]. The basic physical ingredient of these equations is a detailed analysis of energy transfers (scattering, absorption, sources, etc.). Sufficiently far from any boundaries, the long-time and large-spatial-scale limits of these equations give rise, in the simplest cases, to a physically appealing diffusion equation.

One important feature of this theory is to consider that any possible interference effects are washed out under disorder average. This is a *random-phase* assumption. For a long time, it was believed that this was still the case on average for monochromatic light elastically scattered off an optically thick sample even if, for a given disorder realization, one observes a speckle pattern [7] indicating that phase coherence is preserved by the scattering process. Theoretical and experimental work in electronic transport [8–10] soon made clear that this random-phase assumption was wrong in the elastic regime. Depending on the disorder strength, partial (weak-localization regime) or complete (strong-localization regime) suppression of diffusive behavior has been predicted, provided phase coherence is preserved over a sufficiently large number of scattering events [11,12]. In turn, these discoveries have cross-fertilized the field of light transport in the elastic regime [13–16]. In this field, one of the hallmarks of interference effects in elastic transport is the *coherent backscattering* (CBS) phenomenon [17,18]: the average intensity multiply scattered off an optically thick sample is larger than the average background in a small angular range around the direction opposite to the ingoing light. This interference enhancement of the diffuse reflection off the sample is a manifestation of a two-wave interference. As such, it probes the coherence properties of the outgoing light and it has been extensively studied both experimentally and theoretically. It can be shown on general arguments that the CBS enhancement factor (defined as the ratio of the backscattering CBS peak to diffuse background) never exceeds the value 2 and is obtained in the helicity-preserving polarization channel for scatterers with spherical symmetry [19].

Whereas these interference modifications of transport are by now widely understood in the case of linear media, recent experimental developments have required an extension of multiple-scattering theory to the nonlinear case. Even if a few studies already exist, they only cover the simpler case of classical linear scatterers embedded in a nonlinear medium [20,21], whereas in our microscopic approach, the nonlinear behavior of randomly distributed scatterers will affect both the scattering processes and the average propagation. In particular, with the advent of laser cooling, on the one hand, it has become possible to study interference effects in multiple scattering of light by *cold atoms* [22–26]. In the regime where the saturation of the atomic transition sets in, atoms scatter light nonlinearly, i.e., the scattered light is no longer proportional to the incident light. One should note that important nonlinear effects are easily achieved with atoms even at moderate laser intensities. Considering a given driven optical dipole atomic transition, the order of magnitude of the required light intensity to induce nonlinear effects is given by the so-called saturation intensity I_s and is generally low. As typical examples, it is 1.6 mW/cm^2 for rubidium atoms and 42 mW/cm^2 for strontium atoms, for their usual laser cooling transitions. On the other hand, *random lasers*—mirrorless lasers where feedback is provided by multiple scattering [27]—have been realized experimentally [28,29]. Here, nonlinear effects occur in the regime close to or above the laser threshold. Since, at least in the regime of coherent feedback [30], interference is believed to play a decisive role in the physics of the random laser, a better understanding of the influence of nonlinearity (and amplification) on the properties of coherent wave transport becomes necessary.

II. MOTIVATION AND OUTLINE

In a recent contribution [31], we have shown that nonlinear scattering may fundamentally affect interference in multiple scattering. Indeed, in the perturbative regime of at most one scattering event with $\chi^{(3)}$ nonlinearity, there are now three (and no longer two) CBS interfering amplitudes. Depending on the sign of the nonlinearity, i.e., depending whether nonlinear effects enhance or decrease the scattering cross section, the effect of this three-wave interference effect leads to a significant increase or decrease of the nonlinear CBS enhancement factor.

The purpose of the present paper is, on the one hand, to provide a detailed derivation of the equations for the nonlinear coherent backscattering signal used in [31], and, on the other one, to extend the treatment of [31] to the case of atomic scatterers. Here, in contrast to the classical case, light is scattered *inelastically*, i.e., the scattered photons may change their frequencies. This leads to dephasing between interfering amplitudes and, consequently, to a reduction of the CBS enhancement factor in addition to the nonlinear modifications mentioned above. Theoretical studies of this inelastic decoherence mechanism have been so far restricted to the case of two atoms [32–34]. Since the total (linear and nonlinear) elastic signal can be filtered out by means of a suitable frequency-selective detection, a clear experimental study of inelastic, nonlinear CBS becomes possible. Please note that this would be otherwise very difficult to achieve since for weak intensities—the regime where our theory is valid—the linear signal generally greatly dominates over the nonlinear one. In this paper, we will show that the enhancement factor for inelastically scattered light significantly exceeds the linear barrier of 2 in certain frequency windows. In contrast, the total enhancement factor—including also elastically scattered light—is diminished by nonlinear scattering. This is due to the negative sign of the total nonlinear component, since the total (elastic plus inelastic) scattering cross section is decreased by saturation.

The paper is organized as follows. In Sec. III, we present the perturbative theory for nonlinear CBS of light scattered off a sample of cold two-level atoms. "Perturbative" here means that we restrict ourselves to the regime of scalar—i.e., we forget the polarization of the photon—two-photon scattering with at most one nonlinear scattering event. This assumption is valid at sufficiently low probe intensities and not too large optical thicknesses. After briefly sketching the main results of the linear case, Sec. III A, we derive equations for the nonlinear backscattering signal in Sec. III B. The latter contains an inelastic and an elastic component. The latter again splits into a nonlinear and a linear part. In Sec. III C, supplemented by the Appendix, we show how to generalize our scalar theory to the vectorial case by explicitly taking into account the light polarization degrees of freedom. It is shown that nonlinear polarization effects lead to decoherence between interfering paths. In contrast to the linear case, this decoherence mechanism cannot be avoided by a suitable choice of the polarization detection channel. In order to emphasize the generality of our approach, we briefly discuss in Sec. III D a model of classical, nonlinear scatterers, which reproduces the elastic backscattering signal of the atomic model. In Sec. IV, we apply our theory to the case of a disordered atomic medium with slab geometry. We look at the dependence of the backscattering signal as a function of the optical thickness and of the detuning of the laser from the atomic resonance. In particular, we show that the enhancement factor for the inelastic component significantly exceeds the linear barrier of 2 in certain frequency windows. Finally, Sec. V concludes the paper.

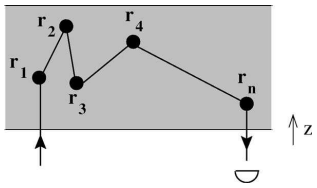

FIG. 1. Scattering path of a single photon entering the medium and leaving it in the backscattering direction to reach the detector. Straight lines depict average propagation in the effective medium while full circles depict scattering events labeled by the $\mathbf{r}_n$.

III. THEORY

In this section, we present the perturbative theory for nonlinear coherent backscattering of light from a gas of cold two-level atoms. We first treat the linear component of the backscattering signal, which results from scattering of independent photons. Thereby we introduce the reader, in Sec. III A, to standard methods used in linear multiple-scattering theory [35], which we will then generalize to the nonlinear case in Sec. III B.

A. Scalar linear regime

1. One-photon scattering amplitude

By definition, the linear component of the photodetection signal is proportional to the incoming intensity, in particular to the number of photons in the initial laser mode. Since this implies that the photons are independent from each other, it is sufficient to know how a single photon propagates in the atomic medium (see Fig. 1). This is equivalent to using the usual Maxwell's equations for a disordered medium [35].

In the weak-scattering regime, which we will consider throughout this paper, transport is depicted as a succession of propagation in an average medium interrupted by scattering events. The important building block to properly describe scattering and average propagation is the one-photon scattering amplitude by a single atom. For near-resonant scattering, and for atoms with no ground-state internal Zeeman degeneracies, it reads

$$S_\omega = \frac{-4\pi i}{k(1-2i\delta/\Gamma)}. \tag{1}$$

It can be derived from the elastically bound electron model in the limit of small light detuning $\delta=\omega-\omega_{\mathrm{at}} \ll \omega, \omega_{\mathrm{at}}$ [35].

The atomic angular transition frequency is ω_{at} whereas the atomic transition width Γ describes radiative decay. The photon wave number is k and the photon angular frequency is $\omega=ck$ (c being the vacuum speed of light).

For simplicity, we work here with scalar photons, i.e., we discard the vectorial nature of the light field. Scattering is then fully isotropic and the differential scattering cross section simply reads

$$\frac{d\sigma}{d\Omega} = \left|\frac{S_\omega}{4\pi}\right|^2 = \frac{\sigma}{4\pi} \tag{2}$$

leading to

$$\sigma = \frac{\sigma_0}{1+(2\delta/\Gamma)^2}, \quad \sigma_0 = \frac{4\pi}{k^2}, \tag{3}$$

where σ_0 is the on-resonance scattering cross section.

The scalar assumption is not a crucial one: as will be shown in Sec. III C, the following treatment can be generalized to the vectorial case. Please note, however, that the inclusion of internal degeneracies is not immediately simple and requires a separate treatment on its own. This is so because then the internal dynamics is no longer simple (optical pumping sets in). In this respect the results presented throughout this paper only apply to nondegenerate ground-state atoms. Please note also that internal degeneracies are already known to strongly reduce the CBS effect in the linear regime [24,25].

2. Linear refraction index

Between two successive scattering events occurring at $\mathbf{r}$ and $\mathbf{r}'$, the photon experiences an effective atomic medium with refractive index n_ω. Formally, the resulting propagation is described by the average Green's function

$$G_\omega(\mathbf{r},\mathbf{r}') = -\frac{e^{in_\omega k|\mathbf{r}-\mathbf{r}'|}}{4\pi|\mathbf{r}-\mathbf{r}'|}, \tag{4}$$

where the refractive index is given by [36]

$$n_\omega = 1 - \frac{\delta}{\Gamma k\ell} + \frac{i}{2k\ell}. \tag{5}$$

The imaginary part of n_ω describes depletion by scattering. This depletion gives rise to the exponential attenuation of the direct transmission through the sample (Beer-Lambert law) and defines, via the optical theorem, the linear mean free path at frequency ω as

$$\ell = \frac{1}{\mathcal{N}\sigma} \tag{6}$$

where $\mathcal{N}$ denotes the density number of atoms in the sample. The weak-scattering condition, where all the previous (and following) results are valid, then simply reads $k\ell \gg 1$.

3. Linear radiative transfer equation

We have now at hand all the necessary ingredients to write down the amplitude of a multiple-scattering process like the one sketched in Fig. 1. We consider a scattering volume V exposed to an initial monochromatic field with amplitude E_0 propagating along axis z. The transverse area of the scattering volume is Σ. Since $k\ell \gg 1$, a semiclassical picture using well-defined scattering paths is appropriate. For a given scattering path $C_n \equiv (\mathbf{r}_1 \to \cdots \to \mathbf{r}_n)$ labeled by the collection of scattering events, the corresponding far-field amplitude radiated at position $\mathbf{R}$ of the detector placed in the backscattering direction is

$$\mathcal{E}(C_n) = -\frac{e^{ikR}}{4\pi kR}\mathcal{A}(C_n)E_0. \tag{7}$$

The complex amplitude $\mathcal{A}(C_n)$ is simply a product of one-photon scattering amplitudes (1) and of Green's functions (4):

$$\mathcal{A}(C_n) = kS_\omega e^{ikn_\omega(z_1+z_n)}\left(\prod_{i=1}^{n-1} S_\omega G_\omega(\mathbf{r}_i,\mathbf{r}_{i+1})\right) \tag{8}$$

where z_i is the distance from the boundary of the medium to the position where scattering event i occurs. The superposition principle then gives the total electric field amplitude $\mathcal{E}$ as a sum over all possible scattering paths C_n:

$$\mathcal{E} = -\frac{e^{ikR}}{4\pi kR}E_0\mathcal{A}, \quad \mathcal{A} = \sum_{C_n}\mathcal{A}(C_n). \tag{9}$$

The total average intensity is obtained by squaring (9) and averaging over all possible scattering events. We define the total dimensionless bistatic coefficient as

$$\gamma_{el}^{(1)} = \frac{4\pi R^2}{\Sigma E_0^2}\langle|\mathcal{E}|^2\rangle_{\text{dis av}} = \frac{1}{4\pi k^2\Sigma}\langle|\mathcal{A}|^2\rangle_{\text{dis av}}. \tag{10}$$

We now assume complete cancellation of interference effects between different scattering paths (random-phase or Boltzmann approximation). We then obtain the background (or "ladder") component of the backscattering signal:

$$\gamma_{el}^{(1)} \approx L_{el}^{(1)} = \sum_{n=1}^{\infty}\frac{\mathcal{N}^n}{4\pi k^2\Sigma}\int_V d\mathbf{r}_1\cdots d\mathbf{r}_n|\mathcal{A}(C_n)|^2. \tag{11}$$

This formula has a well-defined limit when $\Sigma\to\infty$ and thus can be applied to slab geometries. Please note that, in writing Eq. (11), we have also discarded recurrent scattering paths, i.e., paths visiting a given scatterer more than once. Both approximations are justified in the case of a dilute medium, $k\ell \gg 1$ [37].

We rewrite Eq. (11) as

$$L_{el}^{(1)} = \int \frac{d\mathbf{r}}{\Sigma\ell} I_\omega(\mathbf{r})e^{-z/\ell}, \tag{12}$$

with

$$I_\omega(\mathbf{r}) = e^{-z/\ell} + \sum_{n=1}^{\infty} \mathcal{N}^n \int_V d\mathbf{r}_1 \cdots d\mathbf{r}_n \times e^{-z_1/\ell} \prod_{i=1}^{n} |S_\omega G_\omega(\mathbf{r}_i, \mathbf{r}_{i+1})|^2, \quad (13)$$

where $\mathbf{r}_{n+1}=\mathbf{r}$. This dimensionless function describes the average light intensity at $\mathbf{r}$, in units of the incident intensity $I_0=\epsilon_0 c E_0^2/2$ (in $\mathrm{W/m^2}$) with ϵ_0 the vacuum permittivity. The first term in Eq. (13) represents the exponential attenuation of the incident light mode, i.e., light which has penetrated to position $\mathbf{r}$ without being scattered (Beer-Lambert law). The remaining term describes the diffuse intensity, i.e., light which has been scattered at least once before reaching $\mathbf{r}$. From Eq. (13), one can easily show that $I_\omega(\mathbf{r})$ satisfies the radiative transfer integral equation [3]

$$I_\omega(\mathbf{r}) = e^{-z/\ell} + \frac{4\pi}{\ell} \int_V d\mathbf{r}' |G_\omega(\mathbf{r}, \mathbf{r}')|^2 I_\omega(\mathbf{r}'). \quad (14)$$

The required solution of Eq. (14) can be obtained numerically by iteration starting from $I_\omega(\mathbf{r})=0$.

4. Linear CBS cone

In fact, the preceding Boltzmann approximation $\gamma_{\mathrm{el}}^{(1)} \approx L_{\mathrm{el}}^{(1)}$ is wrong around the backscattering direction. Indeed, on top of the background ladder component, one observes a narrow cone of height $C_{\mathrm{el}}^{(1)}$ and angular width $\Delta\theta \propto (k\ell)^{-1}$ [18]. In the regime $k\ell \gg 1$, this so-called CBS cone arises from the interference between amplitudes associated with reversed scattering paths $C_n \equiv (\mathbf{r}_1 \to \cdots \to \mathbf{r}_n)$ and $\widetilde{C_n} \equiv (\mathbf{r}_n \to \cdots \to \mathbf{r}_1)$. Of course single scattering paths where $n=1$ do not participate to this two-wave interference (since they are exactly identical to their reversed counterparts) and must be excluded from $C_{\mathrm{el}}^{(1)}$. Thereby, we obtain the interference (or "crossed") contribution as

$$C_{\mathrm{el}}^{(1)} = \sum_{n=2}^{\infty} \frac{\mathcal{N}^n}{4\pi k^2 \Sigma} \int_V d\mathbf{r}_1 \cdots d\mathbf{r}_n \mathcal{A}(C_n) \mathcal{A}^*(\widetilde{C_n}). \quad (15)$$

Thus, the bistatic coefficient in the backscattering direction reads $\gamma_{\mathrm{el}}^{(1)} = L_{\mathrm{el}}^{(1)} + C_{\mathrm{el}}^{(1)}$. From Eq. (8), we verify that the reciprocity symmetry $\mathcal{A}(C_n)=\mathcal{A}(\widetilde{C_n})$ is satisfied for scatterers without any internal ground-state degeneracies. This allows us to rewrite Eq. (15) as

$$C_{\mathrm{el}}^{(1)} = \int \frac{d\mathbf{r}}{\Sigma \ell} [I_\omega(\mathbf{r}) - e^{-z/\ell}] e^{-z/\ell} = L_{\mathrm{el}}^{(1)} - S_{\mathrm{el}}^{(1)} \quad (16)$$

where $S_{\mathrm{el}}^{(1)}$ is the single-scattering contribution. Hence, the linear CBS enhancement factor, defined as

$$\eta^{(1)} = 1 + C_{\mathrm{el}}^{(1)}/L_{\mathrm{el}}^{(1)} = 2 - S_{\mathrm{el}}^{(1)}/L_{\mathrm{el}}^{(1)}, \quad (17)$$

is always smaller than 2. It equals 2 if single scattering can be filtered out (see Sec. III C).

B. Scalar nonlinear regime

At higher incident intensities, the successive photon scattering events become correlated. Indeed, absorption of one single photon brings the atom into its excited state where it rests for a quite long time Γ^{-1} without being able to scatter other incident photons. This means that saturation of the optical atomic transition sets in, inducing nonlinear effects and inelastic scattering. In a perturbative expansion of the photodetection signal in powers of the incident intensity, the leading nonlinear term arises from scattering of *two* photons. In order to generalize the above linear treatment to the two-photon case, we first need to recall some relevant facts about scattering of two photons by a single atom [32].

1. One-atom two-photon inelastic spectrum

The two-photon scattering matrix S contains an elastic and an inelastic part. The elastic part corresponds to two single photons scattered independently from each other, whereas the inelastic part describes a "true" two-photon scattering process, where the photons become correlated and exchange energy with each other. To obtain the intensity of the photodetection signal, the electric field operator E (evaluated at the position of the detector) is applied on the final two-photon state $|f\rangle = S|i\rangle$, with $|i\rangle$ the initial state. Since E annihilates one photon, this yields a single-photon state $|\psi\rangle = E|f\rangle$, which describes the final state of the undetected photon. Like the scattering matrix S, it consists of an elastic and an inelastic component:

$$|\psi\rangle = |\psi_{\mathrm{el}}\rangle + |\psi_{\mathrm{in}}\rangle. \quad (18)$$

The inelastic part $|\psi_{\mathrm{in}}\rangle$ is a spherical wave emitted by the atom, whereas the elastic part $|\psi_{\mathrm{el}}\rangle$ is a superposition of scattered and unscattered light, thereby taking into account forward scattering of the undetected photon. (Forward scattering of the detected photon does not need to be taken into account, since the detector is placed in the backscattering direction.) Finally, the norm $I=\langle\psi|\psi\rangle$ of $|\psi\rangle$ defines the intensity of the photodetection signal. According to Eq. (18), I is the sum of the following three terms:

$$I_{\mathrm{el}}^{(1)} = \langle\psi_{\mathrm{el}}|\psi_{\mathrm{el}}\rangle, \quad (19)$$

$$I_{\mathrm{el}}^{(2)} = 2\,\mathrm{Re}\{\langle\psi_{\mathrm{el}}|\psi_{\mathrm{in}}\rangle\}, \quad (20)$$

$$I_{\mathrm{in}}^{(2)} = \langle\psi_{\mathrm{in}}|\psi_{\mathrm{in}}\rangle. \quad (21)$$

So far, everything is valid for any two-photon scattering process with an elastic and an inelastic component. In the specific case of a single atom, the following result is obtained:

$$I_{\mathrm{el}}^{(1)} = \frac{\sigma}{4\pi R^2} I_0, \quad (22)$$

$$I_{\mathrm{el}}^{(2)} = -2 I_{\mathrm{el}}^{(1)} s, \quad (23)$$

$$I_{\mathrm{in}}^{(2)} = I_{\mathrm{el}}^{(1)} s, \quad (24)$$

with the incident intensity I_0, and the saturation parameter s defined by [38]

$$s = \frac{s_0}{1 + (2\delta/\Gamma)^2}, \quad s_0 = \frac{I_0}{I_s}, \quad I_s = \epsilon_0 c \left(\frac{\hbar\Gamma}{2d}\right)^2 \tag{25}$$

where d is the atomic dipole strength and I_s the saturation intensity of the atomic transition.

The first term, Eqs. (19) and (22), which arises from two photons scattered independently from each other, reproduces the linear single-photon cross section $4\pi\sigma = |S_\omega|^2$ [see Eq. (1)]. The following two terms correspond to nonlinear elastic and inelastic scattering, respectively. For the case of a single atom, the perturbative two-photon treatment is valid for $s \ll 1$, i.e., if the nonlinear terms are small compared to the linear one.

The frequency spectrum of the elastically scattered light is simply $F_{\mathrm{el}}(\omega') = (I_{\mathrm{el}}^{(1)} + I_{\mathrm{el}}^{(2)})\delta(\omega' - \omega)$ whereas the frequency spectrum of the inelastically scattered light is $F_{\mathrm{in}}(\omega') = I_{\mathrm{in}}^{(2)} P(\omega')$. The continuous spectrum $P(\omega')$ is normalized to unity according to $\int d\omega' P(\omega') = 1$. It is obtained as follows [32]:

$$P(\omega') = \frac{\Gamma}{4\pi} \left| \frac{1}{\delta' + i\Gamma/2} + \frac{1}{2\delta - \delta' + i\Gamma/2} \right|^2, \tag{26}$$

where $\delta' = \omega' - \omega_{\mathrm{at}}$ denotes the final detuning. This inelastic spectrum consists of two peaks with width Γ, one located at the atomic resonance ($\omega' = \omega_{\mathrm{at}}$), and the other one twice as far detuned as the incident laser ($\omega' = \omega_{\mathrm{at}} + 2\delta$). For $\delta < \Gamma/2$, the two peaks merge to a single one centered at $\omega' = \omega$. Please note that, by going beyond the two-photon scattering approximation, one would then get *three* peaks as predicted by the nonperturbative calculation of the inelastic spectrum, also known as the Mollow triplet [38].

2. Nonlinear scattering in a dilute medium of atoms

Now, we generalize the above single-atom treatment to a multiple-scattering process in a dilute medium of atoms. First, we note that the above perturbative treatment—in particular Eqs. (19)–(21)—remains valid for any form of the scattering sample, let it be a single atom, two atoms, or arbitrarily many of them. An important difference from the single-atom case, however, is that the total weight of nonlinear processes may be drastically enhanced if the sample has a large optical thickness $b = L/\ell$, where L is the typical medium size. This implies that the condition $s \ll 1$ is not sufficient to guarantee the validity of the perturbative approach. Instead, as we will argue in Sec. IV, the perturbative condition reads $sb^2 \ll 1$.

A typical two-photon scattering path is sketched in Fig. 2. Here, the incoming photons propagate at first independently from each other to position $\mathbf{r}$ inside the disordered atomic medium, where they undergo a nonlinear scattering event. One of the two outgoing photons then propagates back to the detector. The possibility that the two photons meet again at another atom can be neglected in the case of a dilute medium, similar to recurrent scattering in the linear case [37]. We can hence restrict our analysis to processes like the one shown in Fig. 2, with arbitrary numbers of linear scattering events before and after the nonlinear one. Thus one of the two incoming photons undergoes $n \geqslant 0$ elastic scattering events (labeled by $\mathbf{u}_i$), while the other undergoes $m \geqslant 0$ elastic scattering events (labeled by $\mathbf{v}_j$), before merging at $\mathbf{r}$ where they undergo the inelastic scattering event. One of the outgoing inelastic photons reaches back the detector after having undergone $l \geqslant 0$ elastic scattering events (labeled by positions $\mathbf{w}_k$). For the other undetected inelastic photon, we may assume, without any loss of generality, that it does not interact anymore with the atomic medium. This interaction would anyway be described by a unitary operator (as a consequence of energy conservation), which does not change the norm of the state $|\psi\rangle$ of the undetected photon defining the detection signal.

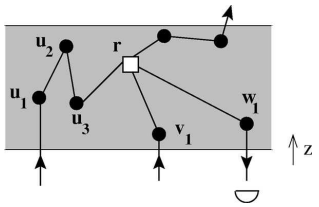

FIG. 2. In the perturbative approach, we assume a single nonlinear two-photon scattering event (□), but arbitrarily many linear scattering events (●). One of the two photons is finally annihilated by the detector, thereby defining the photodetection signal, whereas the other one is scattered into an arbitrary direction.

In general, the state of the inelastic undetected photon corresponding to a scattering path C defined by the position $\mathbf{r}$ of the two-photon scattering event and by the collection of positions of all one-photon scattering events $C \equiv \{\mathbf{u}, \mathbf{v}, \mathbf{r}, \mathbf{w}\}$ is given as follows:

$$\begin{aligned} |\psi_{\mathrm{in}}(C)\rangle = {} & e^{ikn_\omega(z_{u_1} + z_{v_1})} \prod_{i=1}^{n} S_\omega G_\omega(\mathbf{u}_i, \mathbf{u}_{i+1}) \prod_{j=1}^{m} S_\omega G_\omega(\mathbf{v}_j, \mathbf{v}_{j+1}) \\ & \times \int d\omega' \Pi_{\omega'} |\psi_{\mathrm{in}}\rangle \prod_{k=1}^{l} S_{\omega'} G_{\omega'}(\mathbf{w}_k, \mathbf{w}_{k+1}) \\ & \times e^{ikn_{\omega'} z_{w_1}} \begin{cases} 1, & n = m = 0, \\ 2, & n > 0 \text{ or } m > 0, \end{cases} \end{aligned} \tag{27}$$

with $\mathbf{u}_{n+1} = \mathbf{v}_{m+1} = \mathbf{w}_{l+1} = \mathbf{r}$, $\Pi_{\omega'}$ the projector on photon states at frequency ω', and $|\psi_{\mathrm{in}}\rangle$ the inelastic final state of the one-atom case, Eq. (18). Since the inelastic two-photon scattering event takes place at position $\mathbf{r}$, this state describes an outgoing spherical wave emitted at $\mathbf{r}$. Furthermore, note that if the two incoming photons do not both originate from the incident mode, i.e., if $n > 0$ or $m > 0$, a factor 2 arises due to the fact that the incoming photons can be distributed in two different ways among the paths $\{u\}$ and $\{v\}$.

The elastic component $|\psi_{\mathrm{el}}(C)\rangle$ is obtained in a similar way. However, as in the single-atom case, we must take into account forward scattering of the undetected photon, at the position $\mathbf{r}$ of the nonlinear event. This is done by considering the superposition of two diagrams where the undetected photon is scattered or not scattered at $\mathbf{r}$ [see Figs. 3(a) and 3(b)]. Since this approach exactly parallels the one known from the single-atom case [32], it is unnecessary to present the com-

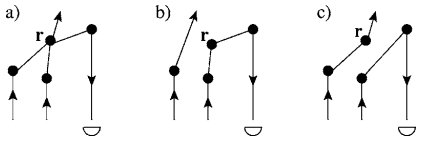

FIG. 3. The elastic component $|\psi(\mathbf{r},\{\mathbf{u},\mathbf{v},\mathbf{w}\})_{\mathrm{el}}\rangle$ of the undetected photon state arises from a superposition of the following three processes: (a) both photons elastically scattered at $\mathbf{r}$, (b) only the detected photon scattered at $\mathbf{r}$, and (c) only the undetected photon scattered at $\mathbf{r}$. The last two diagrams are necessary to take into account the nonlinear average propagation of the undetected (b) or detected (c) photon.

plete calculation of the elastic component in detail—all relevant ingredients to perform the generalization to the multiatom case will be contained in the calculation of the inelastic component. In contrast to the single-atom case, however, the elastic component will enter in the calculation of the nonlinear average propagation, i.e., the nonlinear modification of the refractive index (Kerr effect), and will be discussed later. At first, we concentrate on the processes of nonlinear scattering, i.e., processes changing the direction of propagation of the detected photon.

As for the linear case, we still assume the same dilute medium approximations to hold for the "ladder" and "crossed" contributions. Thus, in order to calculate the average photodetection signal, we just keep scattering diagrams obtained by reversing the path of the detected photon. Furthermore, we also neglect interference between diagrams where the nonlinear scattering event occurs at different atoms. This is justified in the dilute case since the overlap between two spherical waves emitted at $\mathbf{r}$ and $\mathbf{r}'$ vanishes if $k|\mathbf{r}-\mathbf{r}'| \gg 1$.

3. Nonlinear ladder contribution

To obtain the inelastic component of the average backscattering signal, we first get the total final state of the undetected photon by summing Eq. (27) over all possible different scattering paths C. Then we insert this result into Eq. (21) and we finally average over the random positions of the scatterers. As argued above, only identical or reversed scattering paths are retained in the average, giving rise to the background (ladder) and interference (crossed) components. Thus, the inelastic background component reads as follows:

$$L_{\mathrm{in}}^{(2)} = \int_V d\mathbf{r} \sum_{(n,m,l)=0}^{\infty} \frac{\mathcal{N}^{n+m+l+1}}{4\pi k^2 \Sigma} \int_V \prod_{i=1}^{n} d\mathbf{u}_i \prod_{j=1}^{m} d\mathbf{v}_j \prod_{k=1}^{l} d\mathbf{w}_k \times \langle \psi_{\mathrm{in}}(C) | \psi_{\mathrm{in}}(C) \rangle \times \begin{cases} 1 & \text{if } n=m=0, \\ 1/2 & \text{otherwise.} \end{cases} \quad (28)$$

Note that some care must be taken not to sum twice over the same scattering path. In particular, any exchange of the two incoming parts $\{u\}$ and $\{v\}$ leaves the total scattering path unchanged since the two incoming photons are identical. For this reason, a factor $1/2$ must be inserted at the end of Eq. (28). Again, as in Eq. (27), the case $n=m=0$ is exceptional, since then there is no elastic scattering event before the nonlinear one: the two incident photons remain in the same mode.

If we insert now Eq. (27) into Eq. (28), we simply obtain the inelastic nonlinear ladder contribution as

$$L_{\mathrm{in}}^{(2)} = s \int \frac{d\mathbf{r}}{\Sigma \ell} [2I_\omega^2(\mathbf{r}) - e^{-2z/\ell}] \int d\omega' P(\omega') I_{\omega'}(\mathbf{r}), \quad (29)$$

with $I_\omega(\mathbf{r})$ the linear average intensity [see Eq. (14)]. In order to interpret this result, we first note that the inelastic intensity radiated by the atom at position $\mathbf{r}$ is proportional to the mean *squared* intensity at $\mathbf{r}$. An alternative, physically transparent derivation of the latter can be performed as follows. We write the local field amplitude $\mathcal{A}=\exp(-z/2\ell)+\mathcal{A}_D$ as a sum of coherent and diffuse light amplitudes. The latter term exhibits Gaussian speckle statistics [39], i.e., $\langle \mathrm{Re}\mathcal{A}_D\rangle = \langle \mathrm{Im}\,\mathcal{A}_D\rangle = 0$, $2\langle(\mathrm{Re}\mathcal{A}_D)^2\rangle = 2\langle(\mathrm{Im}\,\mathcal{A}_D)^2\rangle = \langle|\,\mathcal{A}_D|^2\rangle$, and $\langle|\mathcal{A}_D|^4\rangle = 2\langle|\mathcal{A}_D|^2\rangle^2$. Thereby, we obtain for the mean squared intensity

$$\langle|\mathcal{A}|^4\rangle = e^{-2z/\ell} + \langle|\mathcal{A}_D|^4\rangle + 4e^{-z/\ell}\langle|\mathcal{A}_D|^2\rangle \quad (30)$$

$$= 2\langle|\mathcal{A}|^2\rangle^2 - e^{-2z/\ell}. \quad (31)$$

Inserting the average intensity $I_\omega = \langle|\mathcal{A}|^2\rangle$, we immediately recognize the first integrand in Eq. (29). Then the atom emits a photon with frequency distribution $P(\omega')$. Finally, due to time-reversal symmetry, the propagation of this photon from $\mathbf{r}$ to the detector is described by the same function $I_{\omega'}(\mathbf{r})$ which represents propagation of incoming photons to $\mathbf{r}$.

Concerning the elastic component, the diagrammatic calculation via Eq. (20) [see also Figs. 3(a)–3(c)] shows that the above argument can be repeated in the same way—except for the fact that the detected photon does not change its frequency. Furthermore, a factor -2 is taken over from the single-atom expression [cf. Eqs. (23) and (24)]. Thereby, we obtain

$$L_{\mathrm{el}}^{(2,\mathrm{scatt})} = -2s \int \frac{d\mathbf{r}}{\Sigma \ell} [2I_\omega^2(\mathbf{r}) - e^{-2z/\ell}] I_\omega(\mathbf{r}). \quad (32)$$

The index "scatt" reminds us that we have treated only nonlinear scattering so far. Below (Sec. III B 5), we will add nonlinear average propagation, which contributes to the elastic nonlinear component, too.

4. Nonlinear crossed contribution

It remains to calculate the crossed contribution, i.e., interference between reversed paths. In contrast to the linear case, where there are always two interfering amplitudes (apart from single scattering), the nonlinear case admits more possibilities to reverse the path of the detected photon. This is due to the photon exchange symmetry at the nonlinear scattering event, which does not allow us to distinguish which one of the two incoming photons finally corresponds to the detected or undetected one. As evident from Fig. 4(c), each multiple-scattering path where both incoming photons, or one incoming and the outgoing detected photon, exhibit at least one linear scattering event besides the nonlinear one has *two* different reversed counterparts, leading in total to *three* interfering amplitudes.

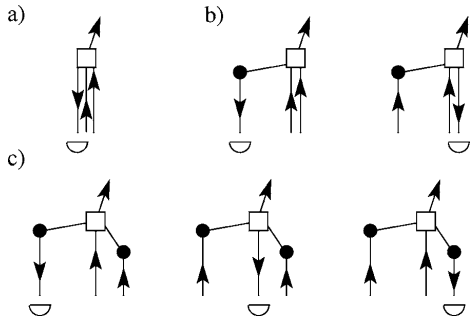

FIG. 4. In the presence of nonlinear scattering (□), there may be either (b) two, or (c) three interfering amplitudes contributing to enhanced backscattering, apart from single scattering (a), which only contributes to the background. In general, the case (c), which corresponds to maximum enhancement factor 3, is realized if either both incoming photons or one incoming and the outgoing detected photon exhibit at least one linear scattering event (●) besides the nonlinear one.

If we look at the scattering process shown in Fig. 2, the two reversed counterparts are obtained by exchanging the outgoing detected photon $\{w\}$ with either one of the incoming photons $\{u\}$ or $\{v\}$. Since both cases are identical in the ensemble average, we may restrict ourselves to one of them, let us say $\{v\}$. We thus denote by $\tilde{C}\equiv\{\mathbf{u},\mathbf{w},\mathbf{r},\mathbf{v}\}$ the reverse path corresponding to $C\equiv\{\mathbf{u},\mathbf{v},\mathbf{r},\mathbf{w}\}$ when $\{v\}$ and $\{w\}$ are exchanged. In total, we obtain for the inelastic interference component

$$C_{\mathrm{in}}^{(2)}=\int_V d\mathbf{r}\sum_{(n,m,l)=0}^{\infty}\frac{\mathcal{N}^{n+m+l+1}}{4\pi k^2\Sigma}\times\int_V\prod_{i=1}^{n}d\mathbf{u}_i\prod_{j=1}^{m}d\mathbf{v}_j\prod_{k=1}^{l}d\mathbf{w}_k\langle\psi_{\mathrm{in}}(C)|\psi_{\mathrm{in}}(\tilde{C})\rangle\times\begin{cases}0 & \text{if } m=l=0,\\ 1 & \text{otherwise.}\end{cases}\tag{33}$$

Here, the case $m=l=0$ identifies processes where the two reversed paths C and $\tilde{C}$ are indistinguishable. Setting their contribution equal to zero accounts in particular for the single-scattering case depicted in Fig. 4(a), i.e., $n=m=l=0$, which does not contribute to the interference cone. The case Fig. 4(b) remains with *two* contributions ($n=m=0$, $l>0$, and $n=l=0$, $m>0$, respectively) in Eq. (33), corresponding to the fact that two amplitudes interfere. Finally, the case (c) of three interfering amplitudes is reflected in Eq. (33) by the absence of the exchange factor $1/2$, as compared to the background Eq. (28). Thereby, the interference contribution can, in principle, become up to twice larger than the background.

If we insert the state of the undetected photon, Eq. (27), into Eq. (33), we encounter the following expression:

$$g_{\omega,\omega'}(\mathbf{r})=e^{ik(n_\omega-n_{\omega'}^{*})z}+\sum_{n=1}^{\infty}\mathcal{N}^n\int_V d\mathbf{r}_1\cdots d\mathbf{r}_n\times e^{ik(n_\omega-n_{\omega'}^{*})z_1}\prod_{i=1}^{n}S_\omega G_\omega(\mathbf{r}_i,\mathbf{r}_{i+1})S_{\omega'}^{*}G_{\omega'}^{*}(\mathbf{r}_i,\mathbf{r}_{i+1}),\tag{34}$$

which generalizes the local intensity Eq. (13) to the case where two different frequencies occur in the interfering paths. Numerically, it can be obtained as the iterative solution of

$$g_{\omega,\omega'}(\mathbf{r})=e^{ik(n_\omega-n_{\omega'}^{*})z}+\mathcal{N}S_\omega S_{\omega'}^{*}\times\int_V d\mathbf{r}'G_\omega(\mathbf{r},\mathbf{r}')G_{\omega'}^{*}(\mathbf{r},\mathbf{r}')g_{\omega,\omega'}(\mathbf{r}').\tag{35}$$

This function describes the ensemble-averaged product of two probability amplitudes, one representing an incoming photon with frequency ω propagating to position $\mathbf{r}$, and the other one the complex conjugate of a photon with frequency ω' propagating from $\mathbf{r}$ to the detector. If $\omega\neq\omega'$, then these amplitudes display a nonvanishing phase difference due both to scattering and to average propagation in the medium. This leads on average to a decoherence mechanism and consequently to a loss of interference contrast. Indeed, both the complex scattering amplitude Eq. (1) and the refractive index Eq. (5) depend on frequency. In contrast, the phase difference due to free propagation (i.e., in the vacuum) can be neglected if $\Gamma\ell\ll c$, which is satisfied for typical experimental parameters [40,41]. In the case $\omega=\omega'$ of identical frequencies, $g_{\omega,\omega}(\mathbf{r})=I_\omega(\mathbf{r})$ reduces to the average intensity [see Eq. (14)].

In terms of the iterative solution of Eq. (34), the inelastic interference term Eq. (33) is rewritten as follows:

$$C_{\mathrm{in}}^{(2)}=4s\int d\omega' P(\omega')\int_V\frac{d\mathbf{r}}{\Sigma\ell}\{I_\omega(\mathbf{r})|g_{\omega,\omega'}(\mathbf{r})|^2-e^{-z/\ell}\,\mathrm{Re}[e^{i(n_\omega-n_{\omega'}^{*})kz}g_{\omega,\omega'}^{*}(\mathbf{r})]-[I_\omega(\mathbf{r})-e^{-z/\ell}]e^{-z/\ell-z/\ell'}\},\tag{36}$$

with ℓ' the linear mean free path at frequency ω'. In the elastic case, where $\omega'=\omega$, dephasing between reversed scattering paths does not occur, and the expression (36) simplifies to:

$$C_{\mathrm{el}}^{(2,\mathrm{scatt})}=-8s\int_V\frac{d\mathbf{r}}{\Sigma\ell}(I_\omega(\mathbf{r})^3-2I_\omega(\mathbf{r})e^{-2z/\ell}+e^{-3z/\ell}).\tag{37}$$

Since, in the elastic case, there is no loss of coherence due to change of frequency, the elastic interference component, Eq. (37), is completely determined by the relative weights of the one-, two-, and three-amplitude cases exemplified in Fig. 4. This can be checked by rewriting the background and interference components, Eqs. (32) and (37), in terms of diffuse

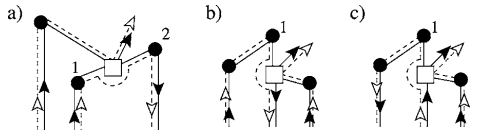

FIG. 5. Diagrammatic description of nonlinear propagation. A two-photon process (solid lines) interferes with two independent single photons (dashed lines). Only one of the latter (the undetected photon) is scattered at □, thereby modifying the propagation of the detected photon (a) between two scattering events at positions 1 and 2, (b) on the way to the detector after the last scattering event at position 1, or (c) in the coherent mode before the first scattering event at position 1.

and coherent light, respectively, i.e., by writing $I=I_D+\exp(-z/\ell)$. One obtains

$$L_{\mathrm{el}}^{(2,\mathrm{scatt})} \propto \langle e^{-3z/\ell} + 5I_D e^{-2z/\ell} + 6I_D^2 e^{-z/\ell} + 2I_D^3 \rangle,$$
$$C_{\mathrm{el}}^{(2,\mathrm{scatt})} \propto \langle \underbrace{\quad}_{(a)} \underbrace{4I_D e^{-2z/\ell}}_{(b)} + \underbrace{12I_D^2 e^{-z/\ell} + 4I_D^3}_{(c)} \rangle, \quad (38)$$

where the angular brackets denote the integral over the volume V of the medium, and (a), (b), (c) correspond to the three cases shown in Fig. 4, identified by different powers of diffuse or coherent light. As expected, the three-amplitude case (c) implies an interference term twice as large as the background. In the two-amplitude case (b), a small complication arises, since one of the two interfering amplitudes is twice as large as the other one (i.e., the one where both incoming photons originate from the coherent mode); cf. the discussion after Eq. (27). In this case, the interference contribution $2\times1+1\times2=4$ is smaller than the background $2\times2+1\times1=5$. Finally, as it should be, the single-scattering term (a) is absent in the interference term $C_{\mathrm{el}}^{(2,\mathrm{scatt})}$.

5. Nonlinear average propagation

So far, we have only considered processes of nonlinear scattering where the direction of propagation of the detected photon is changed. It remains to take into account nonlinear average propagation. This is described by those processes where, in one of the two interfering amplitudes, the detected photon is not scattered at the position $\mathbf{r}$ of the nonlinear event [44]. The corresponding diagrams are depicted in Fig. 5, where the two interfering amplitudes are represented by the solid and dashed lines, respectively. Here, the solid lines correspond to an inelastic two-photon scattering process (like the one shown in Fig. 2), whereas the dashed lines represent an elastic process, where the two photons are independent from each other [see Fig. 3(c)]. Hence, their interference contributes to the nonlinear *elastic* component of the photodetection signal [cf. Eq. (20)].

The three diagrams shown in Fig. 5 differ only by the fact that the nonlinear propagation event takes place either between two scattering events at positions 1 and 2 (a), on the way to the detector, i.e., after the last scattering event at position 1 (b), or in the coherent mode, i.e., before the first scattering event at position 1 (c). First, let us examine the case (a). We imagine that each of the three dots ● may represent an arbitrary number of scattering events. [Only note that the number of events corresponding to the dots and 1 and 2 must be larger than zero—otherwise, the diagram Fig. 5(a) would be identical to Fig. 5(b) or 5(c).] According to the theory of linear radiative transfer outlined in Sec. III A, the ladder diagrams corresponding to the two incoming photons arriving at 1 (position $\mathbf{r}_1$) and at the nonlinear event □ (position $\mathbf{r}_3$) yield the linear local intensities $I_\omega(\mathbf{r}_1)$ and $I_\omega(\mathbf{r}_3)$, respectively. Likewise (due to reciprocity symmetry), the propagation of the outgoing detected photon from 2 (position $\mathbf{r}_2$) to the detector—with arbitrary number of scattering events in between—is given by $I_\omega(\mathbf{r}_2)$. Hence, the only ingredient that we have to calculate is the nonlinear propagation between 1 and 2. Note that, when taking the average over the position $\mathbf{r}_3$ of the nonlinear event, non-negligible contributions arise only if $\mathbf{r}_3$ is situated on the straight line between $\mathbf{r}_1$ and $\mathbf{r}_2$, since this is the only way to satisfy a stationary-phase (or phase-matching) condition. Thereby, the "pump intensity" entering in the nonlinear propagation is given by the average value of the local intensity on this line, which we denote by $\langle I_\omega \rangle_{\mathbf{r}_1\to\mathbf{r}_2}$. We do not want to present the complete calculation here (this requires us to calculate at first the case of a single atom, which can be done with the techniques described in [32]), but just give the final result:

$$|G_\omega^{(\mathrm{nl,a})}(\mathbf{r}_1,\mathbf{r}_2)|^2 = |G_\omega(\mathbf{r}_1,\mathbf{r}_2)|^2 \frac{2sr_{12}}{\ell} \langle I_\omega \rangle_{\mathbf{r}_1\to\mathbf{r}_2}. \quad (39)$$

From this, we deduce the following value for the nonlinear mean free path:

$$\frac{1}{\ell^{(\mathrm{nl})}(\mathbf{r})} = \frac{1}{\ell}[1 - 2sI_\omega(\mathbf{r})], \quad (40)$$

which is consistent with Eq. (39), if we expand the resulting propagator (where the mean free path appears in the exponent) up to first order in s. The same result is also obtained in the case of diagram Fig. 5(b), i.e., for the propagation after the last scattering event. Hence, the corresponding propagator (first order in s) reads

$$|G_\omega^{(\mathrm{nl,b})}(\mathbf{r}_1)|^2 = e^{-z_1/\ell} \frac{2sz_1}{\ell} \langle I_\omega \rangle_{\mathbf{r}_1\to\mathbf{r}_0}, \quad (41)$$

where $\mathbf{r}_0=\mathbf{r}_1-z_1\mathbf{e}_z$, with $\mathbf{e}_z$ the unit vector pointing in the direction of the incident laser, denotes the point where the photon leaves the medium. In the case (c), a small complication arises since the photons arriving at the nonlinear event □ may originate both from the coherent mode, which reduces the two-photon scattering amplitude by a factor 1/2 [cf. the discussion after Eq. (27)]. Hence, the nonlinear mean free path for photons from the coherent mode reads

$$\frac{1}{\ell_c^{(\mathrm{nl})}(\mathbf{r})} = \frac{1}{\ell}[1 - 2sI_\omega(\mathbf{r}) + se^{-z/\ell}], \quad (42)$$

with the corresponding propagator

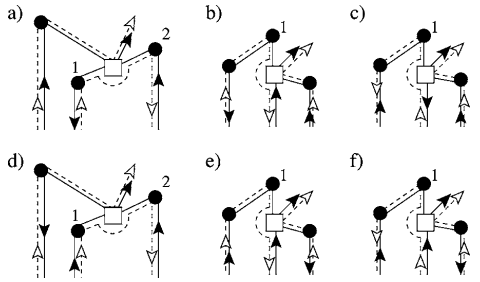

FIG. 6. Interference contributions from nonlinear propagation. The diagrams (a)–(f) are obtained from the ladder diagrams (see Fig. 5) by reversing the paths of the respective photons. Just as in the case of nonlinear scattering, there are twice as many diagrams contributing to the interference cone as to the background.

$$|G_\omega^{(\mathrm{nl,c})}(\mathbf{r}_1)|^2 = e^{-z_1/\ell}\frac{sz_1}{\ell}\langle 2I_\omega(\mathbf{r}) - e^{-z/\ell}\rangle_{\mathbf{r}_0\to\mathbf{r}_1}. \tag{43}$$

The difference between the mean free paths, Eqs. (40) and (42), can also be understood as a consequence of the different properties of intensity fluctuations for diffuse and coherent light [see Eq. (30)], which determine the nonlinear atomic response.

In total, we obtain for the background component

$$L_{\mathrm{el}}^{(2,\mathrm{prop})} = \frac{\mathcal{N}}{\Sigma\ell}\int_V d\mathbf{r}_1 d\mathbf{r}_2 I_\omega(\mathbf{r}_1) I_\omega(\mathbf{r}_2)|S_\omega G_\omega^{(\mathrm{nl,a})}(\mathbf{r}_1,\mathbf{r}_2)|^2 + \int_V \frac{d\mathbf{r}_1}{\Sigma\ell} I_\omega(\mathbf{r}_1)[|G_\omega^{(\mathrm{nl,b})}(\mathbf{r}_1)|^2 + |G_\omega^{(\mathrm{nl,c})}(\mathbf{r}_1)|^2]. \tag{44}$$

In the case of a slab of length L, Eq. (44) can be simplified to

$$L_{\mathrm{el}}^{(2,\mathrm{prop})} = s\int_0^L \frac{dz}{\ell} I_\omega(z)[2I_\omega(z)^2 - 2I_\omega^2(L) + e^{-2z/\ell} - e^{-z/\ell}]. \tag{45}$$

Concerning the interference component, we find the same phenomenon which we have already observed in the case of nonlinear scattering: if we exchange outgoing and incoming propagators, we find twice as many crossed as ladder diagrams (see Fig. 6). In particular, the diagrams (d), (e), (f), which could be seen as a modification of the linear refractive index by the local crossed intensity—thus affecting the (ladder) average propagation—are not considered in previously published papers, concerning either classical linear scatterers in a nonlinear medium [20,21] or nonlinear scatterers in the vacuum [31,42]. Even if, at first sight, these diagrams look unusual, our numerical calculations (see Sec. III D) suggest that they play an important role, at least in our situation where nonlinear scattering and nonlinear propagation originate from the same microscopic process.

Due to the reciprocity symmetry (remember that nonlinear propagation contributes to the elastic component, i.e., no decoherence due to change of frequency), each of the diagrams in Fig. 6 gives the same contribution as the corresponding ladder diagram in Fig. 5. Hence, to first approximation, the interference contribution from nonlinear propagation equals twice the background Eq. (44). Some care must be taken, however, if photons arriving at (or departing from) the nonlinear event (or position 1) originate from the coherent mode. In such cases, it may happen that some of the diagrams depicted in Figs. 5 and 6 coincide, and we should not count them twice. [This is analogous to the distinction between the cases (a), (b), (c) in Fig. 4, or to the suppression of single scattering in the linear case.]

Taking this into account [for details, we refer to the discussion after Eq. (A8) in the Appendix], we find

$$C_{\mathrm{el}}^{(2,\mathrm{prop})} = 2L_{\mathrm{el}}^{(2,\mathrm{prop})} - 3\int_V \frac{d\mathbf{r}_1}{\Sigma\ell}[e^{-z_1/\ell}|G_\omega^{(\mathrm{nl,c})}(\mathbf{r}_1)|^2 + I(\mathbf{r}_1)e^{-z_1/\ell}s(1-e^{-z_1/\ell})]. \tag{46}$$

In the case of a slab, we obtain

$$C_{\mathrm{el}}^{(2,\mathrm{prop})} = 2L_{\mathrm{el}}^{(2,\mathrm{prop})} - 3s\int_0^L \frac{dz}{\ell} I(z)(e^{-z/\ell} - e^{-2b}) + s\left(\frac{1}{2} - \frac{3}{2}e^{-2b} + e^{-3b}\right), \tag{47}$$

where $b = L/\ell$ denotes the (linear) optical thickness of the slab.

Thereby, we have completed the perturbative calculation of the backscattering signal for the scalar case. The total signal is obtained as the sum of the various components discussed above:

$$L = L_{\mathrm{el}}^{(1)} + L_{\mathrm{el}}^{(2,\mathrm{scatt})} + L_{\mathrm{el}}^{(2,\mathrm{prop})} + L_{\mathrm{in}}^{(2)}, \tag{48}$$

$$C = C_{\mathrm{el}}^{(1)} + C_{\mathrm{el}}^{(2,\mathrm{scatt})} + C_{\mathrm{el}}^{(2,\mathrm{prop})} + C_{\mathrm{in}}^{(2)}. \tag{49}$$

Before we present the numerical results in Sec. IV, we will generalize the above results to the vectorial case. This is important since polarization does not only lead to slight modifications for low scattering orders, as in the linear case. Apart from that, we will see that it also induces decoherence between reversed paths, thereby reducing the nonlinear interference components.

C. Incorporation of polarization: Vectorial case

First, including the polarization modifies the scalar expressions Eqs. (1) and (6) for the linear mean free path and the atom-photon scattering amplitude by a factor 2/3:

$$\hat{\ell} = \left(1 + \frac{4\delta^2}{\Gamma^2}\right)\frac{k^2}{6\pi\mathcal{N}}, \tag{50}$$

$$\tilde{S}_\omega = \frac{-6\pi i}{k(1 - 2i\delta/\Gamma)}. \tag{51}$$

The Green's function Eq. (4) remains unchanged, except for the fact that the modified expression for the mean free path,

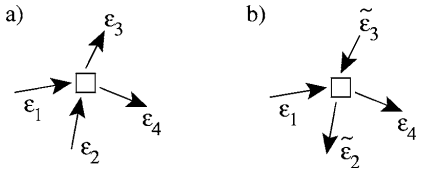

FIG. 7. Polarization vectors associated with the two-photon scattering matrix for two reversed scattering amplitudes (a) and (b). Note that the corresponding reversed scattering amplitudes Eqs. (54) and (56) are different—even in the helicity-preserving polarization channel, i.e., if $\tilde{\boldsymbol{\epsilon}}_{2,3}=\boldsymbol{\epsilon}_{2,3}^{*}$. This leads to a reduction of the CBS interference cone by a factor 3/4, on average.

Eq. (50), must be inserted in the refractive index. However, the angular anisotropic character of the atom-photon scattering is not yet contained in Eq. (51). This is treated by projection of the polarization vector as follows. If the photon, with incoming polarization $\boldsymbol{\epsilon}_1$ is scattered at $\mathbf{r}_1$, and the next scattering event takes place at $\mathbf{r}_2$, the new incoming polarization reads

$$\boldsymbol{\epsilon}_2 = \Delta_{\mathbf{r}_1,\mathbf{r}_2}\boldsymbol{\epsilon}_1, \tag{52}$$

where $\Delta_{\mathbf{r}_1,\mathbf{r}_2}$ denotes the projection onto the plane perpendicular to $\mathbf{r}_1$-$\mathbf{r}_2$. Finally, the detection signal after n scattering events is obtained as $\boldsymbol{\epsilon}_D^{*}\boldsymbol{\epsilon}_n$, with the detector polarization $\boldsymbol{\epsilon}_D$.

Thus, the linear background (ladder) contribution reads [cf. Eqs. (8) and (11)]

$$\hat{L}^{(1,\mathrm{el})} = \sum_{n=1}^{\infty} \int \frac{d\mathbf{r}_1}{A\hat{\ell}} \mathcal{N}^{n-1} \int_V d\mathbf{r}_2 \cdots d\mathbf{r}_n e^{-z_1/\hat{\ell}} \times \left(\prod_{i=1}^{n-1} |\hat{S}_\omega \hat{G}_\omega(\mathbf{r}_i,\mathbf{r}_{i+1})|^2 \right) e^{-z_n/\hat{\ell}} \times \frac{3}{2} |\boldsymbol{\epsilon}_D^{*} \Delta_{\mathbf{r}_{n-1},\mathbf{r}_n} \cdots \Delta_{\mathbf{r}_1,\mathbf{r}_2} \boldsymbol{\epsilon}_L|^2, \tag{53}$$

where $\boldsymbol{\epsilon}_L$ denotes the initial laser polarization. By choosing a given circular polarization, for example $\boldsymbol{\epsilon}_L=(1,i,0)/\sqrt{2}$, and by detecting the signal in the helicity-preserving $h\|h$ polarization channel ($\boldsymbol{\epsilon}_D=\boldsymbol{\epsilon}_L^{*}$), then the single-scattering contribution in Eq. (53) ($n=1$ term) is filtered out. We thus recover the enhancement factor 2, meaning $C_{\mathrm{el}}^{(1)}=L_{\mathrm{el}}^{(1)}$. Apart from that, however, polarization does not play a very important role: the distribution of higher scattering orders $n>1$ is only slightly modified, and the reciprocity symmetry remains valid, provided that $\boldsymbol{\epsilon}_D=\boldsymbol{\epsilon}_L^{*}$.

The situation changes in the nonlinear regime of two-photon scattering. With the initial and final polarizations $\boldsymbol{\epsilon}_{1,2}$ and $\boldsymbol{\epsilon}_{3,4}$, respectively [see Fig. 7(a)], the polarization-dependent term of the two-photon scattering matrix reads

$$S_p = \frac{1}{2}[(\boldsymbol{\epsilon}_1\boldsymbol{\epsilon}_4^{*})(\boldsymbol{\epsilon}_2\boldsymbol{\epsilon}_3^{*}) + (\boldsymbol{\epsilon}_1\boldsymbol{\epsilon}_3^{*})(\boldsymbol{\epsilon}_2\boldsymbol{\epsilon}_4^{*})]. \tag{54}$$

The prefactor 1/2 is chosen such that S_p represents correctly the polarized scattering amplitude in units of the corresponding scalar one. From Eq. (54), the photon exchange symmetry becomes evident: the outgoing photon 3, e.g., can equally well be associated with the incoming photon 1 or 2. If we trace over the undetected photon, which we may label as photon 4, for example, we obtain for the ladder component

$$\Pi^{(L)}(\boldsymbol{\epsilon}_1,\boldsymbol{\epsilon}_2;\boldsymbol{\epsilon}_3) = \sum_{\boldsymbol{\epsilon}_4} |S_p|^2 = \frac{1}{4}\{|\boldsymbol{\epsilon}_2\boldsymbol{\epsilon}_3^{*}|^2 + |\boldsymbol{\epsilon}_1\boldsymbol{\epsilon}_3^{*}|^2 + 2\,\mathrm{Re}[(\boldsymbol{\epsilon}_1\boldsymbol{\epsilon}_2^{*})(\boldsymbol{\epsilon}_2\boldsymbol{\epsilon}_3^{*})(\boldsymbol{\epsilon}_3\boldsymbol{\epsilon}_1^{*})]\}. \tag{55}$$

If we assume a random uniform distribution for the polarization vectors, we obtain $\langle\Pi^{(L)}\rangle=2/9$, which is smaller than the linear counterpart $\langle|\boldsymbol{\epsilon}_n\boldsymbol{\epsilon}_D^{*}|^2\rangle=1/3$. Hence, in the vectorial case, the relative weight of the nonlinear contribution is approximately one-third smaller than in the scalar case—at least far inside the medium, where the polarization is sufficiently randomized.

Concerning the interference (crossed) contribution, we exchange the direction of the outgoing detected photon 3 and one of the incoming photons, for example photon 2. Note that we obtain in general different polarizations $\tilde{\boldsymbol{\epsilon}}_{2,3}$ for the reversed counterparts of $\boldsymbol{\epsilon}_{2,3}$ [see Fig. 7(b)]. Indeed, the reversed photons have the same polarizations, $\tilde{\boldsymbol{\epsilon}}_{2,3}=\boldsymbol{\epsilon}_{2,3}$, only if the laser and detector polarizations are identical ($\boldsymbol{\epsilon}_D=\boldsymbol{\epsilon}_L$). Consequently, the scattering amplitude for the complex conjugate photon pair reads

$$\tilde{S}_p = \frac{1}{2}[(\boldsymbol{\epsilon}_1\boldsymbol{\epsilon}_4^{*})(\tilde{\boldsymbol{\epsilon}}_3\tilde{\boldsymbol{\epsilon}}_2^{*}) + (\boldsymbol{\epsilon}_1\tilde{\boldsymbol{\epsilon}}_2^{*})(\tilde{\boldsymbol{\epsilon}}_3\boldsymbol{\epsilon}_4^{*})]. \tag{56}$$

Note that even in the helicity-preserving polarization channel, i.e., $\tilde{\boldsymbol{\epsilon}}_{2,3}=\boldsymbol{\epsilon}_{2,3}^{*}$, the reversed scattering amplitudes Eqs. (54) and (56) are in general not equal. Only the first term, where photon 2 is associated with photon 3, remains unchanged if those two photons are reversed. As a consequence, the polarization induces a loss of coherence, i.e., a reduction of the crossed term as compared to the scalar case. The sum over the polarization of photon 4 yields

$$\Pi^{(C)}(\boldsymbol{\epsilon}_1,\boldsymbol{\epsilon}_2,\tilde{\boldsymbol{\epsilon}}_3,\boldsymbol{\epsilon}_3,\tilde{\boldsymbol{\epsilon}}_2) = \sum_{\boldsymbol{\epsilon}_4} S_p\tilde{S}_p^{*} = \frac{1}{4}[(\boldsymbol{\epsilon}_2\boldsymbol{\epsilon}_3^{*})(\tilde{\boldsymbol{\epsilon}}_2\tilde{\boldsymbol{\epsilon}}_3^{*}) + (\boldsymbol{\epsilon}_2\boldsymbol{\epsilon}_3^{*})(\boldsymbol{\epsilon}_1\tilde{\boldsymbol{\epsilon}}_3^{*})(\boldsymbol{\epsilon}_2\boldsymbol{\epsilon}_1^{*}) + (\boldsymbol{\epsilon}_1\boldsymbol{\epsilon}_3^{*})(\boldsymbol{\epsilon}_2\tilde{\boldsymbol{\epsilon}}_3^{*})(\boldsymbol{\epsilon}_2\boldsymbol{\epsilon}_1^{*}) + (\boldsymbol{\epsilon}_1\boldsymbol{\epsilon}_3^{*})(\boldsymbol{\epsilon}_2\boldsymbol{\epsilon}_1^{*}) \times (\boldsymbol{\epsilon}_2\boldsymbol{\epsilon}_3^{*})]. \tag{57}$$

If we assume $\tilde{\boldsymbol{\epsilon}}_{2,3}=\boldsymbol{\epsilon}_{2,3}^{*}$, i.e., the $h\|h$ channel, we obtain $\langle\Pi^{(C)}\rangle=3/18$ on average. Hence, in this channel, the polarization-induced loss of contrast is approximately $\langle\Pi^{(C)}\rangle/\langle\Pi^{(L)}\rangle=3/4$.

Finally, to obtain the polarization dependence of nonlinear propagation, we label the photons as shown in Fig. 8. Let us first examine the ladder term, Fig. 8(a). The solid lines are described by the two-photon amplitude Eq. (54), whereas the dashed lines give the complex conjugate of $(\boldsymbol{\epsilon}_2\boldsymbol{\epsilon}_4^{*})(\boldsymbol{\epsilon}_1\boldsymbol{\epsilon}_3^{*})$. After integration over photon 4, the result is

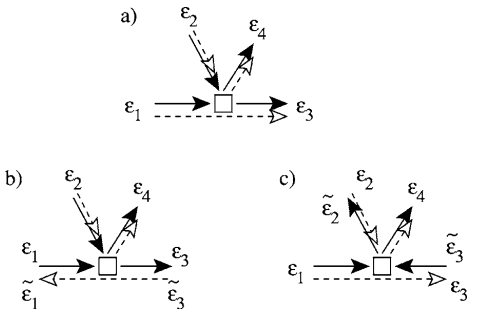

FIG. 8. Polarization dependence of nonlinear propagation for (a) ladder and (b), (c) crossed diagrams.

$$\Pi^{(L,\mathrm{prop})}(\epsilon_1,\epsilon_2,\epsilon_3)=\frac{1}{2}[(\epsilon_1\epsilon_2^*)(\epsilon_2\epsilon_3^*)(\epsilon_3\epsilon_1^*)+(\epsilon_1\epsilon_3^*)(\epsilon_2\epsilon_2^*)(\epsilon_3\epsilon_1^*)]. \quad (58)$$

Concerning the crossed diagrams, we distinguish between the two cases shown in Figs. 8(b) and 8(c). [In Fig. 6, these correspond to (a), (b), (c), on the one hand, and (d), (e), (f), on the other hand.] As for the case (b), nothing changes since the reversed photon does not participate in the nonlinear event. In case (c), we obtain

$$\Pi^{(C,\mathrm{prop})}(\epsilon_1,\epsilon_2,\epsilon_3,\tilde{\epsilon}_2,\tilde{\epsilon}_3)=\frac{1}{2}[(\epsilon_1\epsilon_2^*)(\epsilon_3\epsilon_2^*)(\epsilon_3\epsilon_1^*)+(\epsilon_1\epsilon_2^*)(\epsilon_3\epsilon_2^*)(\epsilon_3\epsilon_1^*)]. \quad (59)$$

When determining the average values of the nonlinear propagation terms, it must be taken into account that ϵ_1 and ϵ_3 are not independent from each other, since they propagate in the same (or opposite) direction. Thus, we find $\langle\Pi^{(L,\mathrm{prop})}\rangle=1/3$ and $\langle\Pi^{(C,\mathrm{prop})}\rangle=1/6$. Hence, the loss of contrast equals $1/2$ in case (c), whereas reciprocity remains conserved (i.e., no loss of contrast) in case (b). Averaging over (b) and (c), this yields the same contrast $3/4$ as for nonlinear scattering.

What remains to be done to obtain the vectorial backscattering signal is to incorporate the above expressions into the corresponding scalar equations. The resulting equations can be found in the Appendix, together with a description of the Monte Carlo method which we use for their numerical solution.

D. Classical model

We want to stress that our perturbative theory of nonlinear coherent backscattering is not only valid for an atomic medium, but can be adapted to other kinds of nonlinear scatterers. In particular, the effect of interference between three amplitudes is always present in the perturbative regime of a small $\chi^{(3)}$ nonlinearity. Specifically, we have also examined the following model: a collection of classical isotropic scatterers, situated at positions $\mathbf{r}_i$, $i=1,\ldots,N$. In analogy to the atomic model, we assume that the field scattered elastically by an individual scatterer at position $\mathbf{r}_i$ is proportional to $E_i/(1+s|E_i|^2)$, where E_i is the local field at $\mathbf{r}_i$, and s measures the strength of the nonlinearity. Writing E_i as a sum of the incident field and the field radiated by all other scatterers, we obtain the following set of nonlinear equations:

$$E_i=e^{i\mathbf{k}_L\cdot\mathbf{r}_i}+i\sum_{j\neq i}\frac{e^{ikr_{ij}}}{kr_{ij}}\frac{E_j}{1+s|E_j|^2}. \quad (60)$$

Employing diagrammatic theory similar to the one outlined above, we have checked that, in the ensemble average over the positions $\mathbf{r}_i$, this model indeed reproduces the elastic components of the backscattering signal of the atomic model. We have checked that the results obtained from direct numerical solutions of the field equations (60)—averaged over a sufficiently large sample of single realizations—agree with our theoretical predictions, in the perturbative regime of small nonlinearity s. In particular, the diagrams (d), (e), (f) of Fig. 6, describing the interference contributions from the nonlinear propagation, are essential to give the correct results. A more detailed analysis will be presented elsewhere.

Furthermore, it remains to be clarified whether the diagrams (d), (e), (f) are also relevant for the description of propagation in *homogeneous* nonlinear media, into which linear scatterers are embedded at random positions. First studies of the resulting CBS cone have been presented in [20,21], without taking into account interference between three amplitudes, however. Experimentally, this question can be resolved by measuring the value of the backscattering enhancement factor η: whereas η is basically unaffected by the nonlinearity according to [20,21] (i.e., $\eta=2$ apart from single scattering), our equations (44) and (46), with s proportional to the incoming intensity and to the $\chi^{(3)}$ coefficient of the nonlinear Kerr medium, predict a significant change of η when varying the incoming intensity.

IV. RESULTS

We return to the atomic model, concentrating on the case of a slab geometry in the following. Using the equations derived in Secs. III A–III C, we are able to calculate the backscattered intensity up to first order in the saturation parameter s. In this section, we will examine its dependence on the optical thickness b and detuning δ, for the scalar and vectorial cases. The main quantity of interest is the backscattering enhancement factor η. It is defined as the ratio between the total detection signal in the exact backscattering direction divided by the background component. If we perform an expansion up to first order in s, we obtain

$$\eta=\frac{L+C}{L}\simeq\eta^{(1)}+(\eta^{(1)}-1)(\gamma_C-\gamma_L)s. \quad (61)$$

Here, $\eta^{(1)}=1+C_{\mathrm{el}}^{(1)}/L_{\mathrm{el}}^{(1)}$ is the enhancement factor in the linear case (i.e., the limit of vanishing saturation). If single scattering is excluded (e.g., in the $h\|h$ channel), we have $\eta^{(1)}=2$. Increasing saturation changes the enhancement factor, and the present approach allows us to calculate the slope $d\eta/ds$ of this change at $s=0$. It is given by the difference

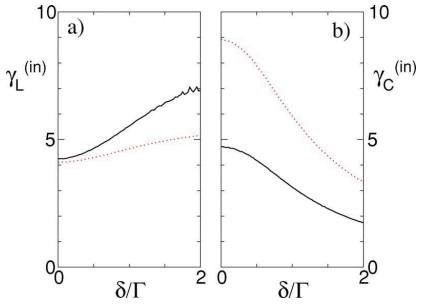

FIG. 9. (Color online) Normalized inelastic ladder and crossed contributions $\gamma_{L,C}^{(in)}$ [cf. Eqs. (62) and (63)], for optical thickness $b=0.5$, as a function of the laser detuning δ. Solid lines: polarized case ($h\|h$ channel). Dotted lines: scalar case. For comparison, the corresponding elastic contributions (independent of δ) are $\gamma_L^{(el)}=-7.04$ ($h\|h$), -6.53 (scalar), and $\gamma_C^{(el)}=-9.56$ ($h\|h$), -18.8 (scalar).

between the nonlinear crossed and ladder contribution, normalized as follows:

$$\gamma_L = \frac{L - L^{(1)}}{sL^{(1)}}, \tag{62}$$

$$\gamma_C = \frac{C - C^{(1)}}{sC^{(1)}}. \tag{63}$$

Obviously, an important question is the domain of validity of the linear expansion Eq. (61). Strictly speaking, this question can only be answered if we know higher orders of s. However, a rough quantitative estimation can be given as follows: if p_1 (p_{2+}) denotes the probability for a backscattered photon to undergo one (more than one) nonlinear scattering event, the perturbative condition reads $p_{2+} \ll p_1$. If we assume that all scattering events have the same probability (proportional to s) to be nonlinear (thereby neglecting the inhomogeneity of the local intensity), we obtain $p_1 \simeq \langle N \rangle s$ and $p_{2+} \simeq \langle N^2 \rangle s^2$, where N denotes the total number of scattering events, and $\langle \ldots \rangle$ the statistical average over all backscattering paths. Evidently, N and N^2 are expected to increase when increasing the optical thickness b. For a slab geometry, we have found numerically that $\langle N \rangle \propto b$ and $\langle N^2 \rangle \propto b^3$ (in the limit of large b), concluding that the perturbative treatment is valid if $sb^2 \ll 1$. Let us note that a similar condition also ensures the stability of speckle fluctuations in a nonlinear medium [43].

In Fig. 9, we show the inelastic ladder and crossed contributions $\gamma_L^{(in)}$ and $\gamma_C^{(in)}$ for a slab of optical thickness $b=0.5$ as a function of the detuning, $\delta=\omega-\omega_{at}$, for the polarized ($h\|h$) and scalar case. Since the optical thickness is kept constant, the elastic quantities are independent of the detuning, and only the inelastic components are affected by δ, via the shape of the power spectrum $P(\omega')$ of the inelastically scattered light, see Eq. (26). The latter exhibits two peaks of width Γ, one of which is centered around the atomic resonance. The increase of the ladder term as a function of δ

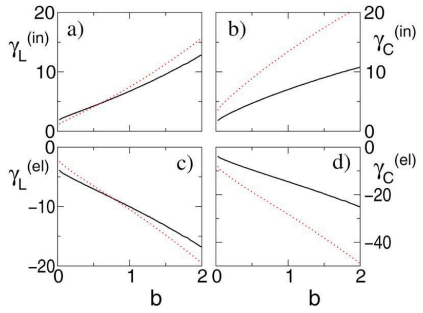

FIG. 10. (Color online) Normalized inelastic and elastic ladder and crossed $\gamma_{L,C}^{(el,in)}$ [cf. Eqs. (62) and (63)], for vanishing detuning $\delta=0$, as a function of the optical thickness $b=0.5$. Solid lines: polarized case ($h\|h$ channel). Dotted lines: scalar case.

which is observed in Fig. 9(a) is due to initially detuned photons, i.e., $\omega=\omega_{at}+\delta$, which are set to resonance ($\omega' \simeq \omega_{at}$) by the nonlinear scattering process. For these photons, the scattering cross section increases, which increases the contribution to the backscattering signal in the sum over all scattering orders—especially in the $h\|h$ case where single scattering is filtered out. The same effect also applies for the crossed term, Fig. 9(b), but here the dephasing between the reversed paths due to the frequency change—which is more effective for higher values of the detuning—is dominant, leading in total to a decrease of $\gamma_C^{(in)}$ as a function of δ. The small ripples in Fig. 9(a), for the polarized case (solid line) at large δ, are due to numerical noise in the Monte Carlo integration.

Figure 10 shows the elastic and inelastic ladder and crossed contributions, as a function of the optical thickness, at detuning $\delta=0$. The main purpose of this figure is to show the increase of the nonlinear contributions as a function of b, which is important to understand the domain of validity of the present approach. The origin of this increase is simple to understand: for larger values of the optical thickness, the average number of scattering events increases, and so does also the probability that at least one of them is a nonlinear one. Thus, for an optically thick medium, even a very small initial saturation may lead to a large inelastic component of the backscattered light. Note, however, that the elastic and inelastic ladder contributions, Figs. 10(a) and 10(c), tend to cancel each other, such that their sum depends less strongly on b. Physically, this fact is related to energy conservation. The latter ensures that the *total* nonlinear scattered intensity—integrated over all final directions—vanishes even exactly, since the total outgoing intensity must equal the incident intensity (meaning a purely linear relationship between outgoing and incident intensity).

Furthermore, we note that both the elastic and inelastic ladder components increase significantly more slowly in the polarized than in the scalar case (solid vs dashed line). This is due to the fact that, as discussed in Sec. III C, polarization effects diminish the weight of nonlinear scattering by approximately 2/3. Concerning the crossed components, Figs. 10(b) and 10(d), the difference is even stronger, due to the

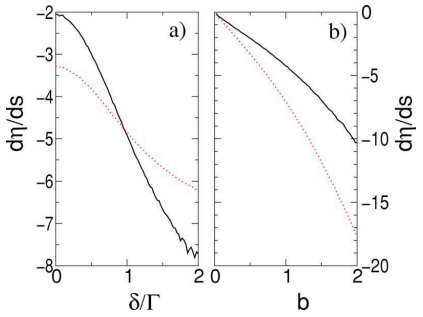

FIG. 11. (Color online) Slope of backscattering enhancement factor, for the parameters of Fig. 9 (b=0.5, left half) and Fig. 10 (δ=0, right half). Solid lines: polarized case ($h\|h$ channel). Dotted lines: scalar case.

additional polarization-induced loss of contrast by a factor 3/4, on average. Please note that the vertical scale for the elastic crossed case, Fig. 10(d), is two times larger than in the other three cases: this reflects the effect of interference between three amplitudes, which renders the crossed component up to two times larger than the ladder. Concerning the inelastic component Fig. 10(b), this effect is diminished by decoherence due to the frequency change at inelastic scattering. Here, crossed and ladder components are of similar magnitude.

In Fig. 11, we show the slope of the backscattering enhancement factor, which follows via Eq. (61) from the data shown in Figs. 9 and 10. Figure 11(b) again points out the importance of even small saturation in the case of an optically thick medium. For example, in the scalar case at b=2, increasing the saturation from s=0 to s=0.01 decreases the enhancement factor from 1.73 (<2 due to single scattering) to 1.55. For very large b, we find a linear decrease of the slope. At the same time, however, the allowed domain of $s \ll 1/b^2$ shrinks to zero *quadratically*. This allows the enhancement factor to remain a continuous function of s, even in the limit $b \to \infty$, where its slope at s=0 diverges. In order to make more precise statements about the behavior in the limit $b \to \infty$, however, it is necessary to generalize our theory to the case of more than one nonlinear scattering event.

On the left-hand side, Fig. 11(a) depicts the dependence of the enhancement factor on detuning, for b=0.5. As already discussed above, the decrease of η with increasing δ originates from the form of the inelastic power spectrum, which results in a stronger dephasing between reversed paths for larger detuning. Thus, the modification of the enhancement factor with the detuning, keeping fixed the linear optical thickness, is a signature of the nonlinear atomic response and has been experimentally observed in Ref. [40]. Let us stress, however, that in the cases shown in Figs. 9 and 11(a) and small detuning, the inelastic component gives a *positive* contribution to the backscattering enhancement factor. Hence, the observed negative slope of η originates from the elastic component, where the nonlinear crossed term is up to two times larger than the ladder, but with negative sign [see Figs. 10(c) and 10(d)].

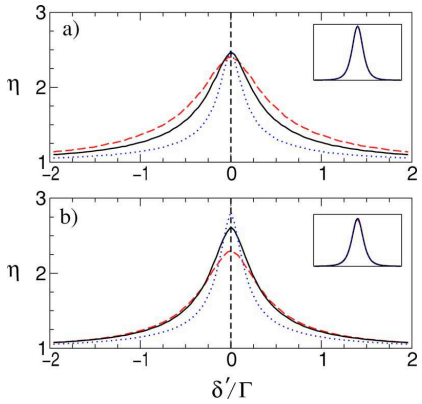

FIG. 12. (Color online) Spectral dependence of the enhancement factor, for detuning δ=0 and optical thickness b=0.5 (dashed line), 1 (solid), and 2 (dotted), in the $h\|h$ channel (a) and the scalar case (b). The vertical dashed line displays the position of the elastic δ peak, which must be filtered out in order to observe an enhancement factor larger than 2. The inset shows the power spectrum of the backscattered light (background component), which is almost identical with the single-atom spectrum.

In order to observe an enhancement factor larger than 2—and thereby demonstrate clearly the effect of interference between three amplitudes—it is therefore necessary to filter out the elastic component. In principle, this can be achieved by means of a spectral filter, i.e., by detecting only photons with a certain frequency ω', different from the laser frequency ω. Thereby, it is possible to measure the spectral dependence of the backscattering enhancement factor (see Fig. 12). Here, the upper (a) and lower (b) parts depict the polarized ($h\|h$) and scalar cases, respectively, for vanishing laser detuning, δ=0. Evidently, the largest values of the enhancement factor are obtained if the final frequency approaches the initial one, since then the dephasing due to different frequencies vanishes. In the scalar case, the value of the enhancement factor in the limit $\delta' \to 0$ is completely determined by the relative weights between the one-, two-, and three-amplitude cases shown in Fig. 4 [cf. Eq. (38)]. As evident from the dashed line in Fig. 12(b), already at the rather moderate value b=0.5 of the optical thickness, the three-amplitude case is sufficiently strong in order to increase the maximum enhancement factor above the linear barrier η=2. With increasing optical thickness (and, if necessary, decreasing saturation parameter, in order to stay in the domain of validity of the perturbative approach; see above), the number of linear scattering events increases, which implies that the three-amplitude case increasingly dominates (see Fig. 4). In this limit, the enhancement factor approaches the maximum value 3. At the same time, however, a larger number of scattering events also leads to stronger dephasing due to different frequencies, $\omega' \neq \omega$. This results in a narrower shape of η as a function of ω' for larger optical thickness. Nevertheless, as evident from Fig. 12(b), the enhancement factor remains larger than 2 in a significant range of frequencies ω'. The same is true for the polarized case, Fig. 12(a). However, here

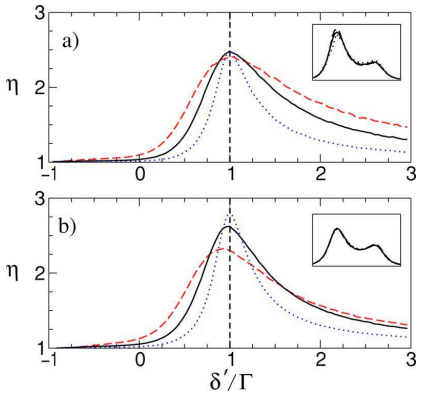

FIG. 13. (Color online) Spectral dependence of the enhancement factor, for detuning $\delta=\Gamma$ and optical thickness $b=0.5$ (dashed line), 1 (solid), and 2 (dotted), in the $h\|h$ channel (a) and the scalar case (b). The vertical dashed line displays the position of the elastic δ peak, which must be filtered out in order to observe an enhancement factor larger than 2. The inset shows the power spectrum of the backscattered light (background component), revealing the amplification of the on-resonance peak with respect to the symmetric single-atom spectrum.

the enhancement factor cannot exceed the value 2.5, due to the polarization-induced loss of contrast. At the same time, the optical thickness has less influence on the maximum enhancement factor at $\delta'=0$, since single scattering, Fig. 4(a)—and partly also the two-amplitude case, Fig. 4(b)—is filtered out, so that interference of three amplitudes already prevails at rather small values of the optical thickness.

In Fig. 13, the influence of an initial detuning (here $\delta=\Gamma$) is displayed. Basically, the above conclusions remain almost equally valid for the detuned case. A small difference is seen in the scalar case Fig. 13(b), where the maximum of $\eta(\delta')$ is found slightly below δ. This is due to the fact that the weight of single scattering increases with increasing δ'. Furthermore, the inset reveals that the power spectrum of the backscattered light differs from the single-atom spectrum Eq. (26), where the two peaks at $\delta'=0$ and 2δ are equally strong. In the multiple-scattering case, the on-resonance peak at $\delta'=0$ is amplified, since the scattering cross section is larger for photons on resonance. As already mentioned above (see the discussion of Fig. 9), this increases the total contribution to the detection signal (in the sum over all scattering paths)—especially in the polarized case, where single scattering is filtered out.

V. CONCLUSION

In summary, we have presented a detailed diagrammatic calculation of coherent backscattering of light from a dilute medium composed of weakly saturated two-level atoms. Our theory applies in the perturbative two-photon scattering regime ($s\ll 1$ and $sb^2\ll 1$), where at most one nonlinear scattering event occurs. The value of the backscattering enhancement factor is determined by the following three effects. First, due to the nonlinearity of the atom-photon interaction, there may be either two or three different amplitudes which interfere in the backscattering direction. This implies a maximal enhancement factor between 2 and 3 for the nonlinear component, where the value 3 is approached for large optical thickness. However, since the contribution from nonlinear scattering has a negative sign, the total enhancement factor (linear plus nonlinear elastic and inelastic components) is *reduced* by the effect of three-amplitude interference. Only if the elastic component is filtered out can a value larger than 2 be observed.

Second, a loss of coherence is implied by the change of frequency due to inelastic scattering—as in the case of two atoms [32]. The random frequency change leads to different scattering phases—and hence on average decoherence—between reversed paths. Finally, a further loss of contrast is induced by nonlinear polarization effects—even in the $h\|h$ channel, which exhibits ideal contrast in the linear case. Nevertheless, the enhancement factor remains larger than 2 in certain frequency windows of the inelastic backscattering signal. Thus, it is experimentally possible to clearly identify the effect of interference between three amplitudes—provided a sufficiently narrow spectral filter is at hand.

A natural way to extend this work is to give up the perturbative assumption, and admit more than one nonlinear scattering event. This is necessary in order to describe media with large optical thickness, even at small saturation. Since the number of interfering amplitudes increases if more than two photons are connected by nonlinear scattering events, we expect the occurrence of even larger enhancement factors in the nonperturbative regime—especially in the case of scatterers with positive nonlinearity, i.e., for scatterers whose cross section *increases* with increasing intensity.

Furthermore, the relation between coherent backscattering and weak localization in the presence of nonlinear scattering remains to be explored. Does a large enhancement of coherent backscattering also imply a strong reduction of nonlinear diffusive transport? If the answer is yes—as is the case in the linear regime—this implies that wave localization can be facilitated by introducing appropriate nonlinearities.

ACKNOWLEDGMENTS

T.W. was supported by the DFG Emmy Noether program. Laboratoire Kastler Brossel is laboratoire de l'Université Pierre et Marie Curie et de l'Ecole Normale Superieure, UMR 8552 du CNRS.

APPENDIX: MONTE CARLO SIMULATION

As discussed in Sec. III C, the incorporation of polarization effects requires one to take into account the projection of polarization vectors in the corresponding scalar equations. For the inelastic ladder component, insertion of the polarization term Eq. (55) into the scalar expression Eq. (28) yields

$$\hat{L}_{\mathrm{in}}^{(2)} = s\int \frac{d\mathbf{r}}{A\hat{\ell}}\int d\omega' P(\omega') \sum_{n,m,l=0}^{\infty} \mathcal{N}^{n+m+l}\int_V d\mathbf{u}_1\cdots d\mathbf{u}_n e^{-u_{1,z}/\hat{\ell}}\left(\prod_{i=1}^{n}|\hat{S}_\omega\hat{G}_\omega(\mathbf{u}_i,\mathbf{u}_{i+1})|^2\right)\int_V d\mathbf{v}_1\cdots d\mathbf{v}_m e^{-v_{1,z}/\hat{\ell}}$$
$$\times\left(\prod_{j=1}^{m}|\hat{S}_\omega\hat{G}_\omega(\mathbf{v}_j,\mathbf{v}_{j+1})|^2\right)\int_V d\mathbf{w}_1\cdots d\mathbf{w}_l e^{-w_{1,z}/\hat{\ell}'}\left(\prod_{k=1}^{l}|\hat{S}_{\omega'}\hat{G}_{\omega'}(\mathbf{w}_k,\mathbf{w}_{k+1})|^2\right)\frac{3}{2}\Pi^{(L)}(\boldsymbol{\epsilon}_u,\boldsymbol{\epsilon}_v;\boldsymbol{\epsilon}_w)\times\begin{cases}1 & \text{if } n=m=0,\\ 2 & \text{if } n>0 \text{ or } m>0,\end{cases} \tag{A1}$$

with $\mathbf{u}_{n+1}=\mathbf{v}_{m+1}=\mathbf{w}_{l+1}=\mathbf{r}$. Furthermore, the polarization vectors are given by

$$\boldsymbol{\epsilon}_u = \Delta_{\mathbf{u}_n,\mathbf{u}_{n+1}}\cdots\Delta_{\mathbf{u}_1,\mathbf{u}_2}\boldsymbol{\epsilon}_L,$$

$$\boldsymbol{\epsilon}_v = \Delta_{\mathbf{v}_m,\mathbf{v}_{m+1}}\cdots\Delta_{\mathbf{v}_1,\mathbf{v}_2}\boldsymbol{\epsilon}_L,$$

$$\boldsymbol{\epsilon}_w = \Delta_{\mathbf{w}_l,\mathbf{w}_{l+1}}\cdots\Delta_{\mathbf{w}_1,\mathbf{w}_2}\boldsymbol{\epsilon}_D. \tag{A2}$$

The analogous procedure for the interference component, inserting Eq. (57) into Eq. (33), yields

$$\hat{C}^{(2,\mathrm{in})} = s\int \frac{d\mathbf{r}}{A\hat{\ell}}\int d\omega' P(\omega') \sum_{n,m,l=0}^{\infty} \mathcal{N}^{n+m+l}\int_V d\mathbf{u}_1\cdots d\mathbf{w}_l e^{-u_{1,z}/\hat{\ell}}\left(\prod_{i=1}^{n}|\hat{S}_\omega\hat{G}_\omega(\mathbf{u}_i,\mathbf{u}_{i+1})|^2\right)e^{ikv_{1,z}(n_\omega+n^*_{\omega'})}$$
$$\times\left(\prod_{j=1}^{m}\hat{S}_\omega\hat{S}^*_{\omega'}\hat{G}_\omega(\mathbf{v}_j,\mathbf{v}_{j+1})\hat{G}^*_{\omega'}(\mathbf{v}_j,\mathbf{v}_{j+1})\right)e^{ikw_{1,z}(n^*_\omega+n_{\omega'})}\left(\prod_{k=1}^{l}\hat{S}^*_\omega\hat{S}_{\omega'}\hat{G}^*_\omega(\mathbf{w}_k,\mathbf{w}_{k+1})\hat{G}_{\omega'}(\mathbf{w}_k,\mathbf{w}_{k+1})\right)$$
$$\times\frac{3}{2}\Pi^{(C)}(\boldsymbol{\epsilon}_u,\boldsymbol{\epsilon}_v,\tilde{\boldsymbol{\epsilon}}_w,\boldsymbol{\epsilon}_w,\tilde{\boldsymbol{\epsilon}}_v)\times\begin{cases}0 & \text{if } m=l=0,\\ 2 & \text{if } n=m=0, \quad l>0,\\ 2 & \text{if } n=l=0, \quad m>0,\\ 4 & \text{otherwise},\end{cases} \tag{A3}$$

with the polarization vectors of the "reversed" photons

$$\tilde{\boldsymbol{\epsilon}}_v = \Delta_{\mathbf{v}_m,\mathbf{v}_{m+1}}\cdots\Delta_{\mathbf{v}_1,\mathbf{v}_2}\boldsymbol{\epsilon}_D,$$

$$\tilde{\boldsymbol{\epsilon}}_w = \Delta_{\mathbf{w}_l,\mathbf{w}_{l+1}}\cdots\Delta_{\mathbf{w}_1,\mathbf{w}_2}\boldsymbol{\epsilon}_L. \tag{A4}$$

The elastic nonlinear scattering components follow simply by inserting $-2\delta(\omega'-\omega)$ instead of the inelastic power spectrum $P(\omega')$ in the above Eqs. (A1) and (A3).

The nonlinear propagation term is obtained by inserting Eq. (58) into Eq. (44):

$$\hat{L}_{\mathrm{el}}^{(2,\mathrm{prop})} = s\sum_{n=1}^{\infty}\mathcal{N}^n\int_V d\mathbf{u}_1\cdots d\mathbf{u}_n e^{-(u_{1,z}+u_{n,z})/\hat{\ell}}\left(\prod_{i=1}^{n}|\hat{S}_\omega\hat{G}_\omega(\mathbf{u}_i,\mathbf{u}_{i+1})|^2\right)\sum_{m=1}^{\infty}\mathcal{N}^{m-1}\int_V d\mathbf{v}_1\cdots d\mathbf{v}_{m-1}\sum_{l=0}^{n}\int_{\mathbf{u}_l}^{\mathbf{u}_{l+1}}\frac{d\mathbf{v}_m}{\hat{\ell}}e^{-v_{1,z}/\hat{\ell}}$$
$$\times\left(\prod_{i=1}^{m-1}|\hat{S}_\omega\hat{G}_\omega(\mathbf{v}_i,\mathbf{v}_{i+1})|^2\right)\Pi^{(L,\mathrm{prop})}(\boldsymbol{\epsilon}_1,\boldsymbol{\epsilon}_v,\boldsymbol{\epsilon}_3)\times\begin{cases}1 & \text{if } m=l=0,\\ 2 & \text{otherwise}.\end{cases} \tag{A5}$$

Here, the nonlinear event takes place between $\mathbf{u}_l$ and $\mathbf{u}_{l+1}$. Correspondingly, $\int_{\mathbf{u}_l}^{\mathbf{u}_{l+1}}$ denotes the one-dimensional integral on a straight line between these points, and $\mathbf{u}_0=\mathbf{u}_1-u_{1,z}\mathbf{e}_z$ and $\mathbf{u}_{n+1}=\mathbf{u}_n-u_{n,z}\mathbf{e}_z$ are defined as the points where the photon enters or leaves the medium, respectively. The three cases Figs. 5(a)–5(c) correspond to $0<l<n$, $l=n$, and $l=0$, respectively. The polarization vectors $\boldsymbol{\epsilon}_1$ and $\boldsymbol{\epsilon}_3$ participating in the nonlinear event (cf. Fig. 8) are obtained as

$$\boldsymbol{\epsilon}_1 = \Delta_{\mathbf{u}_{l+1},\mathbf{u}_l}\cdots\Delta_{\mathbf{u}_2,\mathbf{u}_1}\boldsymbol{\epsilon}_L,$$

$$\boldsymbol{\epsilon}_3 = \Delta_{\mathbf{u}_l,\mathbf{u}_{l+1}}\cdots\Delta_{\mathbf{u}_{n-1},\mathbf{u}_n}\boldsymbol{\epsilon}_D. \tag{A6}$$

Finally, to obtain the interference component $\hat{C}_{\mathrm{el}}^{(2,\mathrm{prop})}$, the last term in Eq. (A5) must be replaced by

$$\Pi^{(L,\mathrm{prop})}(\boldsymbol{\epsilon}_1,\boldsymbol{\epsilon}_v,\boldsymbol{\epsilon}_3)\times\begin{cases}2 & \text{if } n>1, \quad (m,l)\neq(0,0)\\ 1 & \text{if } n>1, \quad m=l=0\\ 0 & \text{otherwise}\end{cases} + \Pi^{(C,\mathrm{prop})}(\boldsymbol{\epsilon}_1,\boldsymbol{\epsilon}_v,\boldsymbol{\epsilon}_3,\tilde{\boldsymbol{\epsilon}}_v,\tilde{\boldsymbol{\epsilon}}_3)\times\begin{cases}4 & \text{if } l=0, \quad n>1, \quad m>0,\\ 2 & \text{if } l=0, \quad n=1, \quad m>0,\\ 2 & \text{if } 0<l<n,\\ 0 & \text{otherwise},\end{cases} \tag{A7}$$

with

$$\tilde{\boldsymbol{\epsilon}}_3=\Delta_{\mathbf{u}_l,\mathbf{u}_{l+1}}\cdots\Delta_{\mathbf{u}_{n-1},\mathbf{u}_n}\boldsymbol{\epsilon}_L. \tag{A8}$$

The first term, $\Pi^{(L,\mathrm{prop})}$, equals the ladder component minus single scattering ($n=1$), whereas the second one, $\Pi^{(C,\mathrm{prop})}$, describes the additional crossed diagrams shown in Figs. 6(d)–6(f). Here, the case $0<l<n$ corresponds to Fig. 6(d), where the nonlinearity occurs between two scattering events. The remaining diagrams, Figs. 6(e) and 6(f), correspond to $l=0$. Here, the case $m=0$ ("pump photon from the coherent mode") does not contribute, since then the diagrams Figs. 6(e) and 6(f) are identical to Figs. 6(b) and 6(c). Furthermore, if $n=1$ ("probe photon singly scattered"), the two diagrams Figs. 6(e) and 6(f) become identical. In this case, we obtain a factor 2, whereas the sum of diagram (e) plus diagram (f) yields $2+2=4$ in the case $n>1$.

Numerically, we solve the above integrals by a Monte Carlo method. Here, we proceed as follows. For Eqs. (A1) and (A3) first the position $\mathbf{r}$ and frequency ω_D of the inelastic scattering event are chosen randomly. Starting from $\mathbf{r}$, three photons are launched, two with frequency ω_L and one with frequency ω_D. After each scattering event, the length r of the next propagation step is determined randomly according to the distribution $P(r)=\exp(-r/\ell)/\ell$, whereas the direction is chosen uniformly. After all photons have left the medium, the triple sum over n, m, and l is performed, taking into account the projection of the polarization vectors. For the nonlinear propagation term Eq. (A5), first the probe photon (path $\mathbf{u}_1,\ldots,\mathbf{u}_n$) is propagated, starting in the laser mode $\mathbf{k}_L,\boldsymbol{\epsilon}_L$. Then, the pump photon is launched from a randomly chosen position $\mathbf{v}_m$ on the path of the probe photon. Finally, the projection of polarization vectors is performed separately for each given path.

[1] A. Schuster, Astrophys. J. **21**, 1 (1905).
[2] D. Mihalas, *Stellar Atmospheres*, 2nd ed. (Freeman, San Francisco, 1978).
[3] S. Chandrasekhar, *Radiative Transfer* (Dover, New York, 1960).
[4] H. C. van de Hulst, *Multiple Light Scattering* (Academic Press, New York, 1980), Vols. I and II.
[5] T. Holstein, Phys. Rev. **72**, 1212 (1947); **83**, 1159 (1951).
[6] A. F. Molisch and B. P. Oehry, *Radiation Trapping in Atomic Vapors*, Oxford Science Publications (Oxford University Press, New York, 1998).
[7] *Laser Speckle and Related Phenomena*, edited by C. Dainty, Topics in Applied Physics Vol. 9 (Springer-Verlag, Berlin, 1984).
[8] P. W. Anderson, Phys. Rev. **109**, 1492 (1958).
[9] J. S. Langer and T. Neal, Phys. Rev. Lett. **16**, 984 (1966).
[10] G. Bergmann, Phys. Rep. **107**, 1 (1984).
[11] *Mesoscopic Quantum Physics*, edited by E. Akkermans, G. Montambaux, J. L. Pichard, and J. Zinn-Justin, Proceedings of the Les Houches Summer School of Theoretical Physics, LXI (North-Holland Elsevier Science, Amsterdam, 1995).
[12] E. Akkermans and G. Montambaux, *Physique Mésoscopique des Électrons et des Photons* (EDP Sciences/CNRS Editions, Paris, 2004).
[13] A. Akkermans and G. Montambaux, J. Opt. Soc. Am. B **21**, 101 (2004), and references therein.
[14] F. Scheffold and G. Maret, Phys. Rev. Lett. **81**, 5800 (1998).
[15] D. S. Wiersma, P. Bartolini, A. Lagendijk, and R. Righini, Nature (London) **390**, 671 (1997).
[16] G. Maret, Curr. Opin. Colloid Interface Sci. **2**, 251 (1997).
[17] M. P. Van Albada and A. Lagendijk, Phys. Rev. Lett. **55**, 2692 (1985); P. E. Wolf and G. Maret, *ibid.* **55**, 2696 (1985).
[18] E. Akkermans, P. E. Wolf, R. Maynard, and G. Maret, J. Phys. (Paris) **49**, 77 (1988).
[19] B. van Tiggelen and R. Maynard, in "Wave Propagation in Complex Media," *IMA Volumes in Mathematics and its Applications*, edited by G. Papanicolaou, Vol. 96 (Springer, Berlin, 1997), p. 247.
[20] V. M. Agranovich and V. E. Kravtsov, Phys. Rev. B **43**, R13691 (1991).
[21] A. Heiderich, R. Maynard, and B. A. van Tiggelen, Opt. Commun. **115**, 392 (1995).
[22] G. Labeyrie, F. de Tomasi, J.-C. Bernard, C. A. Müller, C. Miniatura, and R. Kaiser, Phys. Rev. Lett. **83**, 5266 (1999).
[23] T. Jonckheere, C. A. Müller, R. Kaiser, C. Miniatura, and D. Delande, Phys. Rev. Lett. **85**, 4269 (2000).
[24] C. A. Müller, T. Jonckheere, C. Miniatura, and D. Delande, Phys. Rev. A **64**, 053804 (2001).
[25] C. A. Müller and C. Miniatura, J. Phys. A **35**, 10163 (2002).
[26] D. V. Kupriyanov, I. M. Sokolov, and M. D. Havey, Opt. Commun. **243**, 165 (2004).
[27] V. S. Lethokov, Sov. Phys. JETP **26**, 835 (1968).

[28] N. M. Lawandy, R. M. Balachandran, A. S. L. Gomes, and E. Sauvain, Nature (London) **368**, 436 (1994).
[29] H. Cao, Y. G. Zhao, S. T. Ho, E. W. Seelig, Q. H. Wang, and R. P. H. Chang, Phys. Rev. Lett. **82**, 2278 (1999).
[30] H. Cao, Waves Random Media **13**, R1 (2003), and references therein.
[31] T. Wellens, B. Grémaud, D. Delande, and C. Miniatura, Phys. Rev. E **71**, 055603(R) (2005).
[32] T. Wellens, B. Grémaud, D. Delande, and C. Miniatura, Phys. Rev. A **70**, 023817 (2004).
[33] V. Shatokhin, C. A. Müller, and A. Buchleitner, Phys. Rev. Lett. **94**, 043603 (2005).
[34] B. Grémaud, T. Wellens, D. Delande, and Ch. Miniatura (unpublished).
[35] A. Lagendijk and B. A. van Tiggelen, Phys. Rep. **270**, 143 (1996).
[36] G. Labeyrie, Ch. Miniatura, and R. Kaiser, Phys. Rev. A **64**, 033402 (2001).
[37] D. S. Wiersma, M. P. van Albada, B. A. van Tiggelen, and A. Lagendijk, Phys. Rev. Lett. **74**, 4193 (1995).
[38] C. Cohen-Tannoudji, J. Dupont-Roc, and G. Grynberg, *Atom-Photon Interactions* (Wiley, New York, 1992).
[39] J. W. Goodman, in *Laser Speckle and Related Phenomena*, edited by J. C. Dainty (Springer, Berlin, 1984).
[40] T. Chanelière, D. Wilkowski, Y. Bidel, R. Kaiser, and C. Miniatura, Phys. Rev. E **70**, 036602 (2004).
[41] S. Balik, P. Kulatunga, C. I. Sukenik, M. D. Havey, D. V. Kupriyanov, and I. M. Sokolov, J. Mod. Opt. **52**, 2269 (2005).
[42] In our article [31], the statement in the paragraph following Eq. (11) is thus wrong and so are the numerical results depicted in Fig. 3. The corrected figure can be obtained by sending an email to Thomas.Wellens@spectro.jussieu.fr
[43] S. E. Skipetrov and R. Maynard, Phys. Rev. Lett. **85**, 736 (2000).
[44] In principle, there exists also the possibility that both the detected and undetected photons are not scattered at **r** in one of the interfering amplitudes, corresponding to forward scattering of both photons by the same atom. It can be shown, however, that this case is negligible in the case of a dilute medium.

Nonlinear Coherent Transport of Waves in Disordered Media

Thomas Wellens[1] and Benoît Grémaud[2]

[1]*Institut für Theoretische Physik, Universität Erlangen-Nürnberg, Staudtstrasse 7, 91058 Erlangen, Germany*
[2]*Laboratoire Kastler Brossel, Ecole Normale Supérieure, CNRS, UPMC, 4 place Jussieu, 75252 Paris Cedex 05, France*

(Received 13 July 2007; revised manuscript received 10 October 2007; published 24 January 2008)

We present a diagrammatic theory for coherent backscattering from disordered dilute media in the nonlinear regime. We show that the coherent backscattering enhancement factor is strongly affected by the nonlinearity, and we corroborate these results by numerical simulations. Our theory can be applied to several physical scenarios such as scattering of light in a nonlinear Kerr medium or propagation of matter waves in disordered potentials.

DOI: 10.1103/PhysRevLett.100.033902 PACS numbers: 42.25.Dd, 42.65.−k

The interplay between disorder and—even very weak—nonlinearity can lead to dramatic changes to the system's properties: for example, instabilities occur [1–3], or localization may be destroyed [4]. In the experiments studying the localization properties of matter waves in speckle potentials [5], the nonlinear regime, arising from the atomic interactions, is almost unavoidable. Furthermore, nonlinear behavior is easily observed in coherent backscattering (CBS) experiments with cold atomic gases [6]. Also random lasers exhibit nonlinearities which potentially influence the structure of localized laser modes [7]. In all these cases, even if the systems are governed by simple nonlinear wave equations, a precise description of the impact of this nonlinearity on the interference effects altering the properties of diffuse wave propagation is still lacking. Since exact numerical calculations for realistic situations are at the border of or beyond actual computer capacities, one needs an efficient theory providing directly disorder averaged quantities. For this purpose, the present Letter shows that the standard diagrammatic approach [8] can be extended to the nonlinear regime. Using ladder and crossedlike diagrams, we will derive a nonlinear radiative transfer equation for the averaged wave intensity and then calculate the interference corrections on top of the nonlinear solution.

The general framework for our approach is as follows: we assume a nonlinear wave equation with unique and stationary monochromatic solution, meaning, in particular, that the nonlinear susceptibilities at harmonics frequencies are weak enough such that the latter can be neglected. We also neglect—on the length scale ℓ (mean free path) set by the disorder—effects like self-focusing, pattern formation, and solitons [9], which originate from nonlinear variations Δn_{nl} of the real part of the refractive index. This assumption is valid if $(\Delta n_{\mathrm{nl}})^2 k\ell \ll 1$ [2]. Our theory also applies to imaginary Δn_{nl}, i.e., absorbing or amplifying media, provided, in the latter case, that the solutions remain stable. Within this general scenario, comprising examples like a collection of resonant point scatterers, or a (mean field) matter wave in a disordered potential, the nonlinear effects relevant in connection with the disorder are as follows: first, the wave intensity $I(\mathbf{r})$ becomes a fluctuating quantity, which is especially important in the nonlinear regime; second, the usual picture of weak localization resulting from interference only between pairs of amplitudes propagating along reversed paths breaks down in the nonlinear regime. As a consequence of nonlinear mixing between different partial waves, weak localization must rather be interpreted as a multiwave interference phenomenon [10,11]. In particular, we will show that the height of the coherent backscattering peak is strongly affected by nonlinearities, even if they do respect the reciprocity symmetry. In contrast to [10,11], the present approach is valid in the nonperturbative regime of arbitrarily large scattering media, where expansions in powers of the nonlinearity strength do not converge and even small nonlinearities may have a large impact on the wave propagation.

At first, we consider an assembly of N pointlike scatterers located at randomly chosen positions $\mathbf{r}_i$, $i = 1, \ldots, N$ inside a sample volume V illuminated by a plane wave $\mathbf{k}_L$. We assume the field radiated by each scatterer to be a nonlinear function $f(E_i)$ of the local field E_i. Neglecting higher harmonics, we write $f(E) = g(I)E$, where $I = EE^*$ is the local intensity, and $g(I)$ is proportional to the polarizability of the scatterers. This results in a set of nonlinear equations for the field at each scatterer:

$$E_i = e^{i\mathbf{k}_L\cdot\mathbf{r}_i} + \sum_{j\neq i} \frac{e^{ik|\mathbf{r}_i-\mathbf{r}_j|}}{4\pi|\mathbf{r}_i-\mathbf{r}_j|} g(E_jE_j^*)E_j, \qquad (1)$$

where $k = |\mathbf{k}_L|$, and the field is measured in units of the incident plane wave amplitude. For simplicity, we will consider only scalar fields in this Letter.

We aim at providing a theory providing the relevant quantities (local intensities, CBS cone, etc.) averaged over the random positions of the scatterers. In a first step, we will derive an equation for the mean intensity $\langle I(\mathbf{r})\rangle$. In the dilute regime, where the typical distances $|\mathbf{r}_i - \mathbf{r}_j|$ are much larger than the wavelength, we may neglect correlations between the fields emitted by different scatterers. The scattered field $E_d(\mathbf{r})$ is then a superposition of spherical

waves with random relative phases, depicting thus a speckle pattern. The resulting Gaussian statistics for the complex field $E_d(\mathbf{r})$ [12] are completely determined by a single parameter, the mean diffuse intensity $I_d(\mathbf{r}) = \langle |E_d(\mathbf{r})|^2 \rangle$. In addition to the scattered field, there is also a nonfluctuating coherent component originating directly from the incident field. In total, we have $E(\mathbf{r}) = \langle E(\mathbf{r}) \rangle + E_d(\mathbf{r})$, and the average intensity splits into a coherent and diffuse part: $\langle I(\mathbf{r}) \rangle = I_c(\mathbf{r}) + I_d(\mathbf{r})$, with $I_c = |\langle E \rangle|^2$. The mean density of radiation intensity emitted from point $\mathbf{r}$ is then given by

$$K(\mathbf{r}) = \mathcal{N}\langle f f^* \rangle = \mathcal{N}\langle |g(I(\mathbf{r}))|^2 I(\mathbf{r}) \rangle, \tag{2}$$

where $\mathcal{N} = N/V$ denotes the density of scatterers, and the average $\langle \ldots \rangle$ is taken over the Gaussian statistics of the scattered field.

Between two scattering events, the wave propagates in an effective medium made by the scatterers, described by a refractive index n and mean free path ℓ. Note that, because of the nonlinear behavior of the scatterers, the effective medium is modified by the propagating waves themselves. Because of their different statistical properties, we obtain therefore different refractive indices for coherent and diffuse fields, respectively. (This effect is also known from usual pump-probe configurations in nonlinear optics [9].) In the dilute regime, the diffuse amplitude can be considered as a weak probe, such that the complex refraction index reads as follows:

$$n = 1 + \frac{\mathcal{N}}{2k^2}\left\langle \frac{df}{dE} \right\rangle, \qquad \frac{1}{\ell} = 2k\mathrm{Im}\{n\}, \tag{3}$$

whereas, for the coherent mode, the derivative d/dE is replaced by $1/\langle E \rangle$; i.e., $n_c = 1 + \mathcal{N}\langle f \rangle/(2k^2\langle E \rangle)$, and $1/\ell_c = 2k\mathrm{Im}\{n_c\}$. Since the results of the averages depend on $I_c(\mathbf{r})$ and $I_d(\mathbf{r})$, the nonlinear refractive indices also attain a spatial dependence $n(\mathbf{r})$ and $n_c(\mathbf{r})$. They describe average propagation of one strong and many uncorrelated weak fields.

Recollecting all preceding ingredients, the transport equations for the average intensity read as follows:

$$I_c(\mathbf{r}) = e^{-\overline{z/\ell_c}}, \tag{4}$$

$$I_d(\mathbf{r}) = \int_V d\mathbf{r}' \frac{e^{-\overline{|\mathbf{r}-\mathbf{r}'|/\ell}}}{(4\pi|\mathbf{r}-\mathbf{r}'|)^2} K(\mathbf{r}'). \tag{5}$$

Here, z denotes the distance from the surface of V to $\mathbf{r}$, in the direction of the incident beam. Furthermore, propagation from $\mathbf{r}'$ to $\mathbf{r}$ implies a spatial average of $1/\ell(\mathbf{r})$, which we note as $\overline{|\mathbf{r}-\mathbf{r}'|/\ell} := |\mathbf{r}-\mathbf{r}'| \int_0^1 ds/\ell(\mathbf{r} - s\mathbf{r} + s\mathbf{r}')$, and similarly for $\overline{(z/\ell_c)}$. Since K, ℓ, and ℓ_c depend on $I_c(\mathbf{r})$ and $I_d(\mathbf{r})$, the above Eqs. (4) and (5) form two coupled integral equations. Finally, the intensity scattered into backwards direction, expressed by the "bistatic coefficient" [8], results as

$$\Gamma_L = \int_V \frac{d\mathbf{r}}{4\pi A} e^{-\overline{z/\ell}} K(\mathbf{r}), \tag{6}$$

where A denotes the transverse (with respect to the incident beam) area of the scattering volume V.

The validity of the preceding approach has been tested using the nonlinear function $g(I) = (4\pi i)/k(1 + \alpha I)$ which depicts the (elastic) nonlinear behavior of a two-level atom exposed to an intense laser beam. We must emphasize that, for this particular model of nonlinearity, the stationary solution is always found to be unique and stable, as a consequence of the saturation $g(I) \to 0$ for large α. From the numerical solution of Eq. (1), we calculate the radiated intensity outside the cloud in different directions θ. This procedure is then repeated with many different configurations giving us the disorder averaged field and intensity. The results presented in this Letter are obtained with 3000 configurations of 1500 scatterers, randomly distributed inside a sphere with a homogeneous density ($k\ell = 67$ and optical thickness $b = 2$ for $\alpha = 0$).

The results for the average intensity as a function of the backscattering angle θ are depicted in Fig. 1 for different values of the nonlinear parameter $\alpha = 0$, 0.2, 0.4, and 0.6. For each plot, the solid line depicts the exact numerical results, whereas the dashed line corresponds to Γ_L, Eq. (6). Away from the backward direction, the agreement between the exact numerical calculations and our theoretical prediction for the background is clearly excellent. This is emphasized by the additional curve (long dashed line)

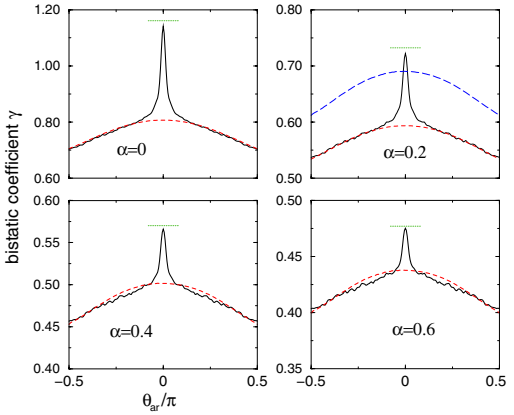

FIG. 1 (color online). Coherent backscattering cones obtained from exact numerical calculations in comparison to the theoretical approach, for various nonlinearity strengths α. The solid lines depict the exact numerical results, whereas the dashed lines correspond to Γ_L including geometrical effects. The dotted lines correspond to the sum $\Gamma_L + \Gamma_C$ exactly in the backward direction. The additional curve (long dashed line) plotted for $\alpha = 0.2$ depicts Γ_L obtained when the fluctuating character of the diffuse field is not taken into account.

plotted for $\alpha = 0.2$ depicting the results obtained when neglecting the fluctuations of $I(\mathbf{r})$, for example, replacing $\langle |g(I)|^2 I\rangle$ by $|g(\langle I\rangle)|^2\langle I\rangle$ in Eq. (2).

In the backward direction, constructive interference between reversed scattering paths results in the well-known coherent backscattering peak. As is obvious from Fig. 1, the height of this peak is strongly reduced by the nonlinearity. Nevertheless, we are perfectly able to incorporate these interference effects in our approach, see the horizontal dotted lines in Fig. 1, which depict the predicted total bistatic coefficient, $\Gamma_L + \Gamma_C$, see Eq. (12) below, in the exact backward direction. These results are obtained by a diagrammatic analysis, whose results we briefly outline in the following. A detailed derivation will be presented elsewhere.

In contrast to a previous attempt for a nonlinear diagrammatic theory [13], we concentrate on the regime $k\ell \gg 1$ of dilute media, which allows us to sum up the diagrammatic series in a simple, closed form, as shown below. As for linear media in the dilute regime, we calculate the CBS effect by so-called "crossed" or "Cooperon" diagrams [8], describing pairs of reversed scattering paths. As a first step, we analyze how a single scatterer responds to two different incident probe fields E and E^*, which represent the two amplitudes propagating along the reversed paths. Note that, due to the nonlinearity, the scattered field f and its complex conjugate f^* depend on both E and E^*. Hence, depending on whether the probe fields act on f or f^*, we obtain the building blocks depicted in Fig. 2. Expressing, as in Eq. (3), the scatterer's response to a small probe field by d/dE (or d/dE^*), the corresponding mathematical expressions read

$$\kappa = \mathcal{N}\left\langle \frac{d}{dE}\left(f\frac{df^*}{dE^*}\right)\right\rangle, \qquad \tilde{\kappa} = \mathcal{N}\left\langle \frac{d}{dE}\left(f^*\frac{df}{dE^*}\right)\right\rangle, \quad (7)$$

where κ represents the sum of diagram (a) + (c), $\tilde{\kappa}$ the sum (b) + (d), and

$$\tau = -\frac{i\mathcal{N}}{2k}\left\langle \frac{d^3 f^*}{(dE^*)^2 dE}\right\rangle \quad (8)$$

diagram (e). If one of the incident fields originates from the coherent mode, d/dE is again replaced by $1/\langle E\rangle$; i.e., $\kappa_c = \mathcal{N}\langle f\, df^*/dE^*\rangle/\langle E\rangle$, $\tilde{\kappa}_c = \mathcal{N}\langle f^*\, df/dE^*\rangle/\langle E\rangle$, and $\tau_c = -i\mathcal{N}\langle d^2 f^*/(dE^*)^2\rangle/(2k\langle E\rangle)$.

In the next step, the crossed transport equation is established by connecting the building blocks shown in Fig. 2 with each other. However, there are some combinations of diagrams, for example, the one shown in Fig. 2(g), which represent unphysical processes. In this diagram the fields radiated by f^* and f mutually depend on one another, and, therefore, one cannot tell which one of the two events f or f^* happens before the other one. In order to avoid closed loops like the one shown in Fig. 2(g), we ignore all combinations where one of the diagrams Fig. 2(c), 2(d), or 2(e) occurs after Fig. 2(b), 2(d), or 2(f) when following the solid arrow along the crossed path.

We account for these forbidden diagrams by splitting the transport equation into two parts, which we call C_1 and C_2. The first part, C_1, contains only diagrams Figs. 2(a), 2(c), and 2(e). As soon as one of the events Fig. 2(b), 2(d), or 2(f) occurs, the crossed intensity changes from type C_1 to type C_2. The subsequent propagation of C_2 is then given by diagrams Figs. 2(a), 2(b), and 2(f). Following these rules, we describe the propagation of $C_{1,2}$ by transport equations similar to Eqs. (4) and (5):

$$C_c(\mathbf{r}) = e^{ik\overline{z(n_c - n^*)}}, \quad (9)$$

$$C_1(\mathbf{r}) = \int_V d\mathbf{r}' P(\mathbf{r},\mathbf{r}')(\sigma C_1 + \sigma_c C_c)(\mathbf{r}'), \quad (10)$$

$$C_2(\mathbf{r}) = \int_V d\mathbf{r}' P(\mathbf{r},\mathbf{r}')(\sigma^* C_2 + \tilde{\sigma} C_1 + \tilde{\sigma}_c C_c)(\mathbf{r}'), \quad (11)$$

where $P(\mathbf{r},\mathbf{r}') = \exp(-\overline{|\mathbf{r}-\mathbf{r}'|/\ell})/(4\pi|\mathbf{r}-\mathbf{r}'|)^2$ is the same as in Eq. (5), and the cross sections σ result as follows: $\sigma = \kappa + \ell K\tau$, $\tilde{\sigma} = \tilde{\kappa} + \ell K\tau^*$, and, similarly, $\sigma_c = \kappa_c + \ell K\tau_c$ and $\tilde{\sigma}_c = \tilde{\kappa}_c + \ell K\tau_c^*$. Finally, the crossed bistatic coefficient reads

$$\Gamma_C = \int_V \frac{d\mathbf{r}}{4\pi A} e^{ik\overline{z(n-n_c^*)}}[(\sigma_c^* + \tilde{\sigma}_c^*)C_1 + \sigma_c^* C_2](\mathbf{r}). \quad (12)$$

For comparison with the background Γ_L, we define diffuson cross sections by writing $K = \sigma^{(d)} I_d + \sigma_c^{(d)} I_c$, such that Eq. (5) attains a form comparable to Eq. (10).

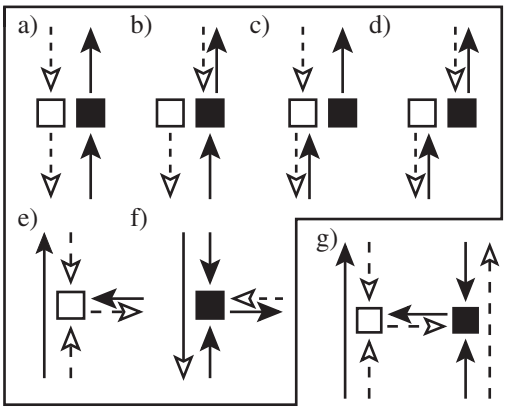

FIG. 2. (a)–(f) Building blocks for the diagrammatic calculation of nonlinear CBS. Filled squares (with outgoing solid arrows) denote the scattered field f, and open squares (with outgoing dashed arrows) the complex conjugate f^*. Incoming solid (dashed) arrows represent probe fields d/dE (d/dE^*). (g) Example of a forbidden combination of diagrams, exhibiting a closed loop (see the main text).

Exploiting the Gaussian properties of the diffuse field, we find $\sigma^{(d)} = \sigma - \tilde{\sigma}^*$ and $\sigma_c^{(d)} = \sigma_c - \tilde{\sigma}_c^*$.

How the nonlinearity affects the CBS effect can now be understood by comparing σ and $\sigma^{(d)}$. For the case of an absorbing nonlinearity, we find $\tilde{\sigma} < 0$, and hence $\sigma < \sigma^{(d)}$. Consequently, the crossed intensity is absorbed more strongly than the background intensity, which explains the decrease of the CBS cone observed in Fig. 1. Let us note that there also exist other models, for example, an amplifying nonlinearity like $g = 4\pi i(1 + \alpha I)/k$, where our theory predicts an enhancement of the CBS cone. However, these models might suffer from instabilities, requiring thus further investigations.

To obtain the relatively simple form of Eqs. (9)–(12), we have performed some approximations valid in the case of large optical thickness b. In the numerical comparison depicted in Fig. 1, we have used the exact version of Eqs. (9)–(12), which will be published elsewhere.

As explained in the introduction, our theoretical scheme also applies to other types of nonlinear systems. Instead of a collection of nonlinear scatterers as described by Eq. (1), we may, for example, also consider linear scatterers embedded in a homogeneous nonlinear medium:

$$\Delta E(\mathbf{r}) + k^2[\epsilon(\mathbf{r}) + \alpha|E(\mathbf{r})|^2]E(\mathbf{r}) = 0 \qquad (13)$$

with δ-correlated disorder $\epsilon(\mathbf{r})$ corresponding to a (linear) mean free path ℓ_0. Here, the dilute medium approximation is valid if $k\ell_0 \gg 1$ and $(\alpha I)^2 k\ell_0 \ll 1$. The latter condition is automatically fulfilled if we assume that we are in the stable regime, where Eq. (13) has a unique solution. According to [2], this is the case (for $\alpha \in \mathbb{R}$) if $(\alpha I)^2 b^2(k\ell_0 + b) < 1$, with b the optical thickness.

In this case, the diagrammatic method applies in the same way as described above. In particular, we obtain the following expressions for the cross sections:

$$\sigma(\mathbf{r}) = \sigma_c(\mathbf{r}) = \frac{4\pi}{\ell_0}\{1 + ik\ell_0\alpha[I_c(\mathbf{r}) + I_d(\mathbf{r})]\}, \qquad (14)$$

$\tilde{\sigma} = \tilde{\sigma}_c = -4\pi ik\alpha^*(I_c + I_d)$, $\sigma^{(d)} = \sigma_c^{(d)} = 4\pi/\ell_0$, and for the mean free paths $n = \langle\epsilon\rangle + \alpha(I_c + I_d) + i/(2k\ell_0)$ and $n_c = \langle\epsilon\rangle + \alpha(I_c/2 + I_d) + i/(2k\ell_0)$. In the energy conserving case $\alpha \in \mathbb{R}$, it can be shown that C_2 does not contribute to the real part of the backscattering coefficient Γ_C. Since, in this case, the Cooperon cross section, Eq. (14), exhibits a complex phase factor, it follows from Eq. (10) that the nonlinearity introduces a phase difference $\Delta\phi = Mk\ell_0\alpha I$ between reversed paths undergoing M linear scattering events. Since $\langle M\rangle \propto b$, we predict a significant reduction of the CBS peak if $bk\ell_0\alpha I \simeq 1$ (which is still inside the stable regime if $k\ell_0$ is large).

In summary, we have extended the usual diagrammatic approach to take into account nonlinear effects for the coherent transport in disordered systems beyond the perturbative regime. The excellent agreement with direct numerical simulations emphasizes the validity of our approach. It readily applies for different nonlinear wave equations. Equation (13), for example, is mathematically equivalent to the Gross-Pitaeskii equation describing nonlinear propagation of matter waves in random potentials. In this case, our method will allow us to describe not only the localization properties of the mean field, but also, extending it within the Bogoliubov framework, the effect of the noncondensed atoms. Furthermore, nonlinear transport of light in cold atomic gases [6] can be described by including inelastic scattering (Mollow's triplet). Finally, our present theory, combined with the usual self-consistent approach of strong localization [14], can possibly allow a quantitative understanding of the impact of the nonlinearity in the strong scattering regime.

We thank D. Delande and C. Miniatura for fruitful discussions. T. W. acknowledges support from the DFG.

[1] B. Spivak and A. Zyuzin, Phys. Rev. Lett. **84**, 1970 (2000).
[2] S. E. Skipetrov and R. Maynard, Phys. Rev. Lett. **85**, 736 (2000).
[3] T. Paul *et al.*, Phys. Rev. A **72**, 063621 (2005).
[4] D. L. Shepelyansky, Phys. Rev. Lett. **70**, 1787 (1993).
[5] D. Clément *et al.*, Phys. Rev. Lett. **95**, 170409 (2005); C. Fort *et al.*, Phys. Rev. Lett. **95**, 170410 (2005); T. Schulte *et al.*, Phys. Rev. Lett. **95**, 170411 (2005).
[6] T. Chanelière *et al.*, Phys. Rev. E **70**, 036602 (2004); S. Balik *et al.*, J. Mod. Opt. **52**, 2269 (2005).
[7] H. Cao, Waves Random Media **13**, R1 (2003).
[8] M. B. van der Mark, M. P. van Albada, and A. Lagendijk, Phys. Rev. B **37**, 3575 (1988).
[9] R. W. Boyd, *Nonlinear Optics* (Academic, San Diego, 1992).
[10] T. Wellens *et al.*, Phys. Rev. E **71**, 055603(R) (2005); Phys. Rev. A **73**, 013802 (2006).
[11] T. Wellens and B. Grémaud, J. Phys. B **39**, 4719 (2006).
[12] J. W. Goodman, J. Opt. Soc. Am. **66**, 1145 (1976).
[13] A. J. van Wonderen, Phys. Rev. B **50**, 2921 (1994).
[14] D. Vollhardt and P. Wölfle, Phys. Rev. Lett. **48**, 699 (1982); S. E. Skipetrov and B. A. van Tiggelen, Phys. Rev. Lett. **96**, 043902 (2006).